Spring 5-30-2021

Hydrodynamic Impacts of Expanding Aquaculture

Zhilong Liu
University of Maine, zhilong.liu@maine.edu

HYDRODYNAMIC IMPACTS OF EXPANDING AQUACULTURE

By

Zhilong Liu

B.S. Tianjin University, 2012

M.S. Tianjin University, 2015

A DISSERTATION

Submitted in Partial Fulfillment of the

Requirements for the Degree of

Doctor of Philosophy

(in Civil and Environmental Engineering)

The Graduate School

The University of Maine

May 2021

Advisory Committee:

Kimberly D. Huguenard, Associate Professor of Civil and Environmental Engineering, Advisor

Lauren Ross, Assistant Professor of Civil and Environmental Engineering

Shaleen Jain, Professor of Civil and Environmental Engineering

Huijie Xue, Professor of Maine Sciences

David W. Fredriksson, Professor of Naval Architecture and Ocean Engineering

HYDRODYNAMIC IMPACTS OF EXPANDING AQUACULTURE

By Zhilong Liu

Dissertation Advisors: Dr. Kimberly Huguenard

An Abstract of the Dissertation Presented
in Partial Fulfillment of the Requirements for the
Degree of Doctor of Philosophy
(in Civil and Environmental Engineering)
May 2021

Climate change may potentially change aquatic systems and bring certain risks for aquaculture development. Understanding interactions between aquaculture and the environment helps to ensure aquaculture expansion is sustainable in the future. It is critical to determine how farms influence tidal flow patterns, turbulence, mixing and material transport in estuaries. This research aims to determine the flow response of an oyster farm, predict how expanding farms and farm placement will alter estuarine dynamics, and understand how the design of a farm influences material transport.

The hydrodynamic response of a floating oyster aquaculture farm in a low inflow estuary (the Damariscotta River estuary) is investigated using hourly field observations covering both neap and spring tidal conditions and an idealized numerical model. Given the importance of lateral processes in estuaries, particularly those with channel complexities such as channel bends, we hypothesize that the farm-imposed drag force will affect the nearby dynamics in the channel and that the farm effects will not be localized to the farm area. A bulk drag coefficient for the whole farm, as well as for a single oyster cage was derived and implemented into an idealized regional scale model to qualitatively repeat patterns observed from field. The qualitative consistency between field observation and idealized model results provides valuable insight into the hydrodynamic response of a floating oyster farm.

The field observations also depicted a reversal in subtidal flow patterns compared with those typically expected in an elongated estuary. To better understand the mechanisms driving subtidal flow reversal, a semi-analytical model for a low inflow estuary with farm drag force was developed. The model captured

surface flow reduction and flow bypassing, consistent with field observations. Without the farm, subtidal flows were laterally sheared with inflow on the right-hand side and outflow on the left. The reduction of tidal flow from drag force in farm area resulted in tidally averaged along channel advection at the seaward and landward farm boundaries that drove subtidal flows into the farm. Inside the farm, the reduced tidal currents near the surface combined with upwelling and downwelling at the channel-shoal interface to produce tidally rectified flow, which altered the subtidal flow structure compared to the case with no farm. The transport of Lagrangian particles demonstrated how various farm expansion scenarios hindered seaward long-term transport in the estuary portions upstream of the farm.

The semi-analytical hydrodynamic model combined with a material transport model was further applied to investigate the sensitivity of farm layout to food uptake, which showed that a bluff layout (wide and narrow) was optimal since more nutrients can be transported into the farm through wider landward or seaward boundary. Expanding individual farm size decays filtration per unit area in the farm, where the filtration over a tidal cycle per unit area yields a logarithmic decay with length expansion and hyperbolic decay with width expansion. Therefore, the feedback between the hydrodynamics and the farm can deteriorate the food supply. Additionally, in shallow estuarine locations, bottom generated turbulence can overcome weak stratification to transport bottom sediment upward, resulting high near surface turbidity that might negatively impact oyster growth. Based on the linkage between near surface turbidity to tidal mixing, and stratification a critical depth for farm siting was proposed to minimize surface water turbidity.

Outcomes from this work highlight the importance of understanding interactions between aquaculture and environments. The hydrodynamic and hydrographic conditions that control species growth factors are highly variable and site specific, therefore acquiring detailed environmental data and thoughtfully evaluating interactions between aquaculture and the environment are beneficial approaches for farm planning. Both a field data collection strategies and modeling tools from this work can be used to promote environmental and economical sustainability in aquaculture expansion in the future.

DEDICATION

To this era and to my parents, my wife, and my daughter.

ACKNOWLEDGEMENTS

On May 20, 2015, the day of my 26-year-old birthday, I boarded the flight from Beijing to the United States. On May 20, 2015, the "another" day of my 26-year-old birthday, I arrived in Bangor and started my new life in Maine. Over the past six years, I learned work in the field, I learned work in front of the computer, and I learned understanding natural philosophy from math. Before May 20, 2021, the day of my 32 years old birthday, I summarize all the work done in the past six years and hope it is worth a doctoral degree.

Looking back, I am grateful for all the support from families, advisors, and friends. I would like to sincerely thank Dr. Qingping Zou for accepting me as a PhD student, which was the beginning of my journey in Maine. I would like to show my most sincere appreciation to my advisor Dr. Kimberly Huguenard for accepting me as a PhD student for the second time, which allowed me to complete the rest of the story. I really appreciate their supervision, guidance, and support during the PhD period. I appreciate their time, effort, and patience. Great acknowledgement to my committee, Dr. Lauren Ross, Dr. Shaleen Jain, Dr. Huijie Xue, and Dr. David W. Fredriksson for their insight and comments on my research.

I appreciate Dr. Shane Moeykens, Dr. Peter van Walsum, and Dr. Denise Skonberg for the support from SEANET project. I am thankful to Stephen Cousins and the Advanced Computing Group at The University of Maine System for computational support. I am also grateful to Dr. Haifei Chen, Dr. Dongmei Xie, Dr. Longhuan Zhu, Mr. Sohaib Alahmed, and Mr. Preston Spicer for sharing and discussing research ideas. Great thanks to Mr. Elliot Huguenard, Dr. Neal Fisher, Mr. Kristopher Bears, Miss Kyah Lucky, Dr. Brandon Lieberthal, and Miss Brigitte Parady for helping to collect data and Mr. Dylan Schlichting for helping with experiments. I would also like to sincerely thank Dr. Kelly Cole for discussions on the numerical simulations using ROMS. Finally, I would send my love to my family for their understanding and support.

This work was financially supported by National Science Foundation award #IIA-1355457 to Maine EPSCoR at the University of Maine.

TABLE OF CONTENTS

DEDICATION iii

ACKNOWLEDGEMENTS iv

TABLE OF CONTENTS v

LIST OF TABLES xii

LIST OF FIGURES xiii

Chapter

1. INTRODUCTION 1

1.1. Motivation and Research goals 1

1.2 Aquaculture Sustainability 3

1.3. Research Gaps 4

1.3.1. Flow Response to Aquaculture Farm 4

1.3.2. Parameterization of Farm Impacts 6

1.3.3. Farm Design 7

1.4. Research Tasks 9

1.4.1. Hydrodynamic Response of a Floating Aquaculture Farm 9

1.4.2. Farm Impact on Estuarine Dynamics 10

1.4.3. Farm design considerations of water depth and layout 10

1.5. Summary 11

2. HYDRODYNAMIC RESPONSE OF A FLOATING AQUACULTURE FARM IN A LOW INFLOW ESTUARY 12

2.1. Introduction 12

2.1.1. Flow Patterns Near Farms 13

2.1.2. Turbulence and Mixing Near Farms 14

2.1.3. Farm - Induced Drag Coefficients 14

2.2. Methods 16

2.2.1. Study Site 16

2.2.2. Data Collection 18

2.2.3. Numerical Modeling 20

2.3. Data Processing 21

2.3.1. Momentum Equation 21

2.3.2. Turbulence and Mixing 23

2.3.3. Drag Coefficient 27

2.4. Results 29

2.4.1. Peak Flood 29

2.4.1.1. Tidal Flow Patterns 29

2.4.1.2. Turbulence and Mixing 31

2.4.1.3. Streamwise and Normal Momentum 34

2.4.2. Peak Ebb 36

2.4.2.1. Tidal Flow Patterns 36

2.4.2.2. Turbulence and Mixing 37

2.4.2.3. Streamwise and Normal Momentum 38

2.4.3. Dependence of Lateral Circulation on Streamwise Advection 41

2.4.4. Mixing Mechanism 43

2.4.5. Bulk Drag Coefficients 47

2.4.6. Model Results 48

2.5. Discussion 51

2.5.1. The farm's Impact on Intratidal Dynamics 51

2.5.2. The farm's Friction Effect Versus. Channel Curvature 54

2.5.3. Uncertainty in the Drag Coefficients 55

2.6. Conclusions 58

3. ANALYTICAL INVESTIGATION INTO FLOATING AQUACULTURE FARM IMPACT ON TIDAL AND SUBTIDAL FLOWS 60

3.1. Introduction 60

3.2. Model 63

3.2.1. Tidal flow 63

3.2.2. Analytical solution of tidal flow 67

3.2.3. Subtidal flow 68

3.3. Analytical model for Damariscotta River estuary 70

3.3.1. Damariscotta River estuary 70

3.3.2. Data collection 71

3.3.3. Model setup 71

3.3.4 Idealized transport time 73

3.4. Results 74

3.4.1. Tidal Flow 75

3.4.2. Subtidal Flow 79

3.4.3 Impact of farm area on material transport 80

3.5. Discussion 83

3.5.1. Mechanisms Driving Subtidal Flow 83

3.5.2 Particle trajectories 88

3.5.3. Model Novelty and Limitations 91

3.6. Conclusions 92

4. FLOATING OYSTER AQUACULTURE FARM DESIGN CONSIDERATIONS: WATER DEPTH AND FARM LAYOUT 94

4.1. Introduction 94

4.2. Field observation 97

4.2.1. Study site 97

4.2.2 Data collection 99

4.3. Hydrodynamic and hydrographic conditions 100

4.3.1. Intratidal variations 100

4.3.2 Chlorophyll a 102

4.3.3 Linkage of turbidity and boundary layer thickness 105

4.3.4 Critical water depth 107

4.4. Material transport 108

4.4.1 Physical model 108

4.4.2 Model setup 110

4.5. Model results 113

4.5.1. Impact of farm layout on filtration 113

4.5.2 Impact of farm expansion and location 114

4.6. Discussion 120

4.6.1. Farm design considerations 120

4.6.2. Limitations 122

4.7. Conclusions 123

5. CONCLUSIONS 124

5.1 Findings and academic contributions 124

5.2. Application for aquaculture sustainability 126

5.3. Future work 127

BIBLIOGRAPHY 129

APPENDIX A: A DEPATH AVERAGED MOMENTUM EQUATION 139

A.1 Depth integrated momentum equation 139

A.2 Transformation from east-north coordinate system to along and across channel coordinate system 141

APPENDIX B: EFFECTIVE DRAG COEFFICIENT OF ISOLATED CAGE 147

B.1 The effective drag coefficient of isolated cage 147

APPENDIX C: FARM IMPACT ON FLOW PATTERNS AND MIXING DURING NEAP TIDE…..... 150

C.1 Tidal Current at Peak Flood 150

C.2 Vertical Eddy Diffusivity During Neap Tide 150

APPENDIX D: SENSITIVITY ANALYSIS OF STREAMWISE ADVECTION TERM 153

APPENXID E: THREE-DIMENSIONAL SEMI-ANALYTICAL MODEL WITH FLOATING AQUACULTURE FARM 155

E.1 Governing Equation for Tidal Flow 155

E.2 Vertical eddy viscosity parameterization 157

E.3 Analytical solution of velocity profile 160

E.3.1 Decouple Coriolis forcing 160

E.3.2 Solutions at Layer $j = \mathrm{I1}, \mathrm{II1}, \mathrm{III}$ 161

E.3.3 Solutions at Layer $j = \mathrm{IV}$ 162

E.3.4 Solutions at Layer $j = \mathrm{V}$ 163

E.3.5 Solution of Tidal amplitude 164

E.4 Subtidal Flow 169

E.5 Solution of velocity profiles 172

E.5.1 Layer 1 $-1 \leq \sigma \leq \sigma h$ 172

E.5.2 Layer 2 $\sigma \geq \sigma h$ 173

E.5.3 Solution for subtidal surface slope 174

E.6 Validation of vertical eddy viscosity parameterization canopy flow 176

E.7. Verification of tidal flow 178

BIOGRAPHY OF THE AUTHOR 181

LIST OF TABLES

Table 2.1 Input parameters for semi-analytical model..... 72

LIST OF FIGURES

Figure 1.1 (a) Global production of mollusks bivalves from Year 2010 to 2018. (b) Major cultured species in Year 2018. 2

Figure 2.1 Study area map of the Damariscotta River and field campaign strategy. 17

Figure 2.2 (a) Example spectrum of vertical shear of velocity, $\Psi(k)$. (b) Spectrum of vertical velocity fluctuation, $S_{w'w'}(f)$, (solid lines). (c) Conceptual sketch of streamwise velocity, u_s, and Reynolds stress, $\overline{u_s'w'}$, profiles for suspended canopy flow 25

Figure 2.3 Velocity and streamwise vorticity distribution across the estuary during peak flood (a.1 and b.1) Contours of streamwise velocity, u_s. (a.2 and b.2) Contours of normal velocity, u_n. (a.3 and b.3) Depth-averaged streamwise vorticity, ω_s. 30

Figure 2.4 Flow, turbulence, and mixing patterns at peak flood 33

Figure 2.5 Momentum terms of streamwise and normal flows along seaward and landward transects at peak flood. 35

Figure 2.6 Velocity and streamwise vorticity distribution across estuary during peak ebb. (a.1 and b.1) Contours of streamwise velocity u_s. (a.2 and b.2) Contours of normal velocity, u_n. (a.3 and b.3) Depth-averaged streamwise vorticity, ω_s. 37

Figure 2.7 Flow, turbulence, and mixing patterns at peak ebb 39

Figure 2.8 Momentum terms of streamwise and normal flows along landward and seaward transects at peak ebb. 40

Figure 2.9 Correlation between downstream transect depth-averaged streamwise vorticity, $\overline{\omega_s}$, and depth-averaged streamwise advection, $\overline{u_s \frac{\partial u_s}{\partial s}}$ 43

Figure 2.10 Time series of vertical eddy diffusivity, K_z, and time scale, τ, analysis for vertical mixing induced by lateral processes. 45

Figure 2.11 (a) Time series of streamwise velocity, u_s, and friction velocity measured by ADV through the entire tidal cycle. (b) Time series of bulk drag coefficient, C_D, estimated from Reynolds stress and dissipation rates; bulk friction coefficient, C_f, estimated Reynolds stress during flood phase..... 47

Figure 2.12 Velocity vectors at the free surface during peak flood from the Regional Ocean Modeling System (ROMS) model simulation with and without the farm 49

Figure 2.13 Velocity and streamwise vorticity distribution across the estuary at peak flood from Regional Ocean Modeling system (ROMS) model simulation with and without farm 51

Figure 2.14 Conceptual sketch of flow patterns and mixing mechanisms at landward and seaward transects: (a) flood phase of tide and (b) ebb phase of tide..... 53

Figure 3.1 The model bathymetry h (x, y)is arbitrary across the channel and converges in width and depth along a curved channel.. 64

Figure 3.2 Shape factor (A_σ) of vertical eddy viscosity without (a) and with farm (b).. 66

Figure 3.3 (a) Local map of floating oyster farm. (b.1 ~ 2) Observations of along (u_T) and across (v_T) channel subtidal velocity near farm's seaward boundary.. 75

Figure 3.4 Semidiurnal (M2) tidal current near farm's seaward boundary..... 77

Figure 3.5 Model results of surface tidal current velocity at peak flood.. 78

Figure 3.6 Along (u_T) and across (v_T) channel subtidal velocity from the model.. 80

Figure 3.7 Normalized change in transport time of particles released at surface in the upstream portion of the estuary.. 81

Figure 3.8 Averaged transport time of all particles released at surface in upstream portion of the estuary with respect to ratio of farm area to cross area of estuary portion..... 82

Figure 3.9 Driving mechanism for along-channel subtidal velocity..... 84

Figure 3.10 Conceptual schematic of along channel subtidal flow reversal inside of farm..... 87

Figure 3.11 Trajectories of particles transport at surface released at end of flood. 89

Figure 4.1 Map of the Damariscotta River and field campaign strategy.. 98

Figure 4.2 Time series of intratidal velocity, density, and turbidity at the farm's seaward and landward boundaries during spring tide..... 101

Figure 4.3 (a) Time series of tidal surface elevation, turbidity, and chlorophyll at a water depth of 1 m collected by the LOBO buoy.. 103

Figure 4.4 (a) turbidity at water depth of 1 m vs. mixing number, $M = h_{bl} / h$ through ebb during spring tide and neap tide. (b) design chart of critical water depth for floating aquaculture farm 106

Figure 4.5 (a)The model bathymetry h (x, y) across channel and converges in width and depth along a curved channel. (b, c) studies cases of different farm designs including layout, expansion, and location..... 112

Figure 4.6 Distributions of filtration F in different farm layouts..... 115

Figure 4.7 Distributions of filtration F in farm expansion and changing location..... 116

Figure 4.8 Subtidal flow patterns at surface with farm located on left side (a) and right side (b) of the estuary ……..……..... 115

Figure 4.9 (a) Impacts of farm length expansion on spatially averaged filtration under different farm width. 119

Figure 4.10 Schematic diagram of changing farm layout from a single blender patch (a) to multiple patches in bluff and staggered layouts (b).. 121

Figure A1 Transformation between *x*-*y* coordinate system and *s*-*n* coordinate system.……..142

Figure C1 Velocity and streamwise vorticity distribution across the estuary at peak flood during neap tide conditions.. 151

Figure C2. Time series of vertical eddy diffusivity, K_z, and time scale, τ, analysis for vertical mixing induced by lateral processes along seaward and landward transects over the entire tidal cycle during neap tide conditions..... 152

Figure D1 Sensitivity analysis of depth-averaged streamwise advection term, $\overline{u_s \frac{\partial u_s}{\partial s}}$ on data selection... 154

Figure E1. Validation of analytical model with laboratory experiments.. 178

Figure E2 Time series of along (u_0) and across (v_0) semidiurnal (M2) tidal current at water depth of -0.9 m in the main channel near farm's seaward boundary. 179

Figure E3 Near surface tidal current velocity at peak flood.. 180

CHAPTER 1

INTRODUCTION

1.1. Motivation and Research goals

According to the Food and Agriculture Organization of the United Nations (FAO 2020), global aquaculture production reached 82.1 million tons in 2018. Development of aquaculture contributes to global food security, where the global per capita food fish consumption grew from 9.0 kg in 1961 to 20.5 kg in 2018. It is anticipated that 62% of seafood consumed will be from aquaculture by 2030 and the demand will continuously grow with time. In 2050, the global population is expected to reach 9 billion (FAO, 2013). Harvesting food from the ocean is the only viable option to meet the demand due to the scarcity of cultivated land resources for farming (Mustafa et al. 2017).

Today, aquaculture is by far the dominant source of bivalves. In 2018, the production of bivalve mollusks reached up to 17.51 million tons (Figure 1.1a), which accounted for 23.1% of total aquaculture production (FAO 2020). The total production of oyster was 5.81 million tons, which was 33.2% of total production of bivalve mollusks (Figure 1.1b). Comparing with 2010, oyster production increased by 38.1%, with an average annual growth of 4.1%. Despite substantial growth from the mid-2010s to the early 2020s, the oyster aquaculture industry is still far behind the required growth rate in aquaculture (9.9% per year) to fill the demand–supply gap. Accordingly, the substantially increasing demand for bivalves over time will catalyze expansion of the oyster aquaculture industry.

In Maine, USA, the harvest of farm-raised eastern oyster *Crassostrea virginica* reached up to 13.9 million pieces with landings worth up to US $9.67 million in 2019. The annual harvests in 2019 were 7.75 times of those in 2011 showing an average annual growth of 29.2%. The Damariscotta estuary is the largest oyster producer in Maine, where nearly 67.5% of the current statewide harvest takes place (Maine Department of Marine Resources 2019). Note that Maine's 5,600 km of shoreline provides high economic and ecological

opportunities for oyster aquaculture. A better understandings of suitable culture habitats would help expand oyster aquaculture into other regional estuaries (Adam et al., 2019).

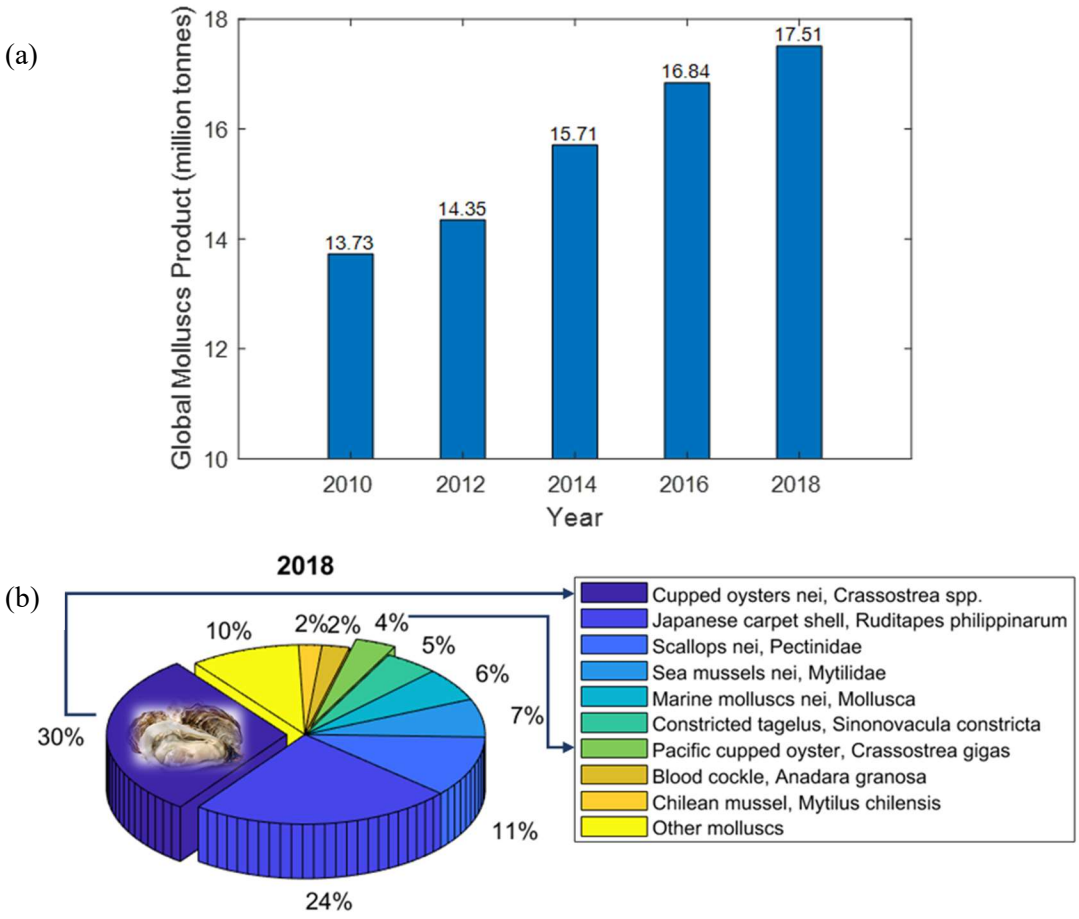

Figure 1.1 (a) Global production of mollusks bivalves from Year 2010 to 2018. (b) Major cultured species in Year 2018(data from FAO 2020).

Furthermore, climate change in the future could potentially change aquatic systems and bring certain risks for aquaculture development. It has been reported that CO_2 concentrations have increased by 40% since pre-industrial times resulting in unequivocal climate warming, sea level rise, ocean acidification,

pronouncing stratification and hypoxia (FAO, 2018). Meanwhile, climate change also affects precipitation and melting of snow and ice, which are changing hydrological systems such as global and local ocean circulation and altering water quantity and quality. All the above factors driven by climate change may have negative impacts on farming conditions and infrastructure failure caused by extreme climate events. Both the realistic demand and potential risks implied by climate change will intensify the tension in sustainable aquaculture development.

1.2 Aquaculture Sustainability

Aquaculture sustainability contains three dimensions: (1) **Environmental sustainability - a**quaculture should not create significant disruption to the ecosystem; (2) **Economic sustainability --** aquaculture must be long-term viable business; and (3) **Social and community sustainability-** aquaculture must be socially responsible and contribute to community well-being (the World Summit on Social Development, 2005; the World Bank, 2014). Sustainable aquaculture is a dynamic concept, and the sustainability of an aquaculture system will vary with species, location, societal norms and the state of knowledge and technology. The key aspects to ensure oyster aquaculture sustainability include environmental practices in order to fully understand oyster aquaculture and environment interaction and to effectively monitor and control water quality. Additionally, sustainable business and farm management practices must be in order to have efficient harvests and economic benefits. Lastly, community practices should be established to delineate well-defined aquaculture zones and encourage community involvement. The above key practices require comprehensive and interdisciplinary research efforts covering the physical, biochemical, ecological, economic, and engineering aspects to promote the sustainable development of aquaculture.

The goal of this research aims to contribute to environmental and economic sustainability in aquaculture expansion. This work intends to understand how existing farms and adding new farms affect hydrodynamics and material transport such as residence times in order to minimize the farm impacts on the system. In addition, hydrodynamic processes may influence food uptake and cause heterogeneity in oyster growth along the farm. This work aims to determine if alternative farm design could potentially improve food uptake (i.e. oyster growth rates). This research has three foci: (1) to determine the flow response to an oyster farm, (2) to predict how expanding farms and farm placement will alter estuarine dynamics, and (3) understand how the design of a farm influences material transport. This will be achieved with a combination of field measurements, as well as analytical and numerical models.

1.3. Research Gaps

Hydrodynamics play a crucial role in oyster aquaculture, where growth is influenced by hydrographic and biochemical factors (salinity, temperature, turbidity, oxygen, particle of organic matter) and the food supply are correlated with the hydrodynamics of the environment through transport and mixing (Campbell and Hall, 2019). The interactions between aquaculture farms and their surrounding environments must be understood to determine the carrying capacity of the system (Weitzman and Filgueira, 2020). Furthermore, understanding biochemical phenomena from a physical point of view could help to reveal control mechanisms and offer instructive guidance to aquaculture.

1.3.1. Flow Response to Aquaculture Farm

Suspended shellfish farms induce drag to the aquatic environment resulting in multiple types of fluid responses including current redistribution and reduction (Lin et al., 2016; Plew et al., 2006; Wu et al., 2014; Wu et al., 2017), turbulence generation (Plew, 2011a), and suppression (Plew et al., 2005; Plew et

al., 2006; Rosman et al., 2007; Stevens and Petersen, 2011), as well as increased residence time and nutrient depletion (Plew, 2011b; Wang et al., 2018). These fluid responses can impact food depletion and renewal, in addition to the carrying capacity of the system (Aure et al., 2007; Johansson et al., 2007). Neglecting the hydrodynamic changes imposed by shellfish farms results in overestimations of the nutrient supply and carrying capacity of a system (Grant and Bacher, 2001; O'Donncha et al., 2013). It remains to be understood how local and surrounding hydrodynamics are impacted by floating shellfish farms.

Field observations and large-scale numerical simulations have previously demonstrated that aquaculture farms can influence tidal flow in realistic settings, such as bays and the open ocean. Flow patterns around the farms during flood and ebb are similar to the unidirectional flow results. Surface shear layers can form under suspended kelp farms (Fan et al. 2009) and mussel rafts (Lin et al. 2016). Flow reduction within farm is identified in both field observations (Lin et al. 2016) and large-scale numerical simulations (Plew et al. 2011, O'Donncha et al. 2013), as well as flow acceleration beneath aquaculture farms (Wu 2017, O'Donncha et al. 2017). In a suspended mussel farm, more flow is diverted around the farm rather than under the farm (Plew et al. 2006).

Turbulence is generated in shear layers around farm structures or near boundary layers and in the wakes behind structures. Indicators of the level of turbulence, such as Reynolds stress and turbulent kinetic energy (TKE), are intensified near farms (Plew 2010; Kervella et al. 2010; Han et al. 2017). In suspended aquaculture farms, vertical mixing within the farm is driven by the shear layer under the farm, in addition to wake turbulence generated by droppers (i.e., mussel chains and oyster cages) within the farm (Plew et al. 2006; Abdolahpour et al. 2017). Unlike uniform density in laboratory conditions, tidal bays and estuaries often feature freshwater input, which has implications for turbulence and mixing. Stratification (layers of vertically varying density) acts to suppress the development of turbulent eddies and the mixing (homogenizing) of density layers. Field observations of a suspended mussel farm in a stratified macrotidal ($t > 4$ m tidal ranges) bay found that the farm enhances stratification at the farm's leading edge. This results in the suppression of vertical mixing driven by the shear layer under the farm, while the turbulence within

the canopy is enhanced due to form drag (Plew et al. 2006). However, in a microtidal (< 2 m) estuary, a suspended mussel farm can reduce flow within the farm, resulting in reduced levels of turbulent kinetic energy and vertical mixing (Stevens and Petersen 2011). Both studies highlight the complexity of studying interactions between farm induced turbulence and stratification due to the natural variability of each system.

Shellfish farm structures include bottom cages and tables, as well as suspended and floating cages. Floating farms are a relatively new orientation that benefit from food being concentrated near the surface due to higher temperature and light availability. Considering this benefit and their recent popularity, floating farms is the focus of this investigation. The above laboratory, field and numerical studies show how various aquaculture farms influence flow locally, that is, directly beneath, behind, or beside farms. **The scientific gap this research will fill is how a floating oyster farm can influence the dynamics in an estuary, including how farms change momentum along and across an estuary, and how farms influence subtidal flow structures, turbulence, and vertical mixing patterns.**

1.3.2. Parameterization of Farm Impacts

One way to consider the effects of aquaculture farms on flow in analytical and numerical models is to implement a drag coefficient. The drag coefficient of submerged canopies (i.e., coral reef and vegetation) and suspended canopies (i.e., mussel and kelp) can be determined experimentally from the directly measured load (Osorio-Cano et al. 2016; Plew et al. 2009; Tseung et al. 2016) or based on the momentum balance between the pressure gradient and drag force (McDonald et al. 2006; Plew 2010). Drag coefficients from both methods are consistent with one another (Asher et al. 2016).

Determination of the bulk drag coefficient of aquatic canopies from field observations is more complicated compared to experimentally derived coefficients. Recent studies reported drag coefficients of submerged oyster and coral reefs using field measurements. Typical approaches are to either fit the velocity profiles above the bottom to the original (Reidenbach et al. 2006, Whitman and Reidenbach 2012) or

modified (Rosman and Hench 2011) log-law profile; use field collected turbulence parameters such as Reynolds stress (Reidenbach et al. 2006, Tarya et al. 2010) and TKE dissipation rate (Reidenbach et al. 2006, Wijesekera et al. 2014); or to use the momentum balance (Rosman and Hench 2011, Lentz et al. 2017).

A limited number of studies have measured drag coefficient of suspended farms directly using field observations. Drag coefficients of kelp (Fan et al. 2009) and mussel farms (Lin et al. 2016) were previously measured by fitting the subsurface velocity profile to log-law profile. Drag coefficients of a suspended salmon farm was obtained by tuning the coefficient in a numerical model to match the velocities from field observations (Wu et al. 2014). The configuration of a floating oyster farm is inherently different from bottom-rooted vegetation, mussel chains and kelp, which represent slender bodies. Therefore, it is unreasonable to directly reference drag coefficients of slender canopies for floating oyster farms. **The scientific gap this research is filling is it will define a drag coefficient for floating oyster farms, which can be used in a regional numerical model and an analytical modeling to reproduce hydrodynamic impacts and to predict how expanding farm size impacts estuarine dynamics and material transport.**

1.3.3. Farm Design

The engineering aspects of aquaculture includes farm siting and design. Field studies have revealed that stratification and flow conditions are the main factors influencing other environmental conditions within aquaculture farm. For example, a reduction in flow passing through salmon cages leads to lower oxygen levels inside the cage compared to the outside (Johansson et al. 2007). High culture densities may cause food depletion, resulting in low growth and inferior-quality products (Aure et al. 2007). Neglecting farm drag can result in over prediction of dispersal and nutrient supply and under prediction of depletion within farms (Plew 2011, Grant and Bacher 2001, O'Donncha et al. 2013). Besides from vertical diffusion, favorable and beneficial horizontal diffusion was reported to dominate material transport based on some

field observation (Stevens and Petersen 2011). Although, it has been conceptually proposed that well-planned stocking density; farm positioning and layout can lower the farm drag effect and enhance food supply and dispersal (Ferreira et al. 2007, Plew 2011, Stevens and Petersen 2011, Aure et al. 2007).

Besides temperature, salinity, and chlorophyll, it has been reported that high turbidity could potentially decrease oyster feeding and growth by diluting algal cells with largely inorganic matter. Dame et al. (1985) reported that chlorophyll a uptake by an oyster reef during the ebb tide was only ~ 43% of that during the flood tide over 33 measured tidal cycles, where higher ebb tide current speeds result in more sediment resuspension (Dame et al., 1992). Oyster clearance and chlorophyll consumption rates were both negatively impacted by high turbidity during spring tides in intertidal zones (Gernez et al., 2017), whereas oysters presented better growth rates in low turbidity offshore areas (Barillé et al., 2020). Lower growth rates were also observed in floating oyster farms in an estuary and corresponded with tidal sediment resuspension (Adams et al., 2019). Although negative impacts from high turbidity have been recognized, the linkage between sediment resuspension and tidal straining as well as turbulence and mixing are not fully understood.

Quantitative studies on the linkage between farm design, including long-line length as well as layout of long-line groups, and local material transport near a farm under realistic hydrodynamic conditions are still required. Note that regional scale simulations could resolve the geophysical flow conditions but not the farm layout (Fan et al. 2020), while small scale studies were able to resolve farm structure yet were unable to represent the realistic conditions (Delaux et al. 2011). Therefore, few studies of farm layout on food delivery or filtered food in farm scale under realistic (or quasi-realistic) flow conditions were reported. Additionally, farm design guidelines corresponding to tidal driven sediment resuspension is not currently available. **The scientific gap this research will fill is understand the linkage between turbidity, vertical mixing, and stratification, as well as how various farm designs and layouts affect food delivery and absorption of the floating oyster farm in farm scale.**

1.4. Research Tasks

To fill the research gaps summarized in previous section, the interaction between a floating oyster farm and the surrounding environment was studied through field observations, numerical, and analytical modeling. The field observations will provide insight into flow patterns around a floating oyster farm, which were combined with simulations using a regional scale model to highlight farm impacts. A newly proposed three-dimensional semi-analytical model is applied to reveal and explain tidal and subtidal flow patterns inside and outside of the farm. The farm impacts on material transport and filtration are investigated as an application of the semi-analytical model.

1.4.1. Hydrodynamic Response of a Floating Aquaculture Farm

The hydrodynamic response of a floating oyster aquaculture farm in a low inflow estuary (the Damariscotta River estuary) are investigated using field observations and an idealized numerical model. Given the importance of lateral processes in estuaries, particularly those with channel complexities such as channel bends, we hypothesize that the farm-imposed friction will affect the nearby dynamics in the channel and that the farm effects will not be localized to the farm area. The research objectives of this work are to (1) determine the impact of surface friction imposed by a floating oyster farm on the intratidal variations of momentum across an estuary; (2) characterize turbulence and mixing related to the farm; (3) derive a bulk drag coefficient for the whole farm, as well as for a single oyster cage; and (4) implement the derived drag coefficient into an idealized model to isolate the farm's impact on the momentum. The field observations are the first of their kind and provide valuable insight into the hydrodynamic response of a floating oyster farm. The details in field campaign, data analysis and results are presented in Chapter 2.

1.4.2. Farm Impact on Estuarine Dynamics

Field observations demonstrated flow reduction, bypassing, and suppression in curvature driven circulation and reversal in subtidal flow patterns comparing with those typically expected in an elongated estuary. However, a comprehensive view of the tidal and subtidal flow patterns in the farm area and the mechanisms of farm induced subtidal flow reversal as well as consequential impacts on residence time remain unknown. Therefore, Chapter 3 aims to develop a semi-analytical model for a low inflow estuary with convergent width in order to simulate the influence of a floating farm on tidal and subtidal flows. The research objectives are to (1) develop a semi-analytical framework that includes a floating aquaculture farm drag coefficient derived from field observation (2) investigate the intratidal flow response of a floating farm, (3) determine how floating farms alter the subtidal flows and (4) investigate changes in residence time in the area upstream of a farm under various farm expansion scenarios including farm sizes and locations. The details of model development and application are presented in Chapter 3.

1.4.3. Farm design considerations of water depth and layout

Field studies in Chapter 2 highlighted that turbidity near the water surface increases during the ebb phase of the tide and reaches a maximum at the end of ebb, which would have negative impact on aquaculture. Analytical model results from Chapter 3 demonstrated farm size and location could change transport of surface particles. However, the linkage between turbidity, tidal mixing and stratification is unknown. Meanwhile the impact of farm layout on food delivery and filtration is still unclear. Therefore, Chapter 4 in this work mainly deal with farm design considerations covering critical depths to minimize surface water turbidity and optimize farm layout to maximize food filtration. The research objectives are to (1) understand the correlation between turbidity, vertical mixing, and stratification, (2) investigate the impact of farm layout on food delivery and filtration, and (3) provide farm design guidelines. Details of field data analysis and models results of material transport are demonstrated in Chapter 4.

1.5. Summary

Both global and local (Maine, USA) oyster aquaculture presents potential expansion. In this chapter, research efforts in physics and engineering were reviewed with research gaps in oyster aquaculture and hydrodynamic interactions highlighted. The research tasks tend to fill the research gaps and outline of the thesis are summarized.

CHAPTER 2

HYDRODYNAMIC RESPONSE OF A FLOATING AQUACULTURE FARM IN A LOW INFLOW ESTUARY

2.1. Introduction

In 2016, the total global aquaculture production reached up to 85 million tons and 232 billion USD (FAO, 2018). The growth of aquaculture production contributes to global food security by growing food fish consumption from 9.0 kg in 1961 to 20.2 kg in 2015 (Barange et al., 2018). By 2050, the global population is expected to reach 9 billion (Food and Agriculture Organization of the United Nations 2013). It is anticipated that 62% of seafood consumed will be from aquaculture by 2030 and demand will continue to grow with time. Harvesting food from the ocean is the ideal option to meet this demand due to the scarcity of cultivated land resources for farming (Mustafa et al., 2017). Therefore, guaranteeing the sustainable growth of aquaculture activities is crucial for the global economy. As compared with culturing in the open ocean, placing farms in sheltered environments like estuaries provides engineering installation and maintenance benefits as they are protected from wave action and generally installed in shallower environments. The goal of this work is to understand the interaction between aquaculture farms and the surrounding environment, so that expansion activities can be conducted sustainably.

Shellfish farm structures include bottom cages and tables, as well as suspended and floating cages. Floating farms are a relatively new orientation that benefit from food being concentrated near the surface due to higher temperature and light availability. Considering this benefit and their recent popularity, floating farms is the focus of this investigation. Floating farms act as obstructions in the water column, which alters flow patterns, turbulence, and mixing characteristics.

Suspended shellfish farms induce drag to the aquatic environment resulting in three types of fluid responses: current redistribution and reduction (Lin et al., 2016; Plew et al., 2006; Wu et al., 2014; Wu et al., 2017), turbulence generation (Plew, 2011a), and suppression (Plew et al., 2005; Plew et al., 2006;

Rosman et al., 2007; Stevens and Petersen, 2011), as well as increased residence time and nutrient depletion (Plew, 2011b; Wang et al., 2018). These fluid responses can impact food depletion and renewal, in addition to the carrying capacity of the system (Aure et al., 2007; Johansson et al., 2007). Neglecting the hydrodynamic changes imposed by shellfish farms results in overestimations of the nutrient supply and carrying capacity of a system (Grant and Bacher, 2001; O'Donncha et al., 2013). It remains to be understood how local and surrounding hydrodynamics are impacted by floating shellfish farms.

2.1.1. Flow Patterns Near Farms

Boundary layers arise from flow interaction with a surface and result in a velocity profile that varies with distance away from a bottom boundary or structure. These layers develop under different types of structures (referred herein as canopies) in unidirectional flow. For suspended canopies with large penetration lengths (i.e., vegetation and mussel droppers), the vertical profiles of velocity are divided into a bottom boundary layer, a canopy shear layer (i.e., a boundary layer caused by the structure), and an internal canopy layer (Plew, 2011a). The canopy shear layer can form some distance downstream and remain nearly constant after it is fully developed (Cornejo et al., 2014; Qiao et al., 2016; Zhao et al., 2017). When the underwater penetration length of canopies is much smaller than the water depth, such as oblate oyster bags and lotus (nelumbo) leaves, only the bottom boundary and canopy boundary layer occur (Gaurier et al., 2011; Han et al., 2018; Kervella et al., 2010). The surface boundary layer was observed under suspended kelp farms (Fan et al., 2009) and mussel rafts (Lin et al., 2016). Velocity is reduced in canopy-induced shear layer and boundary layer zones while it is accelerated out of these zones (Lin et al., 2016; O'Donncha et al., 2013; O'Donncha et al., 2017; Plew, 2011b; Wu et al., 2017).

2.1.2. Turbulence and Mixing Near Farms

Turbulence is inherently generated in shear layers around farm structures or near boundaries. Indicators of the level of turbulence, such Reynolds stress and turbulence kinetic energy (TKE), are intensified near farms (Han et al., 2018; Kervella et al., 2010; Plew, 2011a). In suspended aquaculture farms, vertical mixing within the farm is driven by the shear layer under the farm and wake turbulence generated by droppers (i.e., mussel chains and oyster cages) within the farm (Abdolahpour et al., 2017; Ghisalberti and Nepf, 2004; Plew et al., 2006). Unlike uniform density in laboratory conditions, tidal bays and estuaries often feature freshwater input, which has implications for turbulence and mixing. Stratification suppresses the development of turbulent eddies and the mixing of density layers. Field observations show that a suspended mussel farm can induce stratification at the farm's leading edge resulting in suppression of vertical mixing in the shear layer under the farm. However, form drag from the mussel chains can increase turbulence production within the farm (Plew et al., 2005; Plew et al., 2006).

2.1.3. Farm-Induced Drag Coefficients

In order to simulate the effects of aquaculture farms on flow in numerical models, a drag coefficient is typically utilized. The drag coefficient of submerged canopies (i.e., coral reef and vegetation) and suspended canopies (i.e., mussels and kelp) can be determined experimentally from the directly measured load (Osorio-Cano et al., 2016; Plew et al., 2009; Tseung et al., 2016) or based on the momentum balance between the pressure gradient and drag force (McDonald et al., 2006; Plew, 2011a). The drag coefficients from both methods are consistent with one another (Asher et al., 2016).

Determination of the bulk drag coefficient of aquatic canopies from field observation is more complicated compared to experimentally derived coefficients. Typical approaches used to estimate drag coefficients of submerged oyster reefs and coral reefs are to either fit the velocity profiles above the bottom to the typical log-law profile (Reidenbach et al., 2006; Whitman and Reidenbach, 2012) or deflect law

profile (Rosman and Hench, 2011); use field collected turbulence parameters such as Reynolds stress (Reidenbach et al., 2006; Tarya et al., 2010) and TKE dissipation rates (Reidenbach et al., 2006; Wijesekera et al., 2014); or use the momentum balance between barotropic pressure gradients and bottom friction (Lentz et al., 2017; Rosman and Hench, 2011).

A limited number of studies have measured drag coefficients of suspended farms directly using field observations. Gaylord et al. (2008) proposed drag parameterization of giant kelp based on field collected force. Drag coefficients of kelp (Fan et al., 2009) and mussel farms (Lin et al., 2016) were previously measured by fitting the subsurface velocity profile to log-law profile. Drag coefficients of a suspended salmon farm was obtained by tuning the coefficient in a numerical model to match the velocities from field observations (Wu et al., 2014). The configuration of a floating oyster farm is inherently different from bottom-rooted vegetation, mussel chains, and kelp, which represent slender bodies. Therefore, it is unreasonable to directly reference drag coefficients of slender canopies to floating oyster farms.

Previous laboratory, field and numerical studies show how various aquaculture farms influence flow locally, that is, directly beneath, behind, or beside farms. Given the important of lateral processes in estuaries, particularly those with channel complexities such as channel bends, we hypothesize that the farm imposed friction will affect the nearby dynamics in the channel and that the farm effects will not be localized to the farm area over the western shoal. The research objectives of this work are to (1) determine the impact of surface friction imposed by a floating oyster farm on the intratidal variations of momentum across an estuary; (2) characterize turbulence and mixing related to the farm; (3) derive a bulk drag coefficient for the whole farm, as well as for a single oyster cage; and (4) implement the derived drag coefficient into an idealized model to isolate the farm's impact on the momentum. The field observations, detailed in section 2.2, are the first of their kind and provide valuable insight into the hydrodynamic response of a floating oyster farm. The detailed processing methods are described in section 2.3, respectively. In section 2.4, we will show that the farm influences streamwise and normal momentum and can prevent the development of

lateral circulation. In section 2.5, we discuss the main findings and limitation in drag coefficient estimations. Conclusions and future research needs are drawn in section 2.6.

2.2. Methods

2.2.1. Study Site

This investigation takes place in the Damariscotta River in Mid Coast Maine, located in the northeast United States (Figure 2.1a). The Damariscotta River is a short system (~30 km) spanning from the Gulf of Maine to Damariscotta Lake (Chandler, 2016). The River has a complicated geography with varying bathymetry including multiple constrictions and bends. The width converges from approximately 975 m at the mouth to 450 m near the head. The main channel depth varies from 40 m at the mouth to less than 3 m at the head. This river is classified as a meso-tidal estuary with a semidiurnal tidal forcing that features a spring tidal range of approximately 3.6 m and neap tidal range of 2.2 m. The semidiurnal tidal constituent of surface current was around 0.20 m/s at the coast. It reached up to 0.55 m/s near the surface in the middle reach of the estuary. The subtidal flow structure exhibited a vertically sheared pattern near the mouth and a mix of vertically and laterally sheared patterns in the midstream and upstream reaches (Bears, 2018). In 2016, the freshwater discharge varied from 0.28 m^3/s in the dry season (Fall) to 14.1 m^3/s in the wet season (Spring) due to the existence of a dam upstream. Due to the seasonal variation of freshwater discharge, the river is weakly stratified during the dry season and partially stratified during the wet season.

Field observations were collected after the spring freshet to investigate farm-induced vertical mixing. Measurements were collected around the largest floating oyster farm near Perkins Point, covering a total area of 96,315 m^2 (Figure 2.1a). At this location, the width of the river is around 550 m and features a main channel bend with a radius R_{s1} = 850 m (Figure 2.1b). At the southern side of the farm, the main channel is 6 m deep, while a secondary channel 2.5 m deep emerges directly under the farm (Figure 2.1c).

The river has a constriction north of the farm resulting in a deeper (8 m) main channel and a secondary 5 m deep channel close to the eastern side. Further north, the main channel features an opposing bend with a radius R_{s2} = 700 m that influences the study area during the ebb phase (Figure 2.1b). The Perkins Point farm is located in the western part of the estuary, where the streamwise length is 650 m (Figures 2.1a and 2.1b). The width of the farm at the seaward (southern) transect is 150 m, and it narrows to 25 m at the landward (northern) transect (Figure 2.1c). The penetration length of the oyster cage is ~0.42 m below the water surface.

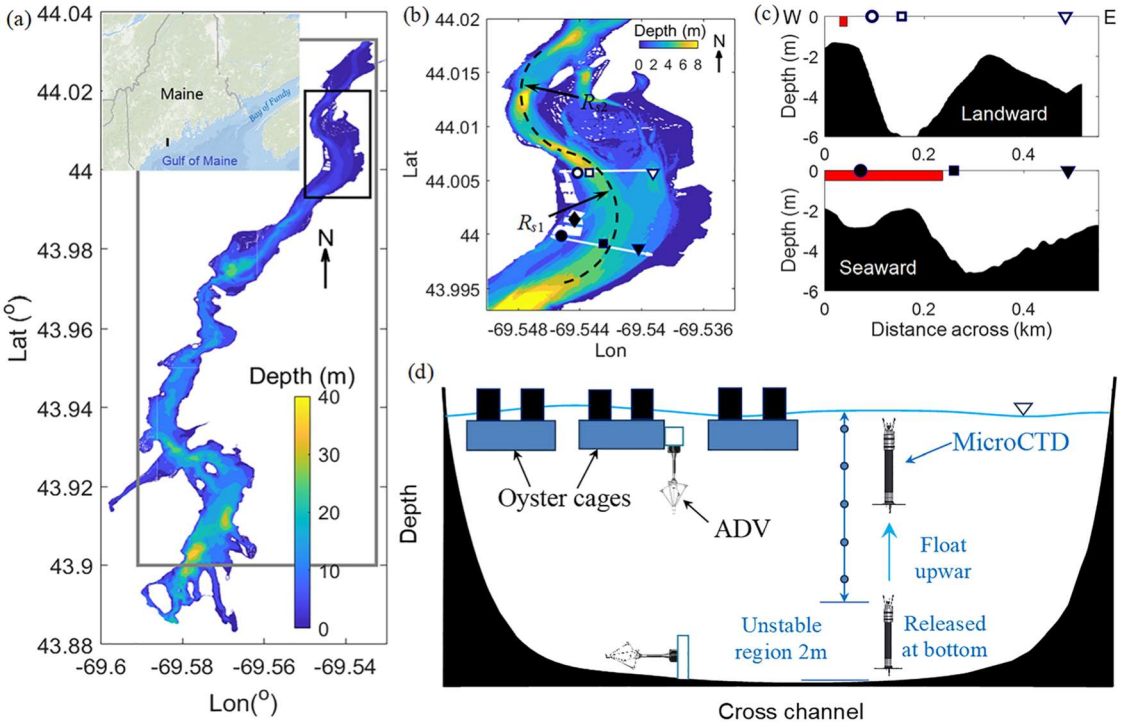

Figure 2.1 Study area map of the Damariscotta River and field campaign strategy. (a) Bathymetry of the Damariscotta River and farm site (Chandler, 2016). Black box denotes study area; gray box denotes the grid domain for the Regional Ocean Modeling system (ROMS) model. (b) Map of study area including farm configuration and locations of ADCPs, MicroCTDs, and ADV. R_{s1} and R_{s2} are curvature radius of bend in farm area and north of farm area. White gaps in the contour show the farm long lines. White double-end arrows mark

transects where ADCPs were towed along the surface. Markers show sampling locations of MicroCTDs across the river, where open and closed circles represent location around the farm near western shoal at two transects, open and closed squares represent location in the main channel at two transects, and open and closed triangles represent location near eastern shoal at two transects. The black diamond represents the ADV location. (c) Cross section of transect displaying bathymetry in reference to mean lower low water (MLLW) level. Red bars represent farm area. Other makers represent the three hydrographic station locations for MicroCTD. (d) Deployment of ADV and MicroCTDs. ADV was first moored to a platform attached to the side of an oyster cage sampling velocities at 1.0 m water depth (0.58 m to bottom of oyster cage) in the gap of two long lines and then moved to the river bottom sampling velocity 0.28 m above the bottom. MicroCTD was released at bottom and sampled the vertical turbulence profile when it was floating upward. Black squares are pontoons attached to oyster basket. Green ellipses are oyster bags.

2.2.2. Data Collection

In order to understand momentum changes across the estuary, cross sections of current velocities, density profiles, and TKE dissipation rates were obtained during an entire tidal cycle (~13 hr survey) on 16 June 2017 during neap tidal conditions and another tidal cycle on 23 June 2017 during spring tidal conditions. Two 1,200 kHz RDI Acoustic Doppler Current Profilers (ADCP) were mounted downward facing on Teledyne boats in order to synchronously sample two lateral transects of current velocity at 2 Hz on landward and seaward boundaries of the farm. For each hourly transect, ADCPs were towed across the river from west to east along the farm's landward and seaward boundaries to get the spatial distribution of velocity, as indicated by white arrows in Figure 2.1b. Data were collected in 0.25 m vertical bins with a 0.55 m blanking distance between the instrument and the first bin at 0.80 m. The bottom 10% of profiles was masked to account for sidelobe effects.

Two Rockland MicroCTDs collected vertical shear of velocity, temperature, conductivity, and pressure simultaneously at farm's landward and seaward transects. Each MircroCTD has two orthogonal air-foil type shear probes that sampled vertical shear of velocity at 512 Hz. Considering an average ascent rate of 0.8 m/s, this provided vertical shear measurements at a resolution of 10^{-3} s^{-1}. In addition, one conductivity-temperature combo sensor collected measurements at 64 Hz, obtaining resolutions of 1×10^{-3} mS/cm and 1×10^{-3} °C, respectively. Also sampling at 64 Hz was pressure sensor, which provided pressure observations at 5×10^{-4} bar. The vertical shear of velocity was used to estimate turbulent kinetic energy dissipation rate, ε, and conductivity, and temperature data were used to compute density, ρ.

The MicroCTD was deployed at three different stations across the river during each transect repetition. At the southern transect, the three stations were located behind the farm, in the channel, and over the eastern shoal, shown in Figure 2.1c. Due to the shallowness of the bathymetry near the farm at the northern transect, a station could not be placed directly behind the farm. Therefore, the northern transect included stations located adjacent to the farm, in the channel, and in the eastern secondary channel. The MicroCTDs were outfitted with a floatation collar and were lowered to the bottom with a cannon ball weight and release mechanism. Once at the bottom, the MicroCTD release mechanism was triggered simultaneously at each transect, which allowed for the profilers to ascent upward in order to collect data near the surface (Figure 2.1d). The instrument ascended upward until reaching a constant speed of 0.8 m/s approximately 2 m above the bottom. Provided that a constant ascent rate is required in the velocity shear data processing, this limited the deepest 2 m of the vertical resolution. Five casts were successively deployed at each station and averaged together to obtain a statistically significant average profile, in order to address potential intermittency in turbulence that could bias the measurements. Huguenard et al. (2019) used this data set to show that four cast averages sufficiently limited bias from small-scale intermittency.

A 6 MHz Nortek Acoustic Doppler Velocimeter (ADV) was deployed in the middle of the farm (black diamond in Figure 2.1b) during the flood phase (Hours 5.5–13.5) of the spring tide to collect high frequency velocity fluctuations approximately 1.0 m below the surface and underneath the farm (

2.1d). Later, the ADV was moved to the bottom to collect velocity measurements 0.28 m above the bottom through the ebb phase (Hours 14 - 8.5, Figure 2.1d). The ADV sampled at 64 Hz in 10 min bursts every 30 min.

2.2.3. Numerical Modeling

The Regional Ocean Modeling System (ROMS) was used to differentiate between the effects of the farm versus the natural bathymetry on the flow field. ROMS is a hydrostatic, primitive-equation ocean model that uses stretched, terrain-following vertical coordinates and orthogonal curvilinear horizontal coordinates on an Arakawa C grid (Shchepetkin and McWilliams, 2005; Shchepetkin and McWilliams, 2009). In order to simulate the effects of the farm, the vegetation module for submerged/emerged canopies in ROMS developed by Beudin et al. (2017) was modified. The canopy penetration was moved from the bottom layer to the surface layer, so that the drag force induced by the suspended canopy can be considered in the momentum.

The model grid included most of the estuary, ranging from 43.9°N up to the head (gray box in Figure 2.1a). The mesh was built with bathymetry data with resolution of 5–6 m obtained from Chandler (2016) in order to capture the bathymetric complexities that may be influencing the flow patterns in the observations. The total model domain has 200 grid cells in the east-west direction, 295 grid cells in the north-south direction, and 20 layers in the vertical direction. The grid resolutions are 50 and 25 m in east and north direction, respectively, and 20 sigma layers vertically. The horizontal grid is uniform, and the vertical grid was refined near the surface and bottom. The study area shown in Figure 2.1b has 35 grid cells in the along-channel direction and 23–25 grid cells in the cross-channel direction.

The model is forced with an idealized semidiurnal M_2 tide with a period of 12.42 hr at the (southern) open boundary. The open-ocean boundary is treated with a Chapman condition for surface elevation and a Flather condition for the barotropic velocity (Li et al., 2014). The upstream (northern) boundary is closed,

and river discharge is neglected. Logarithmic bottom friction is used for the riverbed, under the assumption that the bottom boundary layer is logarithmic with a roughness height of 2 mm. The physical time of the simulation was 36 hr, and the barotropic time step was 0.25 s. The vertical eddy viscosity is computed using the k–ω turbulence closure scheme with background diffusivity and viscosity set at 5×10^{-6} m^2/s. Model runs were also executed using k–ε turbulence closure schemes, but with little difference in the results. The horizontal eddy viscosity was set to 100 m^2/s. The transverse stress tensor rotated along geopotentials (constant depth) is used for horizontal momentum, which aims to substantially reduce the contribution of the transverse stress tensor to the vertical mixing when operating along constant s surfaces (Griffies et al., 1998). The model is initialized with no flow and a flat sea surface. The tidal amplitude was set to 1.65 m, the depth-averaged tidal current amplitude was 0.30 m/s, and the phase difference between tidal current and the surface elevation was 90°. The tidal forcing ramps up using a hyperbolic tangent function of time in the first tidal cycle. The prescribed tidal conditions were similar to those observed in the Damariscotta River (Lieberthal et al., 2019). Salinity and temperature were neglected in these simulations because the influence of density in a low inflow system is not crucial for understanding bathymetric versus farm influences on the flow field.

2.3. Data Processing

2.3.1. Momentum Equation

Due to channel curvature in this portion of the river, geographic east-west and north-south velocity components were rotated to streamwise (major direction, s) and normal (miner direction, n) velocity components, u_s and u_n, based on the principal direction of flow. This work uses a landward perspective, with positive streamwise velocity u_s defined as landward (i.e., the velocity going into the estuary). The positive normal velocity u_n is defined as the direction to the left of the landward direction. Positive z coordinate points upward with $z = 0$ m at the water surface following the right-hand principle. The angles θ

between the primary tidal flow direction and the geographic east direction are 50 ~ 60° at the seaward transect of the farm and 90–120° at the landward transect, which are consistent with the orientation of the bathymetry.

In order to analyze the farm impacts on the momentum, the depth-averaged Navier-Stokes equations (units m/s^2) were transformed from the east-north coordinate system (i.e., *x*-*y* coordinate system) to a streamwise and normal curvilinear coordinate system (i.e., *s*-*n* coordinate system). The momentum equations in the streamwise (equation 2.1a) and normal (equation 2.1b) directions consider the effect of curvature and convergence/divergence caused by the bathymetry and the farm on the fluid dynamics (Kalkwijk and Booij, 1986). In equation 2.1a, R_s denotes radius of the channel bend, f is the Coriolis frequency, ρ is density in the water column, ρ_0 is reference density, g is gravitational acceleration, $\langle u_s' w' \rangle$ and $\langle u_n' w' \rangle$ are the Reynolds stress in s and n direction, and z_s and z_b are the vertical coordinates of the surface and bottom. Note that terms with overbars are spatially averaged while those with angle brackets are temporally averaged. The left-hand side of equation 2.1a includes local acceleration ($\frac{\partial \overline{u_s}}{\partial t}$, $\frac{\partial \overline{u_n}}{\partial t}$), streamwise advection ($\overline{u_s \frac{\partial u_s}{\partial s}}$, $\overline{u_s \frac{\partial u_n}{\partial s}}$), and normal advection ($\overline{u_n \frac{\partial u_s}{\partial n}}$, $\overline{u_n \frac{\partial u_n}{\partial n}}$). The right-hand side of equation 2.1a consists of the forcing terms. The first two terms are referred to as the centrifugal "force" ($-\frac{2\overline{u_s}\overline{u_n}}{R_s}$, $\frac{\overline{u_s{}^2 - u_n{}^2}}{R_s}$) and normal divergence/convergence "force" $[-\overline{(u_s{}^2 - u_n{}^2)}\frac{\partial \theta}{\partial n}, -2\overline{u_s}\overline{u_n}\frac{\partial \theta}{\partial n}]$, even though these terms do not represent a true force in physics and arise from the coordinate transformation. The rest of the terms are the Coriolis force ($f\overline{u_n}$, $-f\overline{u_s}$). Barotropic pressure gradient ($-g\frac{\partial \eta}{\partial s}$, $-g\frac{\partial \eta}{\partial n}$), baroclinic pressure gradient ($-\frac{g}{\rho_0}\overline{\int_z^\eta \frac{\partial \rho(z')}{\partial s} dz'}$, $-\frac{g}{\rho_0}\overline{\int_z^\eta \frac{\partial \rho(z')}{\partial n} dz'}$), surface friction ($\langle u_s' w' \rangle|_{z_s}$), and bottom friction ($\langle u_s' w' \rangle|_{z_b}$),

$$\frac{\partial \overline{u_s}}{\partial t} + \overline{u_s \frac{\partial u_s}{\partial s}} + \overline{u_n \frac{\partial u_s}{\partial n}} = -\frac{2\overline{u_s u_n}}{R_s} - \left(\overline{{u_s}^2 - {u_n}^2}\right)\frac{\partial \theta}{\partial n} + f\overline{u_n} - g\frac{\partial \eta}{\partial s} - \frac{g}{\rho_0}\overline{\int_z^\eta \frac{\partial \rho(z')}{\partial s} dz'}$$

$$-\frac{1}{z_s - z_b}\left(\langle u_s' w' \rangle|_{z_s} - \langle u_s' w' \rangle|_{z_b}\right) \qquad (2.1.\text{a})$$

$$\frac{\partial \overline{u_n}}{\partial t} + \overline{u_s \frac{\partial u_n}{\partial s}} + \overline{u_n \frac{\partial u_n}{\partial n}} = \frac{\overline{{u_s}^2 - {u_n}^2}}{R_s} - 2\overline{u_s u_n}\frac{\partial \theta}{\partial n} - f\overline{u_s} - g\frac{\partial \eta}{\partial n} - \frac{g}{\rho_0}\overline{\int_z^\eta \frac{\partial \rho(z')}{\partial n} dz'}$$

$$-\frac{1}{z_s - z_b}\left(\langle u_n' w' \rangle|_{z_s} - \langle u_n' w' \rangle|_{z_b}\right) \quad . \qquad (2.1.\text{b})$$

The vertical coordinate is 0 at the free surface and $z < 0$ in the water column. In practice, momentum terms related to velocity were calculated where ADCP data were available within $z = -0.8$ m $\sim z = -0.9H$, where H is water depth. Surface friction was calculated using near-surface (around $z_s = -0.5$ m) dissipation data collected by the MicroCTD. Bottom friction was calculated using the typical bottom friction coefficient $C_f = 3 \times 10^{-3}$ and the depth-averaged velocity.

2.3.2. Turbulence and Mixing

Farm-induced turbulence and vertical mixing in momentum are quantified using the TKE dissipation rate, ε, and vertical eddy viscosity, A_z. Utilizing the Taylor frozen turbulence hypothesis and assuming homogeneous and isotropic turbulence, ε was computed by integrating the power spectrum $\Psi(k)$ of velocity shear, $\partial u/\partial z$, in wave number space using equation 2.2 (Lueck, 2013; Lueck et al., 2002), where u denotes fluid horizontal velocity, ν is the kinematic viscosity, and k is the wave number:

$$\varepsilon = \frac{15}{2}\nu\overline{\left(\frac{\partial u}{\partial z}\right)^2} = \frac{15}{2}\nu\int_0^\infty \Psi(k)dk \; . \qquad (2.2)$$

Power spectra of velocity shear, $\Psi(k)$, were calculated using fast Fourier transform (FFT) of each 0.5 s time series record from the shear probes on the MicroCTD. Three FFT segments with 50% overlap

were used to compute the velocity shear spectrum, where the lowest resolved wave number was around 5 cpm. The highest resolved wave number was around 100 cpm by considering the anti-aliasing frequency (98 Hz). Noise contamination from instrument acceleration was removed from the power spectrum using the Goodman coherent noise removal algorithm (Goodman et al., 2006). The velocity shear spectrum, $\Psi(k)$, was integrated using an iterative algorithm by fitting the empirical Nasmyth spectrum (Lueck, 2013), as shown in Figure 2.2a. Two orthogonal shear probe sensors provided two independent profiles of ε for each cast. If the value of ε from one shear probe was larger than two times the value from other shear probe, the larger value of ε was removed assuming that the accuracy of ε should be within a factor of 2 (Peters et al., 1988; Stips, 2005). Reasons otherwise could be due to a piece of debris hitting the shear probe during sampling, leading to erroneous spikes. Additionally, ε data were removed when the instrument inclination angle was larger than 5°. The remaining profiles of ε were bin averaged at every station using 0.25 m bin size and were interpolated onto the ADCP grid.

TKE dissipation rates, ε, were also estimated from a spectrum of vertical velocity fluctuations, $S_{w'w'}$, collected by the ADV under the farm. In the inertial subrange, $S_{w'w'}$ follows the −5/3 power law as shown in Figure 2.2b, where $S_{w'w'}(f)$ is the spectrum of vertical velocity fluctuations in frequency domain and α is constant equal to 0.69 (Sreenivasan, 1995). The spectral model in wave number space was converted to frequency space via Taylor's frozen turbulence hypothesis, $f = \frac{Uk}{2\pi}$, where U is the magnitude of the averaged velocity of each burst and k is the spatial wave number (Reidenbach et al., 2006; Shaw et al., 2001):

$$S_{ww}(f) = \alpha \varepsilon^{2/3} f^{-5/3} \left(\frac{U}{2\pi}\right)^{2/3}. \tag{2.3}$$

The mean velocity and velocity fluctuations were computed by averaging instantaneous measurements from the ADV over 10 min intervals under the assumption that turbulence is stationary during this period. This interval is widely used in turbulence statistical analyses since it balances statistical convergence and temporal variation of tidal flow conditions (Reidenbach et al., 2006; Stacey et al., 1999).

Suspicious spikes (outliers) in the time series of ADV data were detected using Grubbs's test and were filled using shape-preserving piecewise cubic spline interpolation. Spectra $S_{w'w'}(f)$ were computed using Welch's overlapped segment averaging estimator with 2,048 samples in one segment and 50% overlap. There were 38,400 samples in each burst resulting in ~72 degrees of freedom. The resulting spectrum $S_{w'w'}(f)$ are shown in Figure 2.2b. The dissipation rate is estimated by $\varepsilon = \overline{\alpha^{-3/2}\frac{2\pi}{U}S_{w'w'}(f)f^{5/3}\Big|_{f_1}^{f_2}}^{3/2}$, where $f_1 - f_2$ is the frequency range with the slope of frequency range with the slope of $S_{w'w'}(f)\,f^{5/3}$ closest to zero and overbar denotes the average over frequency space (Guerra and Thomson, 2017). The range of frequencies used to estimate the dissipation rate varies according to the position of the inertial subrange for different mean flows over tidal cycle between $1 < f < 10$ Hz to avoid boat wake contamination at $f < 1$ Hz.

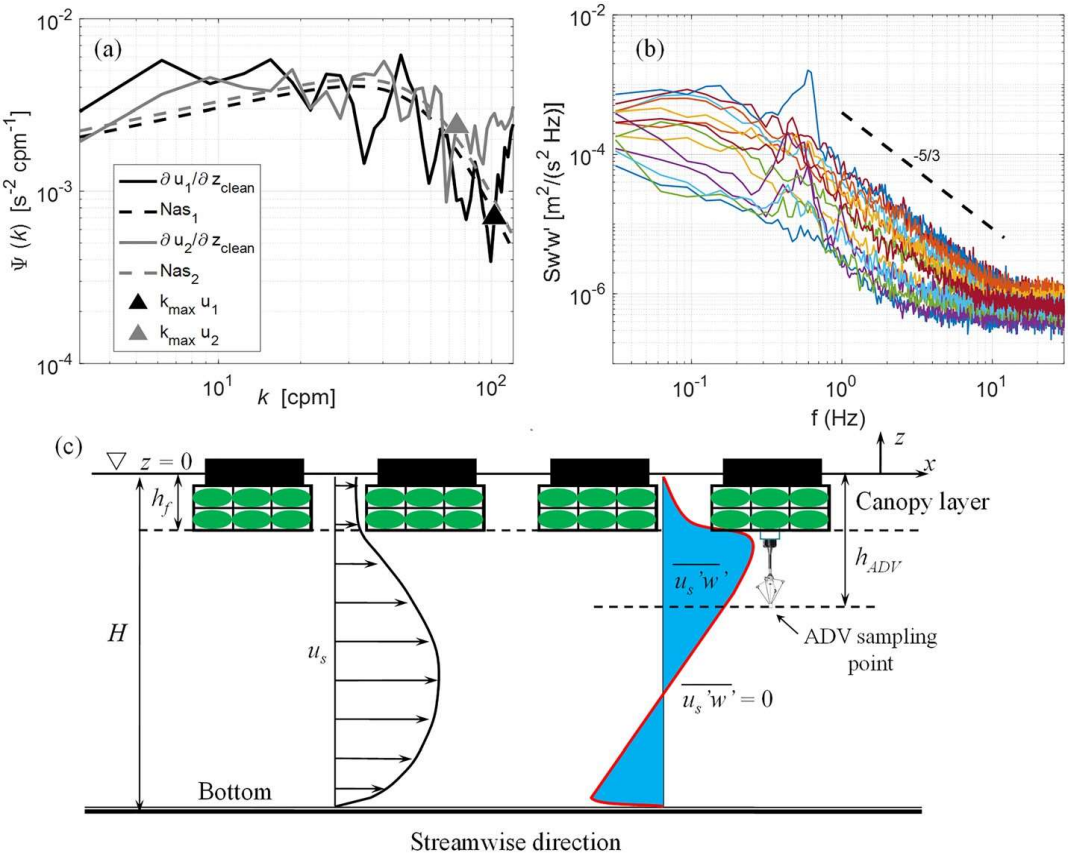

Figure 2.2 (a) Example spectrum of vertical shear of velocity, Ψ(k), collected in the main channel station at seaward transect at peak flood phase of the tide (Hour 9.5). Solid lines are power spectrum calculated from

vertical shear of velocity collected by shear probes via FFT. Dash lines are empirical Nasmyth spectrum fitted using spectrum data in the inertial subrange (Lueck, 2013). Triangles are maximum wave numbers for the integrating Ψ(k). (b) Spectrum of vertical velocity fluctuation, $S_{w'w'}(f)$, (solid lines) collected by the ADV attached to the oyster basket through flood phase. The dashed line indicates −5/3 power law. Peaks around 0.5 Hz indicate potential wave components induced by passing boats in the main channel. (c) Conceptual sketch of streamwise velocity, u_s (vectors), and Reynolds stress, $\langle u_s' w' \rangle$, (red line with shaded blue) profiles for suspended canopy flow. H is the water depth, h_f is the farm penetration, h_{ADV} is the distance from the free surface to ADV data location. Black squares are pontoons attached to the oyster basket. Green ellipses are oyster bags.

The vertical eddy viscosity, A_z, was estimated by taking the ratio of TKE dissipation rate, ε, to the squared vertical shear, S^2, and applying a momentum mixing efficiency factor, Γ_v, where $A_z = \Gamma_v \frac{\varepsilon}{S^2}$. Meanwhile, the vertical eddy diffusivity, K_z, was estimated by taking the ratio of ε to the squared buoyancy frequency, N^2, and applying a tracer mixing efficiency factor Γ_D, where $K_z = \Gamma_D \frac{\varepsilon}{N^2}$. A measure of stratification where ρ is the density of water column and ρ_0 is the reference density, the buoyancy frequency is $N^2 = -\frac{g}{\rho_0}\frac{d\rho}{dz}$. The squared vertical shear is $S^2 = \left(\frac{\partial u_s}{\partial z}\right)^2 + \left(\frac{\partial u_n}{\partial z}\right)^2$, where u_s and u_n are streamwise and normal velocities. Both mixing efficiency factors depend on the flux Richardson number R_f, known as $\Gamma_v = \frac{1}{1-R_f}$ and $\Gamma_D = \frac{R_f}{1-R_f}$ (Peters, 1997). The flux Richardson number R_f is defined as the ratio of the buoyancy term to production term in TKE budget equation (Kay and Jay, 2003). R_f can be calculated as the ratio of the gradient Richardson number, Ri_g, to the turbulent Prandtl number, P_{rt}, as $R_f = \frac{Ri_g}{P_{rt}}$, where the gradient Richardson number is $Ri_g = \frac{N^2}{S^2}$.

P_{rt} has been parameterized as a function of gradient Richardson number Ri_g as $P_{rt} = (1+4.47Ri_g)^{0.5}$ (Tjernström, 1993). Shear and buoyancy reach an equilibrium when $Ri_g = 0.25$ (Drazin and Reid, 1981; Shih et al., 2000). Active mixing by shear production occurs when $Ri_g < 0.25$, while mixing is suppressed

when $Ri_g > 0.25$. Theoretically, the turbulent Prandtl number $P_{rt} = 1$ when $Ri_g = 0.25$ and $P_{rt} \rightarrow \infty$ when $Ri_g = 0.5$. Therefore, $P_{rt} = 10$ was applied during data processing in this work when $Ri_g > 1$ (Ilıcak et al., 2008; Huguenard et al., 2015). In partially stratified estuaries, R_f varies with depth and is assumed to be no larger than 0.19 (Peters et al., 2005). At each station, five density profiles were bin averaged with bin size of 0.25 m in order to be consistent with ADCP grid.

2.3.3. Drag Coefficient

Floating oyster farms consist of long lines and floating oyster cages that are separated by gaps (see Figure 2.2c). In canopy flows, a whole group of single objects (such as coral reef branch, kelp frond, mussel chain, salmon cage, or oyster cage) are treated as a canopy layer (Asher et al., 2016; Lin et al., 2016; Wang et al., 2018; Wu et al., 2014). Drag from single object reduces flow velocity in canopy layer resulting in the development of a mixing layer outside of the canopy with high Reynolds stress (Ghisalberti and Nepf, 2004; Plew, 2011a). The Reynolds stress reaches a maximum at the lower edge of the canopy and approximately linearly decays to the bottom (Huai and Li, 2016; Plew, 2011a). In additions, the Reynolds stress profiles under oyster tables and lotus (nelumbo) leaves present an approximate linear decay with depth as observed from laboratory experiments (Han et al., 2018; Kervella et al., 2009). Therefore, both farm-induced friction velocity u^*_f and bottom friction velocity u^*_b can be estimated from the Reynolds stress, $\langle u_s' w' \rangle$, by assuming that Reynolds stresses linearly decreases with depth from the farm friction stress (u^{*2}_f) at the lower edge of the farm to the bottom friction stress ($-u^{*2}_b$) at the bottom of the river (equation 2.4).

Note that the near-surface and near-bottom deployment of the ADV was not synchronized in time, which requires an assumption of a zero Reynolds stress point in the water column. Therefore, a decay factor γ is introduced to equation 24 in order to account for the location of the zero Reynolds stress, since vertical profiles of Reynolds stress were not available. The value of $\gamma = 2$ assumes the Reynolds stresses is zero at the middle point between the farm bottom and the river bottom. In equation 2.4, H is the total water depth

changing with the tide, h_f is the vertical length of farm penetration (0.42 m), h_{ADV} is the distance from free surface to the ADV data location (1.0 m), ($h_{ADV} - h_f$) is the distance between the data collection point to the bottom of the farm, and ($H - h_f$) is the effective water depth considering the farm penetration (Figure 2.2c), where

$$\left(1 - \gamma \frac{h_{ADV} - h_f}{H - h_f}\right) u_f^{*2} = \sqrt{\overline{u_s'w'}^2 + \overline{u_n'w'}^2}. \tag{2.4}$$

Reynolds stresses, $\langle u_s'w' \rangle$ and $\langle u_n'w' \rangle$, were directly calculated as the ensemble mean of the covariance of velocity fluctuations collected using the ADV. When estimating bottom friction velocity, the distance between the ADV and farm bottom ($h_{ADV} - h_f$) was replaced by the distance from the ADV to the river bottom (i.e., 0.28 m).

If a balance between turbulence production and the rate of TKE dissipation occurs, the law of the wall can be used to relate the friction velocity to the dissipation rate, ε; Von Karman constant, κ (0.41); and mixing length, l (Dewey and Crawford, 1988; Reidenbach et al., 2006; Thorpe, 2005). When deployed under the farm, l is the distance between the ADV and the farm bottom ($h_{ADV} - h_f$). The friction velocity can be estimated using

$$\varepsilon = \frac{u^{*3}}{\kappa l} \ . \tag{2.5}$$

Note that u^*_f estimated from the Reynolds stress and TKE dissipation rates are expected to be similar in a well-developed boundary layer (Reidenbach et al., 2006).

Once friction from the farm and the bottom are obtained, the bulk drag coefficient, C_D, of the canopy layer can be derived based on the momentum balance between barotropic pressure gradients and friction (Lentz et al., 2017; Rosman and Hench, 2011) using in equation 2.6, where , ${U_f}^2 = \frac{1}{h_f}\int_{z=-h_f}^{z=0} u^2 dz$ is the depth averaged squared streamwise velocity in the farm layer, which was not available in this work.

In the estimation of C_D, it was assumed that U_f^2 was equal to velocity magnitude at 1 m depth, which was collected by the ADV. Additionally, we assume $u_b^* = u_f^*$ since data collection was not synchronized in time. Note that the bulk drag coefficient is related to the farm and bottom friction as well as the ratio of farm penetration to the total water depth. For shallow farms $h_f << H$, $C_D = 2\frac{{u_f^*}^2}{{U_f}^2} = 2C_f$, where C_f can be defined as a bulk friction coefficient quantifying the friction effect induced by the farm, following

$$C_D = 2\frac{{u_f^*}^2 + \frac{h_f}{H}{u_b^*}^2}{(1-\frac{h_f}{H}){U_f}^2}. \tag{2.6}$$

Factor 2 comes from the quadratic drag law. The above reported bulk drag coefficient is appropriate for a floating oyster farm of similar size and siting conditions as the one introduced here. It would be useful to obtain a drag coefficient of a single oyster cage and apply that to estimate the bulk drag for a farm with a varying number of cages for regional scale models, which cannot resolve individual oyster cages. We presen

the effective drag coefficient of a single oyster cage as $c_{d,e} = \frac{C_D}{\bar{a}h_f} = 2\frac{{u_f^*}^2 + \frac{h_f}{H}{u_b^*}^2}{\bar{a}h_f(1-\frac{h_f}{H}){U_f}^2}$, where C_D is the bulk drag coefficient and $\bar{a}$ is the total frontal area of entire oyster cage over total volume of water occupied by each cage in the farm layer. The detailed derivation of equation 2.6 is provided in the Appendix B.

2.4. Results

2.4.1. Peak Flood

2.4.1.1. Tidal Flow Patterns

At peak flood (Hour 8.5), the largest u_s occurred at the surface (u_s = 0.5 m/s) in the main channel of the seaward transect (Figure 2.3a.1). Streamwise velocities reduced to the landward transect, where the

largest values (u_s = 0.4 m/s) focused over the secondary channel (*distance across* > 100 m in Figure 2.3b.1. Seaward of the farm, streamwise flow (u_s = 0.4 m/s) traveled through the secondary channel under the farm (*distance across* = 0 m) and decreased to u_s = 0.25 m/s over the western shoal (*distance across* = 100 m) near the edge of the farm. Near the farm at the landward transect (*distance across* < 100 m), u_s reduced to 0.1 m/s.

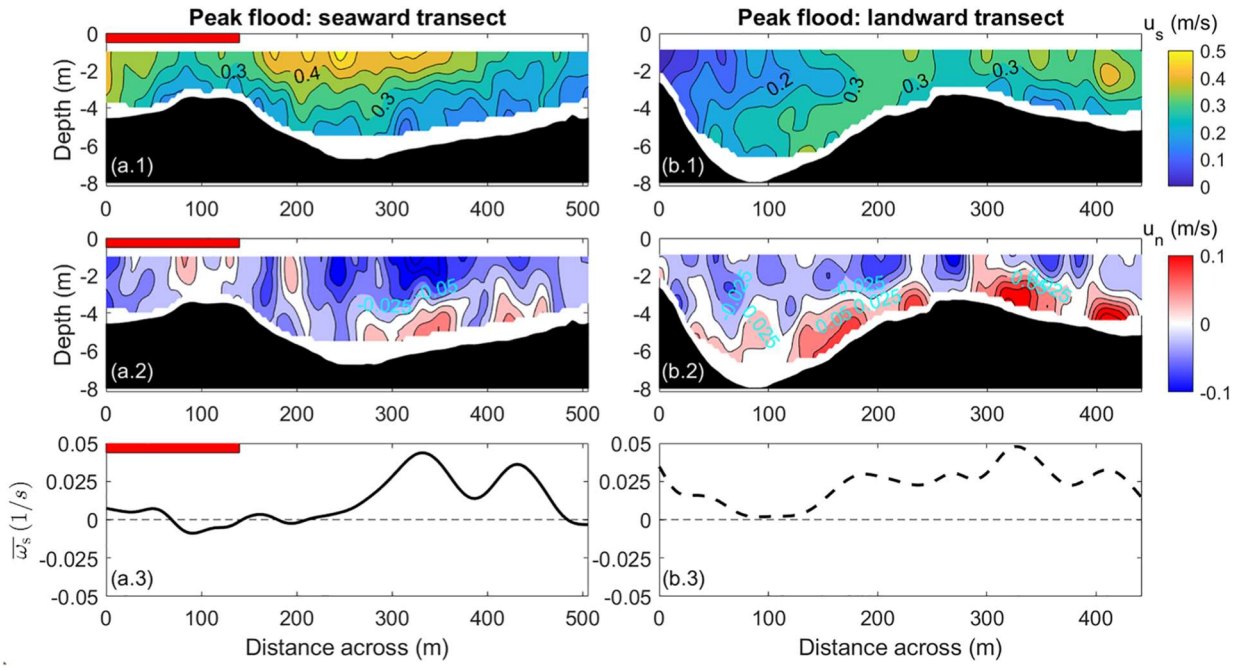

Figure 2.3 Velocity and streamwise vorticity distribution across the estuary during peak flood (Hour 8.5). (a.1 and b.1) Contours of streamwise velocity, u_s. Red bar indicates the oyster farm. (a.2 and b.2) Contours of normal velocity, u_n, where positive (red) values indicate velocity toward the western shoal (left) and negative (blue) values indicate velocity toward the eastern shoal (right). (a.3 and b.3) Depth-averaged streamwise vorticity, ω_s, where positive values (pointing into the paper) indicate clockwise lateral circulation and negative values indicate counterclockwise lateral circulation.

At the seaward transect, a two-layer lateral circulation formed in the main channel (250 m < *distance across* < 475 m) and was characterized by flow to the right at the surface (u_n = −0.05 m/s) and weaker flow to the left near the bottom (u_n = 0.025 m/s in Figure 2.3a.2). At the landward transect, a two-layer lateral circulation developed away from the farm area (*distance across* > 100 m in Figure 2.3b.2). The lateral circulation encompassed more of the transect yet featured larger near-bottom flows (u_n = −0.05 m/s) compared to near the surface (u_n = 0.025 m/s). The depth-averaged streamwise vorticity, $\overline{\omega_s} = -\frac{\overline{du_n}}{dz}$ also highlighted the reduced lateral circulation near the farm, where $|\overline{\omega_s}| < 0.025$ s^{-1} at both transects (Figure 2.3a.3). Away from the farm, $\overline{\omega_s}$ reached up to 0.035 s^{-1} at the seaward transect and increased up to 0.05 s^{-1} at the landward transect.

During the neap tide survey, the streamwise velocity (u_s = 0.3 m/s) seaward of the farm was smaller compared to the spring tide observations, yet similar patterns of streamwise flow reduction were observed over the western shoal (u_s = 0.1 m/s) near the edge of the farm at the landward transect (Figures A1a.1 and A1b.1). This coincided with the limited development of lateral circulation eastward of the thalweg during peak flood (Figure A1b.1), as indicated by small depth-averaged streamwise vorticity, $|\overline{\omega_s}| < 0.02$ s^{-1} near the farm at both transects (Figures A1a.1 and A1b.1).

2.4.1.2. Turbulence and Mixing

The flow patterns around the farm are illustrated using a plan view of near-bottom and near-surface velocity vectors (Figure 2.4a). Flow traveled through the farm on the seaward side (y < 0.2 km), indicated by near-bottom and near-surface velocity vectors that were oriented along the farm. Near-surface velocity tended to increase toward the channel (y = 0.3 km). At the landward transect behind the farm, velocity was substantially reduced. Large near-surface velocities generally followed the secondary channel (y > 0.7 km), though large velocities were confined to the right-hand side in the main channel (0.4 km > y > 0.5 km).

From the trailing side of the farm to the thalweg of the main channel ($y < 0.4$ km), horizontal flows varied significantly.

The streamwise velocity decreased from 0.4 m/s near the surface before the farm to 0.07 m/s alongside the farm at the landward transect (Figure 2.4b.1). The vertical structure of velocity linearly decayed with depth before the farm yet featured a subsurface maximum at $z = -2.5$ m in the wake of the farm. Streamwise velocity also reduced near the surface in the main channel, where $u_s = 0.45$ m/s at the seaward transect and $u_s = 0.10$ m/s at the landward transect (Figure 2.4c.1). In the channel, the vertical structure of velocity decayed with depth at the seaward transect but increased with depth at the landward transect. Streamwise and lateral gradients in density formed after the farm. The density anomaly, $\sigma = \rho - 1{,}000$, decreased from 20 kg/m^3 near the surface before the farm at the seaward transect to 19.3 kg/m^3 after the farm at the landward transect (Figure 2.4b.2). In the channel, the near-surface density anomaly varied from 20 kg/m^3 at the seaward transect to 19.5 kg/m^3 at the landward transect (Figure 2.4c.2).

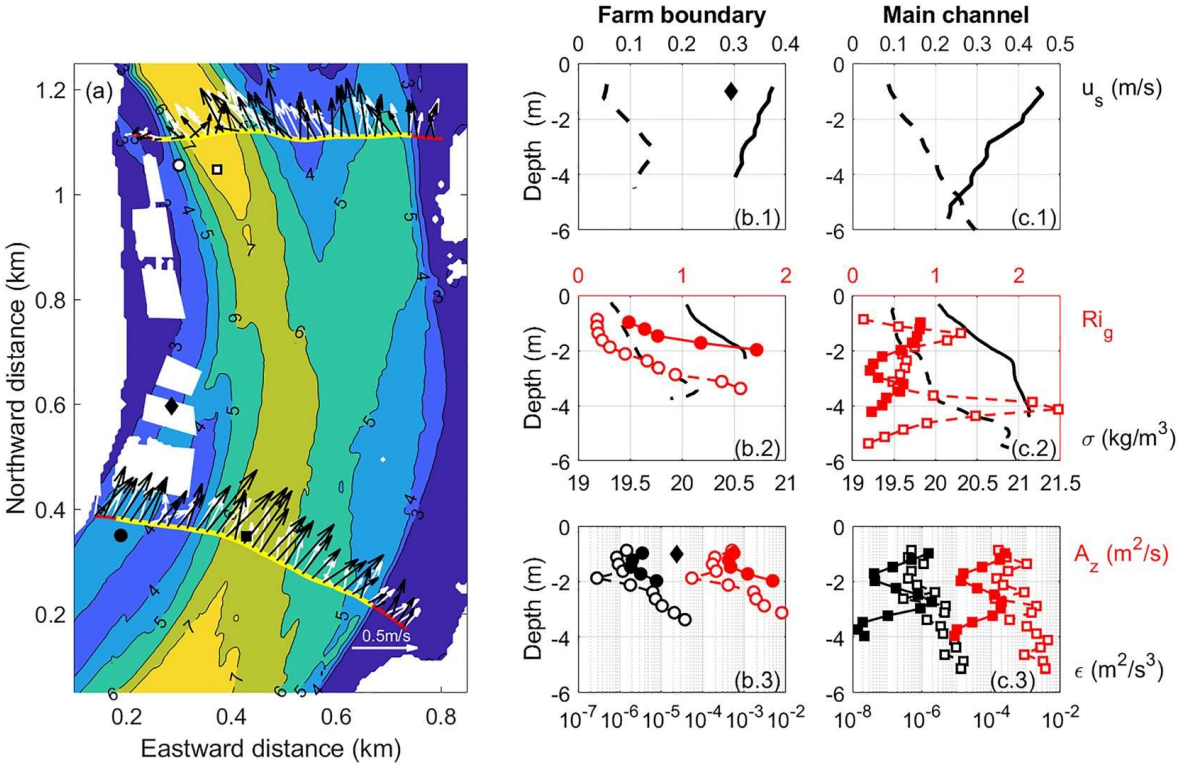

Figure 2.4 Flow, turbulence, and mixing patterns at peak flood (Hour 8.5). (a) Velocity vectors near the free surface (−0.75 m depth, black arrows) and close to bottom (−0.9H, white arrows); contours indicate water depth. Markers present hydrodynamic data collection stations of ADV (black diamond) and MicroCTD (circles and squares). Yellow lines denote the transect region where velocity data are shown in Figure 2.6 and is used for momentum analysis. (b.1 and c.1) Streamwise velocity, u_s, profiles under the farm (black diamond) and at the farm boundary and main channel along landward (dashed line) and seaward (solid line) transects. (b.2 and c.2) Density anomaly, $\sigma = \rho$ (density) $^{-}$ 1,000, (black) and gradient Richardson number, Ri_g, (red) profiles at the farm boundary and main channel along landward (dashed line with open markers) and seaward (solid line with solid markers) transects. (b.3 and c.3) Turbulent kinetic energy dissipation rate, ε, (black) and vertical eddy viscosity, A_z, (red) profiles at the farm boundary and main channel along the landward (dashed line with open markers) and seaward (solid line with solid makers) transects. Black diamond indicates point value of ε under the farm.

The gradient Richardson number decreased along the farm, varying from $Ri_g = 0.5$ near the surface before the farm to $Ri_g < 0.25$ at the end of the farm (Figure 2.4b.2). At the landward transect, two distinct layers formed, where $Ri_g < 0.25$ near the surface and bottom of the main channel and coincided with the location of streamwise flow reduction. This reduction in Ri_g suggested shear-driven mixing was strong enough to destabilize the water column in the upper 2 m. The vertical structure of ε and A_z showed large values near the surface (3.5×10^{-6} m^2/s^3 and 5.5×10^{-4} m^2/s, respectively) and bottom (7.7×10^{-6} m^2/s^3 and 4.8×10^{-3} m^2/s) at the seaward side of the farm (Figure 2.4b.3). Large near-surface values of ε and A_z occurred at the landward side of the farm, though they were reduced along the farm to 1.5×10^{-6} m^2/s^3 and 5.1×10^{-4} m^2/s, respectively. The ADV showed that ε was order of magnitude larger directly under the farm, where ε reached up to 2.4×10^{-5} m^2/s^3 at a vertical distance of 0.58 m under the farm. In the main channel, conditions were favorable for mixing below 2 m at the seaward side (Figure 2.4c.2). Large ε (1.6×10^{-6} m^2/s^3) and A_z (2.5×10^{-4} m^2/s) still occurred at the surface, suggesting that vertical mixing was evident in spite of $Ri_g > 0.5$. At the landward transect both near-bottom and near-surface mixing occurred in the

main channel where $Ri_g < 0.25$ (Figure 2.4c.2). Maximum ε (1.6×10^{-5} m^2/s^3) and A_z (3.7×10^{-3} m^2/s) occurred at the bottom, while large ε (1.1×10^{-6} m^2/s^3) and A_z (1.1×10^{-3} m^2/s) occurred 1 m below the surface.

2.4.1.3. Streamwise and Normal Momentum

In the secondary channel under the farm at the seaward transect (*distance across* < 100 m), bottom friction (-0.89×10^{-4} m/s^2 in Figure 2.5a.1) combined with surface friction (-0.26×10^{-4} m/s^2) to reduce streamwise flow indicated by the negative streamwise advection term (-2.1×10^{-4} m/s^2 in Figure 2.5a.1). The divergence forcing (-1.7×10^{-4} m/s^2) induced negative normal advection (-1.2×10^{-4} m/s^2) at the intersection where water either flows through or bypasses the farm, which also caused streamwise flow to locally decelerate. Closer to the edge of the farm (100 m < *distance across* < 200 m), convergence forcing (0.6×10^{-4} m/s^2) induced positive normal advection (0.4×10^{-4} m/s^2) and accelerated streamwise flow at the junction where the flow that bypassed the farm intersected with streamwise flow in the channel.

At the landward transect, where streamwise flows were reduced near the farm (*distance across* < 100 m), the dominant terms in streamwise momentum were convergence forcing (0.57×10^{-4} m/s^2), balanced by bottom friction (-0.35×10^{-4} m/s^2) and surface friction (-0.12×10^{-4} m/s^2 in Figure 2.5b.1). The streamwise velocity was still decelerated near the farm from the seaward transect to the landward transect, indicated by the negative streamwise advection (-0.35×10^{-4} m/s^2). Farther away from the farm (*distance across* > 200 m), the streamwise advection term switched to positive, which suggested that the decelerating effect was limited to the farm area. Regarding the bathymetry complexities, a sensitivity analysis of the evaluation of the streamwise advection term on the different ways to select upstream and streamwise velocity data is attached in the Appendix D, where results showed that distribution of streamwise advection was insensitive to the data selection.

In the normal direction, the negative centrifugal term was dominant at both transects, which forced the lateral circulation shown in Figure 2.3a.2 and Figure 2.3b.2. At the seaward transect, the centrifugal term was largest where along-channel flows were largest, namely, in the secondary channel under the farm (-1.8×10^{-4} m/s^2 at *distance across* = 0 m) and along the edge of the farm (-2×10^{-4} m/s^2 at *distance across* = 200 m in Figure 2.5a.2). At the landward transect, the centrifugal term was smallest ($< 0.3 \times 10^{-4}$ m/s^2) near the farm (*distance across* < 100 m in Figure 2.5b.2). The centrifugal force increased away from the farm and reached up to (1.0×10^{-4} m/s^2) over the eastern shoal of the main channel (150 m < *distance across* < 250 m) consistent with large vorticity shown in Figure 2.3b.3. The centrifugal force was balanced by the baroclinic pressure gradient (0.6×10^{-4} m/s^2).

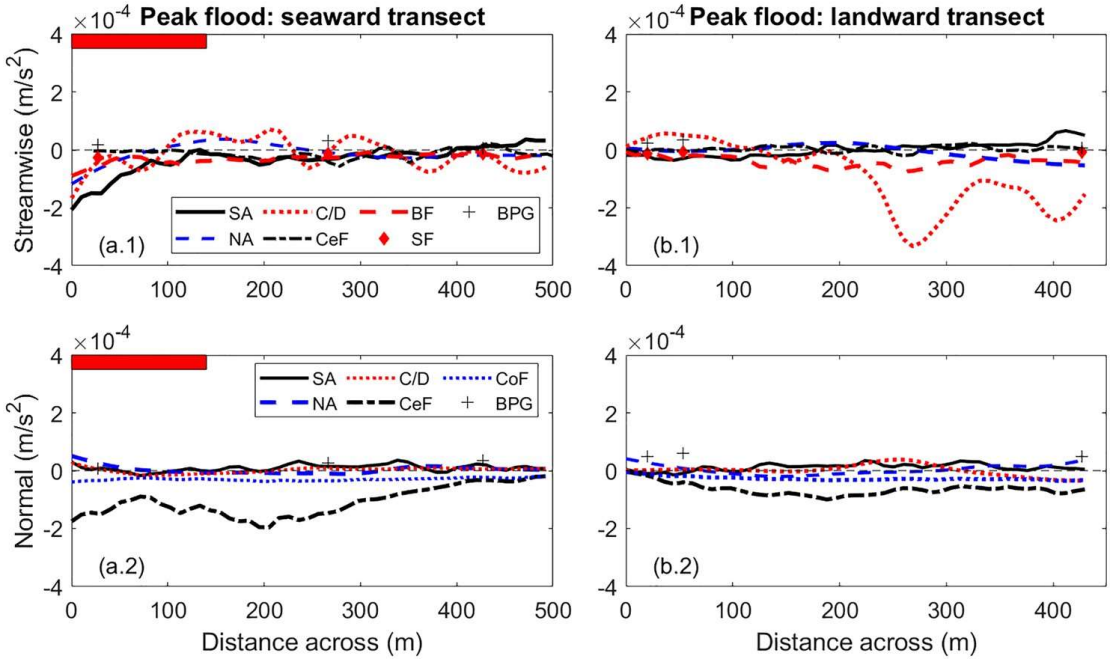

Figure 2.5 Momentum terms of streamwise (a.1 and b.1) and normal (a.2 and b.2) flows along seaward (a.1 and a.2) and landward (b.1 and b.2) transects at peak flood (Hour 8.5). SA is streamwise advection, NA is normal advection, C/D is convergence/divergence, CeF is centrifugal forcing, CoF is Coriolis force, BF is bottom friction, SF is surface friction, and BPG is baroclinic pressure gradient. Note that in (a.1) and (b.1) positive values indicate accelerating cause/effects of streamwise flow, while negative values indicate decelerating cause/effects. In (a.2) and (b.2) positive values indicate accelerating cause/effects of westward (toward the left)

normal flow, while negative values indicate accelerating cause/effects of eastward (toward the right) normal flow.

2.4.2. Peak Ebb

2.4.2.1. Tidal Flow Patterns

The reduction of streamwise flow was a consistent feature at the trailing side of the farm during peak flood and ebb. During peak ebb (Hour 14.5), the largest streamwise velocities at the landward transect occurred on the sides of the main channel and followed the bathymetry. Streamwise flow was larger on the left-hand side (u_s = 0.55 m/s), though, as compared to the right-hand side (u_s = 0.5 m/s in Figure 2.6b.1). In the center of the channel, streamwise flow was smaller (u_s = 0.4 m/s). The largest streamwise velocities that occurred in the seaward transect reduced to u_s = 0.45 m/s and appeared in the center of the channel rather than along the edges (Figure 2.6a.1). On the trailing side of the farm, a two-layer clockwise lateral circulation encompassed most of the transect and featured u_n = 0.10 m/s to the left along the bottom layer and u_n = −0.10 m/s to the right along the upper layer (Figure 2.6a.2).

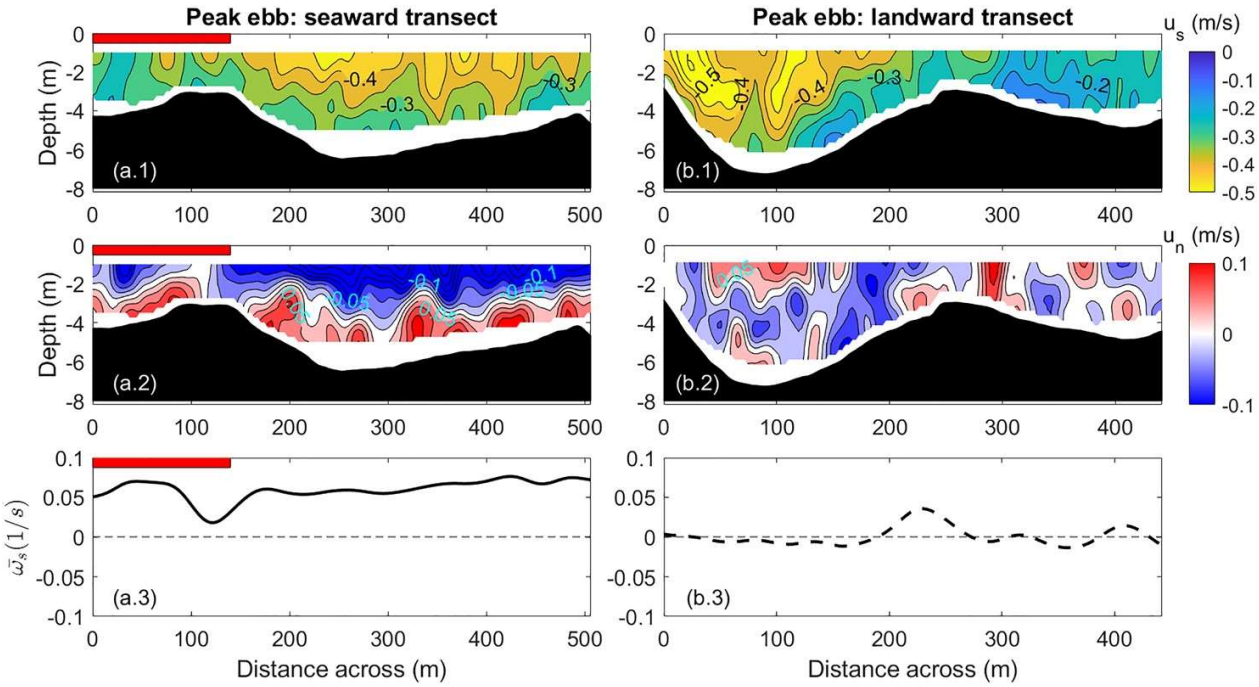

Figure 2.6 Velocity and streamwise vorticity distribution across estuary during peak ebb (Hour 14.5). (a.1 and b.1) Contours of streamwise velocity, u_s. Red bar indicates the location of the oyster farm. (a.2 and b.2) Contours of normal velocity, u_n, where positive (red) values indicate velocity toward the western shoal (left) and negative (blue) values indicate velocity toward the eastern shoal (right). (a.3 and b.3) Depth-averaged streamwise vorticity, ω_s, where positive values (pointing into the paper) indicating clockwise lateral circulation and negative values indicating counterclockwise lateral circulation.

The two-layer circulation cell diminished near the shoal at the edge of the farm (*distance across* = 100 to 150 m), where lateral flows were unidirectional to the right. At the landward transect, the lateral flow structure was irregular during peak ebb. A three-layer lateral flow structure was confined to the main channel (50–150 m), with $u_n = 0.05$ m/s to the left near the surface and bottom and $u_n = -0.05$ m/s in the center (Figure 2.6b.2). At the seaward transect, the depth-averaged streamwise vorticity was large ($\overline{\omega_s} > 0.05$ s^{-1}), except for the shoal near the edge of the farm where $\overline{\omega_s}$ was nearly zero (Figure 2.6a.3). At the landward transect, the depth averaged along channel vorticity, $\overline{\omega_s}$, was small, with magnitudes below 0.05 s^{-1} (Figure 2.6b.3).

2.4.2.2. Turbulence and Mixing

The plan view of near-surface and near-bottom flows during peak ebb differed from the patterns observed during peak flood. Flow tended to bypass the farm on the landward side (Figure 2.7a), influenced by reduced water depths ($H = 3$ m near the farm) as opposed to flowing through the farm during peak flood, where depths were larger ($H = 4$ m). This was indicated by near-surface and near-bottom velocity directed toward the channel before the farm ($y < 0.2$ km). Additionally, flows were larger on the trailing side of the farm during peak ebb as compared to the trailing side during peak flood.

Streamwise flow reduced near the surface from $u_s = -0.5$ m/s near the edge of the farm on the landward transect to $u_s = -0.2$ m/s behind the farm at the seaward transect (Figure 2.7b.1). In the main channel, streamwise flow reduction did not occur near the surface (Figure 2.7c.1). Lateral gradients in density occurred at the seaward transect during peak ebb, where less dense water (σ = 18.5 kg/m^3) was observed in the channel and denser water occurred near the surface behind the farm (σ = 19.2 kg/m^3 in Figure 2.7c.2). Unlike peak flood, vertical mixing was generally suppressed near the surface at all locations by the stratified conditions in the upper water column, indicated by $Ri_g > 0.5$ (Figures 2.7b.2 and 2.7c.2). Values of ε were minimum (3.0–6.0 × 10^{-7} m^2/s^3) at the surface among almost all stations, except at the seaward farm boundary, where elevated near-surface ε was around 1.5 × 10^{-6} m^2/s^3 and A_z was around 2.0 × 10^{-4} m^2/s. However, elevated ε (1 × 10^{-5} m^2/s^3) and A_z (1.0 × 10^{-3} m^2/s^3) did occur 2 m below the surface in the channel of the landward transect.

2.4.2.3. Streamwise and Normal Momentum

The dominant terms in streamwise momentum during peak ebb were divergence forcing, streamwise advection, and bottom friction. Near the farm at the landward transect (*distance across* < 100 m) divergence forcing (4.5 × 10^{-4} m/s^2) and bottom friction (1.8 × 10^{-4} m/s^2) decelerated the seaward directed flow (Figure 2.8b.1), resulting in positive values of streamwise advection (1.8 × 10^{-4} m/s^2). The positive sign associated with divergence forcing indicated that the bathymetry tended to decelerate the flow in the main channel (*distance across* < 100 m). However, a decrease in divergence forcing toward western shoal indicated flow diverting around the farm resulted in a convergence effect, which locally competed with the divergence effect from bathymetry, as shown by the surface velocity vector at the farm's landward boundary (0.2 < x < 0.3 km, y = 1.1 km) in Figure 2.7a. Farther away from the farm (*distance across* > 100 m), convergence forcing (−1.8 × 10^{-4} m/s^2) and streamwise advection (−0.5 × 10^{-4} m/s^2) reversed signs, meaning seaward flow was accelerated. At the seaward transect behind the farm (*distance across* < 200 m),

bottom friction (0.81×10^{-4} m/s^2) combined with surface friction (0.27×10^{-4} m/s^2) to decelerate streamwise flow shown by the positive streamwise advection (1.0×10^{-4} m/s^2 in Figure 2.8a.1), which was countered by normal advection and convergence forcing. The negative sign associated with convergence forcing (-1.4×10^{-4} m/s^2) indicated that the flow converged due to the intersection of the channel and the farm. This resulted in a negative normal advection (-0.55×10^{-4} m/s^2 in Figure 2.8a.1), which locally increased streamwise velocity as flows converged downstream of the farm. Although streamwise flow reduction occurred from the landward station near the farm to the seaward station behind the farm, the flows were not reduced as much as during peak flood because the bathymetric and farm bypassing effects.

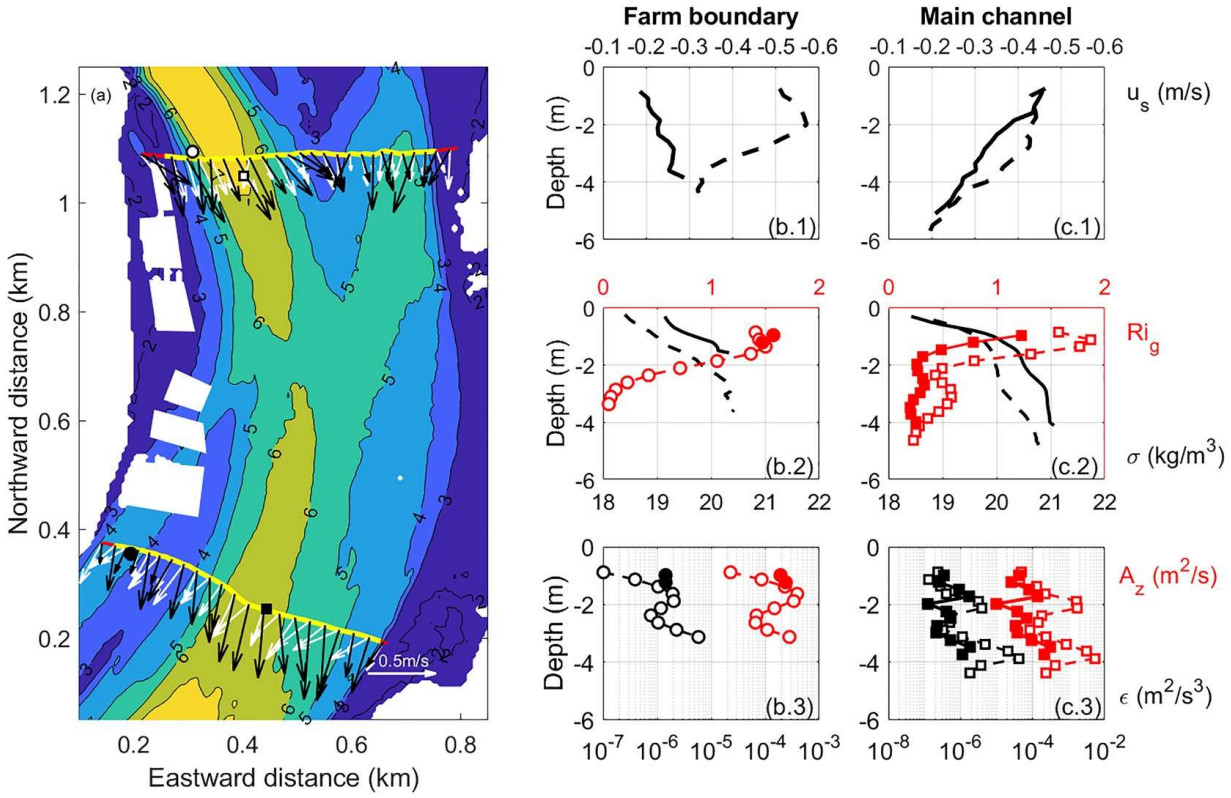

Figure 2.7 Flow, turbulence, and mixing patterns at peak ebb (Hour 14.5). (a) Velocity vectors near the free surface (−0.75 m depth, black arrows) and close to bottom (−0.9H, white arrows); contours indicate water depth. Yellow lines denote the transect region where velocity data are shown in Figure 6 and are used for momentum

analysis. (b.1 and c.1) Streamwise velocity, u_s, (black solid lines) and normal velocity, u_n, (red dashed lines) profiles at the farm boundary and main channel along landward (dashed line) and seaward (solid line) transects. (b.2) (c.2) density anomaly, $\sigma = \rho$ (density) - 1000, (black) and gradient Richardson number, Ri_g, (red) profiles at the farm boundary and main channel along landward (dashed line with open markers) and seaward (solid line with solid markers) transects. (b.3 and c.3) TKE dissipation rates, ε, (black) and vertical eddy viscosity, A_z, (red) profiles at the farm boundary and main channel along landward (dash line with open markers) and seaward (solid line with solid makers) transects.

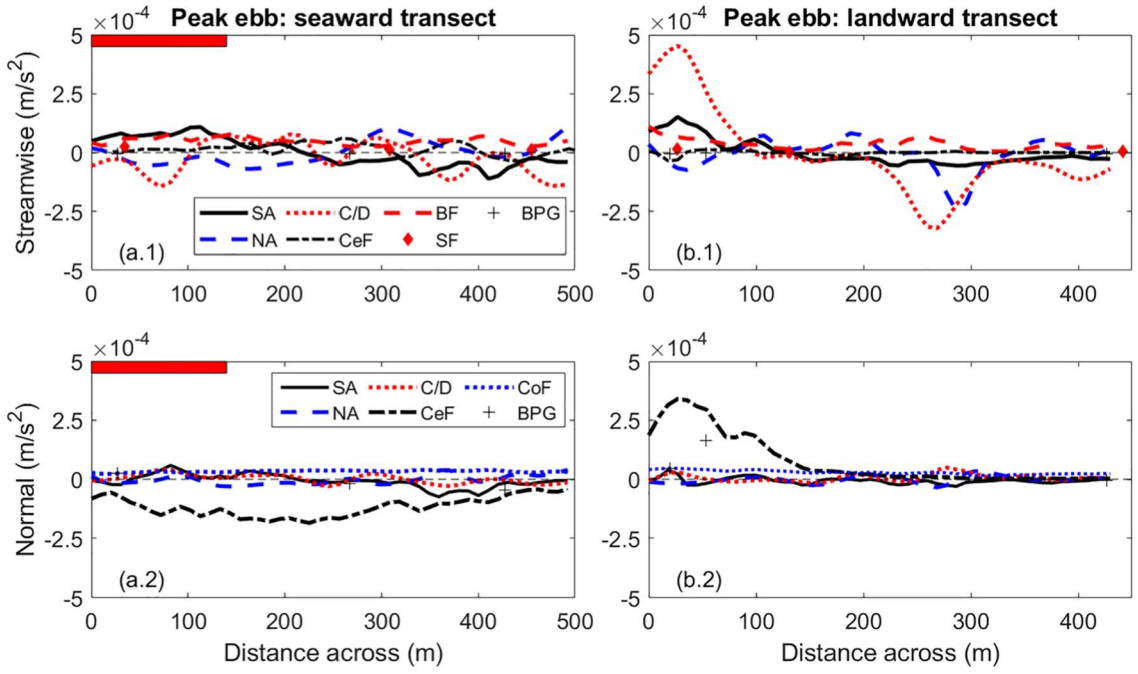

Figure 2.8 Momentum terms of streamwise (a.1 and b.1) and normal (a.2 and b.2) flows along landward (a.1 and a.2) and seaward (b.1 and b.2) transects at peak ebb (Hour 14.5). SA is streamwise advection, NA is normal advection, C/D is convergence/divergence, CeF is centrifugal forcing, CoF is Coriolis force, BF is bottom friction, SF is surface friction, and BPG is baroclinic pressure gradient. Note that in (a.1) and (b.1) positive values indicate decelerating cause/effects of streamwise flow, while negative values indicate accelerating cause/effects. In (a.2) and (b.2) positive values indicate accelerating cause/effects of westward (toward the left)

normal flow, while negative values indicate accelerating cause/ effects of eastward (toward the right) normal flow.

In the normal direction, the centrifugal term was still the dominant term at both transects. At the seaward transect, the centrifugal term was largest (-1.8×10^{-4} m/s^2) in the main channel (*distance across* = 200 m in Figure 2.8a.2), which coincided with where streamwise advection (Figure 2.8a.1) was smallest. Note that during ebb, the landward transect is downstream of a bend located further north, yet the seaward transect is located in the southern bend. Consequently, the radius of the northern bend, R_{s2}, was used to estimate the centrifugal force at the landward transect during ebb. At the landward transect, centrifugal force was greatest near the edge of the farm (3.4×10^{-4} m/s^2 in Figure 2.8b.2), which coincided with where divergence forcing in streamwise momentum was largest (Figure 2.8b.1). In the main channel, the normal baroclinic pressure gradient reached up to 1.7×10^{-4} m/s^2 (Figure 2.8b.2). Although both the centrifugal force and the normal baroclinic pressure gradient were positive, the resulting effect was contrary. A positive centrifugal force drives anticlockwise lateral circulation, where surface flow is directed toward the west and bottom flow is directed toward the east ($\omega_s < 0$). A positive normal baroclinic pressure gradient drives a clockwise lateral circulation, where bottom flow is directed toward the west and surface flow is directed toward the east ($\omega_s > 0$). As a consequence, the centrifugal force was countered by the baroclinic pressure gradient in the main channel, resulting in a three-layer lateral flow structure (50 m < *distance across* < 100 m, Figure 2.6b.2).

2.4.3. Dependence of Lateral Circulation on Streamwise Advection

The momentum analysis showed that streamwise flows decelerated toward the trailing edge of the farm, which was evident through the streamwise advection term. This location also coincided with regions where the clockwise lateral circulation cell tended to not develop, particularly during flood. The lateral circulation

was dominated by centrifugal circulation, which is a function of streamwise velocity. In order to elucidate related flow deceleration on lateral circulation, the streamwise advection, $\overline{u_s \frac{\partial u_s}{\partial s}}$, was the effects of farm plotted against streamwise vorticity, $\overline{\omega_s}$, in the farm area and main channel (*distance across* = 0 ~ 300 m) along the downstream transect for the entire flood (or ebb) phase. For the landward transect during the flood phase, the streamwise vorticity increased as streamwise advection increased (Figure 2.9a). The smallest $\overline{\omega_s}$ < 0.02 s^{-1} occurred when streamwise flow was decelerated ($\overline{u_s \frac{\partial u_s}{\partial s}}$ = -2.5×10^{-5} m/s^2), which coincided with the wake of the farm (*distance across* < 100 m). A similar trend was identified for the seaward transect during the ebb phase. The smallest $\overline{\omega_s}$< 0.02 s^{-1} occurred when the streamwise advection was positive, which indicated deceleration of seaward flow, which only occurred near the farm (Figure 2.9b). The correlation $\overline{u_s \frac{\partial u_s}{\partial s}}$ and $\overline{\omega_s}$ clearly demonstrated the two-layer lateral circulation was suppressed by the reduction of streamwise velocity at the downstream transect.

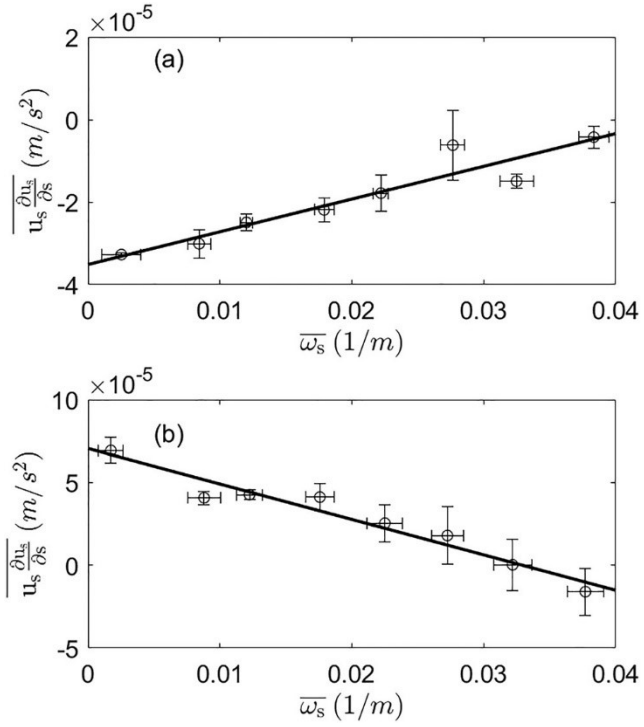

Figure 2.9 Correlation between the downstream transect depth-averaged streamwise vorticity, $\overline{\omega_s}$, and depth-averaged streamwise advection, $\overline{u_s \frac{\partial u_s}{\partial s}}$ through entire flood phase near the farm and in the main channel along the landward transect where across channel distance from 0 ~ 300 m (a) and the entire ebb phase near the farm and in the main channel along the seaward transect where across channel distance from 0 ~ 300 m (b). Negative values of $\overline{u_s \frac{\partial u_s}{\partial s}}$ in (a) and positive values of $\overline{u_s \frac{\partial u_s}{\partial s}}$ in (b) indicate streamwise velocity reduction, and vice versa. The horizontal and vertical bars are the 95% confidence of $\overline{\omega_s}$ and $\overline{u_s \frac{\partial u_s}{\partial s}}$ calculated using bootstrap method. Black lines are linear regression based on mean values.

2.4.4. Mixing Mechanism

Time series of vertical eddy diffusivity, K_z, are shown for two stations across the estuary to display the vertical mixing characteristics over the entire tidal circle. Near-surface mixing was observed at the farm boundary and in the main channel along the landward transect. During the flood phase of the tide (Hours 8–10), elevated values of K_z ($1.1 \times 10^{-4} \sim 1.5 \times 10^{-4}$ m^2/s) were observed in the water column ranging from 0.8 to 2.0 m at the farm boundary in the landward transect (Figure 2.10b.1) and in the main channel ($5.9 \times 10^{-4} \sim 7.2 \times 10^{-4}$ m^2/s; Figure 2.10b.2). At early flood of the following tidal cycle (after Hour 18), high values of K_z (0.02 m^2/s) reappeared from 0.5 ~ 0.8 m in the landward main channel station. During the ebb phase of the tide (Hours 12–16), an enhanced mixing layer occurred at 2 m depth, where K_z was around $6.9 \times 10^{-5} \sim 1.0 \times 10^{-4}$ m^2/s (Figure 2.10b.2). During ebb along the seaward transect, elevated K_z occurred near the surface (0.5 m water depth) at the farm boundary ($3.2\times10^{-5} \sim 8.1\times10^{-5}$ m^2/s, Figure 2.10a.1). Results of K_z indicated that during phase near the farm and in the main channel along the landward transect where the flood phase, mixing not only developed alongside the farm but also extended to the main channel.

During the complementary neap tide observations, near-surface mixing was also observed near the farm and in the main channel along the landward transect during flood. From hr 15 to 17, elevated values

of K_z at the farm boundary in the landward transect (1.6×10^{-3} ~ 9.0×10^{-3} m^2/s) and in the main channel (2.4×10^{-4} ~ 1.1×10^{-3} m^2/s) occurred in the water column within 0.8 m ~ 2.0 m depth (Figure A2b.1, b.2). During the ebb phase of the tide (hr 8 – 10), elevated K_z (1.3×10^{-4} ~ 1.7×10^{-3} m^2/s) was observed at 1 m water depth along the seaward transect (Figure A2a.1).

In order to investigate if the near-surface mixing was related to the farm, the time scale analysis first introduced by Collignon and Stacey (2013) was used. The time scale analysis isolates how certain lateral processes affect vertical mixing and is formulated from the time derivative of the Richardson number, which is rearranged in terms of streamwise vorticity. The resulting time scales are associated with shear straining, τ_u; density straining, τ_ρ; Coriolis, τ_f; and unsteadiness, τ_t (equation 2.7a), where

$$\tau_u = \frac{S^2}{\overline{\omega_s}\left(-2Ri_g \overline{\frac{\partial u_s}{\partial z}}\,\overline{\frac{\partial u_s}{\partial n}}\right)} \tag{2.7.a}$$

$$\tau_\rho = \frac{S^2}{\overline{\omega_s}\left(-\frac{g}{\rho_o}\overline{\frac{\partial \rho}{\partial n}}\right)} \tag{2.7.b}$$

$$\tau_f = \frac{S^2}{\overline{\omega_s}\left(2Ri_g \overline{\frac{\partial u_s}{\partial z}} f\right)} \tag{2.7.c}$$

$$\tau_t = \frac{S^2}{\overline{\omega_s}\left(-2Ri_g \frac{\partial \overline{\omega_s}}{\partial t}\right)}. \tag{2.7.d}$$

The time scales represent the amount of time it would take for that lateral process to destabilize (or stabilize) the water column. Time scales greater than 6 hr are deemed negligible since it would take longer than the flood or ebb phase to stabilize (positive τ) or destabilize (negative τ). Therefore, smaller time scales are more influential.

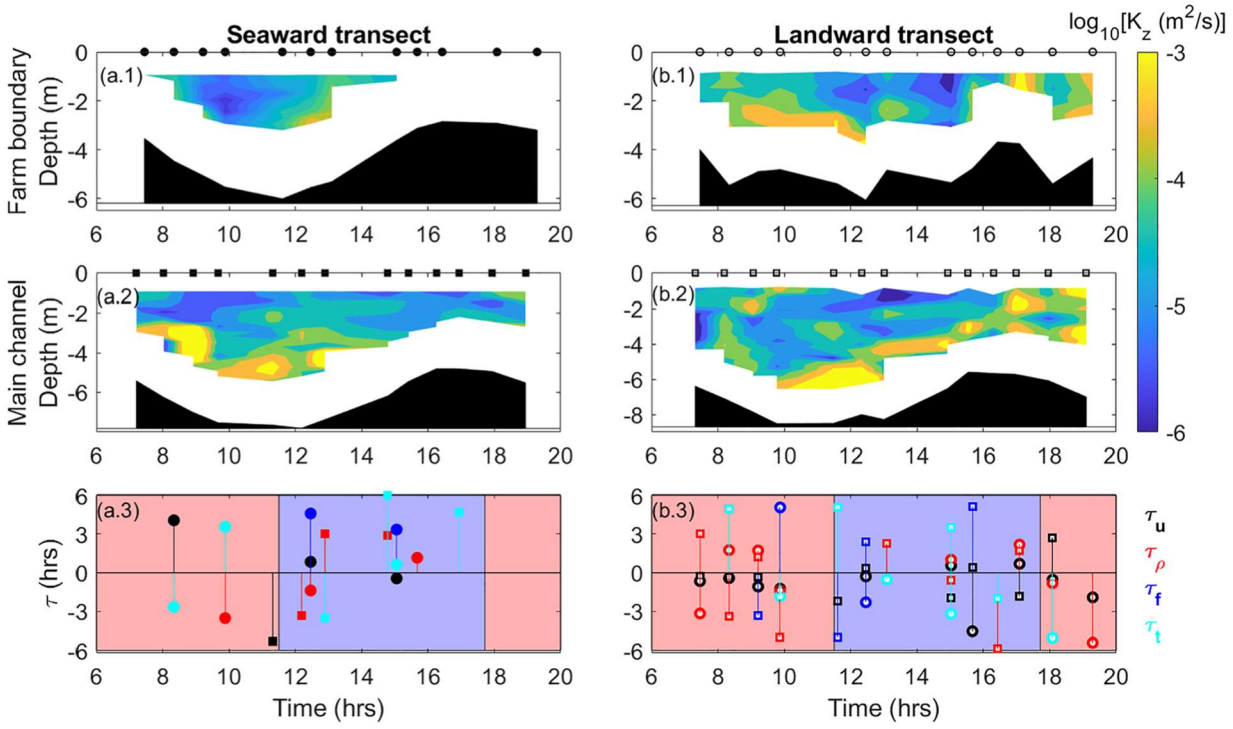

Figure 2.10 Time series of vertical eddy diffusivity, K_z, and time scale, τ, analysis for vertical mixing induced by lateral processes along seaward (a.1–a.3) and landward (b.1–b.3) transects over the entire tidal cycle. Contours in (a.1) and (b.1) are K_z at the farm boundary. Contours in (a.1) and (b.1) are K_z in the main channel. Markers denote data collection time. Squares denote data collected at farm boundary; circles denote data collected in the main channel. Solid makers denote seaward transect; open makers denote landward transect. In (a.3) and (b.3), τ_u is caused by shear straining, τ_ρ is caused by density straining, τ_f is caused by Coriolis, and τ_t is caused by unsteadiness. Positive τ indicates mechanisms that stabilize the water column, and negative τ indicates mechanisms that destabilize the water column. The time scale closest to 0 is the dominant stabilizing/destabilizing mechanism. Red shaded areas indicate the flood phase and blue shaded areas shows the ebb phase.

During flood, the lateral straining of velocity shears was the dominant mechanism for destabilizing the water column near the farm and in the channel at the landward transect, as indicated by $\tau_u < -1$ hr (Figure 2.10b.3). The prevalence of τ_u in destabilizing the water column was due to the enhanced lateral gradients, $\overline{\frac{\partial u_s}{\partial n}}$, in streamwise flows. As the lateral surface flows pushed slower water from the farm area (western shoal) over faster water in the channel, vertical shear in velocity was enhanced, as seen in Figures 2.3b.1 and 2.3b.2, where the low-velocity zone near the surface extended from the western shoal into the main channel.

The dominant mechanism for destabilizing the water column at the landward transect during ebb was again τ_u, where $\tau_u < -2$ hr. However, this was only observed in the channel and coincided with large K_z at 2 m depth in Figure 2.10b.2 and elevated ε at 2 m depth in Figure 2.7c.3. Streamwise flow divergence driven by the bathymetry decelerated streamwise flow in the thalweg of the main channel, while the flow on the western side of the channel was enhanced by flow bypassing the farm as seen in Figure 2.7a. This reinforced the lateral gradient in streamwise velocity. The three-layer lateral flow structure observed in the channel pushed slower water from the thalweg over faster water along the channel wall, which enhanced vertical shear at 2 m, as seen in Figures 2.6b.1 and 2.6b.2.

At the seaward transect, instances where lateral processes destabilized the water column were less frequent (Figure 2.10a.3). Shear straining destabilized the water column in the secondary channel behind the farm, namely, $\tau_u < -1$ hr during peak ebb, as the lateral surface flow pushed water slowed down by the farm from the second channel over faster water on the eastern shoals of the secondary channel (Figures 2.6a.1, 2.6a.2, and 2.10a.1). Density straining stabilized the water column in the main channel at the seaward transect during ebb, since the centrifugal force together with flow bypassing the farm acted to push fresh water over denser water, as indicated by $\tau_\rho = 3$ hr (Figure 2.10a.3).

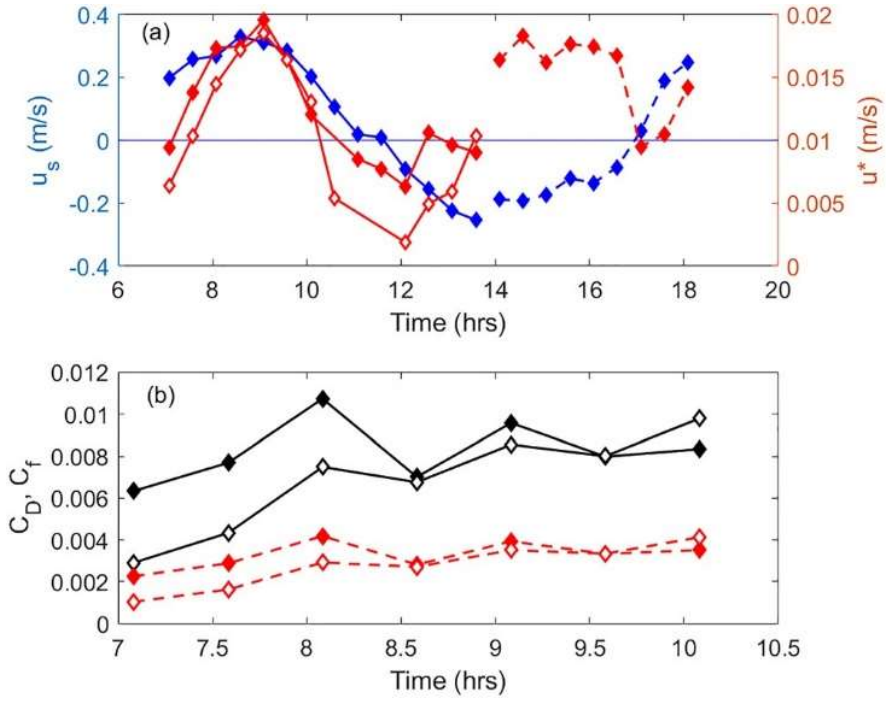

Figure 2.11 (a) Time series of streamwise velocity, u_s, and friction velocity measured by ADV through the entire tidal cycle. Blue solid line denotes u_s at 1.0 m water depth (located 0.58 m under the farm); blue solid line denotes u_s at 0.28 m above the river bottom; red solid line with solid diamonds denotes farm friction velocity,u^*_f, estimated from Reynolds stress; red solid line with open diamonds denotes u^*_f estimated from dissipation rates; red dash line with solid diamonds denotes bottom friction velocity, u^*_b, estimated Reynolds stress. (b) Time series of bulk drag coefficient, C_D, estimated from Reynolds stress (black line with solid diamonds) and dissipation rates (black line with open diamonds); bulk friction coefficient (red diamond), C_f, estimated Reynolds stress during flood phase (Hours 7–10).

2.4.5. Bulk Drag Coefficients

To parameterize the bulk farm impact, surface friction velocity and bottom friction velocity were estimated based on the Reynolds stress and TKE dissipation rates collected with the ADV under the farm and near the bottom. Around peak flood (Hours 8–9.5), the farm-induced surface friction velocity, u_f^*,

estimated from Reynolds stress was around 0.016–0.019 m/s, and the streamwise velocity reached up to 0.27–0.33 m/s at 1 m below the surface (about 0.58 m under the farm, Figure 2.11a). Values of u_f^* estimated from TKE dissipation were consistent with those estimated from Reynolds stress from early flood to the end of flood (Hours 7–10). The bottom friction velocity, u_b^* , was around 0.016 – 0.018 m/s around peak ebb (Hours 14–16), and the streamwise velocity reached up to 0.17–0.19 m/s, located about 0.28 m above the river bottom. Although synchronized data capturing u_f^* and u_b^* were not available, the comparable peak values of u_f^* and u_b^* provided evidence that the farm imposed surface friction, since u_f^* should be zero in the absence of surface friction.

The bulk drag coefficient C_D estimated from Reynolds stress varied from 6.3×10^{-3} to 1.07×10^{-2} through the flood phase (Hours 7–10), while the bulk friction coefficient C_f estimated from Reynolds stress varied from 2.3×10^{-3} to 4.2×10^{-3} (Figure 2.11b). Both C_D and C_f estimated from TKE dissipation rates were consistent with those estimated Reynolds stress. From early flood to the end of flood (Hours 7–10), h_f/H decreased from 0.17 to 0.09, while $C_D/(2C_f)$ decreased from 1.4 to 1.2. Consequently, the farm was relatively shallow compared with depth over this period, meaning that bottom friction increased the bulk drag. Around peak flood (Hours 8–10), the averaged bulk drag and bulk friction coefficients were $C_D = 8.4 \times 10^{-3} \pm 9.1 \times 10^{-4}$ and $C_f = 3.4 \times 10^{-3} \pm 3.8 \times 10^{-4}$, respectively, which were calculated using u_f^* estimated from Reynolds stress and the TKE dissipation rate, along with a reference velocity at 1.0 m below the water surface. The estimation of $c_{d,e}$ around peak flood was $c_{d,e} = 0.58 \sim 0.92$ considering U_f equal to velocity magnitude at 1 m water depth and $u_b^* = u_f^*$.

2.4.6. Model Results

The $c_{d,e}$ derived above was implemented into ROMS to investigate if the reduced flow near the farm was caused by the combination of channel-shoal morphology and a channel bend or by increased friction from the farm. Two cases were simulated: a no farm case and a farm case where $c_{d,e} = 1.0$. The simulations

were not meant to exactly model the measurements observed in the field. Rather, this tool was used in an idealized sense to determine if the farm further enhanced the streamwise flow reduction, which leads to near-surface mixing in the channel and hindered the development of lateral circulation.

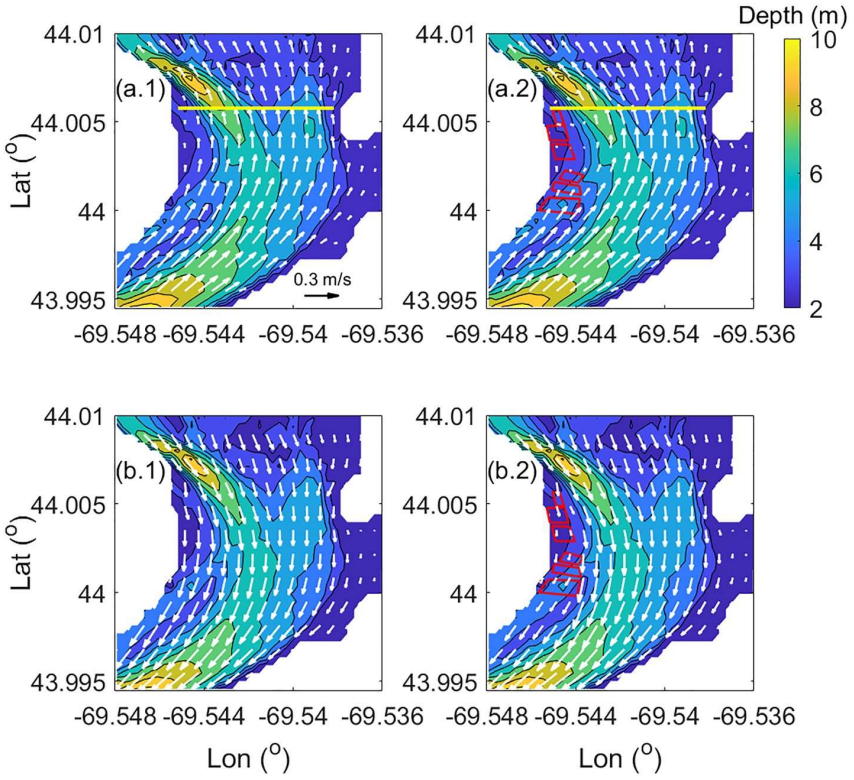

Figure 2.12 Velocity vectors at the free surface during peak flood from the Regional Ocean Modeling System (ROMS) model simulation with and without the farm. (a.1 and b.1) Without the farm; (a.2 and b.2) With the farm and drag coefficient of oyster cage is $c_d = 1.0$. (a.1 and a.2) At peak flood; (b.1 and b.2) at peak ebb. Contours indicate bathymetry. Red quadrangles denote the farm. Yellow lines denote the location where the cross-sectional velocity data taken from that is shown in Figure 13.

At peak flood, the tidal current was directed over the shallow area on the eastern side of the estuary on the downside end of the bend. With the presence of the farm, the velocity decreased from 0.18 m/s at the farm's seaward boundary to 0.04 m/s at the farm's landward boundary, where the velocity was 0.12 m/s

without considering the farm (Figures 2.12a.1 and 2.12a.2). The low-velocity zone extended beyond the footprint of the farm and into the main channel. This pattern was consistent with the field observations shown in Figure 2.4a. At peak ebb, the velocity in the farm area without the presence of the farm slightly increased from 0.19 m/s at farm's landward boundary to 0.22 m/s toward the seaward boundary because of channel convergence (Figure 2.12b.1). However, including the farm caused the flow to bypass along the leading edge of the farm (Figure 2.12b.2).

The tidal current distribution at the landward cross section during flood was examined to determine if the reduced streamwise flows on the western side of the channel were caused by bathymetric complexities or by surface friction induced by the farm. This is an important distinction because weaker flows in the channel ultimately limited the development of lateral circulation in the observations. At peak flood, maximum streamwise velocities occurred over the eastern channel-shoal interface of the main channel. When the farm was included, streamwise velocities were reduced significantly (0.02 m/s) over the western half of the channel as compared to the no farm case, where velocities were 0.1 m/s (Figures 2.13a.1 and 2.13a.2). As a result, streamwise flow was enhanced over the eastern channel-shoal interface. Without the presence of the farm, the normal velocities depicted a clockwise circulation with positive streamwise vorticity that extended across most of the transect. The influence of the farm caused the lateral circulation to encompass less of the transect, limiting its development over the western 100 m. A reduction in depth-averaged streamwise vorticity, ω_s, occurred from 40 to 140 m along the transect compared to the no farm case and was slightly enhanced over the eastern channel-shoal interface, as shown in Figure 2.13c.

Overall, the cross-sectional distribution of streamwise velocity and the reduction of vorticity over the western half of the channel in the simulations including the farm all qualitatively agreed with the field observations shown in Figures 2.3b.1, 2.4b.1, and 2.4c.1. Notable differences were observed between the model and the observations in the vertical shear of streamwise flows, particularly in the western half of the channel, which will be discussed further in the discussion.

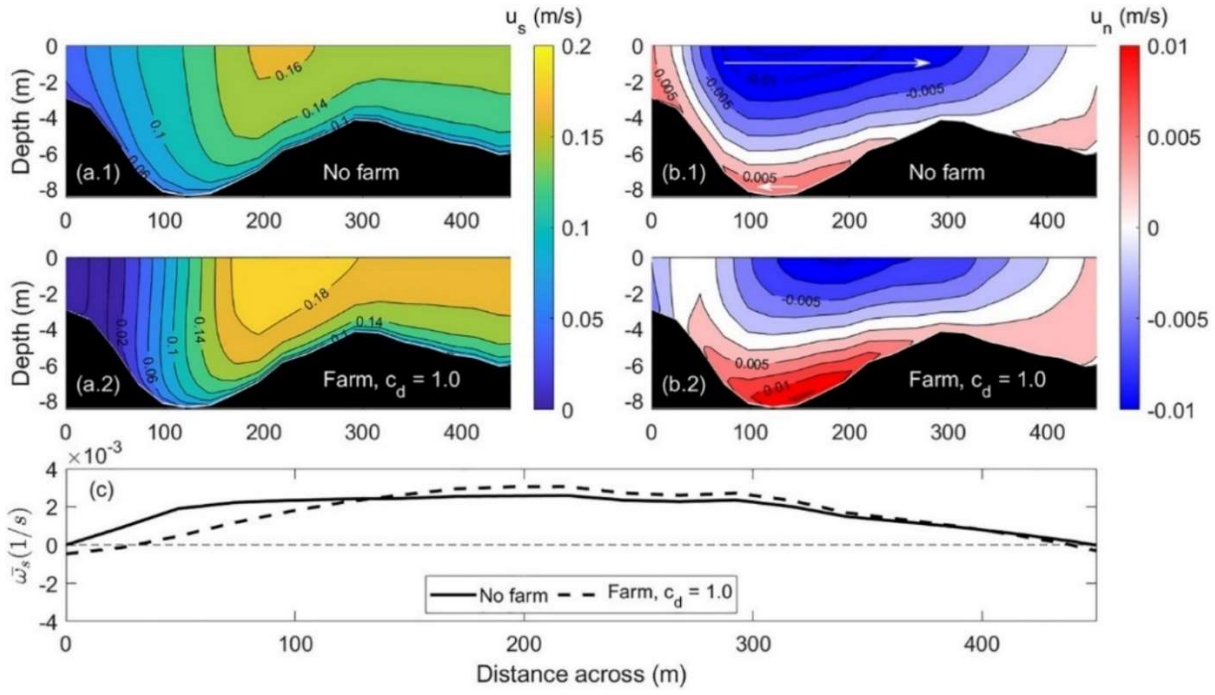

Figure 2.13 Velocity and streamwise vorticity distribution across the estuary at peak flood from the Regional Ocean Modeling system (ROMS) model simulation with and without the farm. (a.1 and a.2) Contours of streamwise velocity, u_s with and without the farm. (b.1 and b.2) contours of normal velocity, u_n, where positive (red) values indicate velocity toward the western shoal (left) and negative (blue) values indicate velocity toward the eastern shoal (right). White arrows denote direction of normal flow (c) depth-averaged streamwise vorticity, ω_s, where positive values (pointing into the paper) indicate clockwise lateral circulation and negative values indicate counterclockwise lateral circulation.

2.5. Discussion

2.5.1. The farm's Impact on Intratidal Dynamics

The farm influenced the local dynamics of the estuary in several ways. Our observations showed that the most important influence of the farm was through the reduction of streamwise flow from surface friction, which affected lateral circulation, momentum across the estuary, and vertical mixing away from

the farm. This flow reduction effect was previously reported in experiments and field observations of other types of aquaculture farms (Fan et al., 2009; Kervella et al., 2010; Lin et al., 2016; Zeng et al., 2015), and the reported consequence was an increase in flushing times within the farm (Plew, 2011b; O'Donncha et al., 2013; Wang et al., 2018).

In this particular cross section, a natural bend in the estuary exists, which promotes normal flows directed toward the outside of the bend during both flood and ebb phases and generates a clockwise lateral circulation. The farm's effect on streamwise flow influenced the centrifugal force from channel curvature, which provided a direct link between the farm and the dynamics across the estuary. The conceptual schematic presented in Figure 2.14 details how the farm impacts vertical mixing and lateral circulation. During flood at the downstream end of the farm, streamwise flows are reduced by the farm, which enhances the lateral gradient in streamwise flow from the farm to the channel. The near-surface normal flow directed toward the right by curvature pushes slower water from the farm over faster water in the channel, which sets up a vertical shear in velocity that induces mixing in the channel. This location is away from the direct influence of surface friction from the farm, and the combined effect acts to enhance the farm's frictional footprint beyond the physical extent of the farm (Figure 2.14a). This vertical mixing mechanism has previously been shown to occur from the interaction of lateral changes in streamwise velocity from channel-shoal morphology and lateral circulation (Collignon and Stacey, 2013; Huguenard et al., 2015). This work is the first to demonstrate that it can be exacerbated by a surface obstruction in conjunction with a channel-shoal interface. The smaller streamwise flows impacted by farm in the channel hinders the development of two-layer flow, thereby confining the two-layer flow structure to the left-hand side, which is supported by model results shown in Figure 2.13. During the ebb phase of the tide, flow tends to bypass the farm along the farm's leading edge. The flow bypassing combines with channel convergence to accelerate flows along the edge of the channel. The complicated three-layer flow structure in the channel pushes slower water from the thalweg over faster water along the channel wall, which enhances vertical shear and induces mixing just below the surface (Figure 2.14b). On the downstream side, flow converges back around the farm, resulting

in a smaller downstream flow reduction. This allows for a two-layer lateral flow structure to encompass the entire transect, even behind the farm. Additionally, during ebb, bypassing around the farm combines with curvature to push fresh water from the western side over denser water on the outer bend, which reinforces stratification and stabilizes the water column (Figure 2.14b).

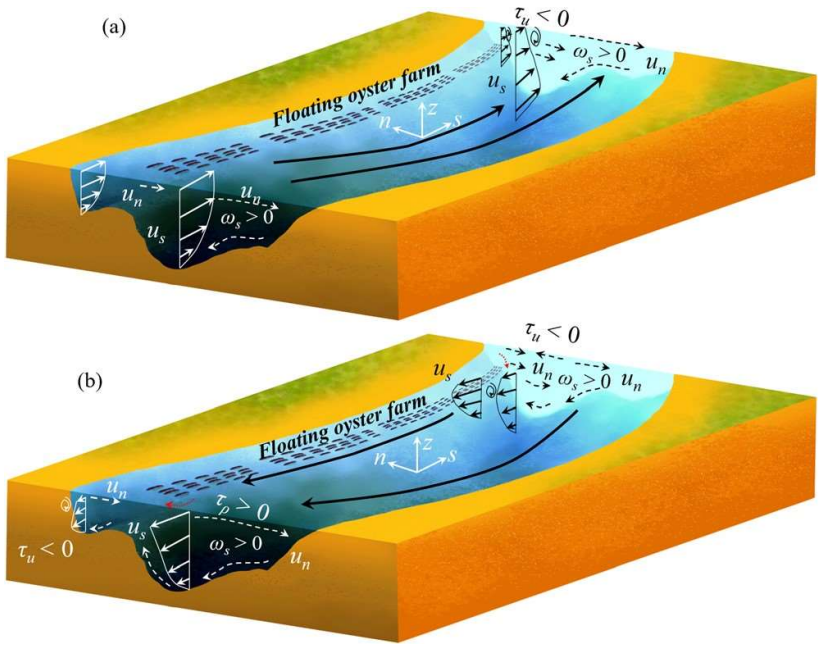

Figure 2.14 Conceptual sketch of flow patterns and mixing mechanisms at landward and seaward transects: (a) flood phase of the tide and (b) ebb phase of the tide. White and black solid arrows denote streamwise velocity, u_s; white and black dashed arrows denote normal velocity, u_n; and red dashed arrows denote local flow patterns around the farm. Curls denote vertical mixing, and ω_s is streamwise vorticity. τ_u is caused by shear straining, and τ_ρ is caused by density straining. Positive τ indicates mechanisms that stabilize the water column, and negative τ indicates mechanisms that destabilize the water column.

Though these patterns are site specific, the streamwise flow reduction is manifested through advection and centrifugal momentum terms outside of the local farm area, making these findings more

generally relevant to other systems. Streamwise flow reduction hindered the development of two-layer clockwise lateral circulation driven by channel curvature, which promoted a general flood-ebb asymmetry in the downstream lateral flow structure. Understanding how farms influence lateral circulation is important, as lateral processes are known to influence the three-dimensional transport of material (such as sediment) in estuaries (McSweeney et al., 2016). For example, Lerczak and Rockwell Geyer (2004) highlighted that intratidal asymmetry in near-bottom flows can shift the location of the channel in straight estuaries through asymmetric sediment movement. Lateral circulation can also influence subtidal flow structures through advection, which controls the streamwise movement of suspended material such as nutrients and plankton (Scully et al., 2009). The role of the farm-induced flow response on sediment transport in an estuary remains to be determined but should be an important consideration in farm siting decisions.

2.5.2. The farm's Friction Effect Versus. Channel Curvature

The argument could be made that the streamwise flow reduction patterns were induced by the shallow shoal combined with channel curvature, rather than surface friction imposed by the farm. In this case, the streamwise flow reduction is due to the centrifugal force since, qualitatively, streamwise velocity is lower in the inner bend and higher in the outer bend. If curvature significantly alters streamwise flow, one would also expect the centrifugal force to be a dominate term in the streamwise momentum.

In order to quantitatively compare the strength of channel curvature with the farm's frictional effect, a non-dimensional parameter is proposed, R_F, to estimate the ratio between farm drag, $\frac{C_D {u_s}^2}{2h_f}$, and centrifugal forcing $\frac{2u_s u_n}{R_s}$, written as $R_F = \frac{\frac{C_D {u_s}^2}{2h_f}}{\frac{2u_s u_n}{R_s}} = \frac{C_D u_s R_s}{4u_n h_f}$. C_D is the bulk drag coefficient of the farm, u_s is the streamwise velocity, u_n is the normal tidal current amplitude, R_s is the curvature in bathymetry and h_f is the farm penetration in water column. In this work, C_D = 8.4×10^{-3} ± 9.1×10^{-4}, u_s = 0.1 ~ 0.3 m/s, u_n =

0.025 ~ 0.05 m/s, R_s= 676 m at the western shoal of the study area and h_f = 0.42 m. Therefore, R_F = 9 ~ 52, which indicated that the farm frictional forcing dominated the streamwise velocity reduction in the inner bend.

This was also supported by the numerical modeling analysis, which isolated the farm's impact from the influence of bathymetry. The model qualitatively reproduced the flow patterns observed in the field, namely streamwise flow reduction, the low velocity zone behind the farm that extended to main channel, the weakened lateral circulation during flood, and the flow bypassing that occurred during ebb. Distinctions between the model and the observations were observed during flood, mainly in the vertical shear of velocity on the western half of the channel. We believe this occurred because the model overrepresented vertical mixing, thus producing uniform flow conditions over the western half of the channel (Figure 2.3b.1). This is in spite of the rotated transverse stress tensor that was used to ensure the horizontal mixing as at the *z*-surface rather than the *s*-surface. River discharge was not included in this idealized simulation in order to simplify the modelling effort. Its inclusion may have limited the simulated vertical mixing due to stratification. Additionally, the curvature-induced lateral circulation was underestimated, where depth-averaged vorticity, $\overline{\omega_s}$, was an order of magnitude lower than the field observations. One potential reason is the horizontal advections at the *s*-surface might promote too much vertical mixing, resulting in the underestimation of both vertical shear and lateral circulation in this complicated portion of the estuary.

2.5.3. Uncertainty in the Drag Coefficients

In order to incorporate the above-mentioned hydrodynamic responses from the floating aquaculture farms into large scale numerical models, such as ROMS, appropriate drag coefficients need to be applied. Researchers have previously recognized the importance of including farm-induced friction into hydrodynamic models (Wu et al., 2014; Plew, 2011b). However, in most of the models, the implemented drag coefficient is determined based on laboratory experimental data of a single cylinder or just by tuning

the settings in the model to match the field observations. Drag coefficients for aquaculture farms obtained directly from field observations have not been widely reported. In this work, we found that the bulk drag coefficient ranges from $8.4 \times 10^{-3} \pm 9.1 \times 10^{-4}$ and the effective drag coefficient of a single oyster cage ranges 0.58–0.92, both of which can be implemented in regional-scale numerical models, as well as analytical models.

The bulk friction coefficient of the floating oyster farm ($3.4 \times 10^{-3} \pm 3.8 \times 10^{-4}$) is larger than the typical bottom friction coefficient (~2.5×10^{-3}), yet smaller than the previously reported friction coefficient of a bottom oyster reef ($6 \times 10^{-3} \pm 2 \times 10^{-3} \sim 1.7 \times 10^{-2} \pm 6 \times 10^{-3}$) and oyster shell restoration ($9 \times 10^{-3} \pm 1 \times 10^{-3}$) from Whitman and Reidenbach (2012). The drag coefficient of the floating oyster farm ($8.4 \times 10^{-3} \pm 9.1 \times 10^{-4}$) is smaller than surface drag coefficient of suspended kelp (0.0547 ± 0.002 in Fan et al., 2009) and suspended mussel farms (0.0875 ~ 0.1694 in Lin et al., 2016).

One possible reason why for the lower bulk drag coefficient associated with the floating oyster farm compared to the suspended mussel farm studied by Lin et al. (2016) could be that the oyster farm has a much shallower penetration than the mussel farm. The penetration length of a mussel rope is 3.5 m, and the ratio of the farm penetration to water depth is 0.17 ~ 0.23 (Lin et al., 2016), while the penetration of oyster farm in this study was only 0.42 m, making the ratio of penetration to water depth range between 0.08 and 0.12. These drag coefficients are different in magnitude because mussels extend much deeper into the water column, making form drag more influential than a surface floating oyster farm. Another potential reason could be the drag coefficients were estimated using different techniques. Lin et al. (2016) estimated the drag coefficient of the suspended mussel farm by fitting the subsurface velocity profile to the log-law profile, while this work estimated drag coefficients using Reynolds stresses and dissipation rates. Reidenbach et al. (2006) found the drag coefficient of a coral reef using three methods: the log-law fit, the Reynolds stress method, and the dissipation method, all of which were similar when the boundary layer was well developed (i.e., TKE production was balanced by dissipation).

The estimated drag coefficient of a single oyster cage was found to range from 0.58 to 0.92. The oyster cage consists of two impermeable pontoons and a basket holding six permeable oyster bags. Following Blevins (1984), the lower limit of $c_{d,e}$ was 0.76 under the assumption that the oyster basket was completely permeable (i.e., empty), while the upper limit of $c_{d,e}$ was 1.62 under the assumption that the oyster basket was an impermeable box. Although the estimation of $c_{d,e}$ is sensitive to $\bar{U}_f$, which is lacking in our measurements, the order of magnitude consistency between $c_{d,e}$ estimated from hydrodynamics and that estimated based on typical drag coefficient justifies the approach to estimate the drag coefficient of a single oyster cage based on field-collected hydrodynamic data. Therefore, $c_{d,e}$ is applicable to estimate bulk drag coefficient C_D of new farms orientations that have the same penetration length but different cage densities (i.e., $\bar{a}$).

The uncertainty in the estimation of drag coefficients arises mainly from the uncertainty in the estimation of the friction velocities u_f^* and u_b^*. The use of Reynolds stress in quantifying u_f^* and u_b^* relies on the assumption of the formation of an equilibrium boundary layer. A single-point measurement of Reynolds stress does not provide vertical distributions of Reynolds stress. In the future, multiple ADVs should be deployed vertically under the farm in order to improve the accuracy of the friction coefficient estimation. The value of drag coefficient is also sensitive to the reference velocity. In this work U_f was not available and was replaced using the velocity under the farm. Generally speaking, U_f in the farm layer is smaller than the velocity under the canopy, so that this estimation likely provided the lower limit of C_D. It is also important to note that the drag coefficient likely changes with farm layout, that is, the area ratio between the long-line covered water surface and the total water surface in the farm area, as well as the oyster size in the growth cycle. The proposed drag coefficient represents an average of the drag imposed by the farm throughout the flood tide. It is important to note that using a constant drag coefficient might result in potential inaccuracies in model predictions during certain phases of the tide, especially at the end of ebb, where the drag may be slightly large. Furthermore, the uncertainty in determining drag coefficient, also raised uncertainty in the mode results from numerical simulation, which might impact the strength of flow

reduction and suppression in lateral circulation by drag force rather than change the flow patterns essentially. Nonetheless, this work is valuable, as it provides a first step toward improving the understanding of the frictional influences of floating oyster farms. The qualitatively consistency between model results and field observation in flow patterns and mixing mechanisms stimulates motivations in further running realistic simulations to achieve better matching between model results and field observation.

2.6. Conclusions

An analysis in the hydrodynamic response of a floating oyster farm indicated that farm-induced friction can play an important role in the momentum and vertical mixing across the estuary. Field measurements were collected around a floating oyster farm in a curved portion of a low inflow estuary. During flood, the farm imposed a surface friction effect that reduced the flow through the farm relative to nonfarm areas, which enhanced the lateral gradient in streamwise flow. Lateral flows driven by curvature then enhanced the vertical shear in velocity near the surface of the channel, which lead to vertical mixing that expanded the farm's frictional footprint. The streamwise flow reduction manifested in the streamwise advection momentum term, which reduced the normal centrifugal force and hindered the development of a two-layer lateral circulation in the farm's expanded footprint. During ebb, the flow tended to bypass the farm and followed the natural bathymetry. The streamwise flow reduction in the farm area was weaker during ebb as compared to flood. The flow bypassing effect emerged in the normal advection and convergence forcing momentum terms. In general, the normal momentum was dominated by the centrifugal acceleration associated with a natural bend in the channel, which promoted a two-layer lateral circulation to form across the downstream transect. These observations indicated that farm-induced friction can affect the momentum and vertical mixing away from the immediate farm area. In order to capture these effects in numerical model simulations, a bulk drag coefficient representative of the farm needs to be implemented. Using the observations, a bulk drag coefficient of $8.4 \times 10^{-3} \pm 9.1 \times 10^{-4}$ was determined for this particular

farm, while a drag coefficient of 0.58 ~ 0.92 was estimated for a single oyster cage within the farm. An idealized simulation that included the calculated drag from the farm showed cross-sectional distributions of streamwise velocity and the reduction lateral circulation that were qualitatively similar to the field observations.

Note that both of the proposed coefficients are limited to floating oyster farms during a certain set of conditions. More studies are required to provide improved drag coefficients for more generalized scenarios, which could be achieved through detailed laboratory experiments, highly instrumented field campaigns, and/or computational fluid dynamics (CFD) simulations. In the general application of such a value, we expect the drag coefficient to change given variations in the farm design, stocking rate, and oyster size at different growth period. There is a need for future studies to understand how floating oyster farms affect subtidal flows and material transport in estuaries. Once these effects are better understood, a sustainable framework can be developed for aquaculture siting locations that considers farm size and orientation while maintaining the health of the natural system.

CHAPTER 3

ANALYTICAL INVESTIGATION INTO FLOATING AQUACULTURE FARM IMPACT ON TIDAL AND SUBTIDAL FLOWS

3.1. Introduction

Despite substantial growth from the mid-2010s to the early 2020s, the aquaculture industry only supplies 40% of the global fish demand, leaving a current supply gap of 28 million tons (FAO, 2018). According to a projection from the Food and Agriculture Organization (FAO, 2018), global aquaculture will need to grow 9.9% per year to fill the demand–supply gap, which provides an economic opportunity for aquaculture industry expansion. The interactions between aquaculture farms and their surrounding environments must be understood to determine the carrying capacity of the system, which is the level that a system can withstand before detrimental effects occur (Weitzman and Filgueira, 2020), as well as nutrient availability and potential depletion. Previous studies related to aquaculture activities were conducted in the open ocean, and mainly focused on hydrodynamics (Grant and Bacher, 2001; Duarte et al, 2014; Lin et al, 2016), transport of dissolvable substances (Plew, 2011; O'Donncha et al, 2013; Wang et al., 2018), species growth rate and production (Nunes, et al, 2003; Shi et al., 2011; Konstantinou and Kombiadou; 2020) as well as the engineering design of related infrastructure (Fredriksson et al., 2000; Stevens et al., 2008). Since estuaries provide a more sheltered environment compared to the open ocean, it is important to evaluate the ecosystem sustainability of expanded aquaculture activities in estuaries. The goal of this work is to better understand how aquaculture farms impact estuarine dynamics, so that both the local ecosystem and the aquaculture industry can be sustained in the future as demand for aquaculture rises.

The interaction between farms and the surrounding flow depends on the type of aquaculture farm (e.g., mussel, oyster, sea vegetable and fin fish). A turbulent boundary layer develops above and beneath oyster tables (Kervella et al. 2010), while a long wake zone forms behind shellfish and salmon farms (Delaux et al, 2011; Cornejo et al, 2014). Drag forcing tends to reduce the flow inside of kelp and mussel

farms, which causes flow redistribution around the farm (Grant and Bacher, 2001, O'Donncha et al, 2013). Fluid-structure interaction with kelp farms reduces water exchange between the farm area and the ambient waters (Shi et al., 2011), which increases flushing and residence times within the farm (Wang et al., 2018). Reduced exchange can affect the nutrient supply, resulting in lower levels of oxygen in salmon cages (Johansson et al, 2007) and lower chlorophyll concentrations inside of mussel farms (Lin et al., 2016). Variations in food supply can create spatially inhomogeneous growth rates inside of kelp farms (Shi et al., 2011), while low exchange rates in nearby areas without farms can promote phytoplankton blooms (Wang et al., 2018). Additionally, farms can cause deposition of particles associated with shellfish aquaculture (Silva et al., 2019) and enlarge the deposition area of sediment (Zhang et al., 2020). In estuaries, floating oyster farms can induce vertical mixing in the nearby channel, which extends the farm's frictional footprint and limits the development of lateral circulation (Liu and Huguenard, 2020).

In estuaries, the health of the ecosystem is related to transport of particulates, such as pollutants, plankton, sediment, and detritus. Tidal currents carry large fluxes of material over tidal timescales, while subtidal flows are primarily responsible for longer term material transport (Stacey et al., 2001; Wong et al., 1994). Subtidal flows can be driven by many factors, some of which include along channel density gradients, wind shear forcing, remote atmospheric forcing, river discharge, Coriolis forcing, nonlinear dynamics of barotropic tides, tidal asymmetries in mixing, and channel curvature (Wong 1994; Friedrichs and Hamrick 1996; Valle-Levinson et al., 2003; Li and O'Donnell 2005; Scully and Friedrichs, 2007; Chant 2002). The addition of aquaculture farms into an estuary could alter the existing tidal current structure, resulting in modified subtidal flows and material transport.

Numerical models are valuable tools for studying local farm impacts on tidal flows and material transport in realistic settings. It is common to include the effects of aquaculture in regional scale models by using either a drag force (Grant and Bacher, 2001; Wu et al., 2014; Sun et al., 2020) or by imposing the farms with porous media (Konstantinou and Kombiadou, 2020). The shortcomings are that the mesh needs

to be very fine to resolve the farm area, requiring the time steps to be small, which results in computationally expensive simulations.

Analytical frameworks are an attractive alternative to numerical models and have been used to study subtidal dynamics by decomposing complex subtidal flows into components that are forced by individual mechanisms (Winant 2008, Huijts et al., 2009; Zitman and Schuttelaa, 2012). Suspended vegetation and floating aquaculture farms such as kelp, mussel and oyster farms are often referred to as canopies. Analytical models have been developed for unidirectional channel flow with a suspended canopy. Huai et al. (2012) proposed a 5-layer analytical model with a mixing length closure of the Reynolds stress for vertical profiles of channel flow influenced by suspended vegetation. Li et al. (2019) proposed a 2-layer model with a porous material for the vegetation layer and a quartic function of vertical eddy viscosity for the layer under the canopy. Both analytical frameworks were developed for steady and prismatic channel flow, and there is yet to be an analytical framework for modeling canopies in unsteady (tidal) flow in estuaries with a realistic, converging width.

This study aims to fill this gap by developing a semi-analytical model for a low inflow estuary with convergent width in order to simulate the influence of a floating canopy on subtidal flows. The research objectives are to (1) develop a semi-analytical framework that includes a floating aquaculture farm in tidal flow (2) investigate the intratidal flow response of a floating farm, (3) determine how floating farms alter the subtidal flows. The analytical framework is presented in section 2 and an application of this framework to an oyster aquaculture farm in the Damariscotta River estuary in Maine, USA is presented in section 3. Section 4 uses field observations and the analytical model to show that the subtidal flow structure in a reach with a floating oyster farm is reversed from what is typically expected in an elongated, rotating system. In the discussion, the analytical model is used to show how the farm influences subtidal flows.

3.2. Model

3.2.1. Tidal flow

The governing equations for geophysical flow in a curved estuary with low river discharge consist of the continuity equation 3.1a and dynamic equations 3.1b, c for along (x, u) and across (y, v) channel velocity components:

$$\frac{\partial u}{\partial x}+\frac{\partial v}{\partial y}+\frac{\partial w}{\partial z}=0 \quad (3.1.a)$$

$$\frac{\partial u}{\partial t}+u\frac{\partial u}{\partial x}+v\frac{\partial u}{\partial y}+w\frac{\partial u}{\partial z}=fv-g\frac{\partial \eta}{\partial x}+\frac{\partial}{\partial z}\left(A_z\frac{\partial u}{\partial z}\right)-\frac{2uv}{R+y}-\frac{1}{2}\frac{C_D}{h_f}u\sqrt{u^2+v^2} \quad (3.1.b)$$

$$\frac{\partial v}{\partial t}+u\frac{\partial v}{\partial x}+v\frac{\partial v}{\partial y}+w\frac{\partial v}{\partial z}=-fu-g\frac{\partial \eta}{\partial y}+\frac{\partial}{\partial z}\left(A_z\frac{\partial v}{\partial z}\right)+\frac{u^2-v^2}{R+y}-\frac{1}{2}\frac{C_D}{h_f}v\sqrt{u^2+v^2} \quad (3.1.c)$$

where, x, y, and z denote along, across and vertical directions and u, v, and w are along, across and vertical velocities. Positive x, u is into the estuary and positive y, v is to the left shoal and z is zero at the mean water surface and positive upward (Figure 3.1a). The Coriolis parameter is f, η is the surface elevation, A_z is the vertical eddy viscosity, R is the bending radius in the main channel, C_D is the bulk drag coefficient of aquaculture farm and h_f is the penetration depth of the farm. Note that the farm drag forcing is only imposed in the farm area and that the baroclinic forcing (i.e., along-channel density gradient) is ignored for tidal flow.

No slip conditions, $u = 0$, $v = 0$, are applied at the bottom ($z = -h$). Zero gradient boundary conditions are applied at the surface (no wind), i.e. $\frac{\partial u}{\partial z}=0$, $\frac{\partial v}{\partial z}=0$ at $z = \eta$. The continuity equation 3.1a is integrated from the bottom to the free surface and kinematic boundary conditions are applied at the free surface, which results in the mass conservation equation,

$$\frac{\partial \eta}{\partial t} + \frac{\partial}{\partial x}\int_{-h}^{\eta} u dz + \frac{\partial}{\partial y}\int_{-h}^{\eta} v dz = 0 \quad (3.2).$$

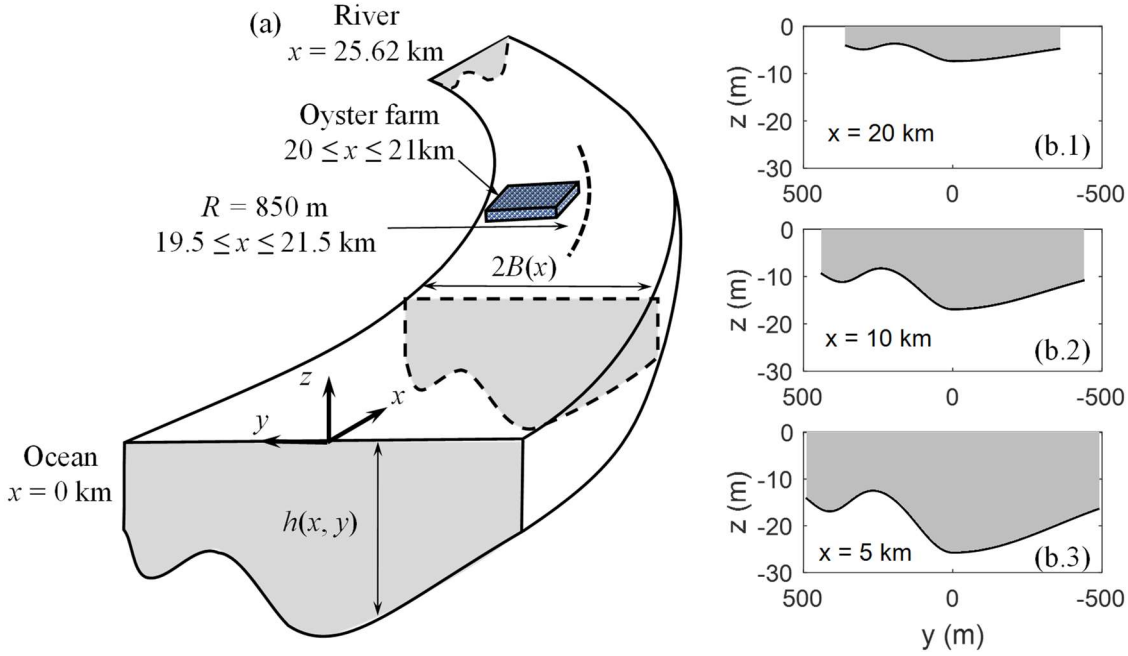

Figure 3.1 The model bathymetry h is arbitrary h (x, y) across the channel and converges in width and depth along a curved channel. A curvilinear coordinate system (x, y, z) is used, where the x- and y-coordinates are along and across, respectively, and z is the vertical. The perspective is looking into the estuary. B(x) is the half width of the estuary. The portion denoted by dashed line (19.5 ≤ x ≤ 21.5 km) has a bend with radius of 850 m in the main channel. (b1~3) cross-sections along the estuary at 5 km, 10 km and 20 km.

The surface elevation and current velocity are decomposed into semidiurnal harmonic components (η_0, u_0, v_0, w_0) and subtidal components (η_s, u_s, v_s, w_s)

$$\eta = \eta_0 + \eta_s = Re\left[N_0 e^{-i\omega t}\right] + \eta_s \quad (3.3.a)$$

$$u = u_0 + u_s = Re\left[U_0 e^{-i\omega t}\right] + u_s \quad (3.3.b)$$

$$v = v_0 + v_s = Re\left[V_0 e^{-i\omega t}\right] + v_s \quad (3.3.c)$$

$$w = w_0 + w_s = Re\left[W_0 e^{-i\omega t}\right] + w_s \quad (3.3.d)$$

where, N_0, U_0, V_0, W_0 are the complex amplitudes of surface elevation, along, across and vertical velocities.

The decompositions in equation 3.3 are substituted into equations 3.1b, c and equation 3.2, and the leading order terms for the semidiurnal component are collected, resulting in the governing equations for tidal flow:

$$-i\omega N_0 + \frac{\partial}{\partial x}\left(h\int_{-1}^{0} U_0 d\sigma\right) + \frac{\partial}{\partial y}\left(h\int_{-1}^{0} V_0 d\sigma\right) = 0 \quad (3.4.a)$$

$$-i\omega U_0 = fV_0 - g\frac{\partial N_0}{\partial x} + \frac{1}{h^2}\frac{\partial}{\partial \sigma}\left(\widetilde{A_z}\frac{\partial U_0}{\partial \sigma}\right) - \frac{1}{2}\frac{8C_D\widehat{U}}{3\pi h_f}U_0 \quad (3.4.b)$$

$$-i\omega V_0 = -fU_0 - g\frac{\partial N_0}{\partial y} + \frac{1}{h^2}\frac{\partial}{\partial \sigma}\left(\widetilde{A_z}\frac{\partial V_0}{\partial \sigma}\right) - \frac{1}{2}\frac{8C_D\widehat{U}}{3\pi h_f}V_0 \quad (3.4.c).$$

Note that equation 3.4 is defined on σ coordinates, where $\sigma = \frac{z}{h}$, is the sigma coordinate in vertical direction, $\sigma = -1$ at the bottom , $\sigma = 0$ at the undisturbed water surface, $\sigma = \frac{\eta}{h}$ at the free surface. Both the internal friction and farm-induced drag force are linearized. The vertical eddy viscosity A_z is replaced by an effective vertical eddy viscosity $\widetilde{A_z}$ (Chen and de Swart, 2016).

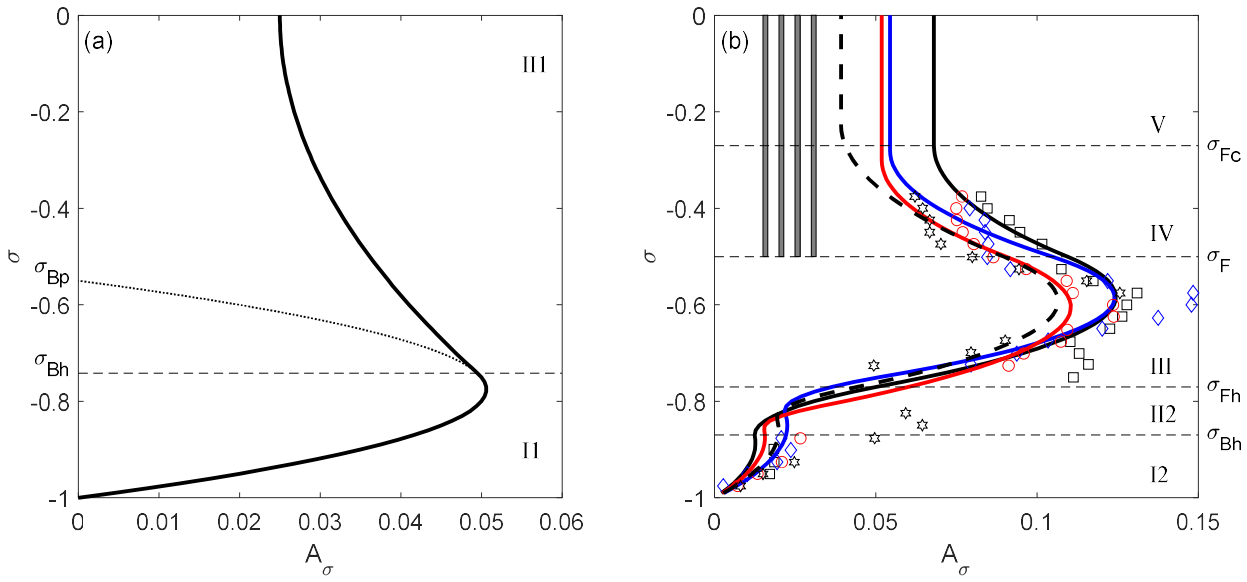

Figure 3.2 Shape factor (A_σ) of vertical eddy viscosity, A_σ, without the farm (a) and with the farm (b). In (a) I1 is the lower layer, II1 is the upper layer. σ_{Bp} is where mixing length scale decays to zero, $\sigma_{Bh}$is the intersection between two layers. In (b) markers denote A_σ profile from Plew (2011). Lines denote the proposed 5-layer piecewise A_σ. Black squares and black line are for the case with canopy density, a = 1.908 m^{-1} (B12); Blue diamonds and blue line are for a = 1.272 m^{-1} (B13); Red circles and red line are for density a = 0.954 m^{-1} (B14); Black hexagons and black dashed line are for a = 0.477 m^{-1} (B15). Grey bars denote canopy layer ($\sigma_F \le \sigma \le 0$). I2: bottom boundary layer ($-1 \le \sigma < \sigma_{Bh}$); II2: transition layer ($\sigma_{Bh} \le \sigma < \sigma_{Fh}$); III: mixing layer beneath canopy ($\sigma_{Fh} \le \sigma < \sigma_F$); IV: canopy mixing layer ($\sigma_F \le \sigma < \sigma_{Fc}$); V: canopy drag layer ($\sigma_{Fc} \le \sigma \le 0$).

The farm-induced drag force in unit volume $\frac{C_D u\sqrt{u^2+v^2}}{h_f}$ is linearized by $\frac{8}{3\pi h_f} C_D \widehat{U} u_0$, i.e. $\frac{8}{3\pi h_f} C_D \widehat{U} Re\left[U_0 e^{-i\omega t}\right]$, where $\widehat{U} = \sqrt{|U_0|^2 + |V_0|^2}$ is the magnitude of the reference velocity. The linearization keeps the total energy dissipated by turbulence and farm drag over one tidal cycle consistent with the energy dissipated without linearization. A two-layer parabolic pricewise vertical eddy viscosity structure (Chen and de Swart, 2016) was applied to no farm region while a five-layer parabolic pricewise vertical eddy viscosity structure was applied to farm region (Figure 3.2), where parametrization of eddy

viscosity structure was in Appendix E. The vertical eddy viscosity parameterization was validated by comparing the analytical solution with the Plew (2011) velocity measurements in a suspended canopy (see Appendix E).

3.2.2. Analytical solution of tidal flow

The along and across channel velocities are coupled when Coriolis forcing is considered in both components. To solve equations 3.4, coupled velocities and barotropic pressure gradients were defined as $\mathbb{W}^{\pm} = U_0 \pm iV_0$, $SL^{\pm} = g\frac{\partial N_0}{\partial x} \pm ig\frac{\partial N_0}{\partial y}$. The general solutions for tidal currents were linear combinations of the Legendre function $P_{\alpha}(x)$ and the Legendre functions of the second kind $Q_{\alpha}(x)$ as shown below,

$$\mathbb{W}_j = C_{j,1}P_{\alpha_j}(\beta_{\sigma,j}) + C_{j,2}Q_{\alpha_j}(\beta_{\sigma,j}) - \frac{iSL}{a} \qquad (3.5.a)$$

$$\mathbb{W}_{\mathrm{IV}} = C_{\mathrm{IV},1}P_{\alpha_{\mathrm{IV}}}(\beta_{\sigma,\mathrm{IV}}) + C_{\mathrm{IV},2}Q_{\alpha_{\mathrm{IV}}}(\beta_{\sigma,\mathrm{IV}}) - \frac{iSL}{a_{F\mathrm{IV}}} \qquad (3.5.b)$$

$$\mathbb{W}_{\mathrm{V}} = C_{\mathrm{V},1}e^{-\frac{(-1)^{3/4}\sqrt{a_{F\mathrm{V}}}h}{\sqrt{A_0A_S^*}}\sigma} + C_{\mathrm{V},2}e^{\frac{(-1)^{3/4}\sqrt{a_{F\mathrm{V}}}h}{\sqrt{A_0A_S^*}}\sigma} - \frac{iSL}{a_{F\mathrm{V}}} \qquad (3.5.c).$$

Note that the region with no farm, equation 3.5a with indices $j = \mathrm{I1}, \mathrm{II1}$ indicates the solution in layer I1 and II1 (Figure 3.2a). While in the farm region, equation 3.5a with $j = \mathrm{I2}, \mathrm{II2}, \mathrm{III}$ together with equations 3.5b and 3.5c indicate the solution in layer I2, II2, III, IV and V (Figure 3.2b). For tidal flow, $\alpha_{\_}$ represents $\alpha_{\_}{}^{+}$ and $\alpha_{\_}{}^{-}$, which are the degree of the Legendre function, $\beta_{\sigma,\_}$ represents $\beta_{\_}(\sigma)^{+}$ and $\beta_{\_}(\sigma)^{-}$ as functions of σ, which are the arguments of the Legendre function. a is equal to $\omega \mp f$, while, $a_{F\mathrm{IV}} = \omega \mp f + i\frac{4C_DU_{F\mathrm{IV}}}{3\pi h_f}$, $a_{F\mathrm{V}} = \omega \mp f + i\frac{4C_DU_{F\mathrm{V}}}{3\pi h_f}$, where $U_{F\mathrm{IV}}$ and $U_{F\mathrm{V}}$ are tidal reference velocities of the farm drag force in the mixing layer and the drag layer within canopy. The coefficients $C_{\_,1}$ and $C_{\_,2}$ are determined

based on bottom and surface boundary conditions together with continuous and smooth interfacial conditions.

The tidal current velocities from equation 3.5 are integrated over the water column, and depth integrated velocities are substituted into equation 3.4a. The result is a linear second order elliptic partial differential equation for tidal amplitude

$$\nabla \cdot (-\boldsymbol{c}\nabla N_0) - 2\omega N_0 = 0 \qquad (3.6)$$

where, $\boldsymbol{c} = g\begin{bmatrix} -(M^+ + M^-) & -i(M^+ - M^-) \\ i(M^+ - M^-) & -(M^+ + M^-) \end{bmatrix}$ is the coefficient matrix and M^+ and M^- are the integration of the velocity shape function over depth, which are functions of *x* and *y*.

For elongated estuaries, $\frac{dN_0}{dy} \ll \frac{dN_0}{dx}$ terms related to $\frac{dN_0}{dy}$ can be neglected. equation 3.6 is often simplified to an ordinary differential equation (Winant 2007; Ross et al, 2017), however, the floating aquaculture farm occupies a finite portion of the estuary, where $\frac{dN_0}{dy}$ and $\frac{dN_0}{dx}$ are likely the same order of magnitude near the farm. Therefore, equation 3.6 is not simplified but solved numerically using a finite element method. The boundary conditions for equation 3.6 are prescribed tidal amplitude at the mouth and zero gradient of tidal amplitude along the shoal and at the end of the estuary. Note that equation 3.6 is generic and applicable to non-elongated estuaries or bays, where $\frac{dN_0}{dy}$ and $\frac{dN_0}{dx}$ are the same order of magnitude.

3.2.3. Subtidal flow

The temporal average of equations 3.1b, c and equation 3.2 provides the governing equations for subtidal flow

$$\frac{\partial}{\partial x}\left(h\int_{-1}^{0}\overline{u_s}d\sigma+\overline{\eta_0 u_0|_{\sigma=0}}\right)+\frac{\partial}{\partial y}\left(h\int_{-1}^{0}\overline{v_s}d\sigma+\overline{\eta_0 v_0|_{\sigma=0}}\right)=0 \quad (3.7.a)$$

$$\frac{1}{h^2}\frac{\partial}{\partial\sigma}\left(\widetilde{A_z}\frac{\partial\overline{u_s}}{\partial\sigma}\right)+f\overline{v_s}-g\frac{\partial\overline{\eta_s}}{\partial x}=\overline{u_0\frac{\partial u_0}{\partial x}}+\overline{v_0\frac{\partial u_0}{\partial y}}+\overline{w_0\frac{\partial u_0}{\partial z}}+\frac{g}{\rho_0}\frac{\partial\rho}{\partial x}h\sigma+\frac{2\overline{u_0 v_0}}{R+y} \quad (3.7.b)$$

$$\frac{1}{h^2}\frac{\partial}{\partial\sigma}\left(\widetilde{A_z}\frac{\partial\overline{v_s}}{\partial\sigma}\right)-f\overline{u_s}-g\frac{\partial\overline{\eta_s}}{\partial y}=\overline{u_0\frac{\partial v_0}{\partial x}}+\overline{v_0\frac{\partial v_0}{\partial y}}+\overline{w_0\frac{\partial v_0}{\partial z}}-\frac{\overline{{u_0}^2-{v_0}^2}}{R+y} \quad (3.7.c)$$

where, $\overline{\eta_s}$, $\overline{u_s}$, $\overline{v_s}$, $\overline{w_s}$ are also known as Eulerian average water level and velocities (Winant, 2008). The subtidal along channel baroclinic pressure gradient is $\frac{g}{\rho_0}\frac{\partial\overline{\rho}}{\partial x}h\sigma$ where it is assumed that the tidally averaged along channel density gradient, $\frac{\partial\overline{\rho}}{\partial x}$, is independent of depth. $\frac{2\overline{u_0 v_0}}{R+y}$ and $\frac{\overline{{u_0}^2-{v_0}^2}}{R+y}$ are the centrifugal forces.

The subtidal velocities are defined as $u_T=\overline{u_s}+\frac{1}{h}\overline{\eta_0 u_0|_{\sigma=0}}$ and $v_T=\overline{v_s}+\frac{1}{h}\overline{\eta_0 v_0|_{\sigma=0}}$ (Robinson, 1983; Li and O'Donnell, 2005). Therefore, equation 3.7a becomes

$$\frac{\partial}{\partial x}\left(h\int_{-1}^{0}u_T d\sigma\right)+\frac{\partial}{\partial y}\left(h\int_{-1}^{0}v_T d\sigma\right)=0 \quad (3.8).$$

Two conservative conditions are introduced, where the cross-sectionally integrated along channel transport is equivalent to the river discharge, which is neglected in this work. Additionally, the depth integrated across channel transport is zero, resulting in

$$\int_{-B}^{B}h\int_{-1}^{0}u_T d\sigma\, dy=0 \quad (3.9.a)$$

$$h\int_{-1}^{0}v_T d\sigma=0 \quad (3.9.b).$$

Assuming the along channel subtidal surface slope $\frac{\partial\overline{\eta_s}}{\partial x}$ is constant across the channel, $\frac{\partial\overline{\eta_s}}{\partial x}$ and $\frac{\partial\overline{\eta_s}}{\partial y}$ were obtained by substituting the depth integrated subtidal current velocity, which was obtained by solving from equations 3.7 to equations 3.9.

3.3. Analytical model for Damariscotta River estuary

3.3.1. Damariscotta River estuary

Estuaries along the Gulf of Maine have complicated morphologies (e.g., constrictions, sills, channel bends) and tidal forcing tends to be meso- or macro-tidal and dominated by the semidiurnal tide. A large portion of the Maine shellfish industry is sited upstream in the shallow, sheltered parts of estuaries. To understand the dynamic influence of a floating aquaculture in an estuary, the developed analytical model was applied to a floating oyster aquaculture farm in the low inflow Damariscotta River estuary; a short system (~30 km) that features multiple constrictions and bends. The upper reach of the Damariscotta is optimal for shellfish due to its long residence time, warm temperature, and high primary production (Bricknell et al., 2020). The estuary width converges from approximately 1000 m at the mouth to 450 m near the head, and the main channel varies from 40 m deep at the mouth to less than 3 m at the head (Chandler, 2016). The semidiurnal tidal amplitude varies from 1.1 m to 1.8 m from neap to spring tides (Lieberthal et al., 2019a; Lieberthal et al., 2019b). Due to the existence of a dam upstream the freshwater discharge only reaches ~15 m^3/s in the wet season (Spring) and is <1 m^3/s in the dry season (fall), making this a low inflow estuary. Due to the seasonal variation of freshwater discharge, the river is weakly stratified during the dry season and partially stratified during the wet season (Huguenard et al., 2019).

A floating oyster farm with an along-estuary length of ~1km is put into the model 20 ~ 21km from the mouth (Figure 3.1a). The farm is located on the left-hand side of the cross section within $0.05B \sim 0.9B$, where B is half of the channel width. The penetration of the floating farm into water column is 0.42 m. The farm, which sits alongside the primary channel, features a secondary channel directly under the farm. The farm area also includes a main channel bend with a radius of 850 m and the left shoal is located at the inner bend and right shoal is at the outer bend (Figure 3.1a).

3.3.2. Data collection

Cross sections of current velocities were collected for two semidiurnal tidal cycles (~13 hr survey) on 16 June 2017 (neap tide) and 23 June 2017 (spring tide). Two 1200 kHz RDI Acoustic Doppler Current Profilers (ADCP) were towed synchronously to sample two lateral transects of current velocity at 2 Hz across the river along the farm's landward and seaward boundaries. Data were collected in 0.25 m vertical bins with a 0.55 m blanking distance between the instrument and the first bin was at 0.80 m depth. The bottom 10% of profiles were masked to account for side lobe interference. Current velocities were rotated to the along and across channel direction. For more information on the measurement scheme, see Liu and Huguenard (2020). A harmonic analysis based on a least squares fit was utilized to obtain tidal current amplitudes in semidiurnal (M2), quarter-diurnal (M4), sixth-diurnal (M6) and subtidal constituents.

3.3.3. Model setup

An idealized bathymetry that is based on the bathymetry found in the field measurements is used in this work, where the convergence in both width and depth is assumed to follow an exponential decay from the mouth. A symbolic bottom bathymetry was applied to mimic the bifurcated bottom bathymetry (Figure 3.1b). The bathymetry over the entire domain is parameterized as,

$$B(x) = B_0 e^{-\frac{x}{L_b}} \qquad (3.10.a)$$

$$h_0(y_0) = \begin{cases} 16 + 9.5e^{-\left(5y_0 - \frac{25}{6}\right)^2} + 23e^{-(3y_0)^2} & 0 \le y_0 \le 1 \\ 16 + 9.5e^{-\left(5y_0 - \frac{25}{6}\right)^2} + 23e^{-{y_0}^2} & -1 \le y_0 < 0 \end{cases}, y_0 = \frac{y}{B(x)} \qquad (3.10.b)$$

$$h(x,y) = h_0\left(\frac{y}{B(x)}\right) e^{-\frac{x}{L_h}} \quad . \qquad (3.10.c)$$

At the mouth, half of the channel width is $B_0 = 550$ m. The width decays with an e-folding length of $L_b = 47.5$ km toward the head, shown as Figure 3.1b. The bottom bathymetry is assumed to have similar topography at each cross section, parameterized in equation 3.10b, where y_0 is the nondimensional across channel coordinate. The convergence of depth moving toward the head exponentially decays with an e-folding length of $L_h = 11.0$ km (equation 3.10c; Figure 3.1b). The total length of the model is 25.62 km, covering the parts of the estuary where tidal forcing dominates the hydrodynamics.

Tidal flow was forced with a tidal amplitude of 1.78 m at the mouth. A typical bottom roughness was applied ($\sigma_0 = 1.0 \times 10^{-3}$). The friction velocity amplitude $\widehat{u^*}$ for the bottom was initially set as 0.15 m/s, and after several iterations varied from 0.11 to 0.17 m/s at different locations. The drag coefficient of the farm was provided by Liu and Huguenard (2020). All other input parameters are listed in Table. 1.

Table 2.1 Input parameters for semi-analytical model

Parameters	**Data**
Channel length, L_c	25.62 km
Half channel width, B	500m at mouth, 254 m at head
E-folding length of width convergence, L_b	47.5 km
E-folding length of depth convergence, L_h	11.0 km
Channel bend radius in main channel, R	850 m, $19.5 \leq x \leq 21.5$ km
Farm location	$20 \leq x \leq 21$ km, $0.05B \sim 0.9B$
Farm penetration, h_f	0.42 m
Bulk drag coefficient of the farm, C_D	0.0084
Tidal amplitude at mouth	1.78 m
Bottom friction velocity amplitude, $\widehat{u^*}$	0.011 ~0.017 m/s

Table 2.1 Continued.

Nondimensional bottom roughness, σ_0	1.0×10^{-3}
2-layer vertical eddy viscosity parameter, σ_0	-0.60
Subtidal along channel density gradient, $\frac{\partial\rho}{\partial x}$	-6×10^{-4} kg/m^4
Nondimensional surface eddy viscosity, A_S^*	0.01
5-layer vertical eddy viscosity parameter, σ_F	$-h_f/h$
5-layer vertical eddy viscosity parameter, σ_{Fp}	$1.6\sigma_F$
Nondimensional eddy viscosity at farm lower edge, A_F^*	0.25

3.3.4 Idealized transport time

An idealized "transport time", defined as the average time taken by Lagrangian particles released at upstream of the farm to be transported away from the farm area, was computed to generally understand how the presence of a farm may affect the material transport of upstream particulates. We clearly note that these transport times do not reflect residence times in the Damariscotta Estuary, but rather timescales in a simplified basin. We expect the actual residence times in the Damariscotta Estuary to vary from those presented here due to channel complexities and wind conditions. The trajectory was calculated based on tidal and subtidal flow at surface obtained from the model:

$$\frac{\partial X}{\partial t} = Re\left[U_0(X,Y,0)e^{-i\omega t+\varphi}\right] + u_T(X,Y,0) \qquad (11.a)$$

$$\frac{\partial Y}{\partial t} = Re\left[V_0(X,Y,0)e^{-i\omega t+\varphi}\right] + v_T(X,Y,0) \qquad (11.b)$$

where, $X(t)$ and $Y(t)$ are the coordinates of a particle at time t; $U_0(X,Y,0)$ and $V_0(X,Y,0)$ are the complex along and across channel tidal amplitudes at surface at particle location; $u_T(X,Y,0)$ and $v_T(X,Y,0)$ are

surface subtidal along and across channel transport velocities at particle location; φ denotes the phase of the tide when the particle is released. In this work, four values of φ were used so that the 4 particles were released in the same initial location over one tidal cycle at peak ebb, slack tide after ebb, peak flood, and slack tide after flood, respectively. The transport time is the average of the time it takes for each particle to be transported away from farm area. The implicit Euler method with a time step of 1 s was applied to numerically solve equation 3.11.

3.4. Results

Field observations revealed along-channel subtidal flows that were laterally sheared in the channel, with landward flow in the farm area and seaward flow in the remainder of the cross-section (Figure 3.3b.1). In the farm area ($0.05 < y < 0.26$ km), landward u_T ranged from 0.04 ~ 0.06 m/s. On the right-hand side of the estuary ($y < 0$), values of u_T reached up to -0.06 m/s over the right shoal on the outside of the channel bend ($y = -0.23$km). Observations of u_T (Figure 3.3b.1) deviated from that typically expected in an elongated tidal basin, where inflow is on the right-hand side of the channel and outflow is on the left (Winant, 2008; Huijts et al., 2009).

Across channel subtidal flows, $v_{T,}$ presented a two-layer clockwise circulation over most of the cross-section, where surface flow was directed to the right and bottom flow was to the left (Figure 3.3b.2). The circulation was intensified over the right shoal of the main channel, where v_T reached up to 0.037 m/s. A departure from the two-layer circulation was observed along the edge of the farm ($0.05 < y < 0.15$ km), where surface and bottom flows were directed to the left and to the right in the middle of the water column. Except for the edge of the farm, the clockwise circulation pattern is expected in regions of curvature (Huijts et al., 2009; Zitman and Schuttelaars, 2012). To understand how the farm impacts subtidal flows, the analytical model is analyzed next by comparing cases with and without the presence of a floating oyster farm.

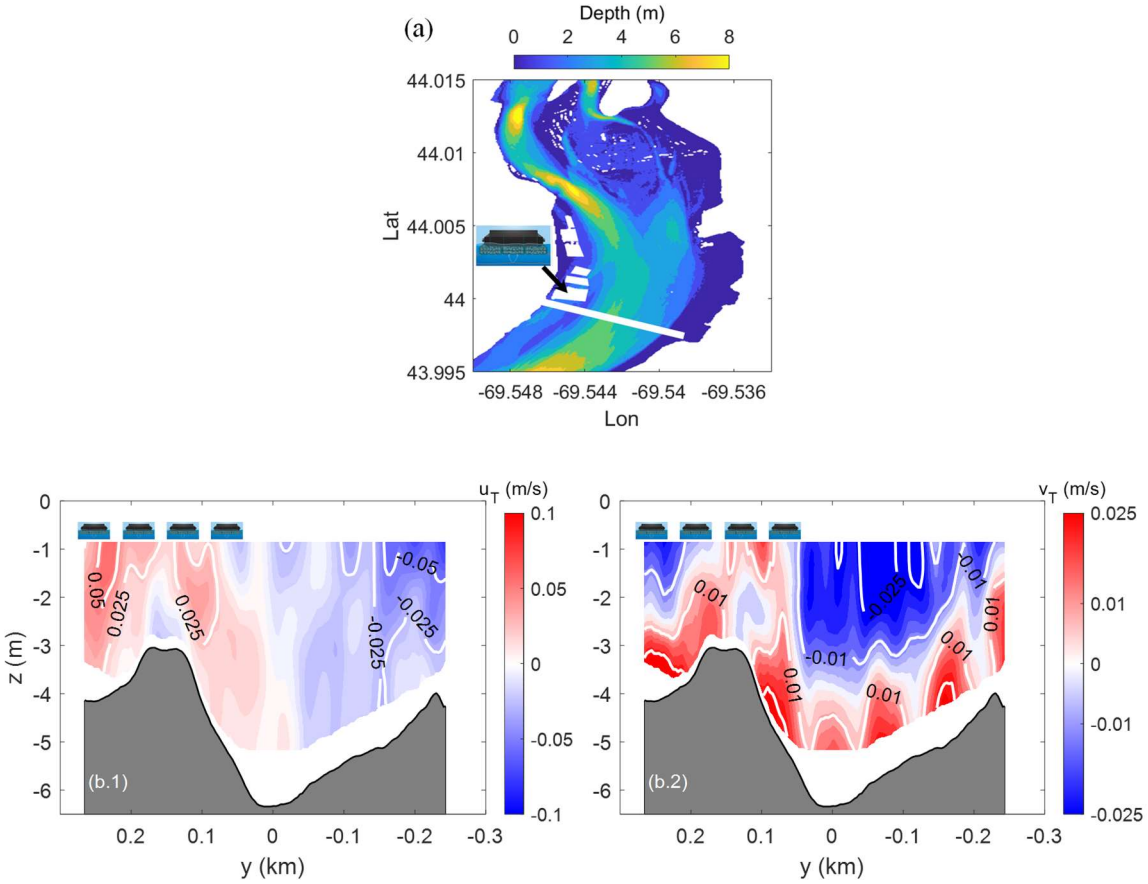

Figure 3.3 (a) Local map of floating oyster farm. Contour denotes mean water depth; white spot denotes farm. (b.1 ~ 2) Observations of along (u_T) and across (v_T) channel subtidal velocity near farm's seaward boundary. Positive (red) values of u_T is into the estuary, negative (blue) is out. Positive (red) value of v_T is to the left, while negative (blue) is to the right.

3.4.1. Tidal Flow

The cross-sectional distribution of the M2 along (u_0) and across (v_0) channel currents near the farm's seaward boundary with and without the farm were compared with the observed reconstructed tidal flow. Without the farm, the maximum amplitude of u_0 was 0.367 m/s at surface in the main channel (Figure 3.4b.1). During the flood phase of the tide, a two-layer clockwise circulation developed across the transect

with a magnitude of 0.019 m/s (Figure 3.4b.1~3). The circulation reversed to counterclockwise during ebb because of the reversal of the along-channel flow (Figure 3.4b.4). The across channel circulation was consistent with Coriolis driven circulation in the northern hemisphere by including the Coriolis force as a leading order term in the across channel dynamics (equation 3.4c).

Due to the existence of the farm, the along channel flow was larger in the main channel and on the right side of the cross section, which was shown over the entire tidal cycle (Figure 3.4c.2 ~ 4). A pattern of vertically uniform cross channel flow (v_0) occurred over the left shoal of the main channel ($0 < y < 0.2$ km), indicating that the farm induced flow bypassing throughout the entire water column (Figure 3.4c.1 ~ 4). During flood, flow diverted away from the farm area and the maximum value of v_0 reached up to 0.067 m/s after peak velocities (Figure 3.4c.2). The Coriolis driven lateral circulation occurred on right side of the cross section ($-0.2 < y < -0.1$ km) with a maximum magnitude of 0.02 m/s (Figure 3.4c.1 ~ 4).

The important flow reduction and redistribution features predicted by the model in the farm case were consistent with field observations. At peak flood, the flow reduction ($u_0 < 0.3$ m/s) in the farm area compared well with that observed in the measurements on the left side of the estuary ($0.1 < x < 0.3$ km, Figure 3.4c.1, 5d.1). Changes in u_0 were also visible at the farm-channel interface of the observations, where u_0 increased from 0.3 m/s at the farm's edge ($y = 0.1$ km) to 0.4 m/s in the main channel ($y = 0$ km). The across channel flow v_0 featured a magnitude of 0.04 m/s towards to the right throughout most of the flood phase in the observations (Figure 3.4d.1~ 3).

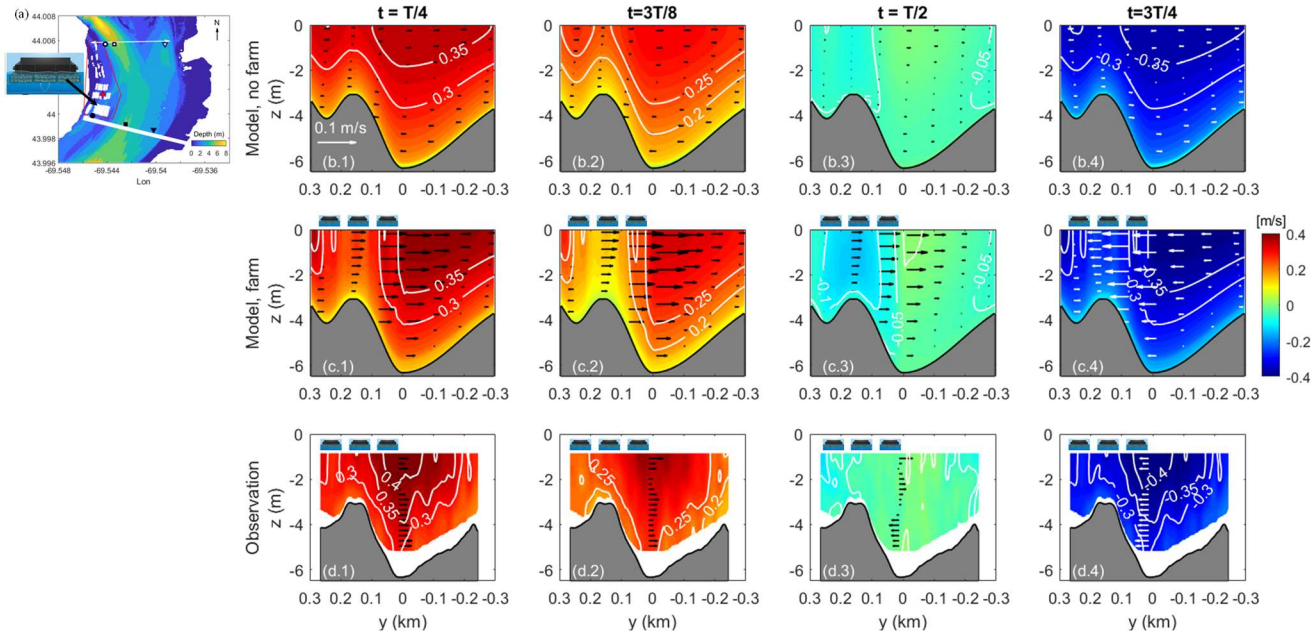

Figure 3.4 Semidiurnal (M2) tidal current near farm's seaward boundary. (a) Local bathymetric map of floating oyster farm. Red box indicated the farm extent. Thick white line denotes the location of cross sections. (b.1 ~ 4) along (contour) and across (vector) channel tidal current from model without farm at peak flood (t = T/4, where T is period of M2 tide), between peak flood and slack tide (t = 3T/8), end of flood (t = 3T/8) and peak ebb (t = 3T/4). (c.1 ~ 4) along and across channel tidal current from model with the farm. Cartoons denote farm area. (d.1 ~ 4) along and across channel tidal current from observations. In panels (b.1 ~ d.4), positive (red) value in contours denote into the estuary (flood), while negative (blue) denotes out of the estuary (ebb).

The model provides a more complete picture, compared to the observations, of the flow response along the farm by comparing surface tidal currents with and without the farm. Here, we only focused on peak flood because the tidal current had the same magnitude but opposite direction at peak ebb. Without the farm, the along surface tidal current (u_0) was uniformly distributed across the estuary and reached its maximum in the main channel (y = 0, Figure 3.5a.1). u_0 in the main channel decreased from 0.38 m/s (x =19.5 km) upstream to 0.31 m/s (x = 21.5 km). The across channel current (v_0) was 0.01 ~ 0.015 m/s and directed to the right (Figure 3.5a.2).

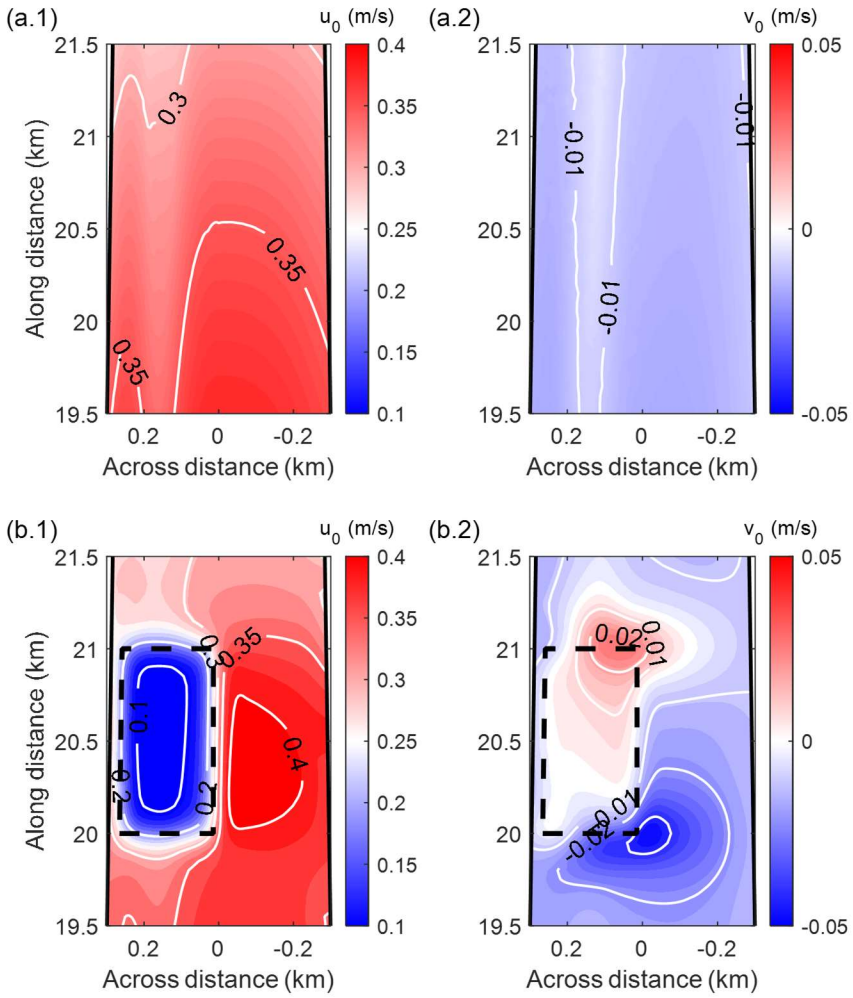

Figure 3.5 Model results of surface tidal current velocity at peak flood. (a.1) along channel tidal current velocity (u_0) without the farm. (a.2) across channel tidal current velocity (v_0) without farm. Red color denotes to the left, blue color is to the right. (b.1) u_0 with the farm. The dashed box denotes farm area. (b.2) v_0 with the farm.

When including the farm, the fluid-structure interaction was most prominent in farm area, where u_0 reduced to below 0.10 m/s inside the farm, compared to values as large as 0.42 m/s outside of the farm (Figure 3.5b.1). The farm also reduced values of u_0 approximately 200 m ahead of and behind the farm. Seaward of the farm, the tidal flow started to bypass the farm approximately 100 m ahead of the farm, indicated by enhanced v_0 towards to the right (> 0.04 m/s) around the right corner at the seaward boundary

(Figure 3.5b.2). Moving further upstream, v_0 was directed toward to the right in locations outside of the farm and to the left inside of the farm. At the farm's landward boundary, maximum v_0 (0.026 m/s) occurred at the right corner.

3.4.2. Subtidal Flow

When including the farm, the farm area ($0.05 < y < 0.26$ km) featured landward values of u_T throughout the water column, ranging from 0.05 ~ 0.1 m/s (Figure 3.6b.1). u_T reversed to seaward from the main channel to the right shoal ($y < 0.05$ km), where the maximum u_T occurred 0.10 m/s near the surface. The model captured the subtidal flow reversal found in the observations (Figure 3.3b.1), though slightly overestimated the velocity magnitude in the main channel. The lateral subtidal flow structure revealed the two-layer clockwise circulation except in the main channel. On the left-hand side, v_T was -0.008 m/s in the surface layer and $v_T = 0.007$ m/s above the bottom (Figure 3.6b.2). Compared with the field observations (Figure 3.3b.2), the model overestimated v_T in the farm area and underestimated v_T throughout the rest of the cross section.

Without the farm, the cross-sectional distribution of u_T was laterally sheared and reversed in direction from that depicted with the farm. From the thalweg to the right shoal ($0 \text{ km} < y < -0.3$ km), u_T was landward ranging from 0 to 0.05 m/s (Figure 3.6c.1). From the thalweg to the shoal adjacent to the secondary channel ($0.25 \text{ km} < y < 0$ km), u_T was seaward and ranged from 0 to -0.09 m/s. The laterally sheared pattered was mimicked over the secondary channel, though smaller in magnitude. The across channel subtidal velocity v_T without the farm presented a two-layer clockwise circulation over the entire cross section, which featured $v_T = 0.015 \sim 0.018$ m/s to the right at the surface and $v_T = 0.01 \sim 0.012$ m/s to the left above the bottom (Figure 3.6c.2). The along channel subtidal flow patterns without the farm were consistent with published analytical model results (Winant, 2008; Huijts et al., 2009; Zitman and

Schuttelaars, 2012). However, when considering the farm, the along channel subtidal flow patterns reversed. Next, the dominant mechanisms contributing to the subtidal flow reversal are analyzed.

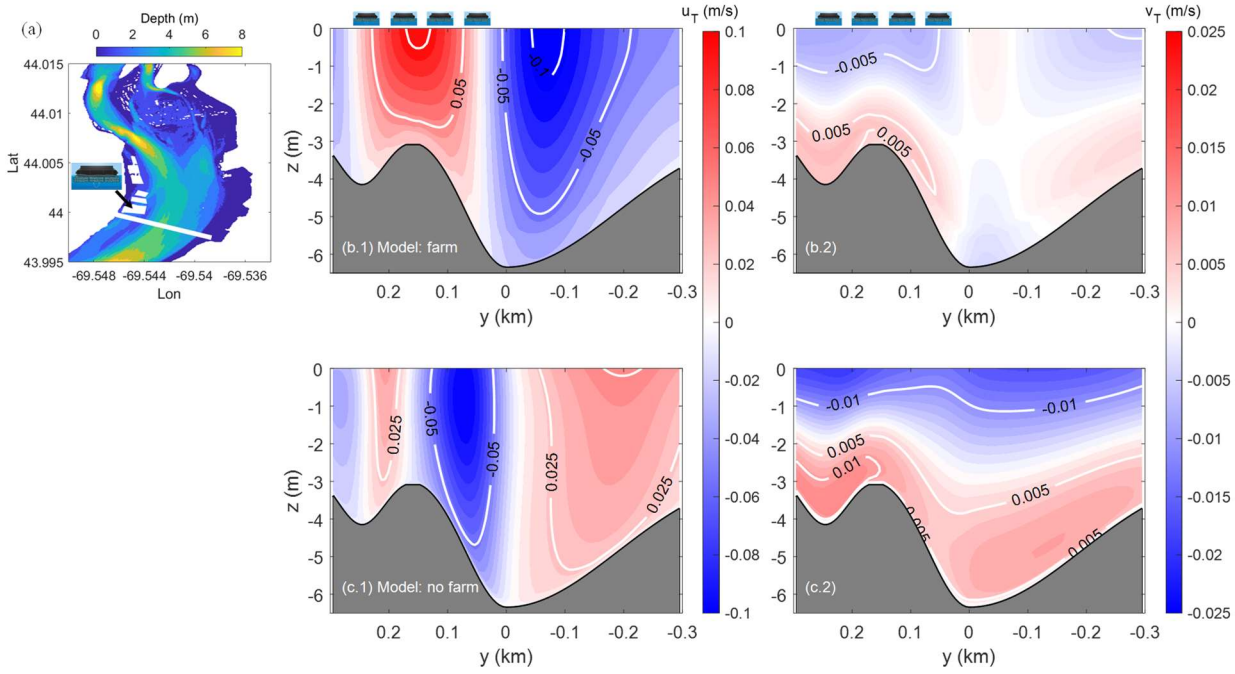

Figure 3.6 Along (u_T) and across (v_T) channel subtidal velocity from the model. (a) Bathymetry of the estuary portion containing floating oyster farm. Contour denotes mean water depth; white spot denotes long-lines. (b.1 ~ 2) distribution of u_T and v_T considering the farm, where cartoons denote farm area. Positive (red) u_T is into the estuary, while negative (blue) u_T is out of the estuary. Positive (red) v_T is to the left, while negative (blue) v_T is to the right. (c.1 ~ 2) u_T and v_T without the farm.

3.4.3 Impact of farm area on material transport

The model revealed that the existence of the farm promoted flow reduction and a reversal in the subtidal flow patterns across the estuary, compared to non-farm conditions, which likely has implications for the transport of material coming from upstream. A “transport time” defined as the time that it takes by

a particle released at a point upstream of the farm to be transported downstream and never return to farm area. The transport time was computed based on model results of tidal and subtidal flow to understand how the farm presence may affect the flushing and residence times of upstream particulates. Transport times are normalized by the no farm case to assess how the presence of a farm my alter the amount of time it takes for an upstream particle to evacuate the region upstream of the study location. The normalized transport time scale increment ranges from 0 to 1, where the value of 0 denotes the farm would not change upstream particle transport while a value of 1 means the farm alters material transport so that it remains "indefinitely" in this idealized system.

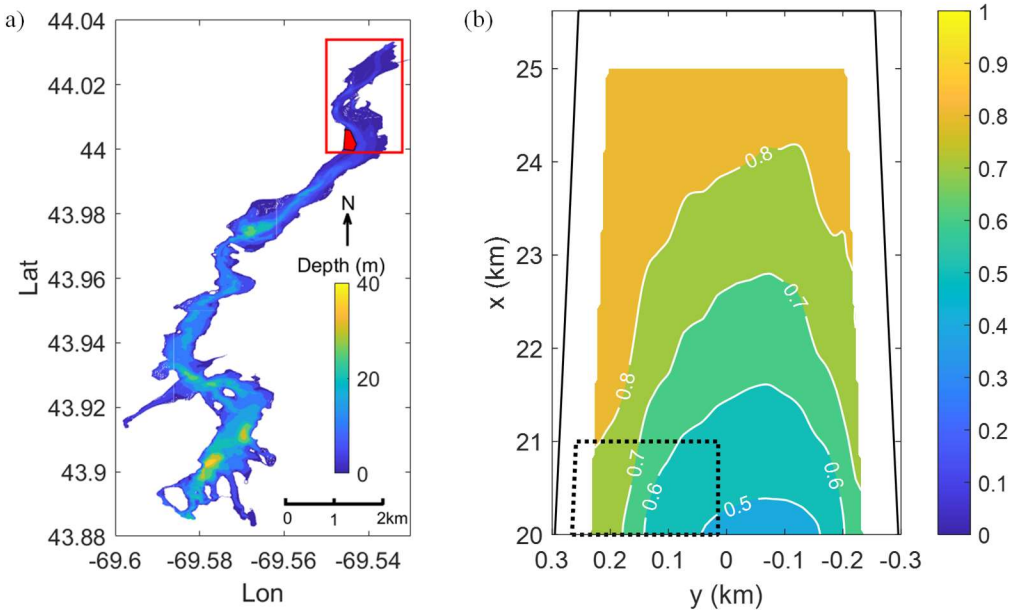

Figure 3.7 Normalized change in transport time of particles released at surface in the upstream portion of the estuary. (a) map of study area, (b) Normalized change in transport time comparing with no farm case. The value ranges from 0 to 1, where "0" denotes no changes in transport time comparing without farm, while "1" denotes the farm increased transport time to "infinity". Black solid line denotes landward boundary of the farm placed on left part of the cross section with an area ratio of 42.5%.

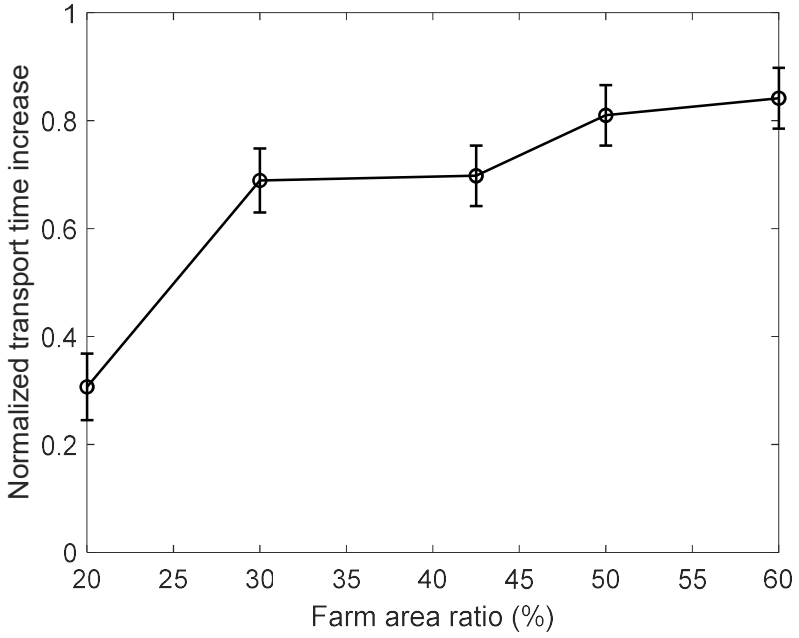

Figure 3.8 Averaged transport time of all the particles released at surface in the upstream portion of the estuary ($20 \leq x \leq 25$ km) with respect to the ratio of farm area to cross area of the estuary portion. Black diamond denotes the averaged transport time without farm, error bar denotes 95% confidence interval. Black circles with error bars denote the averaged transport time and 95% confidence interval where farm area ratio was 10%, 20%, 30%, 42.5%, 50% and 60%.

Note that this is not to say that it is possible for a particle to remain indefinitely in a real system. This analysis was used to understand general changes to upstream transport would in increase or decrease the amount of time a particulate will remain upstream. That is actual time is irrelevant because the low river discharge, irregularities in channel morphology and other nonlinearities are not considered in the model, which would ultimately lead to particles escaping out of the system. The purpose of this analysis is to understand that farms with this configuration may increase or decrease material transport.

The existence of farm increased transport time upstream of the farm, where the normalized increment was around 0.5 ~ 0.8 in most area (Figure 3.7b). Inside of the farm, the normalized increment

was around 0.6 ~ 0.7 (y > 0.1 km), where most of the particles released could not be transported downstream of the farm area. This analysis suggests that the existence of a floating aquaculture farm located in a low inflow estuary and parallel to streamwise direction potentially reduces seaward material transport located upstream of the farm.

To clearly understand relative changes in transport times upstream with respect to farm size, the averaged transport time of all the particles released upstream of farm area was evaluated with varying farm area to total surface area ratios. The normalized change relative to the no farm case was shown in Figure 3.8. The transport time increased with farm area ratio. When the farm occupied 20% of the width of the estuary, the normalized increase was around 0.31. The normalized increase was larger than 0.60 when farm area ratio was larger than 30% and reached a maximum value of 0.84 at farm area ratio of 60%. Therefore, a farm with a narrow width, where area ratio was less than 30% would slightly increase upstream transport times, while wider farms with ratios larger than 40% seem to significantly increase transport times.

3.5. Discussion

3.5.1. Mechanisms Driving Subtidal Flow

The model results indicated that the reversal in subtidal flow was caused by the presence of the farm. To isolate the driving mechanisms behind the subtidal flow structure imposed by the farm, each forcing term in the governing equation 3.7b was quantified at three locations along the farm: the seaward boundary, in the middle of the farm, and at the landward boundary. The magnitude of along channel advection term $-\overline{u_0 \frac{\partial u_0}{\partial x}}$ and vertical advection term $-\overline{w_0 \frac{\partial u_0}{\partial z}}$ were 2 ~ 10 times larger than magnitudes of other terms, therefore, these terms are compared with the subtidal flow patterns at all three locations in Figure 7.

At the farm's seaward boundary, the tidal current magnitude during peak flood and ebb increased from zero at the bottom to the maximum value at a depth of ~2 m and decreased towards the surface due to the drag force from the farm (Figure 3.9a.1, 2). Therefore, $\frac{\partial u_0}{\partial z} > 0$ in the lower water column (z < -2 m) during flood while $\frac{\partial u_0}{\partial z} < 0$ in the lower water column during ebb (z < -2 m). The across channel flow v_0 was unidirectional due to flow bypassing. Over the left shoal of main channel ($0 < y < 0.15$ km) downwelling ($w_0 < 0$) occurred below the farm at peak flood and reversed to upwelling ($w_0 > 0$) at peak ebb (Figures 3.9a.1,2). The up- or downwelling underneath the farm was due to tidal rectification at the channel-shoal interface, where the magnitude of v_0 increased from the shoal to the main channel.

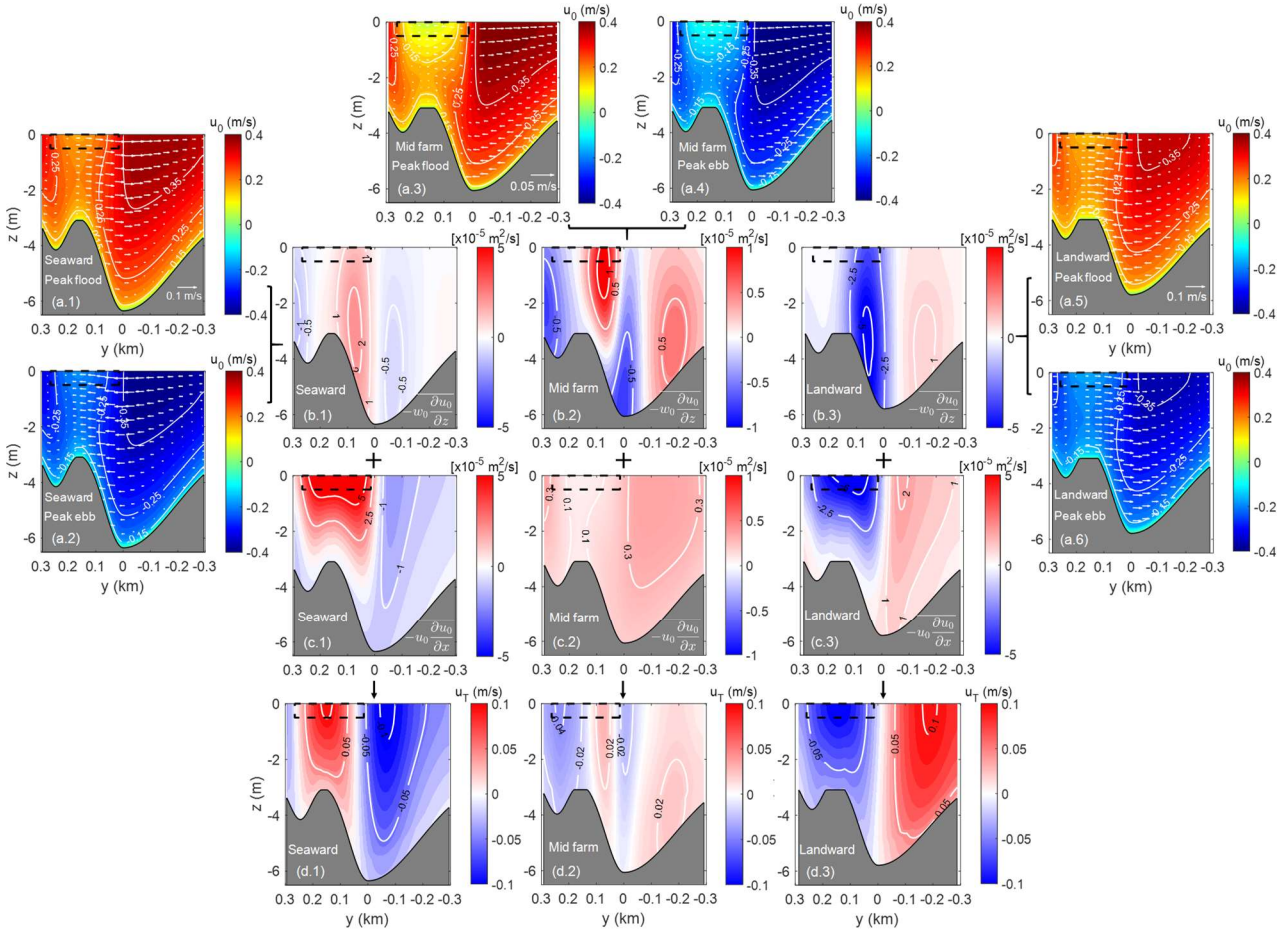

Figure 3.9 Driving mechanism for along-channel subtidal velocity. (a.1 ~ 6) along (contour), across and vertical (vector) M2 tidal current velocity at farm's seaward boundary, middle of the farm and at the landward boundary

at peak flood and ebb. Red color is into the estuary and blue is out. Dashed black box denotes the farm. (b.1 ~ 3) tidally averaged vertical advection force, $-\overline{w_0 \frac{\partial u_0}{\partial z}}$, at the seaward boundary, middle and landward boundary. The red color denotes the forcing term drives subtidal velocity into the estuary while blue color drives seaward flow. (c.1 ~ 3) tidally averaged along channel advection force, $-\overline{u_0 \frac{\partial u_0}{\partial x}}$, at the seaward boundary, the middle and the landward boundary. (d.1 ~ 3) subtidal velocity at the seaward boundary, the middle, and the landward boundary.

As this location, the vertical velocity w_0 was dominated by the across channel gradient in across channel flow, i.e. $w_0 = \int_{-h}^{z} -\frac{\partial v_0}{\partial y} dz$, especially along the farm's lateral edge, where $-\frac{\partial v_0}{\partial y} < 0$ at peak flood and $-\frac{\partial v_0}{\partial y} > 0$ at peak ebb ($0 < y < 0.15$ km, Figure 3.9a.1, 2). In the water column below 2 m, the combination of enhanced vertical shear in along channel tidal velocity, $\frac{\partial u_0}{\partial z}$ with up- or downwelling (elevated vertical velocity, w_0), produced an elevated tidally averaged vertical advection term, i.e., $-\overline{w_0 \frac{\partial u_0}{\partial z}} \sim 2 \times 10^{-5}$ m/s^{-2}, tending to produce tidally rectified landward subtidal flow at the interface between the main channel and the left shoal (Figure 3.9b.1).

When flow approached the farm area from the seaward boundary during the flood phase of the tide ($u_0 > 0$), the along channel tidal current tended to decrease along the estuary at the surface, i.e., $\frac{\partial u_0}{\partial x} < 0$ (Figure 3.5b.1), therefore $u_0 \frac{\partial u_0}{\partial x} < 0$. During ebb ($u_0 < 0$), the tidal current tended to increase along the estuary when exiting the farm at the seaward boundary, therefore $\frac{\partial u_0}{\partial x} > 0$, making $u_0 \frac{\partial u_0}{\partial x} < 0$ at the surface. Consequently, the tidally averaged along channel advection term $-\overline{u_0 \frac{\partial u_0}{\partial x}}$ was landward with a magnitude around 5×10^{-5} m/s^2 in the upper water column at the farm's seaward boundary (Figure 3.9c.1),

which always drove landward subtidal currents (0.05 ~ 0.10 m/s) into the farm together with landward advection term $-\overline{w_0 \frac{\partial u_0}{\partial z}}$, as shown in Figure 3.9d.1.

At peak flood at the mid-farm transect, the lateral circulation was typically clockwise away from the farm (Figure 3.9a.3). However, the lateral circulation was counterclockwise under the farm resulting in $-\frac{\partial v_0}{\partial y} > 0$ near the bottom along the farm's right edge (y = 0.05 km) and $-\frac{\partial v_0}{\partial y} < 0$ along the farm's left edge (y = 0.25 km, Figure 3.9a.3). Therefore, upwelling ($w_0 > 0$) occurred along the farm's right edge and downwelling ($w_0 < 0$) occurred along the farm's left edge in the secondary channel (Figure 3.9a.3). Note that $\frac{\partial u_0}{\partial z} < 0$ in the upper water column during flood, making the vertical advection term positive, $-w_0 \frac{\partial u_0}{\partial z} > 0$, along the farm's right edge (Figure 3.9b.2). On the left edge, $-w_0 \frac{\partial u_0}{\partial z} < 0$, during flood. At peak ebb, the lateral circulation flipped both away from the farm and under the farm, where downwelling ($w_0 < 0$) formed over the left shoal of the main channel and an upwelling ($w_0 > 0$) occurred in the secondary channel. Combing the vertical gradient of along channel tidal current, the tidally averaged vertical advection term $-\overline{w_0 \frac{\partial u_0}{\partial z}}$ was 1×10^{-5} m/s^2 in upper water column over the left shoal of the main channel, $-\overline{w_0 \frac{\partial u_0}{\partial z}}$ ~ -0.5×10^{-5} m/s^2 in the secondary channel and $-\overline{w_0 \frac{\partial u_0}{\partial z}}$ ~ -0.5×10^{-5} m/s^2 at the bottom of the main channel (Figure 3.9b.2). This produced a tidally rectified landward subtidal current (0.02 m/s) at the interface of the main channel and the left shoal and a seaward subtidal flow (-0.04 m/s) in the secondary channel inside of the farm (Figure 3.9d.2). Note that the magnitude of along channel tidal current tended to decrease upstream (Figure 5b.1, b.2), which ended up with a uniformly positive along channel advection term in the no farm portion, $-\overline{u_0 \frac{\partial u_0}{\partial x}}$ ~ 0.3×10^{-5} m/s^2 (Figure 3.9c.2), which forced landward subtidal flow in the right portion of the main channel (0.02 m/s, Figure 3.9d.2).

In contrast to the seaward boundary, both $-\overline{w_0 \frac{\partial u_0}{\partial z}}$ and $-\overline{u_0 \frac{\partial u_0}{\partial x}}$ had opposite signs (Figure 3.9b.3, c.3) at the landward boundary due to flipped tidal flow patterns (Figure 3.9a.5, a.6). Therefore, seaward

subtidal flow occurred in farm area (-0.09 m/s) while landward subtidal flow occurred away from the farm (0.1 m/s, Figure 3.9d.3).

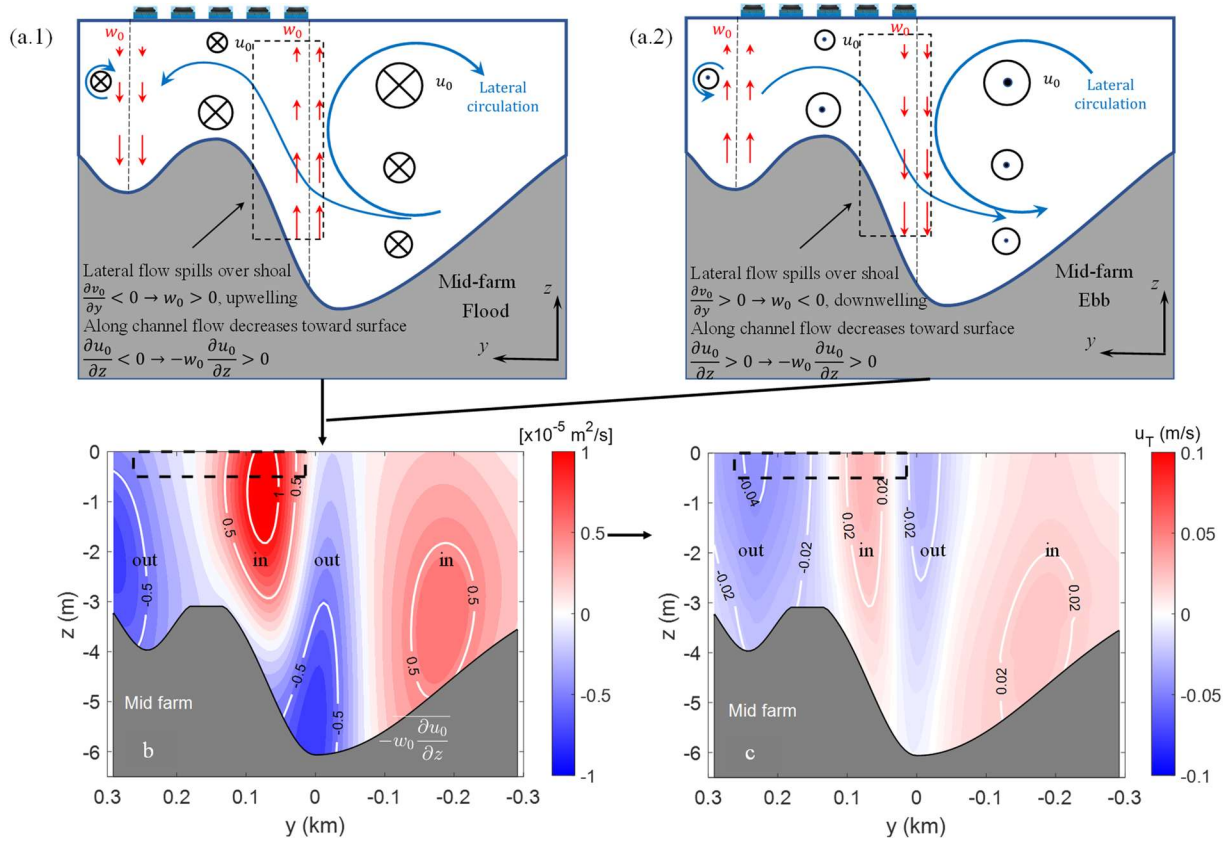

Figure 3.10 Conceptual schematic of along channel subtidal flow reversal inside of the farm. (a.1 ~ 2) along (circles with dot denote inflow and circles with cross denote outflow), across channel circulation (blue arrows), up- and downwelling (red arrows) tidal flow in the middle of the farm at flood and ebb. (b) tidally averaged vertical advection force, $-\overline{w_0 \frac{\partial u_0}{\partial z}}$ and (c) subtidal velocity at the middle section. The red color denotes the forcing term drives subtidal velocity into the estuary while blue color drives seaward flow.

In summary, the existence of the floating oyster farm decreased the along channel tidal current near the surface, which together with upwelling or downwelling at the channel-shoal interface (Figure 3.10a), resulted in a reversed vertical advection term inside the farm compared to that without the farm (Figure

3.10b). These combined influences contributed to the reversal of the subtidal flow pattern (Figure 3.10c). The along channel advection at the farm's seaward and landward boundaries drives subtidal flow that is always pointing into the farm, which likely has implications for the transport of material coming from upstream. This may be achieved by reduced the farm density or staggering the layout of the longlines, though future research is needed to fully understand the relationship between farm siting and layout and subtidal flow structure.

3.5.2 Particle trajectories

The trajectory of individual particles revealed upstream of the farm were examined to understand the impacts of farm area on material transport. Trajectories of three particles released 1 km upstream of farm's landward boundary at end of flood with varying farm areas are shown in Figure 3.11. Without the farm, irrespective of where the particles were released across the channel, the particles were transported to the right shoal due to the rightward across channel flows driven by upstream channel curvature (Figure 3.11a). The particles were transported 7 km downstream by 4 tidal cycles. Although the along channel subtidal transport velocity was landward, the particles accumulate near the right shoal during flood, yet are transported toward the main channel during ebb.

When including the farm, a closed trajectory occurred over the right side of the estuary resulting in an "infinite" transport time. When the farm area ratio was 20%, two of the three particles fell into the closed trajectory after 3 tidal cycles and the net along channel transport was almost zero (Figure 3.11b). Therefore, the particles were rarely transported away from the farm area, corresponded to the increased transport time shown in Figure 3.8. The tidal flow bypassing at the farm edges and tidal flow increasement decreased sojourn time of particles in bare port next to the farm, which consequently decreased contribution of curvature driven lateral transport and resulted in tidal flow dominated closed trajectories.

When the farm area ratio increased to 42.5%, besides the closed trajectory occurring region away from the farm, the particle fell into another closed trajectory right upstream of the farm area (black solid line, Figure 3.11c), where the net seaward transport was stopped by subtidal flow reversal inside the farm. At a farm area ratio of 60%, two of the three particles released upstream of the farm were blocked by the farm and followed the closed trajectory upstream of the farm area (red and black solid lines, Figure 3.11d). Note that even particles released in region away from the farm would potentially run into closed trajectories. Consequently, the farm could potentially increase the transport time upstream of the farm in the estuary.

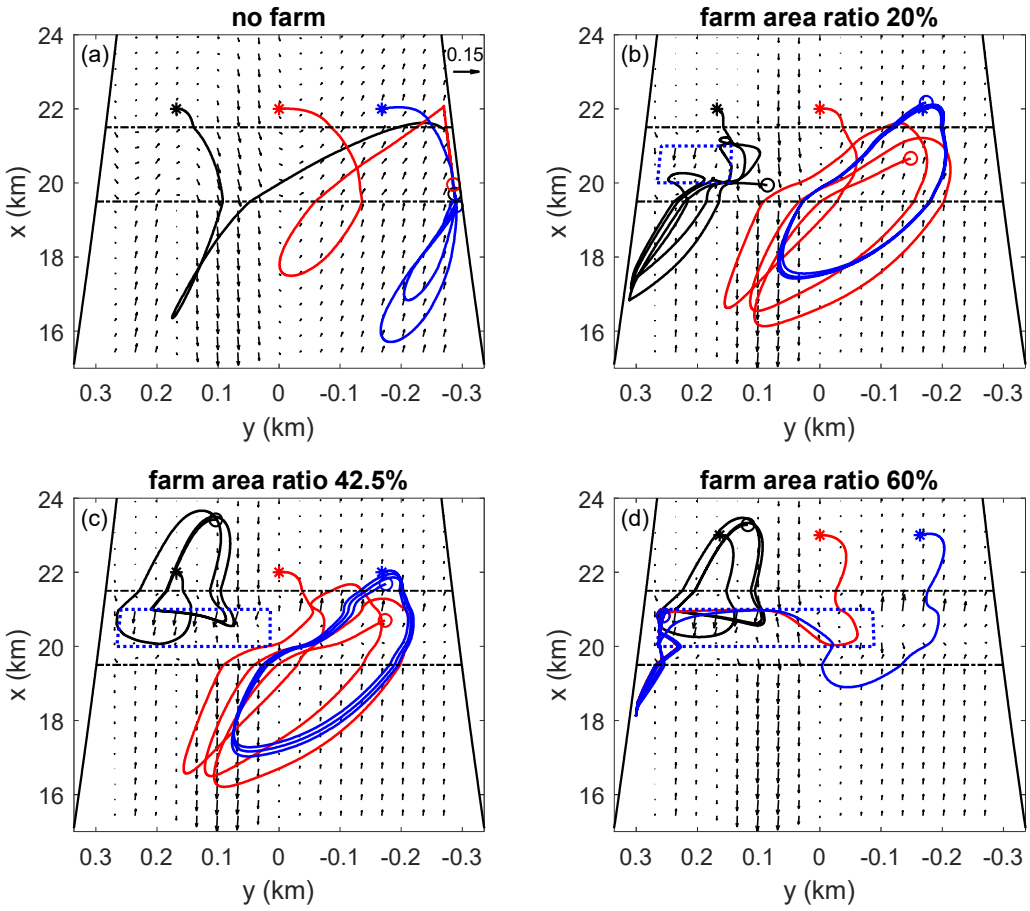

Figure 3.11 Trajectories of particles transport at surface released at end of flood. (a) Trajectories of three particles released at along channel potion of x = 22 km and across channel positions of y = 0.4B (black solid line), y = 0

(red solid line) and y = -0.4B (blue solid line) without farm. Vectors denote subtidal current velocity (u_T, v_T) at surface. Black dotted lines denote the estuary portion having a bend. Stars denote released position; circles denote position after 3 semidiurnal tidal cycles. (b ~ c) Trajectories of three particles released at same locations of panel (a) with farm area ratio of 20%, 42.5% and 60%, respectively. Stars denote released position, circled denote position after 3 semidiurnal tidal cycles. Bule dashed triangles denote farm area.

The upstream reach of the Damariscotta River estuary has high phytoplankton biomass due to its shallowness and warmer temperatures, longer transport times would be beneficial for cultured species in that area (Thompson et al., 2006). Larger upstream transport times allows suspended particulates such as chlorophyll to resident a longer period in the upper portion of the estuary, which is likely beneficial for aquaculture farming activities. However, it still remains to be understood how much a floating oyster farm would impact upstream transport timescales in a real estuary, as this is a linear analysis for a simplified estuary in an idealized setting. Nonetheless, this model does suggest that farms could influence upstream transport times, though the extent to which those times are increased in a realistic setting is not yet understood. The model could be used in the future to optimize farm layout and design in order to reduce the subtidal flow reversal effect, such as reducing cage density or dividing the farm into several parts with staggered layout, thereby decreasing the influence on upstream transport times.

To the author's knowledge, the proposed semi-analytical model is the first model to include both depth and width variations as well as drag forcing from a floating aquaculture farm. The piecewise parabolic eddy viscosity structure allows for consideration of vertical variations in eddy viscosity. The model has potential future applications in both estuarine dynamics and aquaculture engineering. This model is applicable to study tide propagation and subtidal circulation in estuaries and bays with complicated bathymetry and surface obstructions. The model provides a preliminary and fast way to assess general aquaculture farm impacts on material transport and food delivery. It can also be applied in aquaculture siting and layout design. This model could also be modified in the future to include the advection-diffusion

of a concentration, since diffusion was not included particle trajectories. This future improved model could be used to inform siting decisions based on the best location to place a farm in terms of subtidal transport, as well as improve layout designs to optimize food delivery within the farm.

In evaluating siting locations for aquaculture farms, the frictional impacts of existing aquaculture farms are not currently included in regional scale simulations (Beard et al., 2020). We have shown that farms not only impact tidal and subtidal flows across the estuary, but can reverse their patterns, which likely has consequences on material transport, which is important for the carrying capacity of a sytem. Therefore, aquaculture farms need to be represented in hydrodynamic simulations, particularly in systems that have an established aquaculture industry.

3.5.3. Model Novelty and Limitations

To the best of the author's knowledge, the proposed 3D semi-analytical model for tidal propagation and subtidal circulation in estuaries is the first model to include both depth and width variations and the piecewise parabolic eddy viscosity, which allows for the consideration of vertical variations in eddy viscosity. The model also includes the ability to simulate drag forces imposed by floating canopies. With slight modification, the model could also be used to study hydrodynamic impacts from other kinds of surface stresses such as those induced by wind or ice.

In this work, the advection terms were not assumed as leading order terms in the model for tidal flow. However, the magnitude of the advection term $v\frac{\partial u}{\partial y} + w\frac{\partial u}{\partial z}$, including both tidal and subtidal constitutes, is proportional to the local transverse bottom slope and inversely proportional to the local water depth. Therefore, neglecting the advection term in the tidal flow could result in overestimation of subtidal flow in areas without the farm. In addition, a transition zone at the leading edge of the farm and a wake zone at the trailing edge of the farm were observed in previous laboratory experiments of canopy flow,

where along channel advection $u\frac{\partial u}{\partial x}$ is the dominating term (Tseung et al., 2016; Ghisalberti and Nepf, 2002; Zhao et al. 2017). Neglecting $u\frac{\partial u}{\partial x}$ in tidal flow, especially at farm's seaward and landward boundaries, likely leads to overestimation of the tidally averaged along channel advection, $-\overline{u_0\frac{\partial u_0}{\partial x}}$. Therefore, including advection, which can be considered as a harmonic interaction among subtidal and M2 constituents could improve the model results of velocity distributions near the farm.

Another limitation of this work is a lack of detailed measurements of flow inside of a floating oyster farm. The vertical structure of eddy viscosity inside of the farm may differ from that derived from typical canopy flows experiments where the stems of canopy were almost uniformly distributed in space. Drag coefficients may vary along or across the farm due to heterogeneity in oysters, warranting more laboratory and field measurements inside of farms to improve eddy viscosity and drag force parameterizations. Note that the existence of farm is likely to alter vertical stratification by changing salt transport as well as enhancing vertical mixing. The changing in vertical stratification should also be considered as a factor to contribute to subtidal flow patterns both with and without the farm.

3.6. Conclusions

Field observations and a semi-analytical model showed that the presence of a floating oyster farm over a portion of an estuary locally reversed subtidal flows. Without the farm, the model showed laterally sheared subtidal flows, with landward flow on the right side of the cross-section and seaward flow on the left. When the farm was imposed over the left shoal, the subtidal flow structure reversed, with landward flow on the left and seaward flow on the right at the farm's seaward boundary, which compared well with field measurements. The subtidal forcing terms indicated that the farm induced drag reduced tidal currents near the surface and elevated up- and down welling at farm's lateral boundaries, leading to a reversed subtidal flow pattern at the channel-shoal interface compared to the no farm case. In addition, the tidally

averaged along channel advection at the farm's seaward and landward boundaries forced subtidal flows into the farm, i.e., landward flow at the seaward boundary and seaward flow at the landward boundary. The alterations to the subtidal flow likely have decrease seaward transport, highlighting that the hydrodynamic response of estuaries to aquaculture farms is an important consideration in carrying capacity estimates. The newly proposed 3D semi-analytical model provides a simple way to quantitatively study the hydrodynamic impacts of various aquaculture activities in estuarine settings, which could also be used to optimize siting to enhance food delivery.

CHAPTER 4

FLOATING OYSTER AQUACULTURE FARM DESIGN CONSIDERATIONS: WATER DEPTH AND FARM LAYOUT

4.1. Introduction

According to the Food and Agriculture Organization of the United Nations (FAO 2020) the total production of oysters reached up to 5.81 million tons in worldwide aquaculture in 2018, which accounts for 33.2% in total production of bivalve mollusks. Compared with 2010, the oyster production increased by 38.1% with the average annual increases were only 4.1%. However, aquaculture needs to grow 9.9% per year in order to fill the demand–supply gap. Accordingly, the demand for bivalves will increase substantially over time and catalyze the expansion of the oyster aquaculture industry. The key aspects to guarantee oyster aquaculture sustainability are to fully understand the interaction between oyster aquaculture and surrounding environment, to improve carrying capacity estimates and to provide instructive and exercisable guidance to stakeholders for aquaculture development and management.

Multidisciplinary research efforts covering the physical, biochemical, ecological, and economic as well as engineering aspects are required to promote the sustainable development of oyster aquaculture. Hydrodynamics play a crucial role in oyster aquaculture, where factors such as salinity, temperature, turbidity, food supply and oxygen influence oyster growth and are correlated with the hydrodynamics of the environment through transport and mixing (Campbell and Hall, 2019). Besides those biochemical factors, the hydrodynamic loading mainly accounts for infrastructure failure, especially during extreme climatological events. For the biochemical perspective, informative studies focused on oyster feeding and growth as well as survival under various natural and laboratory hydrographic conditions. Previous studies focused on oyster feeding dietary (Galimany et al. 2017, Hawkins et al. 2013, Adams et al. 2019), infectious diseases (Pernet et al. 2016), and optimal habiting hydrographic conditions such as proper salinity and temperature (O'Connor et al., 2004, Butt et al. 2005, Li and Li 2010, Rybovich et al. 2016), low turbidity

(Gernez et al., 2017, Barillé et al., 2020) and sufficient oxygen (Baker and Mann 1994, Meng et al. 2018). Based on findings in oyster's biochemical behavior, empirical feeding and growth models as function of multiple hydrographic factors were proposed (Powell et al. 1992, Cerco and Noel 2005, Fulford et al. 2007, Gangnery et al., 2003, Rueda et al. 2005), some of which have been embedded into hydrodynamic and biochemical models to quantitatively investigate oyster production as well as carrying capacity (Ferreira et al. 2007, Hawkins et al. 2013, Newell et al. 2013, Sun et al. 2020, Weitzman and Filgueira 2020). In an engineering perspective, remote sensing and satellite data have been applied to oyster aquaculture siting in multi-spatial scales (Gernez et al., 2017, Snyder et al., 2017). Proper design of mooring and anchor systems to guarantee infrastructural integrity under extreme loading conditions was also important for a floating oyster farm (Nguyen et al., 2019; Cortes-Garcia 2019).

Furthermore, understanding biochemical phenomena from a physical point of view could help highlight control mechanisms and propose instructive guidance to oyster aquaculture. Besides temperature, salinity, and chlorophyll, it has been reported that high turbidity would potentially decrease oyster feeding and growth by diluting algal cells with largely inorganic matter. Dame et al. (1985) reported that chlorophyll a uptake by an oyster reef during the ebb tide was only ~ 43% of that during the flood tide over 33 measured tidal cycles. One hypothesis was that higher ebb tide current speeds resulted in more sediment resuspension (Dame et al., 1992). Oyster clearance and chlorophyll consumption rates were both negatively impacted by high turbidity during spring tides in the intertidal zone (Gernez et al., 2017), whereas oysters presented better growth rates in low turbidity offshore area (Barillé et al., 2020). Lower growth rates were also observed in a floating oyster farm in an estuary which corresponded to the tidal sediment resuspension (Adams et al., 2019). Snyder et al. (2017) suggest edpotential *Crassostrea virginica* oyster growing areas in estuaries along the Gulf of Maine should exhibit turbidity (below 8 NTU). Besides tidal flow, resuspension due to wind-driven waves would also potentially increase turbidity and decrease seston consumptions by oysters (Grizzle et al. 2008). Although negative impacts from high turbidity have been noted, the linkage between sediment resuspension and tidal straining as well as turbulence and mixing is

not fully understood and farm design considerations corresponding to tidally driven sediment resuspension is not available.

Aquaculture farm layout and orientation potentially impacts production. For example, farm layouts that decrease stock density downstream increase production under constant unidirectional current speed (Ferreira et al. 2007). Carefully optimizing farm position and layout may be possible to increase current speeds in some areas, which would both enhance food supply and dispersal of depleted waters (Plew, 2011). Stevens and Petersen (2011) conceptually proposed sufficient gaps in farm structure would drive heterogeneity in structure-induced mixing, thus driving horizontal exchange flows. Regional scale simulations are able to resolve the geophysical flow conditions but are too coarse to resolve the farm layout (Fan et al. 2020), while small scale studies can resolve the farm structure, but are unable to represent realistic conditions (Delaux et al. 2011). Therefore, few studies investigate the effect of farm layout on food delivery or filtered food in the farm under realistic (or quasi-realistic) flow conditions.

The goal of this chapter is to assess important considerations in floating oyster farm design including depth and layout in order to limit near surface turbidity and optimize food filtration. The research objectives are to: (1) understand the correlation between turbidity, water depth and bottom boundary layer thickness in a weakly stratified estuary, (2) propose a quantitative formular for depth to be used in design, (3) investigate the impacts of farm layout on food uptake, and (4) find the proper farm layout for optimal food filtration. Details on the field campaign measuring hydrographic data around a floating oyster farm are presented in section 2. Section 3 demonstrates temporal and spatial variations in hydrodynamic and hydrographic conditions around a floating oyster farm and correlates turbidity, chlorophyll a and bottom boundary layer thickness. Section 4 introduces a semi-analytical dynamic and material transport model for estuaries with floating oyster farms. Model results of how the farm layout impacts food uptake by the farm are shown in section 5. Section 6 discusses the implications and limitations of this work.

4.2. Field observation

4.2.1. Study site

The Damariscotta River, located on the mid-coast of Maine in the northeast United States, is a thriving estuary for shellfish aquaculture. In particular, the upper reach of the river has long residence times, warm temperatures, and high primary production of Chlorophyll, which makes the upstream optimal for shellfish (Ian et al., 2020). The upper Damariscotta estuary is the most successful aquaculture site in Maine for eastern oysters *Crassostrea virginica* (Adams et al., 2019). The Damariscotta River is a short system (~ 30 km) following a mostly north-south orientation (Figure 4.1a, Chandler 2016). The flow is dominated by a semidiurnal tidal forcing with spring tidal range of approximately 3.6 m and a neap tidal range of 2.2 m (Lieberthal et al., 2019a). This system has low freshwater discharge, which varies from 0.28 m^3/s in the dry season to 14.1 m^3/s in the wet season of the year 2016 due to the existence of a dam upstream (Huguenard et al., 2019).

A floating oyster farm with a length of approximately 1km is located upstream in the estuary around 20 ~ 21km measured from mouth. The farm was placed over the western shoal with a width of 230 m at the south (seaward) end and that decreased to 15 m towards the north (landward) end (Figure 4.1b). The farm consists of 128 floating longlines, which are divided into 6 groups. Each long line has 28 to 50 cages tethered to two parallel ropes. Each cage consists of two floats and one basket containing 6 oyster bags. The oyster bag penetrates ~ 0.42 m below the water surface. The gap between each long line and the spacing between each cage was designed to be approximately 5.0 m and 0.30 m respectively. In reality, the gap between long lines varies from 0 ~ 10 m due to swaying with the tidal current. A bend exists in the farm area, with a radius of R_{s1} = 850 m in the main channel. In the curved portion, the left shoal is located at the inner bend and right shoal is at the outer bend. Further north, the main channel features an opposing bend with a radius R_{s2} = 700 m (Figure 4.1b). At the farm location the estuary has a bifurcated bottom bathymetry, where the main channel is next to the farm while a secondary channel is under the farm (Figure 4.1c).

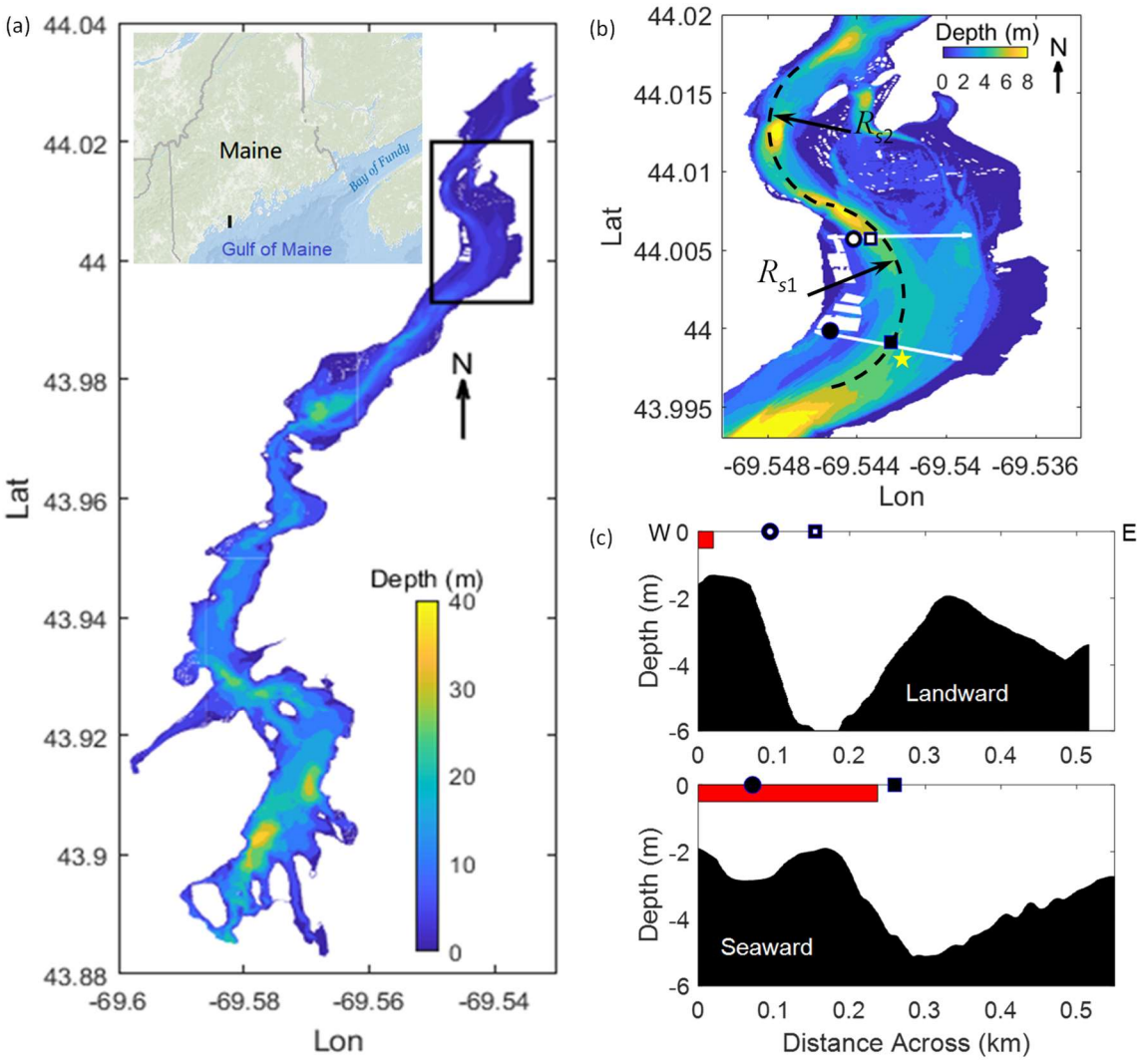

Figure 4.1 Map of the Damariscotta River and field campaign strategy. (a) Bathymetry referred to Mean Lower Low Water level (MLLW) and farm site (Chandler 2016). (b) Sketch of farm layout (white gaps) and deployment of ADCPs (double-end arrows) and MicroCTDs (markers). Open and closed circles represent location around the farm near the western shoal at two transects, open and closed squares represent the location in the main channel along two transects. Yellow star denotes the Land/Ocean Biogeochemical Observatory (LOBO) monitoring system. (c) Cross sections of landward and seaward transects. Red bars represent farm area. Other makers represent the hydrographic station locations.

4.2.2 Data collection

In order to understand water quality around the oyster farm, cross sections of current velocities, profiles of density and turbidity were obtained for an entire semidiurnal tidal cycle (~13 hr survey) on 16 June 2017 during neap tidal conditions and during another tidal cycle on 23 June 2017 in spring tide conditions. Two 1,200 kHz RDI Acoustic Doppler Current Profilers (ADCP) were mounted downward facing on Teledyne river boats to synchronously sample two lateral transects of current velocity at 2 Hz with a resolution of 0.01cm/s along landward and seaward boundaries of the farm. For each hourly transect, ADCPs were towed across the river from west to east along the farm's landward and seaward boundaries to get the spatial distribution of velocity, as indicated by white arrows in Figure 4.1b. Data were collected in 0.25 m vertical bins with a 0.55 m blanking distance between the instrument and the first bin at 0.80 m. The bottom 10% of profiles was masked to account for sidelobe effects.

Two Rockland Scientific MicroCTDs collected temperature, conductivity, turbidity, and pressure simultaneously at two stations along the farm's landward and seaward transects (Figure 4.1b). Each MicroCTD has one conductivity-temperature combo sensor, one fluorometer-turbidity combo sensor and one pressure sensor that collected measurements at 64 Hz. The conductivity-temperature combo sensor has accuracies of 1×10^{-2} mS/cm and 1×10^{-2} °C with resolutions of 1×10^{-3} mS/cm and 1×10^{-3} °C. The fluorometer-turbidity combo sensor has an accuracy of 2% of measured turbidity with resolutions of 0.03 FTU. The pressure sensor has an accuracy of 0.05 bar with a resolution of 5×10^{-4} bar. The conductivity, and temperature data were used to compute density, ρ.

The MicroCTDs were outfitted with a floatation collar and were lowered to the bottom with a cannon ball weight and release mechanism. Once at the bottom, the MicroCTD release mechanism was triggered simultaneously at each transect, which allowed for the profilers to ascend upward collecting data near the surface. At the southern transect, the three stations were located behind the farm and in the channel, shown in Fig. 1c. Due to the shallowness of the bathymetry near the farm at the northern transect, a station

could not be placed directly behind the farm. Therefore, the northern transect included stations located adjacent to the farm and in the channel.

Note that in this work the sensor accuracy of chlorophyll a measurement on MicroCTDs was in the same order of measured value. Therefore, time series data of chlorophyll a and turbidity from 2017-06-22 to 2017-06-29 collected by the Land/Ocean Biogeochemical Observatory (LOBO) monitoring system was adopted to analyze if turbidity negatively affects chlorophyll in the farm area. The LOBO buoy was deployed at water depth of 0.8 ~ 0.9 m in upper Damariscotta river at 43°59.8907'N, 69°32.5516'W (Figure 4.1b).

4.3. Hydrodynamic and hydrographic conditions

Farm siting is dependent on information of hydrodynamic and hydrographic conditions. Snyder et al. (2017) suggest estuaries along the coast of the Gulf of Maine that reach relatively warm temperatures (above 20°C), support high levels of chlorophyll in the summer (above 1 μg/L), and exhibit low turbidity (below 8 NTU) can potentially be oyster growing areas. The upstream portion in typical estuaries along the Gulf of Maine with high temperature and rich chlorophyll are optimal sites for oyster aquaculture. In this section, the temporal and spatial variations in hydrodynamic and hydrographic conditions around the particulate farm were analyzed to understand how the existing siting location is affected by this interplay between chlorophyll and turbidity.

4.3.1. Intratidal variations

The maximum surface velocities at the farm's seaward boundary during flood were larger (u = 0.37 m/s) than observed near the farm's landward boundary (0.12 m/s in Figures 4.2a.1, b.1). Likewise, the maximum surface velocities during ebb were smaller (0.26 m/s) at the seaward boundary than that observed

at the landward transect (0.50 m/s) in front of the farm. The vertical distribution of velocity suggested that flow accelerated under the farm at the seaward transect during flood, indicated by a subsurface velocity maximum (at depths of 1.3 ~ 1.5 m) before the farm (Figure 4.2b.1). Across channel velocity, *v*, were directed eastward across the transect for most of the tidal cycle, which were around 0.05 m/s ~ 0.07 m/s at both boundaries (Figures 4.2a.1, 2b.1). Curvature in the channel likely augments the observed cross-channel (Chapter 2).

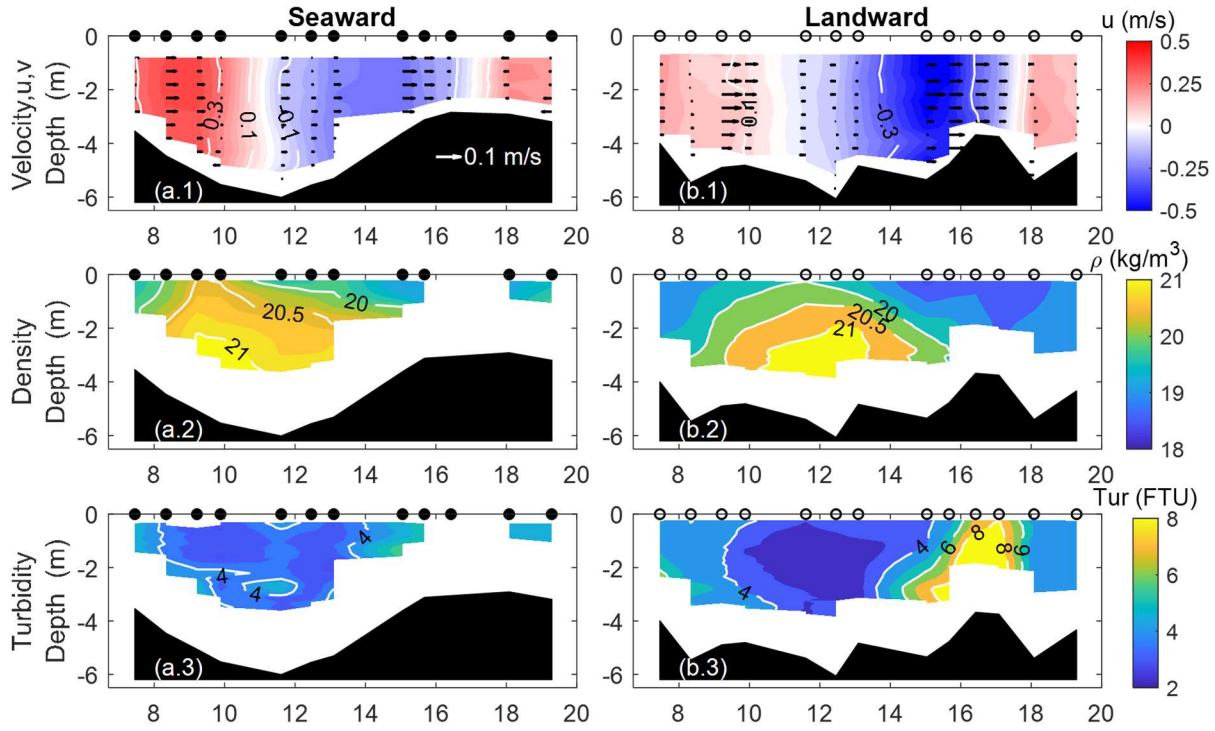

Figure 4.2 Time series of intratidal velocity, density, and turbidity at the farm's seaward and landward boundaries during spring tide. (a.1, b,1) tidal current velocity collected at farm's seaward and landward boundaries, contours denote along-channel velocity, positive velocity comes into the estuary; negative velocity goes out of estuary; vectors are cross-channel velocity, arrows pointing to the left indicating velocity towards western shoal; arrows pointing to the right indicating velocity towards eastern shoal; markers denote data collection time. (a.2, b.2)

density collected at the farm's seaward and landward boundaries. (a.3 b.3) turbidity collected at the farm's seaward and landward boundaries.

At both boundaries, density was observed to vary periodically with the tide. Tidally driven saltwater intrusion was observed as a bottom density front going through the hydrographic stations during peak food and peak ebb. At the end of the flood phase (10 ~ 12 hrs), density reached up to 21 kg/m^3, while at end of the ebb phase (16 ~ 18 hrs), density was below 19 kg/m^3 (Figures 4.2a.2, b.2). Because of saltwater intrusion, the water column gets weakly stratified at peak flood and peak ebb, as indicated by vertical density deviations above 1.5 kg/m^3 from the surface to the bottom.

The water column was more turbid from the end of ebb to early flood compared with other phases of the tide. At early flood (before 8 hr), the turbidity was around 4 FTU at the two boundaries and slightly increased from the surface to the bottom (Figures 4.2a.3, 3b.3). From peak flood to early ebb (10 ~ 14 hrs), as the salinity intrusion front arrived, the turbidity decreased to 2 ~ 3 FTU in the water column. From peak ebb to end of ebb (15 ~ 18 hrs), turbidity was larger than 5 FTU, especially near the farm's landward boundary, where turbidity was 8 ~ 10 FTU in the water column after the saltwater intrusion retreated. Note that high turbidity (> 4 FTU) only occurred near the bottom when the salinity front passed the study site (before 8 hr and 14 ~ 16 hr). It seems that weak stratification associated with the front suppressed the vertical extent of turbidity into the water column. The relationship between turbidity and stratification will be further analyzed in section 4.3.3.

4.3.2 Chlorophyll a

The chlorophyll concentration is an indicator for the amount of organic and inorganic particulates. Chlorophyll levels are an important indicator for farm siting selection (Snyder et al., 2017). The inverse

relationship between turbidity and chlorophyll a could help to explain a lower growth rate in a floating oyster farm with high turbidity (Adams et al., 2019).

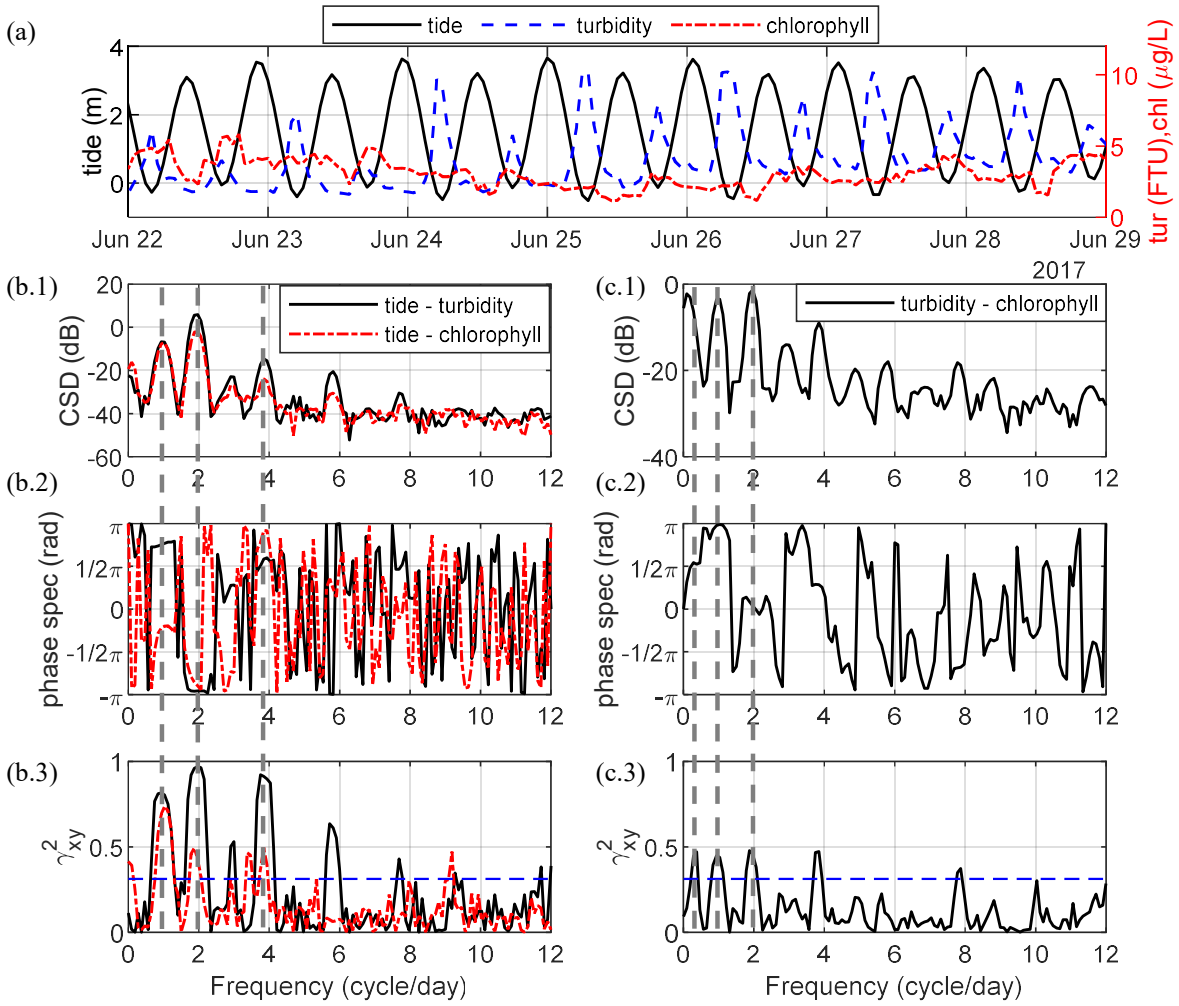

Figure 4.3 (a) Time series of tidal surface elevation, turbidity, and chlorophyll at a water depth of 1 m collected by the LOBO buoy. (b) cross-spectrum analysis of tide-turbidity and tide-chlorophyll a: (b.1) cross spectrum density (CSD); (b.2) phase spectrum; (b.3) significance. (c) cross-spectrum analysis turbidity-chlorophyll a: (c.1) cross spectrum density (CSD); (c.2) phase spectrum; (c.3) significance.

The time series of chlorophyll exhibited maximum values of 4 ~ 5 μg/L during end of ebb (low tide) in the early evening (17:00 – 19:00 EDT), and minimal values occurred at end of food (high tide) close to noon (12:00 – 14:00 EDT, Figure 4.3a). The connection between seaward velocities with the peak occurring at the end of ebb indicating that in this specific location organic particulates were primarily coming from upstream. For turbidity, the time series depicts two peaks (5 ~ 10 FTU) daily at end of ebb (low tide), which was consistent with the data collected by MicroCTDs. Note that an increased in peak values of turbidity was observed between 2017 - 06 - 22 to 2017 - 06 - 27, while chlorophyll reduced during this period, particularly turbidity exceeded 10 FTU.

To understand the connection between turbidity, chlorophyll a, and the tide, a cross spectrum analysis among chlorophyll a, turbidity, and tidal surface elevation was conducted based on the weekly record. The turbidity and tide were correlated in the diurnal, semidiurnal and quarter-diurnal frequencies, where the cross spectra density (CSD) was larger than -20 dB and the significance $\gamma_{xy}^2 > 0.75$. The phase differences in diurnal, semi-diurnal and quarter-diurnal frequencies were $3\pi/2$, $-\pi$ and $\pi/2$ respectively, indicating that the variation in turbidity was almost completely out of phase with the tidal surface elevation in all three frequencies (Figure 4.3b.1~3). The chlorophyll a and tide were also correlated in diurnal, semidiurnal and quarter-diurnal frequencies. However, the phase differences in diurnal and semidiurnal frequencies were $-\pi/4$ and $-\pi$ respectively, indicating that the diurnal variation of chlorophyll a followed the tidal surface elevation, while the semidiurnal variation was out of phase with water levels (Figure 4.4b.1~3). In essence, the chlorophyll a-turbidity cross spectra showed that chlorophyll a and turbidity were out of phase in the diurnal frequency and in phase in the semidiurnal frequency. Additionally, in low frequency (0.281 ~ 0.375 cycles/day, in period of 2.67 ~ 3.56 days) chlorophyll a and turbidity were out of phase by $\pi/2$, meaning that a subtidal increased trend in turbidity was correlated to a decline trend in chlorophyll a concentration, which might decrease oyster growth rate. The negative correlation in subtidal frequency was likely due to spring- neap tidal variation, since an increasing trend in turbidity and decreasing

trend in chlorophyll a occurred simultaneously in the time period of spring tide 2017 - 06 - 25 to 2017 - 06 – 27).

4.3.3 Linkage of turbidity and boundary layer thickness

The negative correlation between turbidity and chlorophyll demonstrated in section 3.2 suggests that a farm site with limited turbidity is ideal for high levels of chlorophyll. The variations in turbidity seemed to connect to stratification (section 3.1) and water depth (section 3.2). One argument is that mixing in the bottom boundary layer resuspends sediment and increases turbidity, but in the presence of stratification, this is confined to the lower water column.

To demonstrate the competition between bottom mixing and stratification on turbidity near surface, a mixing number $M = \frac{h_{bl}}{h}$ (Geyer and MacCready, 2014) was calculated based on field data, where h_{bl} is the bottom boundary layer thickness, h is the water depth. $M > 1$ indicates that bottom fiction induced vertical mixing could extend up to the free surface resulting in high turbidity near surface, while $M < 1$ indicates that mixing remains in the lower water column resulting in low turbidity near the surface.

Neglecting the influence of horizontal density gradients, the rate of growth of the estuarine bottom boundary layer can be parameterized as

$$\frac{dh_{bl}}{dt} = C\frac{{u_b^*}^2}{N_\infty h_{bl}} \qquad (4.1)$$

Where $C \approx 0.6$ is a constant related to the mixing efficiency (Kato and Phillips 1969, Trowbridge 1992). N_∞ is the buoyancy frequency above the bottom boundary layer, which was referenced as the maximum N_{max} in this work. Note that $N^2 = -\frac{1}{\rho_0}\frac{\partial \rho}{\partial z}$ was computed from the vertical gradient of density with respect to a refence density ρ_0. u_b^* is the bottom friction velocity. Note that both N_{max} and u_b^* can vary over tidal

cycles (i.e., are functions of time). u_b^* can be parameterized as $u_b^* = C_f \bar{u}^2$, where C_f is the bottom friction coefficient (~ 0.003) and u is depth averaged tidal current speed. Therefore, the solution of Eq (1) is

$$h_{bl} = \sqrt{2 \int_0^t C \frac{C_f \bar{u}^2}{N_{max}}} \qquad (4.2)$$

In this work, the bottom boundary layer thickness h_{bl} during ebb was computed based on the tidal current speed $\bar{u}$ and the maximum buoyancy frequency N_{max} in the water column near the floating oyster farm. The scatter plot of turbidity at a 1m water depth vs. *M* (Figure 4.4a) presented positive correlation with R^2 = 0.8 and a correlation coefficient of 0.9. Near surface turbidity increased with the mixing number *M*. Note that two extreme values of turbidity (> 8 FTU) were found when *M* > 2, i.e., boundary layer thickness was estimated as twice of the actual water depth. It also supported the argument that during ebb, bottom mixing stimulates sediment resuspension and vertically transports sediment upward, thus resulting in high turbidity near the surface. Therefore, the farm site should be deep enough for given tidal current and stratification conditions to avoid high near surface turbidity.

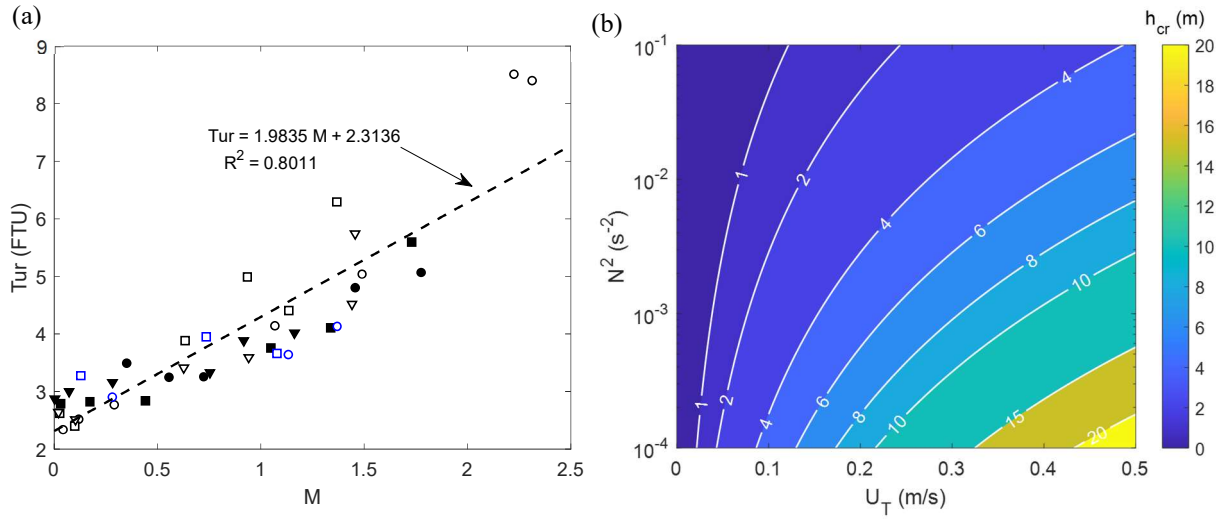

Figure 4.4 (a) turbidity at water depth of 1 m vs. mixing number, M = h_{bl} / h through ebb during spring tide

(black makers) and neap tide (blue makers). Circles denote data collected near the farm, squares denote data in the main channel, triangles denote data over eastern shoal. Solid markers denote data collected along the farm's seaward boundary while open markers denote data collected along the farm's landward boundary. (b) design chart of critical water depth for floating aquaculture farm. U_T is depth averaged along channel velocity, N^2 is maximum squared bouncy frequency.

4.3.4 Critical water depth

It has been shown that turbidity is positively correlated to the bottom boundary layer thickness. Therefore, in farm siting, site selection should be carefully chosen based on local water depths in order to avoid high turbidity events. Since the turbidity is related to stratification and velocity shear, we can propose a critical depth to guarantee the mixing number $M \leq 1$, i.e., bottom boundary layer thickness is no larger than twice the water depth for given tidal current and stratification conditions. Acritical depth $h_{cr} = \sqrt{\frac{C_D {U_T}^2}{\omega N_{max}}}$ is proposed to limit the ability for bottom sediment to be resuspended into the farm. A depth design chart based on the depth averaged tidal current amplitude and the maximum stratification N^2_{max} in the water column is shown in Figure 4.4b. In weakly stratified estuaries where depth averaged tidal current amplitude is around 0.3 m/s and maximum stratification $N^2_{max} = 10^{-3}\sim10^{-2}\ s^{-2}$, the farm should be placed where water depth is larger than 4 m at low tide. When depth averaged tidal current amplitude reaches up to 0.4 m/s the required minimum water depth is 6 m at low tide. Note that this design chart is only applicable to weakly stratified estuaries with low river run off and the limitations of this will be further discussed in section 6.

4.4. Material transport

To understand the impacts of farm layout, location, and size expansion on overall food uptake by the farm, a semi-analytical hydrodynamic and material transport model of chlorophyll a concentration was proposed to estimate the amount of food filtered by a floating oyster farm with different designs. The optimal farm layout and design considerations for expanding farm size will be based on model results.

4.4.1 Physical model

The physical model applied in this work is a combination of a 3D semi-analytical hydrodynamic model for idealized estuaries with the convection-diffusion model for concertation transport. The semi-analytical hydrodynamic model provides tidal and subtidal (mean) velocities as input for the convection-diffusion model. The governing equations for tidal flow in a curved estuary with low river discharge consist of continuity equation 4.3a and dynamic equations 4.3b, c for along (x, u) and across (y, v) channel velocity components:

$$\frac{\partial u_0}{\partial x} + \frac{\partial v_0}{\partial y} + \frac{\partial w_0}{\partial z} = 0 \quad (4.3.a)$$

$$\frac{\partial u_0}{\partial t} = f v_0 - g\frac{\partial \eta_0}{\partial x} + \frac{\partial}{\partial z}\left(A_z \frac{\partial u_0}{\partial z}\right) - \frac{1}{2}\frac{C_D}{h_f} u\sqrt{{u_0}^2 + {v_0}^2} \quad (4.3.b)$$

$$\frac{\partial v_0}{\partial t} = -f u_0 - g\frac{\partial \eta_0}{\partial y} + \frac{\partial}{\partial z}\left(A_z \frac{\partial v_0}{\partial z}\right) - \frac{1}{2}\frac{C_D}{h_f} v\sqrt{{u_0}^2 + {v_0}^2} \quad (4.3.c)$$

where, x, y, z denotes along, across and vertical direction. u_0, v_0, w_0 are semi-diurnal tidal current in along, across and vertical direction. f is the Coriolis parameter, η_0 is the semi-diurnal tidal elevation, A_z is the vertical eddy viscosity, R is the bending radius in the main channel, h_f is the penetration depth of the farm. The farm imposed drag force on flow was parameterized as a bulk drag coefficient C_D derived from Chapter

2. The terms on the left-hand side of equations 4.3b.c are local acceleration, while the terms on right-hand side are Coriolis forcing, barotropic forcing, vertical gradient of Reynolds stress, centrifugal forcing and farm drag forcing. Note that the farm drag forcing is only imposed in the farm area.

The governing equations for subtidal flow are

$$\frac{\partial}{\partial x}\left(h\int_{-1}^{0}\overline{u_s}d\sigma+\overline{\eta_0\int_{-1}^{0}u_0d\sigma}\right)+\frac{\partial}{\partial y}\left(h\int_{-1}^{0}\overline{v_s}d\sigma+\overline{\eta_0\int_{-1}^{0}v_0d\sigma}\right)=0 \quad (4.4.a)$$

$$\frac{1}{h^2}\frac{\partial}{\partial\sigma}\left(\widetilde{A_z}\frac{\partial\overline{u_s}}{\partial\sigma}\right)+f\overline{v_s}-g\frac{\partial\overline{\eta_s}}{\partial x}=\overline{u_0\frac{\partial u_0}{\partial x}}+\overline{v_0\frac{\partial u_0}{\partial y}}+\overline{w_0\frac{\partial u_0}{\partial z}}+\frac{2\overline{u_0v_0}}{R+y} \quad (4.4.b)$$

$$\frac{1}{h^2}\frac{\partial}{\partial\sigma}\left(\widetilde{A_z}\frac{\partial\overline{v_s}}{\partial\sigma}\right)-f\overline{u_s}-g\frac{\partial\overline{\eta_s}}{\partial y}=\overline{u_0\frac{\partial v_0}{\partial x}}+\overline{v_0\frac{\partial v_0}{\partial y}}+\overline{w_0\frac{\partial v_0}{\partial z}}-\frac{\overline{{u_0}^2-{v_0}^2}}{R+y} \quad (4.4.c)$$

where, $\overline{\eta_s}$, $\overline{u_s}$, $\overline{v_s}$, $\overline{w_s}$ are also known as Eulerian average water level and velocities (Winant, 2008). Terms similar to $\overline{u_0\frac{\partial u_0}{\partial x}}$ are temporally averaged advection terms from semidiurnal constituents, also known as tidal rectification, while $\frac{2\overline{u_0v_0}}{R+y}$ and $\frac{\overline{{u_0}^2-{v_0}^2}}{R+y}$ are the centrifugal forces.

The net transport velocities are defined as $u_T=\overline{u_s}+\frac{1}{h}\overline{\eta_0u_0}$ and $v_T=\overline{v_s}+\frac{1}{h}\overline{\eta_0v_0}$ (Robinson, 1983; Li and O'Donnell, 2005), which account for both the subtidal flow driven by time averaged tidal advection and nonlinear component from finite tidal amplitude. Note that two more conditions were required to solve for subtidal surface slopes $\frac{\partial\overline{\eta_s}}{\partial x}$ and $\frac{\partial\overline{\eta_s}}{\partial y}$. The first one is that cross-sectionally integrated along channel transport is equivalent to the river discharge, which was neglected in this work due to low river discharge in the Damariscotta river, i.e., $\int_{-B}^{B}\int_{-h}^{0}v_T dz\,dy=0$. And the other condition is that the depth integrated across channel transport is zero, $\int_{-h}^{0}v_T dz=0$, since there is no net depth integrated transport in and out of the rive sides.

Since the oyster cage was 0.27m high which was much smaller than water depth (3 ~ 4m) and the profile data of chlorophyll was not available, the two-dimensional advection-diffusion equation for transport chlorophyll concentration near the surface was applied in this work,

$$\frac{\partial C}{\partial t} + u\frac{\partial C}{\partial x} + v\frac{\partial C}{\partial y} = K_h\left(\frac{\partial^2 C}{\partial x^2} + \frac{\partial^2 C}{\partial y^2}\right) - kC \qquad (4.5)$$

where, C is the chlorophyll a concentration as an indicator for oyster food, which is all kinds of organic matter (Adams et al., 2019). u, v are the surface velocity in along channel and across channel direction, which are components of tidal and subtidal current velocity known as $u = u_0 + u_T$, and $v = v_0 + v_T$. K_h is horizontal eddy diffusivity, k is the volumetric filtering rate of oysters.

4.4.2 Model setup

An idealized bathymetry that is based off the Damariscotta River bathymetry is used in this work, where the convergence in both width and depth is assumed to follow an exponential decay from the mouth. A symbolic bottom bathymetry was applied to mimic the bifurcated bottom bathymetry observed near the oyster farm (Figure 4.1b). The bathymetry over the entire domain is parameterized as,

$$B(x) = B_0 e^{-\frac{x}{L_b}} \qquad (4.6.a)$$

$$h_0(y_0) = \begin{cases} 16 + 9.5e^{-\left(5y_0 - \frac{25}{6}\right)^2} + 23e^{-(3y_0)^2} & 0 \le y_0 \le 1 \\ 16 + 9.5e^{-\left(5y_0 - \frac{25}{6}\right)^2} + 23e^{-{y_0}^2} & -1 \le y_0 < 0 \end{cases}, y_0 = \frac{y}{B(x)} \qquad (4.6.b)$$

$$h(x,y) = h_0\left[\frac{y}{B(x)}\right]e^{-\frac{x}{L_h}} \quad . \qquad (4.6.c)$$

Half of the channel width at the mouth is $B_0 = 550$ m. The width decays with an e-folding length of $L_b = 47.5$ km toward the head, shown as Figure 4.5b. The bottom bathymetry is assumed to have similar

topography at each cross section, parameterized in equation 4.6b, where y_0 is the nondimensional across channel coordinate. The convergence of depth moving toward the head exponentially decays with an e-folding length of $L_h = 11.0$ km (equation 4.6c; Figure 4.5b). The total length of the model is 25.62 km, which covers the parts of the estuary where tidal forcing dominates the hydrodynamics. Tidal flow was forced with a tidal amplitude of 1.78 m at the mouth.

A typical bottom roughness was applied ($\sigma_0 = 1.0 \times 10^{-3}$). The friction velocity amplitude $\widehat{u^*}$ for the bottom was initially set as 0.015 m/s, and after several iterations varied from 0.011 to 0.017 m/s at different locations, which was consistent with the field observation from Chapter 2. A temporal and spatial constant bulk filter rate over entire farm with 3×10^{-4} /s was applied in this study, which derived based on filtration rate from individual oyster (2.5 L individual^{-1} min^{-1}) with shell length of 7.62 cm at temperature of 20 ºC (Powell et al. 1992) and stocking density. Note that the filter rate depends on oyster species, age, and the bulk filter rate also depends on stocking density.

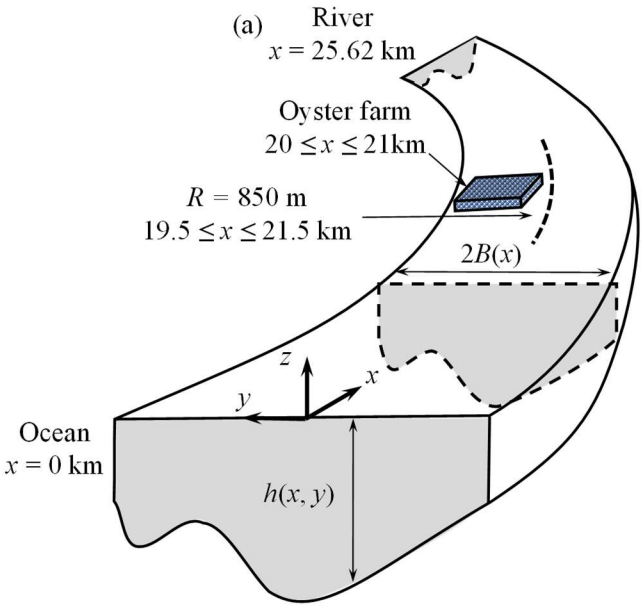

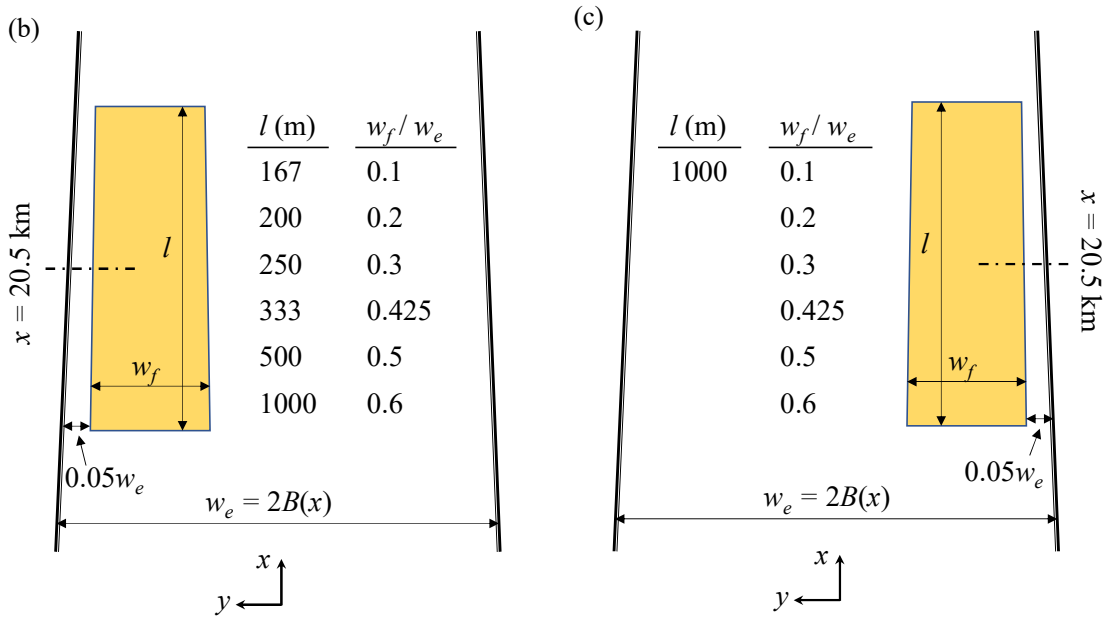

Figure 4.5 (a)The model bathymetry h is arbitrary h (x, y) across the channel and converges in width and depth along a curved channel. A curvilinear coordinate system (x, y, z) is used, where the x- and y-coordinates are along and across, respectively, and z is the vertical. The perspective is looking into the estuary. B(x) is the half width of the estuary. The portion denoted by dashed line ($19.5 \leq x \leq 21.5$ km) has a bend with radius of 850 m in the main channel. (b, c) studies cases of different farm designs including layout, expansion, and location. Yellow boxes denote farm, l is farm length, w_f is farm width, $w_e = 2B(x)$ is estuary width. For all study cases, the farm center in the along channel direction is at x = 20.5 km and the gap between farm edges to left or right side is 0.05 w_e. There are 36 cases when farm was placed over the left portion of the estuary (b) and 6 cases when farm was placed over the right portion of the estuary (c).

For simplicity, in this work the stocking density is assumed constant as the layout of a present farm. A spatially and temporally constant horizontal eddy diffusivity is set as 5 m^2/s. Initially, a patch of chlorophyll a distribution was assigned as 8 µg/L (peak values from LOBO data) within the portion $22.5 < x < 24$ km. Since the chlorophyll was primarily located upstream and advected past the farm during ebb in

the observations, the simulation started at the end of flood in order to mimic the seaward transport of chlorophyll a.

In order to investigate various farm designs including layout, farm size (ratio of farm width to estuary width), location (inner and outer bend) on filtration, a total of 42 cases were considered in this work: 36 cases were for a farm located on the west portion of the estuary (Figure 4.5b) and 6 cases for farm located east portion of the estuary (Figure 4.5c). Since the total amount of food filtered by the farm depends on farm size (A) and filtering time (t), a normalized filtration parameter $F = h_f \int_0^T kCdt$ which is defined as the food filtered by the oyster per unit farm area over one tidal cycle (T), together with an spatially averaged filtration $\tilde{F} = \frac{1}{A}\iint Fdxdy$ were proposed to compare the food delivery efficiency of different farm designs.

4.5. Model results

In this section, the effective filtration among various farm design scenarios including farm layouts (long - narrow vs. short - wide layouts), location (west or east portion of the cross section) and size expansions in length and width were examined using the model.

4.5.1. Impact of farm layout on filtration

To understand how changes in farm layout impact filtration, multiple farm design scenarios with constant area (57,150 m^2) but various lengths and widths were simulated. The spatial variation in normalized filtration F for each scenario were present in Figure 4.6. In the slender layout where farm length, l = 500 m, ratio of farm width to estuary width w_f/w_e = 0.2, filtration F was larger than 8.5 mg/m^2 in the zone closest to the landward and seaward boundaries, while F < 8.0 mg/m^2 in the middle zone (Figure 4.6a.1) indicating that chlorophyll a delivery decayed from the boundaries to the central zone. Changing

the farm layout from slender to bluff, (i.e., decreasing farm length and increasing the farm width) clearly enhanced filtration (Figure 4.6a.2 ~ 6a.4). In the bluff layout where the farm length was 200 m, and the ratio of the farm width to estuary width w_f/w_e was 0.5, filtration F was around 8.5 ~ 9.1 mg/m^2 and was almost uniformly distributed over the farm (Figure 4.6a.3). The spatially averaged filtration $\tilde{F}$ increased from 8.3 mg/m^2 to 8.9 mg/m^2 (7.2%) when width ratio w_f/w_e increased from 0.2 to 0.6, while farm length l decreased from 500 m to 167 m. Therefore, the bluff layout demonstrated a better filtration since along channel advection could supplement more chlorophyll a through landward and seaward boundaries.

4.5.2 Impact of farm expansion and location

Besides farm layout, extending the farm size (increasing farm length or width) and changing the farm siting across the estuary might also impact filtration. Extending farm length along the estuary dramatically decreased filtration F. For scenarios with constant width ratio $w_f/w_e = 0.5$, when the farm size extended from l = 200 m to l = 1000 m, filtration F in the central zone decreased from 9.0 mg/m^2 to 5.0 mg/m^2, a striking 44.4% reduction (Figures 4.7a.1 ~ a.3). Particularly, a length expansion reduced filtration in the downstream zone closest to the left shore (Figure 4.7a.3), where flow reduction due to farm drag force reduces chlorophyll advected to the central zone of the farm.

Similar to the length expansion, increasing farm width also decreased filtration. For scenarios with constant farm length l = 1000 m, when width ratio w_f/w_e increased from 0.2 to 0.6, filtration F in the central zone decreased from 6.6 mg/m^2 to 3.5 mg/m^2, yielding a 47.0% reduction (Figures 4.7b.1 ~ b.3). The downstream zone closest to the left shore exhibits the maximum decrease due to reduced chlorophyll supply (Figure 4.7b.3). F in the upstream zone closest to landward boundary only decreased by around 1.0 mg/m^2, likely from more chlorophyll being advected into the farm through the landward boundary with a larger farm width (Figure 4.7b.1~3).

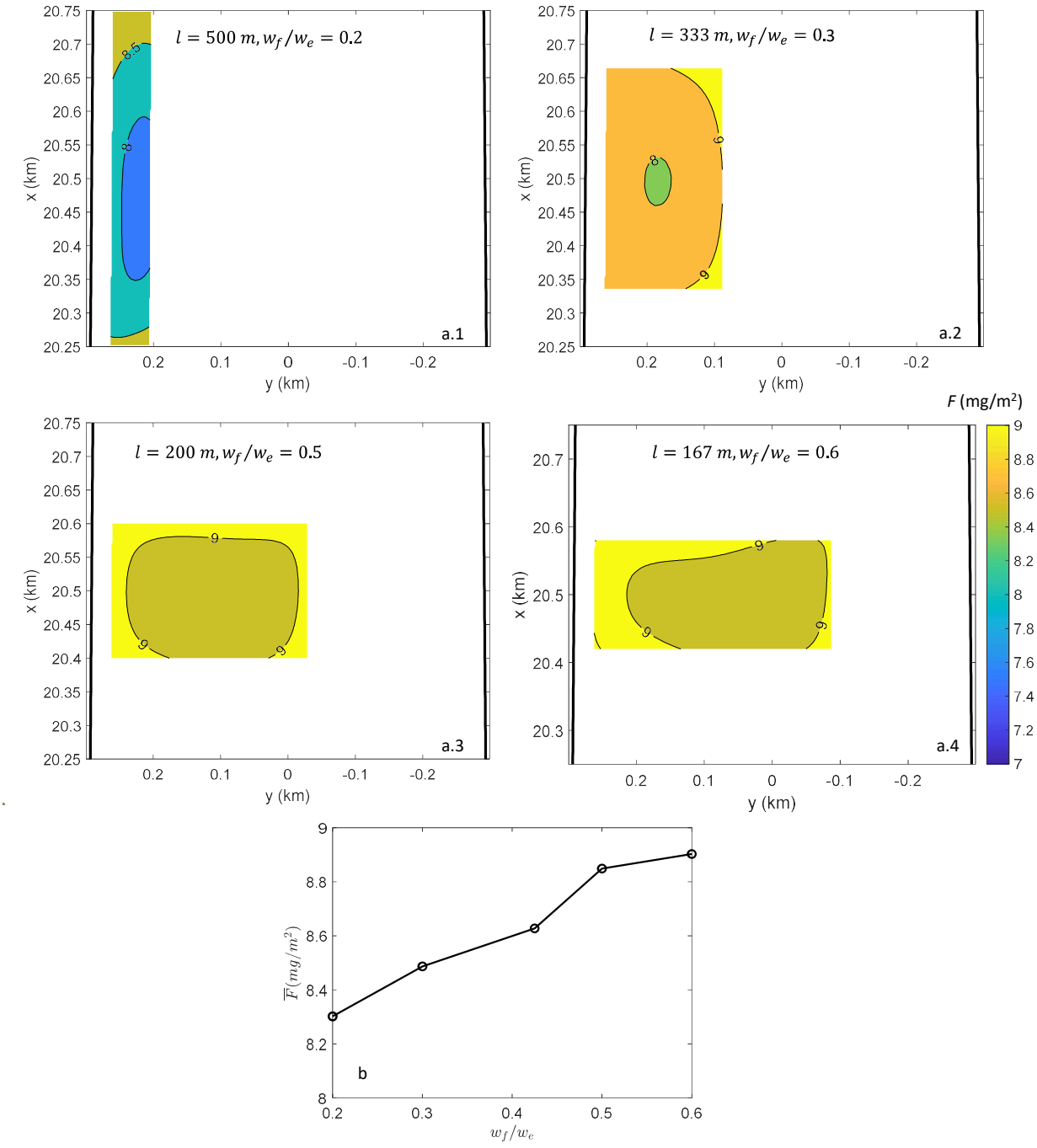

Figure 4.6 (a.1-a.4) Distributions of filtration F in different farm layouts. Contours denote spatial distribution of F in farm area, white spots denote portion without the farm, x denote along channel distance, y denote across channel distance, l is farm length. w_f/w_e is ratio of farm width to estuary width. (b) Spatially averaged filtration $\tilde{F}$ of cases (a.1-a.4).

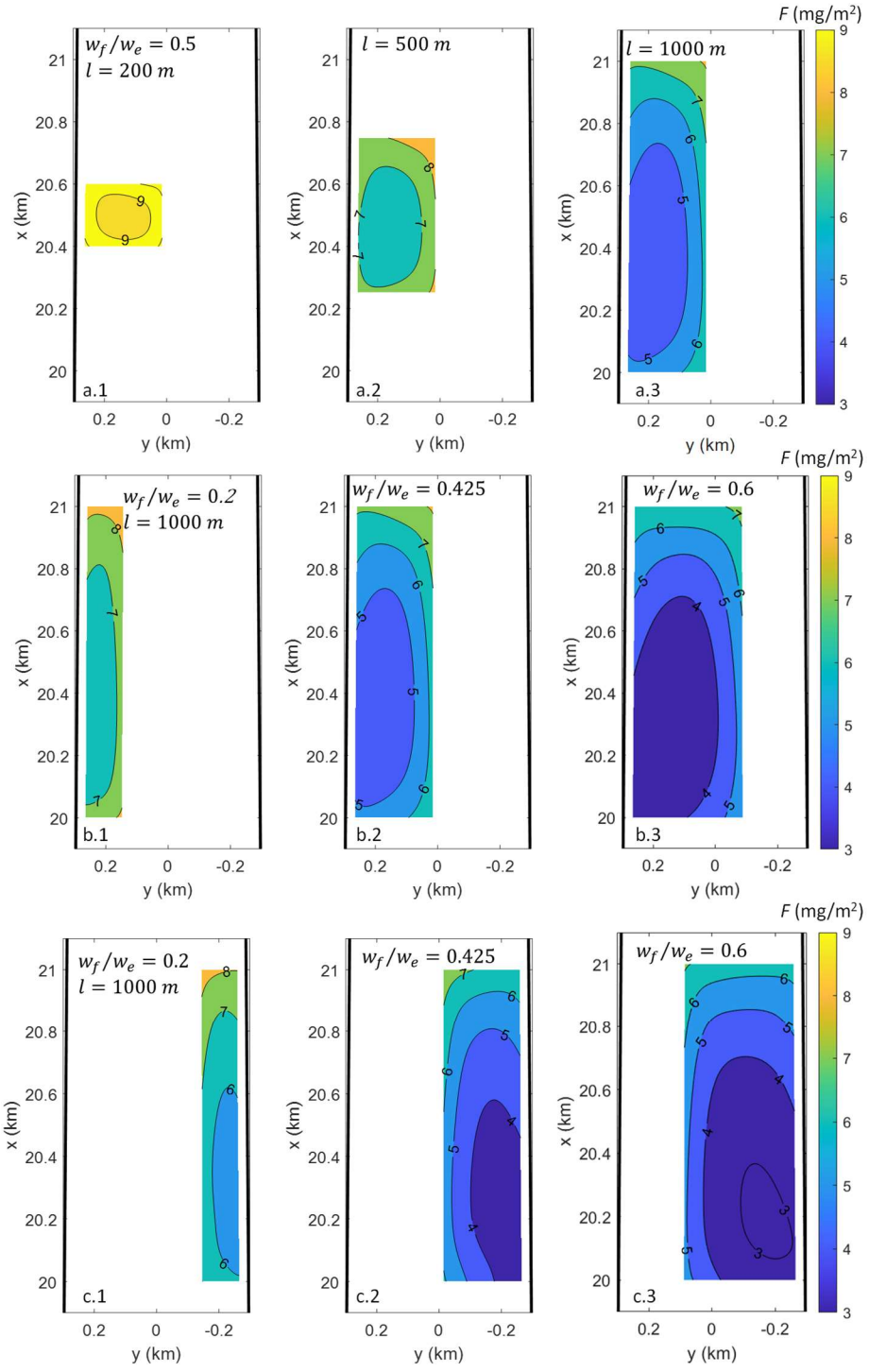

Figure 4.7 Distributions of filtration F in farm expansion and changing location. (a.1 - a.3) Farm length expansion. Contours denote spatial distribution of F in farm area, white spots denote locations without a farm, x denote along channel distance, y denote across channel distance, l is farm length. w_f / w_e is ratio of farm width

to estuary width. (b.1 - b.3) Farm width expansion. (c.1 - c.3) Change farm location to right portion of the cross section, farm sizes are same as (b.1 - b.3).

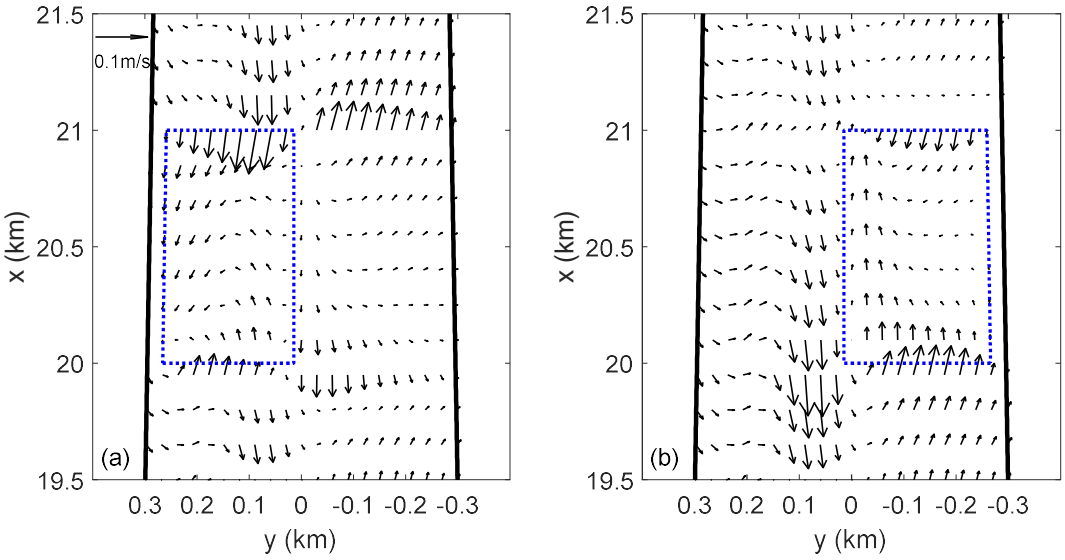

Figure 4.8 Subtidal flow patterns at surface with farm located on left side (a) and right side (b) of the estuary. The farm length is l=1000 m, ratio of farm width to estuary width w_f / w_e = 0.425. Arrows denotes subtidal velocity, bule dashed rectangles denote farm, x is across channel distance, y is across channel distance.

All the above results were obtained by locating the farm over left portion of the estuary, which was also at the inner bend. By moving the farm from the west side (inner bend) to the east side (outer bend) of the estuary, the filtration decreased over the entire farm. Comparing corresponding scenarios with the same farm size and placed over the west portion, the overall filtration decreased by 0.4 ~ 1.0 mg/m^2 when the farm was placed over the east portion, where the spatially averaged filtration $\tilde{F}$ decreased by 5.5 ~ 13.0%. The deviations in filtration at different location might be due to the deviations in subtidal along channel flow across the estuary. When the farm was placed over the west side of the estuary, the subtidal current toward the farm was 0.188 m/s along landward boundary (Figure 4.8a). However, when farm was placed

over east side of the estuary, the subtidal current toward the farm was 0.082 m/s (Figure 4.8b). Therefore, less the chlorophyll a was transported into the farm through the landward boundary during the ebb phase of the tide when place was placed over right side of the estuary.

The above case studies qualitatively demonstrate the decay in filtration with farm size expansion. The quantitative relationship between filtration decay and farm size expansion ratio remains unknown. Regression analyses among spatially averaged filtration $\tilde{F}$, expansion ratio in length r_l and width r_w was conducted to illustrate the relationships. When only expanding the farm length but keeping the farm width constant, regressions with highest R^2 (> 0.989) were achieved when $\tilde{F}/\widetilde{F_0} = a \ln r_l + b$, as shown in Figure 4.9a, where $\widetilde{F_0}$ is the spatially averaged filtration of the base scenario, $\tilde{F}$ is the spatially averaged filtration of cases with length expansions, r_l is the expansion ratio in length, a and b are constants obtained from regression, which are related to farm width. Note that the slope of $\tilde{F}/\widetilde{F_0} - \ln r_l$ curves, i.e., $|a|$ increased with farm width ratio w_f/w_e, indicating that extended length of a wider farm resulted in a higher decay in $\tilde{F}$ (Figure 4.9a). Alternatively, when only extending the farm length, the spatially averaged filtration $\tilde{F}$ over the entire farm can be parameterized as a logarithmic function of farm length l, i.e., $\tilde{F} = \alpha \ln l + \beta$, where α and β are constants but depends on the farm width. This relation illustrates that the spatially averaged filtration follows a logarithmic decay with farm length expansion.

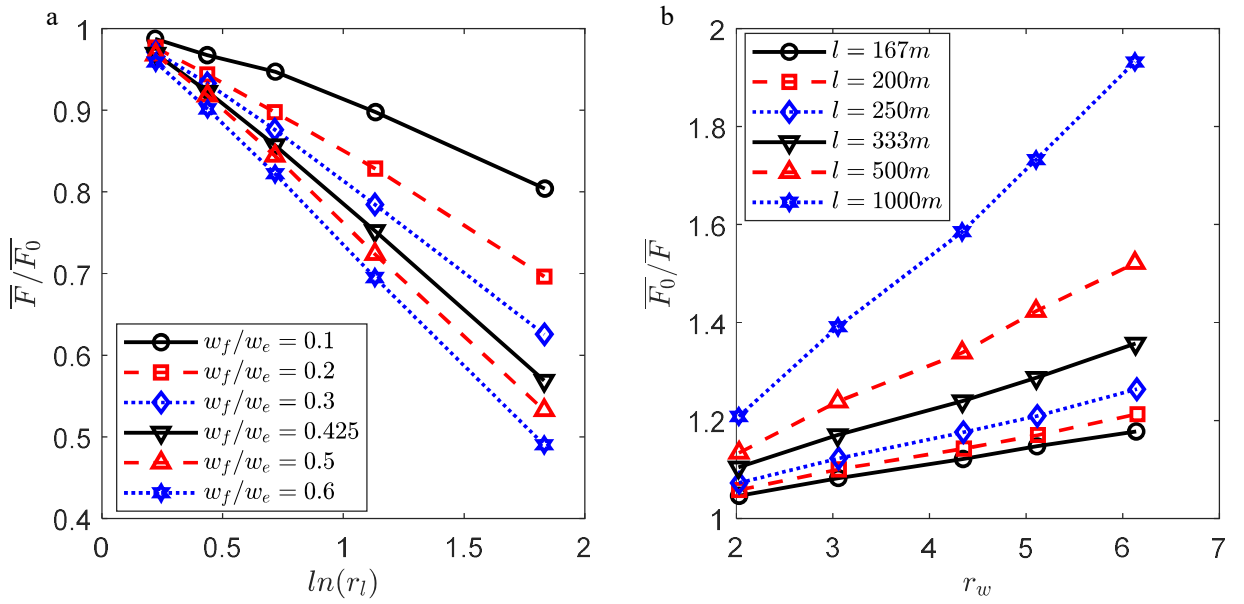

Figure 4.9 (a) Impacts of farm length expansion on spatially averaged filtration under different farm width. $\widetilde{F_0}$ is the spatially averaged filtration of the base scenario, $\tilde{F}$ is the spatially averaged filtration of cases with length expansions, r_l is the expansion ratio in length, w_f/w_e is ratio of farm width to estuary width (b) Impacts of farm width expansion on spatially averaged filtration under different farm length. $\widetilde{F_0}$ is the spatially averaged filtration of the base scenario, $\widetilde{F_0}$ is the spatially averaged filtration of cases with width expansions, r_w is the expansion ratio in width.

When only expanding the farm width but keeping farm length constant, regressions with highest R^2 (> 0.997) were achieved when $\widetilde{F_0}/\tilde{F} = cr_w + d$ or $\tilde{F}/\widetilde{F_0} = \frac{1}{cr_w+d}$ as shown in Figure 4.9b. Where $\widetilde{F_0}$ is the spatially averaged filtration of the base scenario, $\bar{F}$ is the spatially averaged filtration of cases with width expansions, r_w is the expansion ratio in width. c and d are constants obtained from regression, which are related to farm length. Note that the slope of $\widetilde{F_0}/\tilde{F} - r_w$ curves, i.e., $|c|$ increased with farm length l, indicating that the extended width of a longer farm resulted in a higher decay in $\tilde{F}$ (Figure 4.9b). Alternatively, when only extending the farm width, the spatially averaged filtration $\tilde{F}$ over the entire farm

can be parameterized as a homographic function of farm width w_f, i.e., $\tilde{F} = \frac{1}{\gamma w + \delta}$, where γ and δ are constants but depends on farm length. This relationship illustrates that spatially averaged filtration follows a hyperbolic decay with farm width expansion.

4.6. Discussion

4.6.1. Farm design considerations

Floating oyster farm design considerations including water depth and farm layout were analyzed based on filed analysis and simulations of material transport. Field data and analysis found that during ebb, bottom mixing stimulates sediment resuspension and vertically transports sediment upward resulting in high turbidity near the surface. This led to the development of a critical depth criteria that considers tidal currents and stratification, aimed at minimizing near surface turbidity in farm siting decisions. The design chart proposed in this work is only applicable to weakly stratified estuaries with low river discharge, where turbidity is mainly caused by sediment resuspension from bottom stress rather than downstream transport by river run off. Weak stratification likely limits surface turbidity by suppressing the upward flux of bottom boundary layer.

This material transport studies based on the convection-diffusion model under periodic tidal current conditions, demonstrates the impacts of farm design on filtration. Several principles in farm layout are proposed. First, in estuaries where chlorophyll is focused upstream and then transported seaward to the farm area, the farm should be placed in a location with seaward subtidal flows, which would enhance nutrition filtration by the farm. Secondly, a slender layout should be avoided in practice where the filtration reduces dramatically in the central zone.

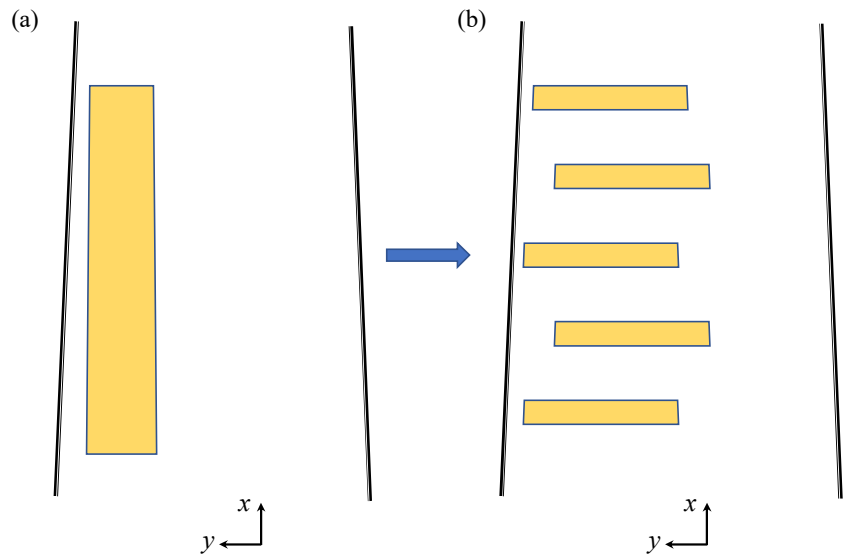

Figure 4.10 Schematic diagram of changing farm layout from a single blender patch (a) to multiple patches in bluff and staggered layouts (b). Yellow boxes denote farm patches.

The optimal layout for a farm is a bluff layout, where a short and wide layout yields increased filtration since most nutrient was transported in the farm through landward and seaward boundaries. In addition, decreasing farm length avoid low nutrient concentration in the central zone of the farm. Lastly, when farm expansion is required, directly enlarging farm size is unadvisable since filtration decays with farm size (Figure 4.9), especially extending farm length. The optimal option is to break up a large farm into multiple clusters with a bluff and staggered layout with sufficient gaps in the along channel direction (Figure 4.10). The bluff layout guarantees each cluster having optimal filtration and the staggered layout increases the effective width of the farm where nutrients can be transported in. Sufficient gaps between each cluster allows lateral horizontal transport of nutrients into the gap zone between each cluster and eventually allows more nutrient to be transported into the cluster downstream. Further research efforts are still required to study the impacts of the gap between clusters in order to quantitatively determine optimal gaps in staggered layout.

4.6.2. Limitations

In the calculation of mixing number and critical depths, since all the data were collected outside of the farm, the contribution of surface boundary layer and change in stratification to boundary layer development and turbidity was not included in this work. It is still unknown whether farm impact on vertical mixing and stratification would enhance or reduce transport of resuspended sediment to the upper layer occupied by the farm. Further research efforts such as collecting profiles of density, salinity, and turbulence characteristics both inside and outside the farm will help to identify the contributions of farm impact on vertical transport of resuspended sediments.

The proposed design considerations for farm layout are only applicable to estuaries where chlorophyll or nutrients are transported along the channel and through the landward and seaward boundaries rather than lateral edges. Therefore, new studies are required in other systems where nutrients are transported into the farm through all the edges. Note that due to shallow penetration of the farm in this work, the two-dimensional material transport model was applied, where vertical transport and mixing were not included. Vertical transport like up- or downwelling together with vertical eddy diffusion at the lower edge of the farm might not only change the vertical distribution of nutrient in the water column but also bring nutrient vertically into the floating oyster farm or take it away, resulting in an altered total filtration. More efforts such as a three-dimensional material transport model are required to take account of vertical transport and mixing.

In this work, for simplification, a constant filter rate was applied in the simulation. Note that the filter rate depends on oyster age (or size) and temperature (Powell et al. 1992). Therefore, the actual filtration over one tidal cycle might deviated from the filtration reported in this work due to temperature variations in one tidal cycle. But the patterns of impacts from farm layout on filtration remains similar if spatial variation in filter rate is negligible.

Up until to now, almost all the modeling tools related to aquaculture are designed for individual processes such as hydrodynamics, biochemistry, oyster feeding and growth, or engineering such as mooring and anchor design. In the long term, a comprehensive system integrating modeling tools from multiple disciplines is required to complete farm siting, design, and management all at once. The system can also predict evolution in all aspects related to aquaculture due to the changing environment in the future.

4.7. Conclusions

A large portion of local aquaculture farm are sited upstream in the shallow parts of estuaries along the meandering coastline of the Gulf of Maine. Material transport in those estuaries is vitally import for aquaculture activities. This chapter mainly addresses the linkage between turbidity and vertical mixing from field observation as well as the impact of farm layout on chlorophyll absorption by applying a semi-analytical dynamic and material transport model for estuaries.

Data analysis demonstrated that high near surface turbidity during the ebb phase of the tide was caused by bottom stress which fluxed suspended sediment upward in the water column. Correspondingly, a critical water depth related to tidal currents and stratification should be considered in farm siting to avoid high turbidity near the surface. Material transport simulations proved that directly increasing the farm length and width could dramatically decrease food delivery to the central zone of the farm due to flow reduction inside the farm induced by the farm drag force. The normalized filtration showed a logarithmic decay with the farm length expansion, and a hyperbolic decay with the width expansion. Therefore, the highlighted farm design principles include placing the farm in a location with net seaward transport, avoiding extending the farm length and breaking the large and blender farm into multiple pieces with bluff layout.

To date, farm drag force and impact of farm layout on material transport has not been considered in carrying capacity models. Vertical mixing induced turbidity should also be included to better parameterize oyster filtering. Furthermore, a framework integrating physics, biochemical and engineering system should be built in the future to cover interdisciplinary aspects of aquaculture.

CHAPTER 5

CONCLUSIONS

5.1 Findings and academic contributions

The overarching goals of this work were to understand how the presence of aquaculture farms impacted estuarine conditions, in addition to looking at how the farm layout and placement within certain estuarine conditions impact food uptake. Comprehensive studies including field observations, analytical and numerical modeling were conducted to understand how farms influence the hydrodynamics in estuaries, which is important to consider in planning sustainable aquaculture expansion in the future. One major finding in this work is that farm-induced drag forces alter estuarine hydrodynamics and delay material transport through the farm. Farm induced streamwise flow reduction near the farm limits the development of lateral circulation, which likely has consequences for food uptake and material transport. The farm drag forces also enhance the lateral straining of velocity shears, which induce vertical mixing near the surface and extends the farm's frictional footprint. These results show that even though a farm may encompass a small portion of the estuary, it can affect the momentum and mixing outside of the immediate farm area. A bulk drag coefficient for the farm was calculated as $8.4 \times 10^{-3} \pm 9.1 \times 10^{-4}$ from field data, while the drag coefficient for a single cage ranged from 0.58 to 0.92. The drag coefficient for a single cage was implemented into a regional scale hydrodynamic model, and the model results qualitatively reproduced patterns observed from field.

The floating oyster farm not only induces flow reduction and redistribution, but also alters the subtidal flow patterns. The farm drag force reverses subtidal flow patterns compared to that without the farm. The transport time of particulates to travel from upstream to the farm site in an idealized estuary increased with increasing farm size, which indicated that particulates would stay longer in the upstream and in the farm area with larger farm sizes. Additionally, farm layout, location, and expansion impacts material transport inside the farm (i.e., total filtration by the farm). A sensitivity analysis of farm layout on food

uptake showed that a bluff layout (wide and narrow) is optimal for aquaculture farm design because more nutrients can be transported into the farm through wider landward or seaward boundaries. Furthermore, shorter farm lengths avoid low nutrient concentration in the middle of the farm. The rising demand for aquaculture will enhance farm expansion in the future. This work showed that expanding individual farm size decays the filtration per unit area in the farm, where the filtration over a tidal cycle per unit area yields a logarithmic decay with length expansion and hyperbolic decay with width expansion. Although in this study, the simulations of the farm impact on material transport and filtration analysis were conducted just using chlorophyll a tracer. Both the material transport model and filtration analysis are applicable to study other substances filtered, absorbed, or caught by oysters such as debris, pollutants, dissolved oxygen as well as pathogenic bacteria. By introducing source terms, the material transport model can be extended to further study production and transport of oyster excreta and feces.

Regardless of how material is transported in and out of the farm, another important aspect is adequate food uptake within the farm due to the water quality. In shallow estuarine locations, bottom generated turbulence can overcome weak stratification to transport bottom sediment upward, resulting in high near surface turbidity that might negatively impact oyster growth. Accordingly, a farm depth design criterion was proposed based on the mixing and stratification, $h_{cr} \geq \sqrt{\frac{C_D {U_T}^2}{\omega N_{max}}}$, which can be applied to farm siting to avoid high turbidity water in the farm area in certain tidal and stratification conditions.

Even though a farm may encompass a small portion of the estuary, it can affect the momentum, mixing and subtidal flow patterns outside of the immediate farm area. The consistency between field observations, numerical and analytical model results highlight the importance of considering the hydrodynamic responses of farms in estimates of carrying capacity and siting decisions. Although flow reduction inside of the farm could delay the nutrient supply into the farm, particularly the interior location of the farm, designing the farm in a bluff layout increases filtration compared to farms with slender layouts in estuaries where nutrients are transported from upstream. Farm siting could be informed if an

understanding of hydrodynamic, hydrographic and water quality conditions were considered, so that optimal production could be achieved with minimal impact to the surrounding dynamics. More research efforts including observation and numerical modeling within the farm would contribute to a framework that could be used by farmers to inform farm siting decisions.

5.2. Application for aquaculture sustainability

Outcomes from this work aims to contribute to environmental and economic sustainability in aquaculture. The hydrodynamic and hydrographic conditions are highly variable and site specific, therefore acquiring environmental data and thoroughly evaluating interactions between aquaculture and environment are beneficial for environmental sustainability. This work details field data collection strategies and modeling tools, which quantitatively determined environmental impact from aquaculture. Findings from this work highlighted that the hydrodynamic impacts of aquaculture raised from farm drag force. Therefore, approaches to reduced bulk farm drag coefficient including reducing stock density, increasing gaps between long-lines and control ratio between farm size and estuary dimensions are expected to effectively limit hydrodynamic impacts from aquaculture farm.

The outcomes of this work also introduce a comprehensive strategy for stake holders to plan new aquaculture farms in the future including preliminary site surveys and optimal farm design. Site surveys with multiple instruments to collect hydrodynamic data (tidal elevation, current speed) and hydrographic data (temperature, salinity, chlorophyll, turbidity, oxygen) helps to identify potential farm sites with rich nutrient, proper net transport direction, appropriate salinity and temperature conditions, which can minimize hypoxia and turbidity. The numerical and analytical models are quantitative tools to evaluate changes in flow patterns when placing a farm and search for optimal farm layouts to maximize food delivery and filtration. The modeling framework is also applicable to assessing harmful risks to aquaculture activities, such as spreading of pathogenic bacteria, pollution, hypoxia, and algae blooms. In addition, the current

speed data from field surveys and modeling can be the basic input for facility or mooring design. Consequently, the outcomes form this work could help to optimize oyster growth and harvest thus promoting economic sustainability in aquaculture.

The overall qualitative principles for floating oyster farm siting and management aiming to promote improved growth rates are as follows. Avoid placing a floating oyster farm in a shallow part of the estuary since strong bottom mixing might increase turbidity within the farm, which could potentially impact oyster growth. The farm should be placed where the net transport coincides with the transport of food, such as having farms placed where seaward net flows are dominant if plankton are prevalent upstream. Design the farm as a bluff (wide and short) layout. For farms where nutrient delivery is mainly through landward or seaward boundaries enlarging farm width, i.e., increasing number of longline across the estuary is more advisable than directly extending length of longlines for farm expansion. Therefore, the combination of field observations with numerical simulations provides scientific and feasible ways to guarantee both environmental and economic sustainability in future aquaculture development.

5.3. Future work

Since the existence of farm redistributed tidal flow, suppressed curvature driven lateral circulation, and altered subtidal flow, one of the implications is that the farm might potentially locally change the sediment transport in the estuary. Therefore, further field and modeling studies of aquaculture farm impacts on sediment transport are required to understand if floating oyster farms could cause deposition or erosion as well as the long-term changes in bathymetry. Although this work demonstrated that the farm induced low velocity zone was expanded to the channel, the farm induced vertical mixing right below the farm was still unknow in estuaries with stratification and periodic flows. Note that the farm induced flow reduction and redistribution could potentially modify the bottom boundary layer and stratification under the farm. Therefore, the interaction among the farm boundary layer, the bottom boundary layer and stratification

would be an important topic to study in the future. Field campaign to collect hydrographic and velocity microstructure data will be required to reveal the physics. Fine scale models such as large eddy simulation with computational fluid dynamic (LES/CFD) models are also applicable as a supplement.

From long-term perspective, a comprehensive hydro-biochemical-engineering modeling system for aquaculture would be valuable for aquaculture engineering. The development of aquaculture needs a combination of interdisciplinary tools to cover multiple aspects from biology to engineering. Handy tools have been developed in each discipline. It would be advantageous to integrate well developed models into a system, which can be applied for aquaculture siting, farm design and planning, production prediction as well as risk management. The modeling system would be applied to comprehensively investigate aquaculture resilience to changing environments such as changing local circulation patterns, temperature, pH, eutrophication, and hypoxia. Therefore, a systematic study of aquaculture resilience to potential climate change scenarios could benefit aquaculture sustainability in the coming future.

BIBLIOGRAPHY

Abdolahpour, M., Ghisalberti, M., Lavery, P., and McMahon, K. (2017). Vertical mixing in coastal canopies. *Limnology and Oceanography*, *62*(1), 26–42. https://doi.org/10.1002/lno.10368

Adams, C.M., Mayer, L.M., Rawson, P., Brady, D.C. and Newell, C., 2019. Detrital protein contributes to oyster nutrition and growth in the Damariscotta estuary, Maine, USA. *Aquaculture Environment Interactions*, *11*, pp.521-536.

Asher, S., Niewerth, S., Koll, K., and Shavit, U. (2016). Vertical variations of coral reef drag forces. *Journal of Geophysical Research: Oceans*, *121*, 3549–3563. https://doi.org/10.1002/2015JC011428

Aure, J., Strohmeier, T., and Strand, Ø. (2007). Modelling current speed and carrying capacity in long-line blue mussel (Mytilus edulis) farms. *Aquaculture Research*, *38*(3), 304–312. https://doi.org/10.1111/j.1365-2109.2007.01669.x

Barange, M., Bahri, T., Beveridge, M. C., Cochrane, K. L., Funge-Smith, S., and Poulain, F. (2018). Impacts of climate change on fisheries and aquaculture: synthesis of currrent knowledge, adaptation and mitigation options. FAO.

Barillé, L., Le Bris, A., Goulletquer, P., Thomas, Y., Glize, P., Kane, F., Falconer, L., Guillotreau, P., Trouillet, B., Palmer, S. and Gernez, P., 2020. Biological, socio-economic, and administrative opportunities and challenges to moving aquaculture offshore for small French oyster-farming companies. *Aquaculture*, *521*, p.735045.

Barillé, L., Lerouxel, A., Dutertre, M., Haure, J., Barillé, A.L., Pouvreau, S. and Alunno-Bruscia, M., 2011. Growth of the Pacific oyster (Crassostrea gigas) in a high-turbidity environment: comparison of model simulations based on scope for growth and dynamic energy budgets. *Journal of sea research*, *66*(4), pp.392-402.

Beard, K., Kimble, M., Yuan, J., Evans, K. S., Liu, W., Brady, D., and Moore, S., 2020: A Method for Heterogeneous Spatio-Temporal Data Integration in Support of Marine Aquaculture Site Selection. Journal of Marine Science and Engineering, 8(2), 96.

Bears, K., 2018, The dynamics of mixing and subtidal flow in a Maine Estuary. *Electronic Theses and Dissertations*. 2877. https://digitalcommons.library.umaine.edu/etd/2877

Beudin, A., Kalra, T. S., Ganju, N. K., and Warner, J. C. (2017). Development of a coupled wave-flow-vegetation interaction model. *Computers & Geosciences*, *100*, 76–86. https://doi.org/10.1016/j.cageo.2016.12.010

Blevins, R. D. 1984. *Applied fluid dynamics handbook*. New York, Van Nostrand Reinhold Co., 1984, 568 p.

Bricknell, I.R., Birkel, S.D., Brawley, S.H., Van Kirk, T., Hamlin, H., Capistrant-Fossa, K., Huguenard, K., Van Walsum, G.P., Liu, Z.L., Zhu, L.H. and Grebe, G., 2020: Resilience of cold water aquaculture: a review of likely scenarios as climate changes in the Gulf of Maine. *Reviews in Aquaculture*.

Campbell, M.D. and Hall, S.G., 2019. Hydrodynamic effects on oyster aquaculture systems: a review. *Reviews in Aquaculture*, *11*(3), pp.896-906.

Chant, R. J., 2002: Secondary circulation in a region of flow curvature: Relationship with tidal forcing and river discharge. *Journal of Geophysical Research: Oceans*, *107*(C9), 14-1.

Chandler, E. A., 2016, Sediment accumulations patterns in the Damariscotta River Estuary. *Electronic Theses and Dissertations*. 2470. https://digitalcommons.library.umaine.edu/etd/2470

Chen, W., and De Swart, H. E., 2016: Dynamic links between shape of the eddy viscosity profile and the vertical structure of tidal current amplitude in bays and estuaries. *Ocean Dynamics*, *66*(3), 299-312.

Collignon, A. G., and Stacey, M. T. (2013). Turbulence dynamics at the shoal-channel interface in a partially stratified estuary. *Journal of Physical Oceanography*, *43*(5), 970–989. https://doi.org/10.1175/JPO-D-12-0115.1

Cornejo, P., Sepúlveda, H. H., Gutiérrez, M. H., and Olivares, G. (2014). Numerical studies on the hydrodynamic effects of a salmon farm in an idealized environment. *Aquaculture*, *430*, 195–206. https://doi.org/10.1016/j.aquaculture.2014.04.015

Cortes-Garcia, Leon D., "Assessment of Helical Anchors Bearing Capacity for Offshore Aquaculture Applications" (2019). *Electronic Theses and Dissertations*. 3094. https://digitalcommons.library.umaine.edu/etd/3094

Dame, R.F. and Kenneth, M.J., 2011. *Ecology of marine bivalves: an ecosystem approach* (p. 284). Taylor & Francis.

Dame, R.F., Spurrier, J.D. and Zingmark, R.G., 1992. In situ metabolism of an oyster reef. *Journal of Experimental Marine Biology and Ecology*, *164*(2), pp.147-159.

Delaux, S., Stevens, C. L., and Popinet, S, 2011: High-resolution computational fluid dynamics modelling of suspended shellfish structures. *Environmental fluid mechanics*, *11*(4), 405-425.

Dewey, R. K., and Crawford, W. R. (1988). Bottom stress estimates from vertical dissipation rate profiles on the continental shelf. *Journal of Physical Oceanography*, *18*(8), 1167–1177. https://doi.org/10.1175/1520-0485(1988)018<1167:BSEFVD>2.0.CO;2

Drazin, P. G., Reid, W. H., 1981. Hydrodynamic stability.

Duarte, P., Alvarez-Salgado, X. A., Fernández-Reiriz, M. J., Piedracoba, S., and Labarta, U., 2014: A modeling study on the hydrodynamics of a coastal embayment occupied by mussel farms (Ria de Ares-Betanzos, NW Iberian Peninsula). *Estuarine, Coastal and Shelf Science*, *147*, 42-55.

Ehrich, M.K. and Harris, L.A., 2015. A review of existing eastern oyster filtration rate models. *Ecological Modelling*, *297*, pp.201-212.

Fan, X., Wei, H., Yuan, Y., and Zhao, L. (2009). Vertical structure of tidal current in a typically coastal raft-culture area. *Continental Shelf Research*, *29*(20), 2345–2357. https://doi.org/10.1016/j.csr.2009.10.007

Ferreira, J.G., Hawkins, A.J.S. and Bricker, S.B., 2007. Management of productivity, environmental effects and profitability of shellfish aquaculture—the Farm Aquaculture Resource Management (FARM) model. *Aquaculture*, *264*(1-4), pp.160-174.

Filgueira, R., Comeau, L.A., Guyondet, T., McKindsey, C.W. and Byron, C.J., 2015. *Modelling carrying capacity of bivalve aquaculture: a review of definitions and methods*. Fisheries and Oceans Canada, Ecosystems and Oceans Science.

Filgueira, R., Grant, J., Bacher, C. and Carreau, M., 2012. A physical–biogeochemical coupling scheme for modeling marine coastal ecosystems. *Ecological Informatics*, *7*(1), pp.71-80.

Food and Agriculture Organization. (2013). The State of Food and Agriculture 2013: Food Systems for Better Nutrition. Food Agriculture Organization (FAO).

Food and Agriculture Organization, 2018: The State of World Fisheries and Aquaculture 2018 - Meeting the sustainable development goals (Report No. ISBN 978-92-5-130562-1). Report by United Nations (UN).

Food and Agriculture Organization. 2020. The State of World Fisheries and Aquaculture 2020. Sustainability in action. Rome.

Fredriksson, D. W., Muller, E., Baldwin, K., Robinson Swift, M., and Celikkol, B, 2000: Open ocean aquaculture engineering: system design and physical modeling. *Marine Technology Society Journal*, *34*(1), 41-52.

Friedrichs, C. T., and Hamrick, J. M., 1996: Effects of channel geometry on cross-sectional variations in along-channel velocity in partially stratified estuaries. *Coastal and Estuarine Studies*, 283-300.

Gangnery, A., Chabirand, J.M., Lagarde, F., Le Gall, P., Oheix, J., Bacher, C. and Buestel, D., 2003. Growth model of the Pacific oyster, Crassostrea gigas, cultured in Thau Lagoon (Méditerranée, France). *Aquaculture*, *215*(1-4), pp.267-290.

Gaurier, B., Germain, G., Kervella, Y., Davourie, J., Cayocca, F., and Lesueur, P. (2011). Experimental and numerical characterization of an oyster farm impact on the flow. *European Journal of Mechanics - B/Fluids*, *30*(5), 513–525. https://doi.org/10.1016/jeuromechflu.2011.05.001

Gaylord, B., Denny, M. W., and Koehl, M. A. R. (2008). Flow forces on seaweeds: Field evidence for roles of wave impingement and organism inertia. *The Biological Bulletin*, *215*(3), 295–308. https://doi.org/10.2307/25470713

Gernez P, Doxaran D and Barillé L (2017) Shellfish Aquaculture from Space: Potential of Sentinel2 to Monitor Tide-Driven Changes in Turbidity, Chlorophyll Concentration and Oyster Physiological Response at the Scale of an Oyster Farm. *Front. Mar. Sci.* 4:137. doi: 10.3389/fmars.2017.00137

Ghisalberti, M., and Nepf, H. M., 2002: Mixing layers and coherent structures in vegetated aquatic flows. *Journal of Geophysical Research: Oceans*, *107*(C2), 3-1.

Ghisalberti, M., and Nepf, H. M. (2004). The limited growth of vegetated shear layers. *Water Resources Research*, *40*, W07502. https://doi.org/ 10.1029/2003WR002776

Gohin, F., 2011. Annual cycles of chlorophyll-a, non-algal suspended particulate matter, and turbidity observed from space and in-situ in coastal waters. *Ocean Science*, *7*(5), pp.705-732.

Goodman, L., Levine, E. R., and Lueck, R. G. (2006). On measuring the terms of the turbulent kinetic energy budget from an AUV. *Journal of Atmospheric and Oceanic Technology*, *23*(7), 977–990. https://doi.org/10.1175/JTECH1889.1

Grant, J., and Bacher, C. (2001). A numerical model of flow modification induced by suspended aquaculture in a Chinese bay. *Canadian Journal of Fisheries and Aquatic Sciences*, *58*(5), 1003-1011. https://doi.org/10.1139/f01-027

Grant, J. and Filgueira, R., 2011. The application of dynamic modeling to prediction of production carrying capacity in shellfish farming. *Shellfish aquaculture and the environment*, pp.135-154.

Griffies, S. M., Gnanadesikan, A., Pacanowski, R. C., Larichev, V., Dukowicz, J. K., and Smith, R. D. (1998). Isoneutral diffusion in a *z*-coordinate ocean model. *Journal of Physical Oceanography*, *28*(5), 805–830. https://doi.org/10.1175/1520-0485(1998)028<0805: IDIAZC>2.0.CO;2

Grizzle, R.E., Greene, J.K. and Coen, L.D., 2008. Seston removal by natural and constructed intertidal eastern oyster (Crassostrea virginica) reefs: a comparison with previous laboratory studies, and the value of in situ methods. *Estuaries and coasts*, *31*(6), pp.1208-1220.

Guerra, M., and Thomson, J. (2017). Turbulence measurements from five-beam acoustic Doppler current profilers. *Journal of Atmospheric and Oceanic Technology*, *34*(6), 1267–1284. https://doi.org/10.1175/JTECH-D-16-0148.1

Han, L., Zeng, Y., Chen, L., and Li, M. (2018). Modeling streamwise velocity and boundary shear stress of vegetation-covered flow. *Ecological Indicators*, *92*, 379–387. https://doi.org/10.1016/j.ecolind.2017.04.012

Hawkins, A.J.S., Pascoe, P.L., Parry, H., Brinsley, M., Black, K.D., McGonigle, C., Moore, H., Newell, C.R., O'Boyle, N., Ocarroll, T. and O'Loan, B., 2013. Shellsim: a generic model of growth and environmental effects validated across contrasting habitats in bivalve shellfish. *Journal of Shellfish Research*, *32*(2), pp.237-253.

http://functions.wolfram.com/HypergeometricFunctions/LegendreQGeneral/26/01/01/

https://www1.maine.gov/dmr/aquaculture/data/documents/americanoyster2005-19.pdf

Huai, W., Hu, Y., Zeng, Y., and Han, J., 2012: Velocity distribution for open channel flows with suspended vegetation. *Advances in Water Resources*, *49*, 56-61.

Huai, W., and Li, C. (2016). Longitudinal dispersion in open channel flow with suspended canopies. *Water Science and Technology*, *74*(3), 722–728. https://doi.org/10.2166/wst.2016.236

Huguenard, K., Bears, K., and Lieberthal, B. (2019). Intermittency in estuarine turbulence: A framework toward limiting bias in microstructure measurements. *Journal of Atmospheric and Oceanic Technology*, *36*(10), 1917–1932. https://doi.org/10.1175/JTECH-D-180220.1

Huguenard, K. D., Valle-Levinson, A., Li, M., Chant, R. J., and Souza, A. J. (2015). Linkage between lateral circulation and near-surface vertical mixing in a coastal plain estuary. *Journal of Geophysical Research: Oceans*, *120*, 4048–4067. https://doi.org/10.1002/ 2014JC010679.

Huijts, K. M. H., Schuttelaars, H. M., De Swart, H. E., and Friedrichs, C. T., 2009: Analytical study of the transverse distribution of along-channel and transverse residual flows in tidal estuaries. *Continental Shelf Research*, *29*(1), 89-100.

Ilıcak, M., Özgökmen, T.M., Peters, H., Baumert, H.Z. and Iskandarani, M., 2008. Performance of two-equation turbulence closures in three-dimensional simulations of the Red Sea overflow. *Ocean Modelling*, *24*(3-4), pp.122-139. https://doi.org/10.1016/jocemod.2008.06.001

Johansson, D., Juell, J. E., Oppedal, F., Stiansen, J. E., and Ruohonen, K. (2007). The influence of the pycnocline and cage resistance on current flow, oxygen flux and swimming behaviour of Atlantic salmon (Salmo salar L.) in production cages. *Aquaculture*, *265*(1-4), 271–287. https://doi.org/10.1016/j.aquaculture.2006.12.047

Kalkwijk, J. P. T., and Booij, R. (1986). Adaptation of secondary flow in nearly-horizontal flow. *Journal of Hydraulic Research*, *24*(1), 19–37. https://doi.org/10.1080/00221688609499330

Kay, D. J., and Jay, D. A. (2003). Interfacial mixing in a highly stratified estuary 1. Characteristics of mixing. *Journal of Geophysical Research*, *108*(C3), 3072. https://doi.org/10.1029/2000JC000252

Kervella, Y., Germain, G., Gaurier, B., Facq, J., Cayocca, F., Lesueur, P., 2009. Boundary layer development and shear stresses measurements around oysters tables. AMT, 9, 358–368.

Kervella, Y., Germain, G., Gaurier, B., Facq, J. V., Cayocca, F., and Lesueur, P. (2010). Experimental study of the near-field impact of an oyster table on the flow. *European Journal of Mechanics - B/Fluids*, *29*(1), 32–42. https://doi.org/10.1016/j.euromechflu.2009.09.002

Konstantinou, Z. I., Kombiadou, K., and Krestenitis, Y. N. (2015). Effective mussel-farming governance in Greece: Testing the guidelines through models, to evaluate sustainable management alternatives. *Ocean & Coastal Management*, *118*, 247-258.

Konstantinou, Z. I., and Kombiadou, K. (2020). Rethinking suspended mussel-farming modelling: Combining hydrodynamic and bio-economic models to support integrated aquaculture management. *Aquaculture*, 735179.

Lenihan, H.S., 1999. Physical–biological coupling on oyster reefs: how habitat structure influences individual performance. *Ecological Monographs*, *69*(3), pp.251-275.

Lentz, S. J., Davis, K. A., Churchill, J. H., and DeCarlo, T. M. (2017). Coral reef drag coefficients—Water depth dependence. *Journal of Physical Oceanography*, *47*(5), 1061–1075. https://doi.org/10.1175/JPO-D-16-0248.1

Lerczak, J. A., and Rockwell Geyer, W. (2004). Modeling the lateral circulation in straight, stratified estuaries. *Journal of Physical Oceanography*, *34*(6), 1410–1428. https://doi.org/10.1175/1520-0485(2004)034<1410:MTLCIS>2.0.CO;2

Li, C., and O'Donnell, J., 2005: The effect of channel length on the residual circulation in tidally dominated channels. *Journal of Physical Oceanography*, *35*(10), 1826-1840.

Li, L. and Li, Q., 2010. Effects of stocking density, temperature, and salinity on larval survival and growth of the red race of the sea cucumber Apostichopus japonicus (Selenka). *Aquaculture International*, *18*(3), pp.447-460.

Li, M., Cheng, P., Chant, R., Valle-Levinson, A., and Arnott, K. (2014). Analysis of vortex dynamics of lateral circulation in a straight tidal estuary. *Journal of Physical Oceanography*, *44*(10), 2779–2795. https://doi.org/10.1175/JPO-D-13-0212.1

Li, S., Katul, G., and Huai, W., 2019: Mean velocity and shear stress distribution in floating treatment wetlands: An analytical study. *Water Resources Research*, *55*(8), 6436-6449.

Lieberthal, B., Huguenard, K., Ross, L., and Bears, K., 2019a: The generation of overtides in flow around a headland in a low inflow estuary. *Journal of Geophysical Research: Oceans*, *124*(2), 955-980.

Lieberthal, B., Huguenard, K., Ross, L., and Liu, Z., 2019b: Intratidal Variability of Water Quality in the Damariscotta River, Maine. *Water*, *11*(12), 2603. https://doi.org/10.3390/w11122603

Lin, J., Li, C., and Zhang, S., 2016: Hydrodynamic effect of a large offshore mussel suspended aquaculture farm. *Aquaculture*, *451*, 147-155.

Lin, F., Du, M., Liu. H., Fang, J., Asplin, L., Jiang, Z. 2020. A physical-biological coupled ecosystem model for integrated aquaculture of bivalve and seaweed in sanggou bay. *Ecological Modelling*, *431*, 109181. https://doi.org/10.1016/j.ecolmodel.2020.109181.

Lin, J., Li, C., and Zhang, S. (2016). Hydrodynamic effect of a large offshoal mussel suspended aquaculture farm. *Aquaculture*, *451*, 147–155. https://doi.org/10.1016/j.aquaculture.2015.08.039

Liu, Z., and Huguenard, K., 2020: Hydrodynamic response of a floating aquaculture farm in a low inflow estuary. *Journal of Geophysical Research: Oceans*, *125*(5), e2019JC015625.

Luckenbach, M., Mann, R.L. and Wesson, J.A., 1999. Oyster reef habitat restoration: a synopsis and synthesis of approaches; proceedings from the symposium, Williamsburg, Virginia, April 1995.

Lueck, R. G., 2013. Calculating the rate of dissipation of turbulent kinetic energy. *Rockland Scientific International Tech. Note TN-028*.

Lueck, R. G., Wolk, F., and Yamazaki, H. (2002). Oceanic velocity microstructure measurements in the 20th century. *Journal of Oceanography*, *58*(1), 153–174. https://doi.org/10.1023/A:1015837020019

McDonald, C. B., Koseff, J. R., and Monismith, S. G. (2006). Effects of the depth to coral height ratio on drag coefficients for unidirectional flow over coral. *Limnology and Oceanography*, *51*(3), 1294–1301. https://doi.org/10.4319/lo.2006.51.3.1294

McSweeney, J. M., Chant, R. J., and Sommerfield, C. K. (2016). Lateral variability of sediment transport in the Delaware estuary. *Journal of Geophysical Research: Oceans*, *121*, 725–744. https://doi.org/10.1002/2015JC010974

Mizuta, D. D., Wikfors, G. H., 2019. Depth selection and in situ validation for offshore mussel aquaculture in northeast United States federal waters. *Journal of Marine Science and Engineering*, *7*(9), 293.

Mustafa, S., Estim, A., Al-Azad, S., Shaleh, S. R. M., and Shapawi, R. (2017). Aquaculture sustainability: Multidisciplinary perspectives and adaptable models for seafood security. *Journal of Fisheries Aquaculture Development*, *2017*(06), JFAD-126. https://doi.org/10.29011/ JFAD-126/100026

Newell, C.R., Brady, D.C. and Richardson, J., 2019. Farm-scale production models. In *Goods and Services of Marine Bivalves* (pp. 485-506). Springer, Cham.

Newell, C.R., Hawkins, A.J., Morris, K., Richardson, J., Davis, C. and Getchis, T., 2013. ShellGIS: a dynamic tool for shellfish farm site selection. *World Aquacult*, *44*, pp.50-53.

Nguyen, N.Q., Thiagarajan, K. and Auger, J., 2019. Integrity assessment of an oyster farm mooring system through in-situ measurements and extreme environment modeling. *Ocean Engineering*, *172*, pp.641-659.

Nunes, J. P., Ferreira, J. G., Gazeau, F., Lencart-Silva, J., Zhang, X. L., Zhu, M. Y., and Fang, J. G., 2003: A model for sustainable management of shellfish polyculture in coastal bays. *Aquaculture*, *219*(1-4), 257-277.

O'Connor, W.A. and Lawler, N.F., 2004. Salinity and temperature tolerance of embryos and juveniles of the pearl oyster, Pinctada imbricata Röding. *Aquaculture*, *229*(1-4), pp.493-506.

O'Donncha, F., Hartnett, M., and Nash, S. (2013). Physical and numerical investigation of the hydrodynamic implications of aquaculture farms. *Aquacultural Engineering*, *52*, 14–26. https://doi.org/10.1016/j.aquaeng.2012.07.006

O'Donncha, F., James, S. C., and Ragnoli, E. (2017). Modelling study of the effects of suspended aquaculture installations on tidal stream generation in Cobscook Bay. *Renewable Energy*, *102*, 65–76. https://doi.org/10.1016/j.renene.2016.10.024

Osorio-Cano, J., Osorio, A., and Oumeraci, H. (2016). Laboratory study of drag and inertia forces on a branched coral colony of acropora palmata. In *Proceedings of the 6th International Conference on the Application of Physical Modelling in Coastal and Port Engineering and Science (Coastlab16)* (pp. 1–10). Ghent: Ghent University.

Pernet, F., Lupo, C., Bacher, C. and Whittington, R.J., 2016. Infectious diseases in oyster aquaculture require a new integrated approach. *Philosophical Transactions of the Royal Society B: Biological Sciences*, *371*(1689), p.20150213.

Peters, H. (1997). Observations of stratified turbulent mixing in an estuary: Neap-to-spring variations during high river flow. *Estuarine, Coastal and Shelf Science*, *45*(1), 69–88. https://doi.org/10.1006/ecss.1996.0180

Peters, H., Baumert, H., and Jacob, J. P. (2005). Partially mixed estuaries: The Hudson River. In *Marine turbulence, theories, observations and models* (pp. 324–333). Cambridge: Cambridge University Press.

Peters, H., Gregg, M. C., and Toole, J. M. (1988). On the parameterization of equatorial turbulence. *Journal of Geophysical Research*, *93*(C2), 1199–1218. https://doi.org/10.1029/JC093iC02p01199

Plew, D. R. (2011a). Depth-averaged drag coefficient for modeling flow through suspended canopies. *Journal of Hydraulic Engineering*, *137*(2), 234–247. https://doi.org/10.1061/(ASCE)HY.1943-7900.0000300

Plew, D. R. (2011b). Shellfish farm-induced changes to tidal circulation in an embayment, implications for seston depletion. *Aquaculture Environment Interactions*, *1*(3), 201–214. https://doi.org/10.3354/aei00020

Plew, D. R., Enright, M. P., Nokes, R. I., and Dumas, J. K. (2009). Effect of mussel bio-pumping on the drag on and flow around a mussel crop rope. *Aquacultural Engineering*, *40*(2), 55–61. https://doi.org/10.1016/j.aquaeng.2008.12.003

Plew, D. R., Spigel, R. H., Stevens, C. L., Nokes, R. I., and Davidson, M. J. (2006). Stratified flow interactions with a suspended canopy.*Environmental Fluid Mechanics*, *6*(6), 519–539. https://doi.org/10.1007/s10652-006-9008-1

Plew, D. R., Stevens, C. L., Spigel, R. H., and Hartstein, N. D. (2005). Hydrodynamic implications of large offshore mussel farms. *IEEE Journal of Oceanic Engineering*, *30*(1), 95–108. https://doi.org/10.1109/JOE.2004.841387

Poizot, E., Méar, Y., Guillou, S. and Bibeau, E., 2021. High resolution characteristics of turbulence tied of a fish farm structure in a tidal environment. *Applied Ocean Research*, *108*, p.102541.

Qiao, J. D., Delavan, S. K., Nokes, R. I., and Plew, D. R. (2016). Flow structure and turbulence characteristics downstream of a spanwise suspended linear array. *Environmental Fluid Mechanics*, *16*(5), 1021–1041. https://doi.org/10.1007/s10652-016-9465-0

Reid, G. K., Lefebvre, S., Filgueira, R., Robinson, S. M., Broch, O. J., Dumas, A., and Chopin, T. B. (2020). Performance measures and models for open-water integrated multi-trophic aquaculture. *Reviews in Aquaculture*, *12*(1), 47-75.

Reidenbach, M. A., Monismith, S. G., Koseff, J. R., Yahel, G., and Genin, A. (2006). Boundary layer turbulence and flow structure over a fringing coral reef. *Limnology and Oceanography*, *51*(5), 1956–1968. https://doi.org/10.4319/lo.2006.51.5.1956

Robinson, I. S., 1983: Tidally induced residual flow. *Physical Oceanography of Coastal and Shelf Seas*, B. Johns, Ed., Elsevier, 321–356.

Rosman, J. H., and Hench, J. L. (2011). A framework for understanding drag parameterizations for coral reefs. *Journal of Geophysical Research*, *116*, C08025. https://doi.org/10.1029/2010JC006892

Rosman, J. H., Koseff, J. R., Monismith, S. G., and Grover, J. (2007). A field investigation into the effects of a kelp forest (Macrocystis pyrifera) on coastal hydrodynamics and transport. *Journal of Geophysical Research*, *112*, C02016. https://doi.org/10.1029/2005JC003430

Ross, L., de Swart, H., Ensing, E., and Valle-Levinson, A., 2017: Three-dimensional tidal flow in a fjord-like basin with converging width: An analytical model. *Journal of Geophysical Research: Oceans*, *122*(9), 7558-7576.

Scully, M.E. and Friedrichs, C.T., 2007. Sediment pumping by tidal asymmetry in a partially mixed estuary. *Journal of Geophysical Research: Oceans*, *112*(C7).

Scully, M. E., Geyer, W. R., and Lerczak, J. A. (2009). The influence of lateral advection on the residual estuarine circulation: A numerical modeling study of the Hudson River estuary. *Journal of Physical Oceanography*, *39*(1), 107–124. https://doi.org/10.1175/ 2008JPO3952.1

Shaw, W. J., Trowbridge, J. H., and Williams, A. J. (2001). Budgets of turbulent kinetic energy and scalar variance in the continental shelf bottom boundary layer. *Journal of Geophysical Research*, *106*(C5), 9551–9564. https://doi.org/10.1029/2000JC000240

Shchepetkin, A. F., and McWilliams, J. C. (2005). The regional oceanic modeling system (ROMS): A split-explicit, free-surface, topography-following-coordinate oceanic model. *Ocean Modelling*, *9*(4), 347–404. https://doi.org/10.1016/j.ocemod.2004.08.002

Shchepetkin, A. F., and McWilliams, J. C. (2009). Correction and commentary for "ocean forecasting in terrain-following coordinates: Formulation and skill assessment of the regional ocean modeling system" by Haidvogel et al., J. comp. Phys. 227, pp. 3595–3624. *Journal of Computational Physics*, *228*(24), 8985–9000. https://doi.org/10.1016/j.jcp.2009.09.002

Shi, J., Wei, H., Zhao, L., Yuan, Y., Fang, J., and Zhang, J., 2011: A physical–biological coupled aquaculture model for a suspended aquaculture area of China. *Aquaculture*, *318*(3-4), 412-424.

Shih, L. H., Koseff, J. R., Ferziger, J. H., and Rehmann, C. R. (2000). Scaling and parameterization of stratified homogeneous turbulent shear flow. *Journal of Fluid Mechanics*, *412*, 1–20. https://doi.org/10.1017/S0022112000008405

Silva, E., Garbossa, L. H. P., Nuñer, A. P. O., and Lapa, K. R., 2019: Hydrodynamic modelling of the dispersion and deposition of biodeposits from marine bivalve mollusc farming under neap and spring tides in Santa Catarina Island Bays. *Aquaculture*, *501*, 507-514.

Sreenivasan, K. R. (1995). On the universality of the Kolmogorov constant. *Physics of Fluids*, *7*(11), 2778–2784. https://doi.org/10.1063/1.868656

Stacey, M. T., Burau, J. R., and Monismith, S. G., 2001: Creation of residual flows in a partially stratified estuary. *Journal of Geophysical Research: Oceans*, *106*(C8), 17013-17037.

Stacey, M. T., Monismith, S. G., and Burau, J. R. (1999). Measurements of Reynolds stress profiles in unstratified tidal flow. *Journal of Geophysical Research*, *104*(C5), 10,933–10,949. https://doi.org/10.1029/1998JC900095

Stevens, C., Plew, D., Hartstein, N., and Fredriksson, D., 2008: The physics of open-water shellfish aquaculture. *Aquacultural Engineering*, *38*(3), 145-160.

Stevens, C. L., and Petersen, J. K. (2011). Turbulent, stratified flow through a suspended shellfish canopy: Implications for mussel farm design. *Aquaculture Environment Interactions*, *2*(1), 87–104. https://doi.org/10.3354/aei00033

Stips, H. (2005). Dissipation measurement: Theory. In H. Baumert, J. Simpson, and J. Sündermann (Eds.), *Marine turbulence, theories, observations and models* (pp. 115–126). Cambridge, UK: Cambridge University Press.

Sun, K., Zhang, J., Lin, F., Ren, J. S., Zhao, Y., Wu, W., and Liu, Y., 2020: Evaluating the influences of integrated culture on pelagic ecosystem by a numerical approach: A case study of Sungo Bay, China. *Ecological Modelling*, *415*, 108860.

Tarya, A., Hoitink, A. J. F., and Van der Vegt, M. (2010). Tidal and subtidal flow patterns on a tropical continental shelf semi-insulated by coral reefs. *Journal of Geophysical Research*, *115*, C09029. https://doi.org/10.1029/2010JC006168

The World Bank, 2014, Sustainable Aquaculture. https://www.worldbank.org/en/topic/environment/brief/sustainable-aquaculture.

Thorpe, S. A. (2005). *The turbulent ocean*. Cambridge: Cambridge University Press.

Tjernström, M. (1993). Turbulence length scales in stably stratified free shear flow analyzed from slant aircraft profiles. *Journal of Applied Meteorology*, *32*(5), 948–963. https://doi.org/10.1175/1520-0450(1993)032<0948:TLSISS>2.0.CO;2

Tseung, H. L., Kikkert, G. A., and Plew, D. (2016). Hydrodynamics of suspended canopies with limited length and width. *Environmental Fluid Mechanics*, *16*(1), 145–166. https://doi.org/10.1007/s10652-015-9419-y

United Nations General Assembly (2005). 2005 World Summit Outcome, Resolution A/60/1, adopted by the General Assembly on 15 September 2005. Retrieved on: 17 February 2009.

Valle-Levinson, A., Reyes, C., Sanay, R., 2003. Effects of bathymetry friction and rotation on estuary-ocean exchange. Journal of Physical Oceanography 33, 2375–2393.

Wang, B., Cao, L., Micheli, F., Naylor, R. L., and Fringer, O. B. (2018). The effects of intensive aquaculture on nutrient residence time and transport in a coastal embayment. *Environmental Fluid Mechanics*, *18*(6), 1321–1349. https://doi.org/10.1007/s10652-0189595-7

Weitzman, J., and Filgueira, R. (2020). The evolution and application of carrying capacity in aquaculture: towards a research agenda. *Reviews in Aquaculture*, *12*(3), 1297-1322.

Whitman, E. R., and Reidenbach, M. A. (2012). Benthic flow environments affect recruitment of Crassostrea virginica larvae to an intertidal oyster reef. *Marine Ecology Progress Series*, *463*, 177–191. https://doi.org/10.3354/meps09882

Wijesekera, H. W., Jarosz, E., Teague, W. J., Wang, D. W., Fribance, D. B., Moum, J. N., and Warner, S. J. (2014). Measurements of form and frictional drags over a rough topographic bank. *Journal of Physical Oceanography*, *44*(9), 2409-2432. https://doi.org/10.1175/JPO-D-130230.1

Winant, C. D., 2007: Three-dimensional tidal flow in an elongated, rotating basin, J. Phys. Oceanogr., 37, 2345–2362, doi:10.1175/ JPO3122.1.

Winant, C. D., 2008: Three-dimensional residual tidal circulation in an elongated, rotating basin. *Journal of Physical Oceanography*, *38*(6), 1278-1295.

Wong, K.C., 1994. On the nature of transverse variability in a coastal plain estuary. Journal of Geophysical Research 99C7, 14,209–14,222.

Wu, Y., Chaffey, J., Law, B., Greenberg, D. A., Drozdowski, A., Page, F., and Haigh, S. (2014). A three-dimensional hydrodynamic model for aquaculture: A case study in the bay of Fundy. *Aquaculture Environment Interactions*, *5*(3), 235–248. https://doi.org/10.3354/aei00108

Wu, Y., Hannah, C. G., O'Flaherty-Sproul, M., and Thupaki, P. (2017). Representing kelp forests in a tidal circulation model. *Journal of Marine Systems*, *169*, 73–86. https://doi.org/10.1016/j.jmarsys.2016.12.007

Zeng, D., Huang, D., Qiao, X., He, Y., and Zhang, T. (2015). Effect of suspended kelp culture on water exchange as estimated by in situ current measurement in Sanggou Bay, China. *Journal of Marine Systems*, *149*, 14–24. https://doi.org/10.1016/j.jmarsys.2015.04.002

Zhang, Z., Huang, H., Liu, Y., Bi, H., and Yan, L., 2020: Numerical study of hydrodynamic conditions and sedimentary environments of the suspended kelp aquaculture area in Heini Bay. *Estuarine, Coastal and Shelf Science*, *232*, 106492.

Zhao, F., Huai, W., and Li, D. (2017). Numerical modeling of open channel flow with suspended canopy. *Advances in Water Resources*, *105*,132–143. https://doi.org/10.1016/j.advwatres.2017.05.001

Zitman, T. J., and Schuttelaars, H. M., 2012: Importance of cross-channel bathymetry and eddy viscosity parameterisation in modelling estuarine flow. *Ocean Dynamics*, *62*(4), 603-631.

APPEDIX: A

A DEPATH AVERAGED MOMENTUM EQUATION

A.1 Depth integrated momentum equation

The conservative form of Reynolds-averaged Navier-Stokes equation for estuarine dynamics is

$$\frac{\partial u}{\partial t}+\frac{\partial u^2}{\partial x}+\frac{\partial (uv)}{\partial y}+\frac{\partial (uw)}{\partial z}=fv-g\frac{\partial \eta}{\partial x}-\frac{g}{\rho_0}\int_z^0\frac{\partial \rho}{\partial x}dz-\frac{\partial\left(\overline{u'w'}\right)}{\partial z} \qquad (A1.a)$$

$$\frac{\partial v}{\partial t}+\frac{\partial (uv)}{\partial x}+\frac{\partial v^2}{\partial y}+\frac{\partial (vw)}{\partial z}=-fu-g\frac{\partial \eta}{\partial y}-\frac{g}{\rho_0}\int_z^0\frac{\partial \rho}{\partial y}dz-\frac{\partial\left(\overline{v'w'}\right)}{\partial z} \quad (A1.b)$$

The corresponding terms are local acceleration, advection acceleration, Coriolis force, barotropic pressure gradient and baroclinc pressure gradient and Reynolds stress divergence. Integrate equation A1(a) and (b) from certain bottom location z = z_0 to certain subsurface location z = z_1. In the *x*-direction

$$\int_{z_0}^{z_1}\frac{\partial u}{\partial t}dz+\int_{z_0}^{z_1}\frac{\partial u^2}{\partial x}dz+\int_{z_0}^{z_1}\frac{\partial (uv)}{\partial y}dz+\int_{z_0}^{z_1}\frac{\partial (uw)}{\partial z}dz$$
$$=f\int_{z_0}^{z_1}vdz-g\int_{z_0}^{z_1}\frac{\partial \eta}{\partial x}dz-\frac{g}{\rho_0}\int_{z_0}^{z_1}\left(\int_z^0\frac{\partial \rho}{\partial x}dz\right)dz-\int_{z_0}^{z_1}\frac{\partial\left(\overline{u'w'}\right)}{\partial z}dz \qquad (A2)$$

Applying Newton- Leibniz integral rule,

$$\int_{z_0}^{z_1}\frac{\partial u}{\partial t}dz=\frac{\partial}{\partial t}\int_{z_0}^{z_1}udz-u|_{z=z_1}\frac{\partial z_1}{\partial t}+u|_{z=z_0}\frac{\partial z_0}{\partial t} \qquad (A3)$$

$$\int_{z_0}^{z_1}\frac{\partial u^2}{\partial x}dz=\frac{\partial}{\partial x}\int_{z_0}^{z_1}u^2dz-u^2|_{z=z_1}\frac{\partial z_1}{\partial x}+u^2|_{z=z_0}\frac{\partial z_0}{\partial x} \qquad (A4)$$

$$\int_{z_0}^{z_1}\frac{\partial (uv)}{\partial y}dz=\frac{\partial}{\partial y}\int_{z_0}^{z_1}(uv)dz-(uv)|_{z=z_1}\frac{\partial z_1}{\partial y}+(uv)|_{z=z_0}\frac{\partial z_0}{\partial y} \qquad (A5)$$

Since g and $\frac{\partial \eta}{\partial x}$ are independent on depth, the barotropic term becomes:

$$\int_{z_0}^{z_1} g \frac{\partial \eta}{\partial x} dz = g(z_1 - z_0) \frac{\partial \eta}{\partial x} \quad \text{(A6)}$$

The stress term becomes

$$\int_{z_0}^{z_1} \frac{\partial(\overline{u'w'})}{\partial z} dz = \overline{u'w'}\big|_{z=z_1} - \overline{u'w'}\big|_{z=z_0} \quad \text{(A7)}$$

Substitute equation A3 ~ A7 into equation A2 and recognize the equation, we get

$$\begin{aligned} &\frac{\partial}{\partial t}\int_{z_0}^{z_1} u dz + \frac{\partial}{\partial x}\int_{z_0}^{z_1} u^2 dz + \frac{\partial}{\partial y}\int_{z_0}^{z_1} (uv) dz + u|_{z=z_0}\left(\frac{\partial z_0}{\partial t} + u|_{z=z_0}\frac{\partial z_0}{\partial x} + v|_{z=z_0}\frac{\partial z_0}{\partial y} - w|_{z=z_0}\right) \\ &\quad - u|_{z=z_1}\left(\frac{\partial z_1}{\partial t} - u|_{z=z_1}\frac{\partial z_1}{\partial x} - v|_{z=z_1}\frac{\partial z_1}{\partial y} - w|_{z=z_1}\right) \\ &\quad = f\int_{z_0}^{z_1} v dz - g(z_1 - z_0)\frac{\partial \eta}{\partial x} - \frac{g}{\rho_0}\int_{z_0}^{z_1}\int_{z}^{0}\frac{\partial \rho}{\partial x} dz dz - \overline{u'w'}\big|_{z=z_1} \\ &\quad + \overline{u'w'}\big|_{z=z_0} \end{aligned} \quad \text{(A8)}$$

At each vertical layer, the kinetics of the tidal wave follows:

$$\begin{cases} \dfrac{\partial z_0}{\partial t} + u|_{z=z_0}\dfrac{\partial z_0}{\partial x} + v|_{z=z_0}\dfrac{\partial z_0}{\partial y} - w|_{z=z_0} = 0 \\ \dfrac{\partial z_1}{\partial t} + u|_{z=z_1}\dfrac{\partial z_1}{\partial x} + v|_{z=z_1}\dfrac{\partial z_1}{\partial y} - w|_{z=z_1} = 0 \end{cases} \quad \text{(A9)}$$

The derivation for y-direction is similar. Consequently, the depth integrated equations, i.e., momentum flux equations show in equation A10. Note that these equations are in conservative form which considers the vertical variance in velocity *u* and *v* and avoids vertically uniform velocity assumption during the derivation.

$$\underbrace{\frac{\partial}{\partial t}\int_{z_0}^{z_1} u dz}_{M_{x1}} + \underbrace{\frac{\partial}{\partial x}\int_{z_0}^{z_1} u^2 dz + \frac{\partial}{\partial y}\int_{z_0}^{z_1} (uv) dz}_{M_{x2}} = \underbrace{f\int_{z_0}^{z_1} v dz}_{M_{x3}} \underbrace{- g(z_1 - z_0)\frac{\partial \eta}{\partial x}}_{M_{x4}} \underbrace{- \frac{g}{\rho}\int_{z_0}^{z_1}\int_{z}^{0} \frac{\partial \rho}{\partial x} dz dz}_{M_{x5}} \underbrace{- \overrightarrow{u'w'}|_{z=z_1}}_{M_{x6}} + \underbrace{\overrightarrow{u'w'}|_{z=z_0}}_{M_{x7}} \quad \text{(A10. a)}$$

$$\underbrace{\frac{\partial}{\partial t}\int_{z_0}^{z_1} v dz}_{M_{y1}} + \underbrace{\frac{\partial}{\partial x}\int_{z_0}^{z_1} (uv) dz + \frac{\partial}{\partial y}\int_{z_0}^{z_1} v^2 dz}_{M_{y2}} = \underbrace{-f\int_{z_0}^{z_1} u dz}_{M_{y3}} \underbrace{- g(z_1 - z_0)\frac{\partial \eta}{\partial y}}_{M_{y4}} \underbrace{- \frac{g}{\rho}\int_{z_0}^{z_1}\int_{z}^{0} \frac{\partial \rho}{\partial y} dz dz}_{M_{y5}} \underbrace{- \overline{v'w'}\big|_{z=z_1}}_{M_{y6}} + \underbrace{\overline{v'w'}\big|_{z=z_0}}_{M_{y7}} \quad \text{(A10. b)}$$

where, M_{x1} and M_{y1} are local accelerations, M_{x2} and M_{y2} are advection terms, M_{x3} and M_{y3} are Coriolis force, M_{x4} and M_{y4} are barotropic pressure gradient, M_{x5} and M_{y5} are baroclinic pressure gradient, M_{x6} and M_{y6} are surface friction, M_{x7} and M_{y7} are bottom friction.

A.2 Transformation from east-north coordinate system to along and across channel coordinate system

Velocity data were collected under east-north (*x*-*y*) coordinate system. A right-hand, orthogonal, curvilinear coordinate system was defined at each data collection station with one coordinate direction pointing in the along channel direction (s) and the other pointing in the across-channel direction (n) (Fig. A1). Rotation angle $\alpha(x, y)$ is angle between along-channel direction (major tidal flow direction) and eastern direction. It is independent on time and depth. We also assume that the flow direction follows the bathymetry orientation.

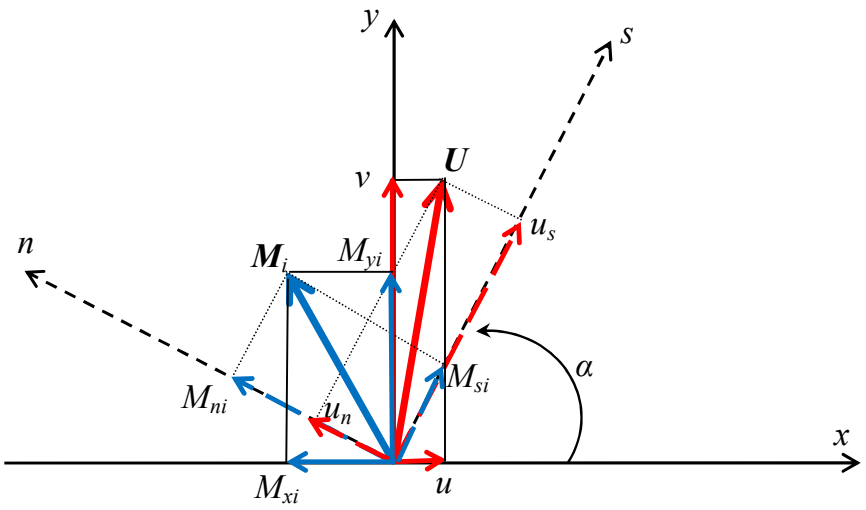

Figure A1 Transformation between *x*-*y* coordinate system and *s*-*n* coordinate system. α is the angle measuring the rotation of *s*-*n* coordinate with the reference to *x*-*y* coordinate. Vector $\boldsymbol{U}$ (red line) and $\boldsymbol{M_i}$ (blue line) indicates the tidal current velocity vector and i^{th} (i = 1:7) component vector in momentum equation.

The momentum terms transformation from *x*-*y* coordinate system to *s*-*n* coordinate by equation A11.

$$\begin{bmatrix} M_{si} \\ M_{ni} \end{bmatrix} = \begin{bmatrix} \cos\alpha & \sin\alpha \\ -\sin\alpha & \cos\alpha \end{bmatrix} \begin{bmatrix} M_{xi} \\ M_{yi} \end{bmatrix} \qquad \text{(A11)}$$

$$\begin{bmatrix} u \\ v \end{bmatrix} = \begin{bmatrix} \cos\alpha & -\sin\alpha \\ \sin\alpha & \cos\alpha \end{bmatrix} \begin{bmatrix} u_s \\ u_n \end{bmatrix} \qquad \text{(A12)}$$

Partial differential operators under *x*-*y* coordinate system related to s-n coordinate system by equationA13 (Hench and Luettich, 2003).

$$\frac{\partial}{\partial x} = \frac{\partial}{\partial s}\frac{\partial s}{\partial x} + \frac{\partial}{\partial n}\frac{\partial n}{\partial x} = \cos\alpha\frac{\partial}{\partial s} - \sin\alpha\frac{\partial}{\partial n} \qquad \text{(A13.a)}$$

$$\frac{\partial}{\partial y} = \frac{\partial}{\partial s}\frac{\partial s}{\partial y} + \frac{\partial}{\partial n}\frac{\partial n}{\partial y} = \sin\alpha\frac{\partial}{\partial s} + \cos\alpha\frac{\partial}{\partial n} \qquad \text{(A13. b)}$$

Where, $\partial s/\partial x = \cos\ \alpha, \partial s/\partial y = \sin\ \alpha, \partial n/\partial x = -\sin\ \alpha, \partial n/\partial y = \cos\ \alpha$, $\partial\alpha/\partial s = 1/R_s$ is the curvature of bend in bathymetry, R_s is the radius of the bend, $\partial\alpha/\partial n$ is the lateral convergence or divergence of the bathymetry.

The location acceleration terms under curvilinear coordinates are:

$$\begin{bmatrix} M_{s1} \\ M_{n1} \end{bmatrix} = \begin{bmatrix} \cos\alpha & \sin\alpha \\ -\sin\alpha & \cos\alpha \end{bmatrix}\begin{bmatrix} M_{x1} \\ M_{y1} \end{bmatrix} = \begin{bmatrix} \cos\alpha & \sin\alpha \\ -\sin\alpha & \cos\alpha \end{bmatrix}\frac{\partial}{\partial t}\int_{z_0}^{z_1}\begin{bmatrix} u \\ v \end{bmatrix}dz$$

$$= \begin{bmatrix} \cos\alpha & \sin\alpha \\ -\sin\alpha & \cos\alpha \end{bmatrix}\frac{\partial}{\partial t}\int_{z_0}^{z_1}\begin{bmatrix} \cos\alpha & -\sin\alpha \\ \sin\alpha & \cos\alpha \end{bmatrix}\begin{bmatrix} u_s \\ u_n \end{bmatrix}dz$$

$$= \begin{bmatrix} \cos\alpha & \sin\alpha \\ -\sin\alpha & \cos\alpha \end{bmatrix}\begin{bmatrix} \cos\alpha & -\sin\alpha \\ \sin\alpha & \cos\alpha \end{bmatrix}\frac{\partial}{\partial t}\int_{z_0}^{z_1}\begin{bmatrix} u_s \\ u_n \end{bmatrix}dz = \frac{\partial}{\partial t}\int_{z_0}^{z_1}\begin{bmatrix} u_s \\ u_n \end{bmatrix}dz \qquad \text{(A14)}$$

The coordinate system transformation is similar to all other linear terms M_{s3}, M_{n3}, M_{s4}, M_{n4}, M_{s5} and M_{n5}. The Reynolds stress terms are generally parameterized as $\overline{u'w'} = -A_z\frac{\partial u}{\partial z}$ and $\overline{v'w'} = -A_z\frac{\partial v}{\partial z}$, where A_z is vertical eddy viscosity . This linearization allows the coordinate system transformation shown in equation A15. It is similar to derive M_{s7} and M_{n7}.

$$\begin{bmatrix} M_{s6} \\ M_{n6} \end{bmatrix} = \begin{bmatrix} \cos\alpha & \sin\alpha \\ -\sin\alpha & \cos\alpha \end{bmatrix}\begin{bmatrix} M_{x6} \\ M_{y6} \end{bmatrix} = -\begin{bmatrix} \cos\alpha & \sin\alpha \\ -\sin\alpha & \cos\alpha \end{bmatrix}\left[\begin{matrix} -A_z\frac{\partial u}{\partial z} \\ -A_z\frac{\partial v}{\partial z} \end{matrix}\right]_{z=z_1}$$

$$= \begin{bmatrix} \cos\alpha & \sin\alpha \\ -\sin\alpha & \cos\alpha \end{bmatrix}\left(A_z\frac{\partial}{\partial z}\begin{bmatrix} u \\ v \end{bmatrix}\right)\Big|_{z=z_1}$$

$$= \begin{bmatrix} \cos\alpha & \sin\alpha \\ -\sin\alpha & \cos\alpha \end{bmatrix}\left(A_z\frac{\partial}{\partial z}\begin{bmatrix} \cos\alpha & -\sin\alpha \\ \sin\alpha & \cos\alpha \end{bmatrix}\begin{bmatrix} u_s \\ u_n \end{bmatrix}\right)\Big|_{z=z_1} = \left(A_z\frac{\partial}{\partial z}\begin{bmatrix} u_s \\ u_n \end{bmatrix}\right)\Big|_{z=z_1}$$

$$= -\left[\begin{matrix} \overline{u_s{}'w'} \\ \overline{u_n{}'w'} \end{matrix}\right]_{z=z_1} \qquad \text{(A15)}$$

For nonlinear advection terms

$$M_{s2} = M_{x2}\cos\alpha + M_{y2}\sin\alpha$$

$$= \cos\alpha\left(\frac{\partial}{\partial x}\int_{z_0}^{z_1} u^2 dz + \frac{\partial}{\partial y}\int_{z_0}^{z_1}(uv)dz\right)$$

$$+ \sin\alpha\left(\frac{\partial}{\partial x}\int_{z_0}^{z_1}(uv)dz + \frac{\partial}{\partial y}\int_{z_0}^{z_1} v^2 dz\right) \qquad \text{(A16. a)}$$

$$M_{n2} = -\sin\alpha\, M_{x2} + \cos\alpha\, M_{y2}$$

$$= -\sin\alpha\left(\frac{\partial}{\partial x}\int_{z_0}^{z_1} u^2 dz + \frac{\partial}{\partial y}\int_{z_0}^{z_1}(uv)dz\right)$$

$$+ \cos\alpha\left(\frac{\partial}{\partial x}\int_{z_0}^{z_1}(uv)dz + \frac{\partial}{\partial y}\int_{z_0}^{z_1} v^2 dz\right) \qquad \text{(A16. b)}$$

Substitute equation A12 and the partial differential operators into equation A16 and after tedious manipulation we get:

$$M_{s2} = \frac{\partial}{\partial s}\int_{z_0}^{z_1} {u_s}^2 dz + \frac{\partial}{\partial n}\int_{z_0}^{z_1}(u_s u_n)dz + \frac{2}{R_s}\int_{z_0}^{z_1} u_s u_n dz + \frac{\partial\alpha}{\partial n}\int_{z_0}^{z_1}({u_s}^2 - {u_n}^2)dz \qquad \text{(A17. a)}$$

$$M_{n2} = \frac{\partial}{\partial s}\int_{z_0}^{z_1} u_s u_n dz + \frac{\partial}{\partial n}\int_{z_0}^{z_1} {u_n}^2 dz - \frac{1}{R_s}\int_{z_0}^{z_1}({u_s}^2 - {u_n}^2)dz + 2\frac{\partial\alpha}{\partial n}\int_{z_0}^{z_1} u_s u_n dz \qquad \text{(A17. b)}$$

Where, the first two terms are the advection accelerations, the third term is centrifugal acceleration due to the bend in bathymetry and the last term presents the acceleration due to convergence or divergence in bathymetry.

Therefore, the equations are

$$\frac{\partial}{\partial t}\int_{z_0}^{z_1} u_s dz + \frac{\partial}{\partial s}\int_{z_0}^{z_1} {u_s}^2 dz + \frac{\partial}{\partial n}\int_{z_0}^{z_1} (u_s u_n) dz + \frac{2}{R_s}\int_{z_0}^{z_1} u_s u_n dz + \frac{\partial \alpha}{\partial n}\int_{z_0}^{z_1} ({u_s}^2 - {u_n}^2) dz$$

$$= f\int_{z_0}^{z_1} u_n dz - g(z_1 - z_0)\frac{\partial \eta}{\partial s} - \frac{g}{\rho}\int_{z_0}^{z_1}\left(\int_z^{\eta}\frac{\partial \rho}{\partial s}dz\right)dz - \overline{{u_s}'w'}\Big|_{z_1}$$

$$+ \overline{{u_s}'w'}\Big|_{z_0} \qquad \text{(A18. a)}$$

$$\frac{\partial}{\partial t}\int_{z_0}^{z_1} u_n dz + \frac{\partial}{\partial s}\int_{z_0}^{z_1} u_s u_n dz + \frac{\partial}{\partial n}\int_{z_0}^{z_1} {u_n}^2 dz - \frac{1}{R_s}\int_{z_0}^{z_1} ({u_s}^2 - {u_n}^2) dz + 2\frac{\partial \alpha}{\partial n}\int_{z_0}^{z_1} u_s u_n dz$$

$$= -f\int_{z_0}^{z_1} u_s dz - g(z_1 - z_0)\frac{\partial \eta}{\partial n} - \frac{g}{\rho}\int_{z_0}^{z_1}\left(\int_z^{\eta}\frac{\partial \rho}{\partial n}dz\right)dz - \overline{{u_n}'w'}\Big|_{z_1}$$

$$+ \overline{{u_n}'w'}\Big|_{z_0} \qquad \text{(A18. b)}$$

To dived by water depth, the depth averaged momentum equations are

$$\frac{\partial \overline{u_s}}{\partial t} + \overline{u_s\frac{\partial u_s}{\partial s}} + \overline{u_n\frac{\partial u_s}{\partial n}} = -\frac{2\overline{u_s u_n}}{R_s} - \left(\overline{{u_s}^2 - {u_n}^2}\right)\frac{\partial \theta}{\partial n} + f\overline{u_n} - g\frac{\partial \eta}{\partial s} - \frac{g}{\rho_0}\overline{\int_z^{\eta}\frac{\partial \rho(z')}{\partial s}dz'}$$

$$-\frac{1}{z_1 - z_0}\left(\langle u_s' w'\rangle|_{z_1} - \langle u_s' w'\rangle|_{z_0}\right) \qquad \text{(A19. a)}$$

$$\frac{\partial \overline{u_n}}{\partial t} + \overline{u_s\frac{\partial u_n}{\partial s}} + \overline{u_n\frac{\partial u_n}{\partial n}} = \frac{\overline{{u_s}^2 - {u_n}^2}}{R_s} - 2\overline{u_s u_n}\frac{\partial \theta}{\partial n} - f\overline{u_s} - g\frac{\partial \eta}{\partial n} - \frac{g}{\rho_0}\overline{\int_z^{\eta}\frac{\partial \rho(z')}{\partial n}dz'}$$

$$-\frac{1}{z_1 - z_0}\left(\langle u_n' w'\rangle|_{z_1} - \langle u_n' w'\rangle|_{z_0}\right) \quad . \qquad \text{(A19. b)}$$

The depth integrated momentum equations A19 were similar to Kalkwijk and Booij (1986). The distinction between the derivation in this work and that in Hench and Luettich (2003) are: (1) this work starts from conservative momentum equation and allows vertically variable velocity profiles; (2) α was

determined based on tidal flow on intertidal time scale not on instantaneous flow, so that α was depended on time and is more related to bathymetry orientation; (3) effects from both along channel bending and lateral convergence were considered in the momentum flux.

APPENDIX: B

EFFECTIVE DRAG COEFFICIENT OF ISOLATED CAGE

B.1 The effective drag coefficient of isolated cage

The linkage of the farm's bulk drag and the friction effect to the drag from an isolated cage is derived in this section. In the farm layer ($-h_f < z < 0$, Figure 1.1.2c), we assume a balance among streamwise pressure gradient, $\frac{\partial P}{\partial x}$, internal friction, $\frac{\partial \langle u'w' \rangle}{\partial z}$, and a farm drag force, $\frac{1}{2} a c_d u^2$. The momentum equation is then

$$0 = -\frac{1}{\rho}\frac{\partial P}{\partial x} - \frac{\partial \langle u'w' \rangle}{\partial z} - \frac{1}{2} a c_d u^2 . \tag{B.1}$$

Where $c_d\ (z)$ is the drag coefficient of an oyster cage, $a(z)$ is the frontal area of the oyster cage per unit water volume, $u(z)$ is the streamwise velocity. The momentum equation underneath the farm ($-H < z < -h_f$, Figure 1.1.2c) is

$$0 = -\frac{1}{\rho}\frac{\partial P}{\partial x} - \frac{\partial \langle u'w' \rangle}{\partial z}. \tag{B.2}$$

We vertically integrate equation B.2 from the lower edge of the farm ($z = -h_f$) to the free surface ($z = 0$) by assuming $\frac{\partial P}{\partial x}$ is vertically constant and there is zero friction at the free surface ending up with

$$\frac{1}{\rho}\frac{\partial P}{\partial x} h_f - \frac{\partial \langle u'w' \rangle}{\partial z}_{z=-h_f} + \frac{1}{2}\int_{-h_f}^{0} a c_d u^2 dz = 0 \tag{B.3}$$

where $\overline{u'w'}_{z=-h_f}$ is the Reynolds stress at the lower edge of the farm.

Next, we approximate the drag momentum flux $\int_{z=-h_f}^{z=0} a c_d u^2 dz$ by an the effective drag coefficient of a single oyster cage, $c_{d,e}$, a mean frontal area of the cage, $\bar{a} h_f$, and a squared depth-averaged

streamwise velocity in the farm layer, ${U_f}^2$, known as $\int_{z=-h_f}^{z=0} a c_d u^2 dz = c_{d,e}\bar{a}h_f {U_f}^2$. Where $\bar{a}$ is the total frontal area of entire oyster cage over the total volume of water occupied by each cage in the farm layer and ${U_f}^2 = \frac{1}{h_f}\int_{z=-h_f}^{z=0} u^2 dz$. Furthermore, the effective bulk drag coefficient of the farm is defined as $C_D = c_{d,e}\bar{a}h_f$.

From equation B.2, the streamwise pressure gradient can be derived from the Reynolds stress divergence profile under the farm, where $\frac{1}{\rho}\frac{\partial P}{\partial x} = -\frac{\partial \langle u'w' \rangle}{\partial z}$. Substituting $\frac{1}{\rho}\frac{\partial P}{\partial x}$ and $\int_{-h_f}^{0} a c_d u^2 dz$ into equation B.3 leads to

$$-h_f \frac{\partial \langle u'w' \rangle}{\partial z}_{-H<z<-h_f} - \overline{u'w'}_{z=-h_f} + \frac{1}{2} C_D {U_f}^2 = 0 \ . \qquad \text{(B. 4)}$$

Therefore, the effective drag coefficient of an isolated cage is $C_D = 2\frac{h_f \frac{\partial \langle u'w' \rangle}{\partial z}_{-H<z<-h_f} + \langle u'w' \rangle_{z=-h_f}}{{U_f}^2}$. Assuming Reynolds stress $\langle u'w' \rangle$ decreases linearly from the bottom edge of the farm to the bottom of the water column, we obtain

$$\frac{\partial \langle u'w' \rangle}{\partial z}_{-H<z<-h_f} = \frac{\langle u'w' \rangle_{z=-h_f} - \langle u'w' \rangle_{z=-H}}{H - h_f} = \frac{{u_f^*}^2 + {u_b^*}^2}{H - h_f}. \qquad \text{(B. 5)}$$

Finally, farm's bulk drag coefficient, C_D, and effective drag coefficient of an oyster cage, $c_{d,e}$, are

$$C_D = 2\frac{H{u_f^*}^2 + h_f {u_b^*}^2}{(H - h_f){U_f}^2} = 2\frac{{u_f^*}^2 + \frac{h_f}{H}{u_b^*}^2}{(1 - \frac{h_f}{H}){U_f}^2} \qquad \text{(B. 6)}$$

$$c_{d,e} = \frac{C_D}{\bar{a}h_f} = 2\frac{{u_f^*}^2 + \frac{h_f}{H}{u_b^*}^2}{\bar{a}h_f(1 - \frac{h_f}{H}){U_f}^2} \ . \qquad \text{(B. 7)}$$

The oyster cage consists of two pontoons providing buoyancy and a basket containing six bags. The effect of the entire cage, $c_{d,e}$, can be estimated using the drag coefficient of each pontoon, $c_{d,p}$ (= 0.71), and the drag coefficient of the basket, $c_{d,b}$, known as $c_{d,e} = \frac{2c_{d,p}A_p + c_{d,b}A_b}{2A_p + A_b}$. Where A_p and A_b are the frontal area of the pontoon and the basket, respectively. If the basket is considered as a solid box, then $c_{d,e} = 1.81$ [*Blevins* 1984]. Therefore, an upper estimate of $c_{d,e}$ is 1.62, when considering the basket is totally impermeable. While a lower estimate of $c_{d,e}$ is 0.71 if the basket is totally permeable.

APPENDIX: C

FARM IMPACT ON FLOW PATTERNS AND MIXING DURING NEAP TIDE

C.1 Tidal Current at Peak Flood

The tidal current velocity distribution across the estuary was supplemented in order to demonstrate that patterns were similar to the spring tide conditions presented in section 2.4.1.1. Seaward of the farm, streamwise flow (u_s = 0.3 m/s) traveled through the secondary channel under the farm (*distance across* = 0 m) and decreased to u_s = 0.15 m/s over the western shoal (*distance across* = 100 m) near the edge of the farm. Near the farm at the landward transect (*distance across* < 100 m), u_s reduced to 0.1 m/s. A two-layer lateral circulation formed on east side of the estuary along both seaward and landward transect. However, at the landward transect, the near-surface normal velocity (u_n = 0.01 m/s) was smaller than the near-bottom flow (u_n = -0.04 m/s, Figure C1.b2). The depth-averaged streamwise vorticity, $\overline{\omega_s} = -\frac{\overline{du_n}}{dz}$ also highlighted the reduced lateral circulation near the farm, where $|\overline{\omega_s}| < 0.02$ s^{-1} near the farm at both transects (Figure C1a.3). Away from the farm, $\overline{\omega_s}$ reached up to 0.03 s^{-1} at the seaward transect and increased up to 0.06 s^{-1} at the landward transect.

C.2 Vertical Eddy Diffusivity During Neap Tide

Time series of vertical eddy diffusivity, K_z, at each station across the estuary demonstrates consistency in mixing characteristic between neap and spring conditions. Farm-induced near-surface mixing was observed at the farm boundary and in the main channel along the landward transect. During the ebb phase of the tide (Hours 8–10), an enhanced mixing layer occurred at 1 m water depth along the seaward transect (the farm's trailing edge), where K_z was around $1.3 \times 10^{-4} \sim 1.7 \times 10^{-3}$ m^2/s (Figure C2a.1). During the flood phase of the tide (Hours 15–17), elevated values of K_z ($1.6 \times 10^{-3} \sim 9.0 \times 10^{-3}$ m^2/s) were observed in the water column within 0.8–2.0 m depth range at the farm boundary in the landward transect (Figure

C2b.1) and in the main channel ($2.4 \times 10^{-4} \sim 1.1 \times 10^{-3}$ m^2/s, Figure C2b.2). Farm-enhanced mixing at the landward transect during the flood phase was consistent with that observed in the spring tide survey presented in section 4.4.

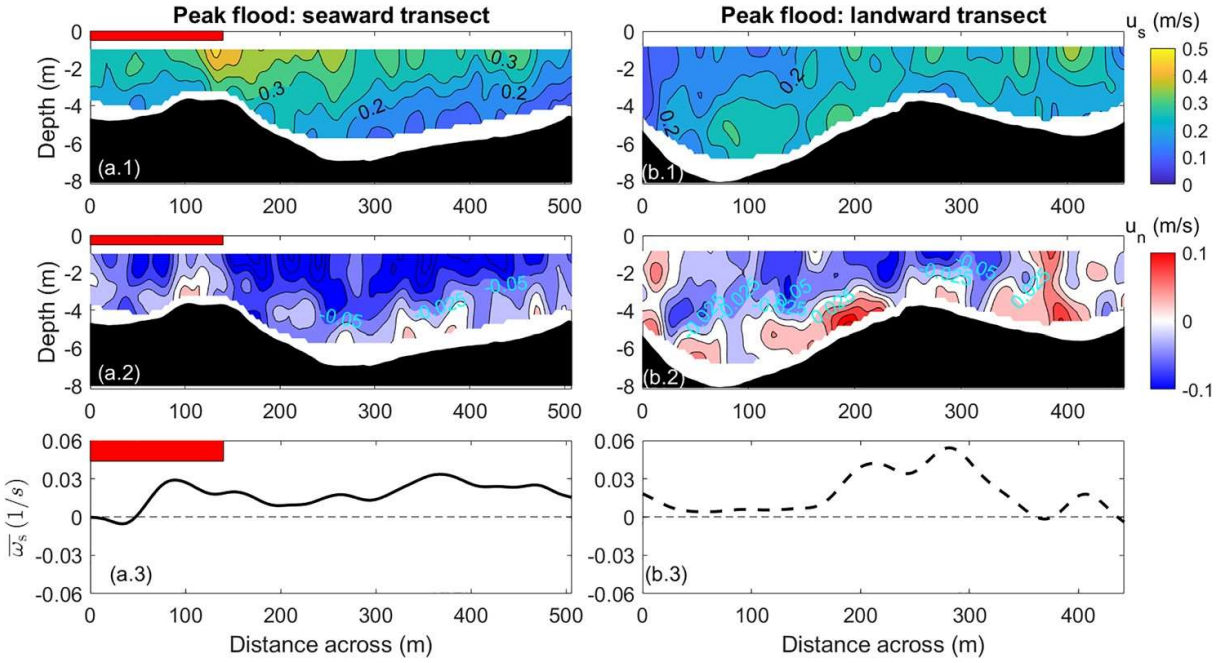

Figure C1 Velocity and streamwise vorticity distribution across the estuary at peak flood (Hour 15.7) during neap tide conditions. (a.1 and b.1) contours of streamwise velocity, u_s. Red bar indicates the oyster farm. (a.2 and b.2) Contours of normal velocity, u_n, where positive (red) values indicate velocity toward the western shoal (left) and negative (blue) values indicate velocity toward the eastern shoal (right). (a.3 and b.3) Depth-averaged streamwise vorticity, ω_s, where positive values (pointing into the paper) indicate clockwise lateral circulation and negative values indicate counterclockwise lateral circulation.

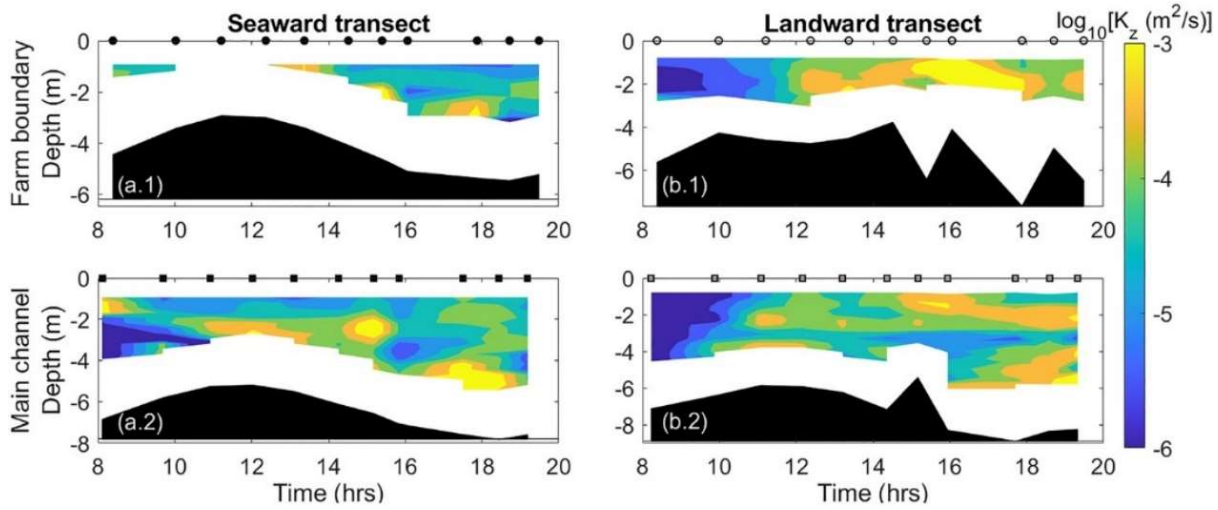

Figure C2. Time series of vertical eddy diffusivity, K_z, and time scale, τ, analysis for vertical mixing induced by lateral processes along seaward (a.1–a.3) and landward (b.1–b.3) transects over the entire tidal cycle during neap tide conditions. Contours in (a.1) and (b.1) are K_z at the farm boundary. Contours in (a.1) and (b.1) are K_z in the main channel. Markers denote data collection time. Squares denote data collected at farm boundary; circles denote data collected in the main channel. Solid makers denote seaward transect; open makers denote landward transect. In (a.3) and (b.3), τ_u is caused by shear straining, τ_ρ is caused by density straining, τ_f is caused by Coriolis, and τ_t is caused by unsteadiness. Positive τ indicates mechanisms that stabilize the water column, and negative τ indicates mechanisms that destabilize the water column. The time scale closest to 0 is the dominant stabilizing/destabilizing mechanism. Red shaded areas indicate the flood phase, and blue shaded areas shows the ebb phase.

APPENDIX: D

SENSITIVITY ANALYSIS OF STREAMWISE ADVECTION TERM

Since the landward and seaward transects are not parallel in Cartesian coordinates, special attention should be paid to quantifying the streamwise advection due to bathymetric complexities. In this section, we assess the sensitivity of the streamwise advection term to the data selection and method used to quantify it. By following the orientation of the main channel, the cross-section was partitioned into three segments including western section, main channel and eastern section, where the depth-averaged streamwise advection, $\overline{u_s \frac{\partial u_s}{\partial s}}$, was computed using velocity data in each segment (shown in Figure D1.a). In order to examine how different partitions influence the evaluation of $\overline{u_s \frac{\partial u_s}{\partial s}}$, three types of partitions were applied at both peak flood and peak ebb (shown in Figure D1.b~c). Although the calculations of $\overline{u_s \frac{\partial u_s}{\partial s}}$ are slightly different among the three methods, the overall trends were similar across the transect. The streamwise advection term was maximum in the farm area at the western side of the estuary and switched sign toward east of the estuary, meaning that estimation of $\overline{u_s \frac{\partial u_s}{\partial s}}$ was insensitive to the data selection. Values of $\overline{u_s \frac{\partial u_s}{\partial s}}$ from partition II were adopted in the momentum analysis because partition II divided the cross-section based on the natural topographic relief in the bathymetry.

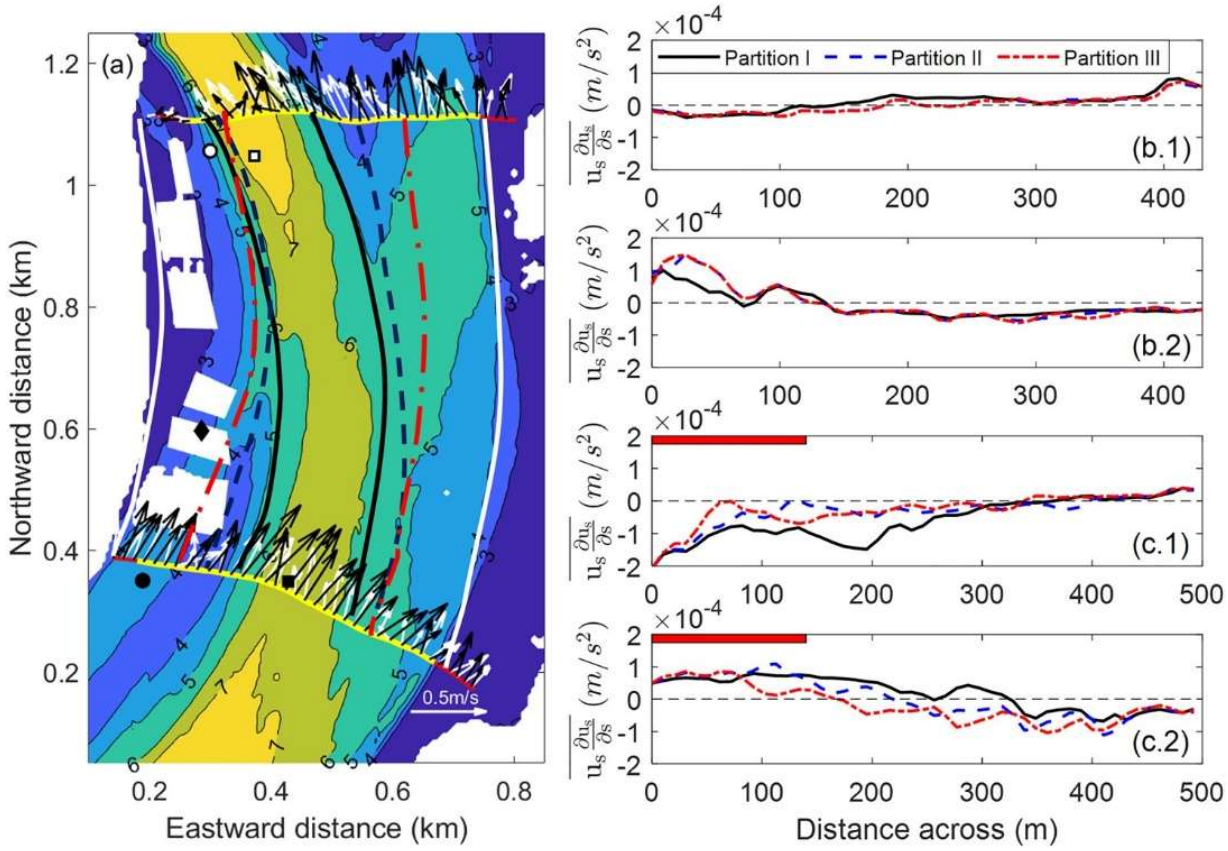

Figure D1 Sensitivity analysis of depth-averaged streamwise advection term, $\overline{u_s \frac{\partial u_s}{\partial s}}$ on data selection. (a) Three types of bathymetry partitions, I (white solid line - black solid line - black solid line - white solid line), II (white solid line -blue dash line - blue dash line - white solid line), III (white solid line - red dash dot line -red dash dot line - white solid line). Markers represent deployment location of ADV (diamond) and MicroCTDs (circles and squares). (b.1~b.2) depth-averaged streamwise advection, $\overline{u_s \frac{\partial u_s}{\partial s}}$, at seaward transect at peak flood and peak ebb. (c.1~c.2) streamwise advection term at landward transect at peak flood and peak ebb. In the panels (b.1~c.2) line types are corresponding to different types of partitions. Results of Type II partition (blue dashed lines) were shown in Figure 5 and Figure 8.

APPENDIX: E

THREE-DIMENSIONAL SEMI-ANALYTICAL MODEL WITH FLOATING AQUACULTURE FARM

E.1 Governing Equation for Tidal Flow

The governing equations for geophysical flow in a curved estuary with low river discharge consist of the continuity equation E1a and dynamic equations E1b, c for along (x, u) and across (y, v) channel velocity components:

$$\frac{\partial u}{\partial x}+\frac{\partial v}{\partial y}+\frac{\partial w}{\partial z}=0 \quad (E1.a)$$

$$\frac{\partial u}{\partial t}+u\frac{\partial u}{\partial x}+v\frac{\partial u}{\partial y}+w\frac{\partial u}{\partial z}=fv-g\frac{\partial \eta}{\partial x}+\frac{\partial}{\partial z}\left(A_z\frac{\partial u}{\partial z}\right)-\frac{2uv}{R+y}-\frac{1}{2}\frac{C_D}{h_f}u\sqrt{u^2+v^2} \quad (E1.b)$$

$$\frac{\partial v}{\partial t}+u\frac{\partial v}{\partial x}+v\frac{\partial v}{\partial y}+w\frac{\partial v}{\partial z}=-fu-g\frac{\partial \eta}{\partial y}+\frac{\partial}{\partial z}\left(A_z\frac{\partial v}{\partial z}\right)+\frac{u^2-v^2}{R+y}-\frac{1}{2}\frac{C_D}{h_f}v\sqrt{u^2+v^2} \quad (E1.c)$$

where, x, y, and z denote along, across and vertical directions and u, v, and w are along, across and vertical velocities. Positive x, u is into the estuary and positive y, v is to the left shoal and z is zero at the mean water surface and positive upward (Figure 3.1a). The Coriolis parameter is f, η is the surface elevation, A_z is the vertical eddy viscosity, R is the bending radius in the main channel, C_D is the bulk drag coefficient of aquaculture farm and h_f is the penetration depth of the farm. Note that the farm drag forcing is only imposed in the farm area and that the baroclinic forcing (i.e., along-channel density gradient) is ignored for tidal flow.

No slip conditions, $u = 0$, $v = 0$, are applied at the bottom ($z = -h$). Zero gradient boundary conditions are applied at the surface (no wind), i.e. $\frac{\partial u}{\partial z}=0$, $\frac{\partial v}{\partial z}=0$ at $z = \eta$. The continuity equation E1a is integrated

from the bottom to the free surface and kinematic boundary conditions are applied at the free surface, which results in the mass conservation equation,

$$\frac{\partial \eta}{\partial t} + \frac{\partial}{\partial x}\int_{-h}^{\eta} u dz + \frac{\partial}{\partial y}\int_{-h}^{\eta} v dz = 0 \quad (E2).$$

The surface elevation and current velocity are decomposed into semidiurnal harmonic components (η_0, u_0, v_0, w_0) and subtidal components ($\eta_s, u_s,\ v_s, w_s$)

$$\eta = \eta_0 + \eta_s = Re\left[N_0 e^{-i\omega t}\right] + \eta_s \quad (E3.a)$$

$$u = u_0 + u_s = Re\left[U_0 e^{-i\omega t}\right] + u_s \quad (E3.b)$$

$$v = v_0 + \ v_s = Re\left[V_0 e^{-i\omega t}\right] + \ v_s \quad (E3.c)$$

$$w = w_0 + w_s = Re\left[W_0 e^{-i\omega t}\right] + w_s \quad (E3.d)$$

where, N_0 , U_0 , V_0 , W_0 are the complex amplitudes of surface elevation, along, across and vertical velocities.

The decompositions in equation E3 are substituted into equation E1b, c and equation E2, and the leading order terms for the semidiurnal component are collected, resulting in the governing equations for tidal flow:

$$-i\omega N_0 + \frac{\partial}{\partial x}\left(h\int_{-1}^{0} U_0 d\sigma\right) + \frac{\partial}{\partial y}\left(h\int_{-1}^{0} V_0 d\sigma\right) = 0 \quad (E4.a)$$

$$-i\omega U_0 = fV_0 - g\frac{\partial N_0}{\partial x} + \frac{1}{h^2}\frac{\partial}{\partial \sigma}\left(\widetilde{A_z}\frac{\partial U_0}{\partial \sigma}\right) - \frac{1}{2}\frac{8C_D\widehat{U}}{3\pi h_f}U_0 \quad (E4.b)$$

$$-i\omega V_0 = -fU_0 - g\frac{\partial N_0}{\partial y} + \frac{1}{h^2}\frac{\partial}{\partial \sigma}\left(\widetilde{A_z}\frac{\partial V_0}{\partial \sigma}\right) - \frac{1}{2}\frac{8C_D\widehat{U}}{3\pi h_f}V_0 \quad (E4.c).$$

Note that equation E4 is defined on σ coordinates, where $\sigma = \frac{z}{h}$, is the sigma coordinate in vertical direction, $\sigma = -1$ at the bottom , $\sigma = 0$ at the undisturbed water surface, $\sigma = \frac{\eta}{h}$ at the free surface. Both the internal friction and farm-induced drag force are linearized. The vertical eddy viscosity A_z is replaced by an effective vertical eddy viscosity $\widetilde{A_z}$ (Chen and de Swart, 2016). The farm-induced drag force in unit volume $\frac{C_D u\sqrt{u^2+v^2}}{h_f}$ is linearized by $\frac{8}{3\pi h_f} C_D \hat{U} u_0$, i.e. $\frac{8}{3\pi h_f} C_D \hat{U} Re\left[U_0 e^{-i\omega t}\right]$, where $\hat{U} = \sqrt{|U_0|^2 + |V_0|^2}$ is the magnitude of the reference velocity. The linearization keeps the total energy dissipated by turbulence and farm drag over one tidal cycle consistent with the energy dissipated without linearization. A two-layer parabolic pricewise vertical eddy viscosity structure (Chen and de Swart, 2016) was applied to no farm region while a five-layer parabolic pricewise vertical eddy viscosity structure was applied to farm region (Figure 3.2), where parametrization of eddy viscosity structure was in Appendix E.2. The vertical eddy viscosity parameterization was validated by comparing the analytical solution with the Plew (2011) velocity measurements in a suspended canopy (see Appendix E.6).

E.2 Vertical eddy viscosity parameterization

An analytical model that resolves the vertical structure of velocity (equation E4b, c and E5b, c) requires a parametric distribution of the vertical eddy viscosity. Previous studies applied a constant eddy viscosity (Winant, 2007; Winant, 2008; Ross et al. 2017), linear profiles of eddy viscosity (Huijts et al, 2009), as well as parabolic and piecewise profiles of eddy viscosity (Zitman and Schuttelaars 2012; Chen and de Swart, 2016). This work adopts the 2-layer piecewise parabolic distribution from Chen and de Swart (2016) for the effective vertical eddy viscosity in areas without the farm, i.e. $\widetilde{A_z} = A_0 A_\sigma$, where $A_0 = \kappa\widetilde{u_b^*}(h+\eta)$, $\kappa = 0.41$ is the von Karman's constant, $\widetilde{u_b^*} = \frac{8}{3\pi}\widehat{u_b^*}$ is the linearized friction velocity, $\widehat{u_b^*}$ is the amplitude of bottom friction velocity over one tidal cycle. A_σ describes the profile factor of the eddy viscosity coefficient defined as

$$A_\sigma = (\sigma + 1)\left(\sigma_{Bp} - \sigma\right) \qquad -1 \le \sigma \le \sigma_{Bh} \quad (\text{I1}) \qquad (E6.a)$$

$$A_\sigma = (A_{Bh}^* - {A_s}^*)\left(\frac{\sigma}{\sigma_{Bh}}\right)^2 + {A_s}^* \qquad \sigma_{Bh} \le \sigma \le 0 \quad (\text{II1}) \qquad (E6.b).$$

Where ${A_s}^* = \frac{A_s}{A_0}$ is the nondimensional eddy viscosity at the surface, A_s is the dimensional eddy viscosity at the surface. The term σ_{Bp} is linked to the degree of stratification in the water column, meaning that the mixing length scale in bottom boundary layer decays away from bottom (Figure 3.2a, Chen and de Swart, 2016). In this work $\widehat{u_b^*}$ is determined based on the typical bottom drag coefficient, $C_b = 0.003$, where $\widehat{u_b^*}^2 = C_b\left(\sqrt{\left|\int_{-1}^{0} U_0 d\sigma\right|^2 + \left|\int_{-1}^{0} V_0 d\sigma\right|^2}\right)$.

In steady channel flow with a suspended canopy, the vertical profile of the along channel velocity presents a 5-layer structure (Figure 3.2b), which includes a bottom boundary layer (I2), a transition layer (II2), a mixing layer beneath the canopy (III), a canopy mixing layer (IV), and a canopy drag layer (V, Huai et al. 2012, Zhao et al. 2017). It is assumed that the tidally averaged eddy viscosity profile presents a similar structure to that in a steady channel with a suspended canopy. A 5-segment piecewise profile factor (Figure 2b) of vertical eddy viscosity was proposed based on laboratory experiments (Plew 2011) to mimic the five-layer flow structure in canopy flow

$$A_\sigma = (\sigma + 1)\left(\sigma_{Bp} - \sigma\right) \quad -1 \le \sigma < \sigma_{Bh} \quad (\text{I2}) \quad (E7.a)$$

$$A_\sigma = (a_2\sigma^2 + b_2\sigma + c_2) \quad \sigma_{Bh} \le \sigma < \sigma_{Fh} \quad (\text{II2}) \quad (E7.b)$$

$$A_\sigma = (a_3\sigma^2 + b_3\sigma + c_3) \qquad \sigma_{Fh} \le \sigma < \sigma_F \quad (\text{III}) \quad (E7.c)$$

$$A_\sigma = \left[({A_F}^* - {A_s}^*)\left(\frac{\sigma - \sigma_{Fc}}{\sigma_F - \sigma_{Fc}}\right)^2 + {A_s}^*\right] \quad \sigma_F \le \sigma < \sigma_{FC} \quad (\text{IV}) \quad (E7.d)$$

$$A_\sigma = {A_s}^* \quad \sigma_{FC} \le \sigma \le 0 \quad (\text{V}) \qquad (E7.e)$$

where σ_{Bp} is the upper limit of bottom boundary layer, $\sigma_{Bh} = \frac{2\sigma_{Bp}}{\sigma_{Bp}-1}$. ${A_F}^*$ is a nondimensional eddy viscosity at the lower edge of canopy, which is equal to $\frac{A_F}{A_0}$. A_F is a dimensional eddy viscosity at the lower edge of canopy, σ_F, and $A_0 = \kappa\sqrt{{\widetilde{u_b^*}}^2 + {\widetilde{u_f^*}}^2}(h+\eta)$. The linearized farm friction velocity is $\widetilde{u_f^*}$, which is equal to $\frac{8}{3\pi}\widehat{u_f^*}$. $\widehat{u_f^*}$ is the amplitude of farm friction velocity over one tidal cycle. It is assumed that the Reynolds stress changes linearly both under the farm and within the farm, ${\widehat{u_f^*}}^2 = \frac{1}{2}C_D(1+\sigma_F)\widehat{U}^2 + \sigma_F{\widehat{u_b^*}}^2$ (Liu and Huguenard, 2020). As shown in Figure 3.2b, σ_{Fh} is the lower location of the mixing layer beneath the canopy. σ_{FC} is the upper location of the penetration depth of the mixing layer into the canopy. Similar to σ_{Bp}, σ_{Fp} is introduced to describe the vertical decay of the mixing length scale in the mixing layer underneath the canopy, where ${a_3\sigma_{Fp}}^2 + b_3\sigma_{Fp} + c_3 = 0$. Once, σ_{Fp}, ${A_F}^*$ and ${A_s}^*$ are prescribed, σ_{Fh} together with the coefficients $a_2, b_2, c_2, a_3, b_3, c_3$ can be determined, shown as below.

$$ {A_s}^* = \frac{A_s}{A_0} \quad {A_F}^* = \frac{A_F}{A_0}, \qquad A_0 = \kappa\widetilde{u^*}h \quad A_F = \quad A_S = \kappa\widetilde{u^*}h $$

$$ a_2 = -\frac{4a_3\left({\sigma_{Bh}}^2 + \sigma_{Bp} - c_3\right) + \left(b_3 + 2\sigma_{Bh} - \sigma_{Bp} + 1\right)^2}{4\left[a_3{\sigma_{Bh}}^2 + b_3\sigma_{Bh} + c_3 - (1+\sigma_{Bh})(\sigma_{Bp} - \sigma_{Bh})\right]} $$

$$ b_2 $$

$$ = -\frac{2c_3\left[1 + 2(1+a_3)\sigma_{Bh} - \sigma_{Bp}\right] + 2(1+a_3){\sigma_{Bh}}^2(1-\sigma_{Bp}) - 2(1-\sigma_{Bp})\sigma_{Bp} + \sigma_{Bh}\left(1 - {b_3}^2 - 6\sigma_{Bp} - 4a_3\sigma_{Bp} + {\sigma_{Bp}}^2\right)}{2\left[a_3{\sigma_{Bh}}^2 + b_3\sigma_{Bh} + c_3 - (1+\sigma_{Bh})(\sigma_{Bp} - \sigma_{Bh})\right]} $$

$$ c_2 = \frac{-{\sigma_{Bh}}^2\left(b_3 - \sigma_{Bp} + 1\right)^2 + 4\sigma_{Bh}\sigma_{Bp}\left(b_3 - \sigma_{Bp} + 1\right) + 4(a_3+1)c_3{\sigma_{Bh}}^2 + 4\left(c_3 - \sigma_{Bp}\right)\sigma_{Bp}}{4\left[a_3{\sigma_{Bh}}^2 + b_3\sigma_{Bh} + c_3 - (1+\sigma_{Bh})(\sigma_{Bp} - \sigma_{Bh})\right]} $$

$$ a_3 = \frac{{A_F}^*\left(\sigma_F + \sigma_{Fc} - 2\sigma_{Fp}\right) - 2{A_s}^*\left(\sigma_F - \sigma_{Fp}\right)}{\left(\sigma_F - \sigma_{Fc}\right)\left(\sigma_F - \sigma_{Fp}\right)^2} $$

$$ b_3 = -2\frac{{A_F}^*\left(\sigma_F\sigma_{Fc} - {\sigma_{Fp}}^2\right) - {A_s}^*\left({\sigma_F}^2 - {\sigma_{Fp}}^2\right)}{\left(\sigma_F - \sigma_{Fc}\right)\left(\sigma_F - \sigma_{Fp}\right)^2} $$

$$c_3 = \frac{-A_s{}^* \sigma_F \sigma_{Fp} - A_F{}^* \sigma_{Fp}\left[\sigma_F \sigma_{Fp} - \sigma_{Fc}\left(2\sigma_F - \sigma_{Fp}\right)\right]}{\left(\sigma_F - \sigma_{Fc}\right)\left(\sigma_F - \sigma_{Fp}\right)^2}$$

$$\sigma_{Bh} = \frac{2\sigma_{Bp}}{1 - \sigma_{Bp}}$$

$$\sigma_{Fh} = \frac{(\sigma_{Bh} + 2)\sigma_{Bp} - (b_3 + 1)\sigma_{Bh} - 2c_3}{2(a_3 + 1)\sigma_{Bh} + b_3 - \sigma_{Bp} + 1}$$

E.3 Analytical solution of velocity profile

E.3.1 Decouple Coriolis forcing

The along and across channel velocities are coupled when Coriolis forcing is considered in both components. To solve equation E4, coupled velocities and barotropic pressure gradients were defined as $\mathbb{W}^{\pm} = U_0 \pm iV_0$, $SL^{\pm} = g\frac{\partial N_0}{\partial x} \pm ig\frac{\partial N_0}{\partial y}$.

$$-i\omega\mathbb{W}^{+} = -if\mathbb{W}^{+} - SL^{+} + \frac{1}{h^2}\frac{\partial}{\partial\sigma}\left(A_z\frac{\partial\mathbb{W}^{+}}{\partial\sigma}\right) - \frac{4U_F C_D}{3\pi}\mathbb{W}^{+}$$

$$-i\omega\mathbb{W}^{-} = if\mathbb{W}^{-} - SL^{-} + \frac{1}{h^2}\frac{\partial}{\partial\sigma}\left(A_z\frac{\partial\mathbb{W}^{-}}{\partial\sigma}\right) - \frac{4U_F C_D}{3\pi}\mathbb{W}^{-}$$

Apply no slip boundary conditions at bottom and zero gradient boundary conditions are surface, i.e.,

$\sigma = -1 + \sigma_0$, $\mathbb{W}_1 = 0$

$\sigma = 0$, $A_z\frac{\partial\mathbb{W}_5}{\partial\sigma} = 0$

Apply velocity and velocity gradient continuity conditions are interface

$\sigma = \sigma_{Bh}$, $\mathbb{W}_1 = \mathbb{W}_2$, $\frac{\partial\mathbb{W}_1}{\partial\sigma} = \frac{\partial\mathbb{W}_2}{\partial\sigma}$

$\sigma = \sigma_{Fh}, \mathbb{W}_2 = \mathbb{W}_3, \frac{\partial \mathbb{W}_2}{\partial \sigma} = \frac{\partial \mathbb{W}_3}{\partial \sigma}$

$\sigma = \sigma_F, \mathbb{W}_3 = \mathbb{W}_4, \frac{\partial \mathbb{W}_3}{\partial \sigma} = \frac{\partial \mathbb{W}_4}{\partial \sigma}$

$\sigma = \sigma_{Fc}, \mathbb{W}_4 = \mathbb{W}_5, \frac{\partial \mathbb{W}_4}{\partial \sigma} = \frac{\partial \mathbb{W}_5}{\partial \sigma}$

The bottom friction velocity can be iteratively determined busing a typical bottom drag coefficient.

$$u^* = \sqrt{C_f}\sqrt{\left|\int_{-1+\sigma_0}^{0} U_0 d\sigma\right|^2 + \left|\int_{-1+\sigma_0}^{0} V_0 d\sigma\right|^2}$$

E.3.2 Solutions at Layer $j = \mathbf{I1}, \mathbf{II1}, \mathbf{III}$

The general solutions for tidal currents were linear combinations of the Legendre function $P_\alpha(x)$ and the Legendre functions of the second kind $Q_\alpha(x)$ as shown below,

$$\mathbb{W}_j = C_{j,1} P_{\alpha_j}(\beta_{\sigma,j}) + C_{j,2} Q_{\alpha_j}(\beta_{\sigma,j}) - \frac{iSL}{a} \qquad (E8.a)$$

$$\mathbb{W}_1 = \left[C_{1,1,2} P_{\alpha_1}(\beta_{\sigma,1}) + C_{1,2,2} Q_{\alpha_1}(\beta_{\sigma,1}) + 1\right]\frac{-isl}{a} + \left[C_{1,1,3} P_{\alpha_1}(\beta_{\sigma,1}) + C_{1,2,3} Q_{\alpha_1}(\beta_{\sigma,1})\right] isl\left(\frac{1}{a} - \frac{1}{a_{F4}}\right)$$

$$+ \left[C_{1,1,4} P_{\alpha_1}(\beta_{\sigma,1}) + C_{1,2,4} Q_{\alpha_1}(\beta_{\sigma,1})\right] isl\left(\frac{1}{a_{F4}} - \frac{1}{a_{F5}}\right) - \frac{isl}{a}(1 + \sigma_{Bh} - \sigma_0)$$

$a^{\pm} = \omega \mp f$

$$\alpha_1 = \frac{1}{2}\left(-1 + \frac{\sqrt{A_0 + 4iah^2}}{\sqrt{A_0}}\right)$$

$$\beta_{\sigma,1} = \frac{1 + 2\sigma - \sigma_{Bp}}{1 + \sigma_{Bp}}$$

$$\alpha_2 = \frac{1}{2}\left(-1 + \frac{\sqrt{A_0 a_2 - 4ia\,h^2}}{\sqrt{A_0 a_2}}\right)$$

$$\beta_{\sigma,2} = i\frac{\sqrt{{b_2}^2 + 4a_2c_2}}{\sqrt{\frac{-{b_2}^4 + 16{a_2}^2{c_2}^2}{{a_2}^2}}}\left(\frac{b_2}{a_2} + 2\sigma\right)$$

$$\alpha_3 = \frac{1}{2}\left(-1 + \frac{\sqrt{A_0 a_3 - 4ia\,h^2}}{\sqrt{A_0 a_3}}\right)$$

$$\beta_{\sigma,3} = i\frac{\sqrt{{b_3}^2 + 4a_3c_3}}{\sqrt{\frac{-{b_3}^4 + 16{a_3}^2{c_3}^2}{{a_3}^2}}}\left(\frac{b_3}{a_3} + 2\sigma\right)$$

E.3.3 Solutions at Layer *j* =IV

$$\mathbb{W}_{\mathrm{IV}} = C_{\mathrm{IV},1}P_{\alpha_{\mathrm{IV}}}(\beta_{\sigma,\mathrm{IV}}) + C_{\mathrm{IV},2}Q_{\alpha_{\mathrm{IV}}}(\beta_{\sigma,\mathrm{IV}}) - \frac{iSL}{a_{F\mathrm{I}}} \qquad (E8.b)$$

where

$$a_{Fp4} = \left(\omega + i\frac{4U_{F4}C_{D4}}{3\pi}\right) - f$$

$$a_{Fn} = \left(\omega + i\frac{4U_{F4}C_{D4}}{3\pi}\right) + f$$

$$\alpha_4 = \frac{1}{2}\left(-1 + \frac{\sqrt{A_0 a_4 - 4ia_{F4}\,h^2}}{\sqrt{A_0 a_4}}\right)$$

$$\beta_{\sigma,4} = i\frac{\sqrt{{b_4}^2 + 4a_4c_4}}{\sqrt{\frac{-{b_4}^4 + 16{a_4}^2{c_4}^2}{{a_4}^2}}}\left(\frac{b_4}{a_4} + 2\sigma\right)$$

$$a_4 = \frac{{A_F}^* - {A_s}^*}{(\sigma_F - \sigma_{Fc})^2}$$

$$b_4 = -\frac{2\sigma_{Fc}({A_F}^* - {A_s}^*)}{(\sigma_F - \sigma_{Fc})^2}$$

$$c_4 = \frac{({A_F}^* - {A_s}^*){\sigma_{Fc}}^2}{(\sigma_F - \sigma_{Fc})^2} + {A_s}^*$$

E.3.4 Solutions at Layer $j = \mathrm{V}$

$$\mathbb{W}_{\mathrm{V}} = C_{\mathrm{V},1}e^{-\frac{(-1)^{3/4}\sqrt{a_{F\mathrm{V}}}h}{\sqrt{A_0A_s^*}}\sigma} + C_{\mathrm{V},2}e^{\frac{(-1)^{3/4}\sqrt{a_{F\mathrm{V}}}h}{\sqrt{A_0A_s^*}}\sigma} - \frac{iSL}{a_{F\mathrm{V}}} \qquad (E8.c).$$

where

$$a_{Fp} = \left(\omega + i\frac{4U_{F5}C_{D5}}{3\pi}\right) - f$$

$$a_{Fn} = \left(\omega + i\frac{4U_{F5}C_{D5}}{3\pi}\right) + f$$

Note that the region with no farm, equation E8a with indices $j = \mathrm{I1}, \mathrm{II1}$ indicates the solution in layer I1 and II1 (Figure 3.2a). While in the farm region, equation E8a with $j = \mathrm{I2}, \mathrm{II2}, \mathrm{III}$ together with equation E8b and E8c indicate the solution in layer I2, II2, III, IV and V (Figure 3.2b). For tidal flow, $\alpha_{\_}$ represents $\alpha_{\_}{}^+$ and $\alpha_{\_}{}^-$, which are the degree of the Legendre function, $\beta_{\sigma,\_}$ represents $\beta_{\_}(\sigma)^+$ and $\beta_{\_}(\sigma)^-$ as functions of σ, which are the arguments of the Legendre function. a is equal to $\omega \mp f$, while, $a_{F\mathrm{IV}} =$

$\omega \mp f + i\frac{4C_D U_{FIV}}{3\pi h_f}$, $a_{FV} = \omega \mp f + i\frac{4C_D U_{FV}}{3\pi h_f}$, where U_{FIV} and U_{FV} are tidal reference velocities of the farm drag force in the mixing layer and the drag layer within canopy. The coefficients $C_{\_,1}$ and $C_{\_,2}$ are determined based on bottom and surface boundary conditions together with continuous and smooth interfacial conditions.

E.3.5 Solution of Tidal amplitude

The tidal current velocities from equation E8 are integrated over the water column, and depth integrated velocities are substituted into equation E4a. The result is a linear second order elliptic partial differential equation for tidal amplitude

$$\nabla \cdot (-\boldsymbol{c}\nabla N_0) - 2\omega N_0 = 0 \qquad (E9)$$

where, $\boldsymbol{c} = g\begin{bmatrix} -(M^+ + M^-) & -i(M^+ - M^-) \\ i(M^+ - M^-) & -(M^+ + M^-) \end{bmatrix}$ is the coefficient matrix and M^+ and M^- are the integration of the velocity shape function over depth, which are functions of *x* and *y*, shown as below

$$M = h\left\{-\frac{1}{a}\left(C_{1,1,2}\int_{-1+\sigma_0}^{\sigma_{Bh}} P_{\alpha_1}(\beta_{\sigma,1})d\sigma + C_{1,2,2}\int_{-1+\sigma_0}^{\sigma_{Bh}} Q_{\alpha_1}(\beta_{\sigma,1})d\sigma + C_{2,1,2}\int_{\sigma_{Bh}}^{\sigma_{Fh}} P_{\alpha_2}(\beta_{\sigma,2})d\sigma + C_{2,2,2}\int_{\sigma_{Bh}}^{\sigma_{Fh}} Q_{\alpha_2}(\beta_{\sigma,2})d\sigma\right.\right.$$

$$+ C_{3,1,2}\int_{\sigma_{Fh}}^{\sigma_F} P_{\alpha_3}(\beta_{\sigma,3})d\sigma + C_{3,2,2}\int_{\sigma_{Fh}}^{\sigma_F} Q_{\alpha_3}(\beta_{\sigma,3})d\sigma + C_{4,1,2}\int_{\sigma_F}^{\sigma_{Fc}} P_{\alpha_4}(\beta_{\sigma,4})d\sigma + C_{4,2,2}\int_{\sigma_F}^{\sigma_{Fc}} Q_{\alpha_4}(\beta_{\sigma,4})d\sigma$$

$$+ C_{5,1,2}\left[-\frac{\sqrt{A_0A_s^*}}{(-1)^{\frac{3}{4}}\sqrt{a_F}h}\left(1 - e^{-\frac{(-1)^{\frac{3}{4}}\sqrt{a_F}h}{\sqrt{A_0A_s^*}}\sigma_{Fc}}\right)\right] + C_{5,2,2}\left[\frac{\sqrt{A_0A_s^*}}{(-1)^{\frac{3}{4}}\sqrt{a_F}h}\left(1 - e^{\frac{(-1)^{\frac{3}{4}}\sqrt{a_F}h}{\sqrt{A_0A_s^*}}\sigma_{Fc}}\right)\right] + 1 - \sigma_0$$

$$\left.\left. + \sigma_F\right)\right.$$

$$+ \left(\frac{1}{a} - \frac{1}{a_{F4}}\right)\left[C_{1,1,3}\int_{-1+\sigma_0}^{\sigma_{Bh}} P_{\alpha_1}(\beta_{\sigma,1})d\sigma + C_{1,2,3}\int_{-1+\sigma_0}^{\sigma_{Bh}} Q_{\alpha_1}(\beta_{\sigma,1})d\sigma + C_{2,1,3}\int_{\sigma_{Bh}}^{\sigma_{Fh}} P_{\alpha_2}(\beta_{\sigma,2})d\sigma\right.$$

$$+ C_{2,2,3}\int_{\sigma_{Bh}}^{\sigma_{Fh}} Q_{\alpha_2}(\beta_{\sigma,2})d\sigma + C_{3,1,3}\int_{\sigma_{Fh}}^{\sigma_F} P_{\alpha_3}(\beta_{\sigma,3})d\sigma + C_{3,2,3}\int_{\sigma_{Fh}}^{\sigma_F} Q_{\alpha_3}(\beta_{\sigma,3})d\sigma + C_{4,1,3}\int_{\sigma_F}^{\sigma_{Fc}} P_{\alpha_4}(\beta_{\sigma,4})d\sigma$$

$$+ C_{4,2,3}\int_{\sigma_F}^{\sigma_{Fc}} Q_{\alpha_4}(\beta_{\sigma,4})d\sigma - C_{5,1,3}\frac{\sqrt{A_0A_s^*}}{(-1)^{\frac{3}{4}}\sqrt{a_F}h}\left(1 - e^{-\frac{(-1)^{\frac{3}{4}}\sqrt{a_F}h}{\sqrt{A_0A_s^*}}\sigma_{Fc}}\right)$$

$$\left. + C_{5,2,3}\frac{\sqrt{A_0A_s^*}}{(-1)^{\frac{3}{4}}\sqrt{a_F}h}\left(1 - e^{\frac{(-1)^{\frac{3}{4}}\sqrt{a_F}h}{\sqrt{A_0A_s^*}}\sigma_{Fc}}\right)\right]$$

$$+ \left(\frac{1}{a_{F4}} - \frac{1}{a_{F5}}\right)\left[C_{1,1,4}\int_{-1+\sigma_0}^{\sigma_{Bh}} P_{\alpha_1}(\beta_{\sigma,1})d\sigma + C_{1,2,4}\int_{-1+\sigma_0}^{\sigma_{Bh}} Q_{\alpha_1}(\beta_{\sigma,1})d\sigma + C_{2,1,4}\int_{\sigma_{Bh}}^{\sigma_{Fh}} P_{\alpha_2}(\beta_{\sigma,2})d\sigma\right.$$

$$+ C_{2,2,4}\int_{\sigma_{Bh}}^{\sigma_{Fh}} Q_{\alpha_2}(\beta_{\sigma,2})d\sigma + C_{3,1,4}\int_{\sigma_{Fh}}^{\sigma_F} P_{\alpha_3}(\beta_{\sigma,3})d\sigma + C_{3,2,4}\int_{\sigma_{Fh}}^{\sigma_F} Q_{\alpha_3}(\beta_{\sigma,3})d\sigma + C_{4,1,4}\int_{\sigma_F}^{\sigma_{Fc}} P_{\alpha_4}(\beta_{\sigma,4})d\sigma$$

$$+ C_{4,2,4}\int_{\sigma_F}^{\sigma_{Fc}} Q_{\alpha_4}(\beta_{\sigma,4})d\sigma - C_{5,1,4}\frac{\sqrt{A_0A_s^*}}{(-1)^{\frac{3}{4}}\sqrt{a_F}h}\left(1 - e^{-\frac{(-1)^{\frac{3}{4}}\sqrt{a_F}h}{\sqrt{A_0A_s^*}}\sigma_{Fc}}\right)$$

$$\left. + C_{5,2,4}\frac{\sqrt{A_0A_s^*}}{(-1)^{\frac{3}{4}}\sqrt{a_F}h}\left(1 - e^{\frac{(-1)^{\frac{3}{4}}\sqrt{a_F}h}{\sqrt{A_0A_s^*}}\sigma_{Fc}}\right)\right] - \frac{1}{a_{F4}}(\sigma_{Fc} - \sigma_F) + \frac{1}{a_{F5}}\sigma_{Fc}\Bigg\}$$

where,

$$P_{\alpha_1}(\beta_{k,1}) = \sqrt{\pi}\left[\frac{1}{\Gamma\left(\frac{1-\alpha_1}{2}\right)\Gamma\left(\frac{\alpha_1}{2}+1\right)} \quad {}_2F_1\left(\frac{1+\alpha_1}{2}, -\frac{\alpha_1}{2}; \frac{1}{2}; {\beta_{k,1}}^2\right)\right.$$

$$\left. - \frac{2\beta_{k,1}}{\Gamma\left(-\frac{\alpha_1}{2}\right)\Gamma\left(\frac{\alpha_1+1}{2}\right)} \quad {}_2F_1\left(\frac{1-\alpha_1}{2}, \frac{\alpha_1+2}{2}; \frac{3}{2}; {\beta_{k,1}}^2\right)\right]$$

$$Q_{\alpha_1}(\beta_{k,1}) = \sqrt{\pi}\left[\frac{\cos\frac{\alpha_1\pi}{2}\Gamma\left(\frac{\alpha_1}{2}+1\right)}{\Gamma\left(\frac{\alpha_1+1}{2}\right)}\beta_{k,1}\,{}_2F_1\left(\frac{1-\alpha_1}{2}, \frac{\alpha_1}{2}+1; \frac{3}{2}; {\beta_{k,1}}^2\right)\right.$$

$$\left. - \frac{\sin\frac{\alpha_1\pi}{2}\Gamma\left(\frac{\alpha_1+1}{2}\right)}{2\Gamma\left(\frac{\alpha_1}{2}+1\right)} \quad {}_2F_1\left(-\frac{\alpha_1}{2}, \frac{\alpha_1+1}{2}; \frac{1}{2}; {\beta_{k,1}}^2\right)\right]$$

$$\int_{-1+\sigma_0}^{\sigma_{Bh}} P_{\alpha_1}(\beta_{\sigma,1})d\sigma = \frac{1+\sigma_{Bp}}{2(1+2\alpha_1)}\left\{P_{\alpha_1+1}(\beta_{\sigma_{Bh},1}) - P_{\alpha_1-1}(\beta_{\sigma_{Bh},1}) - \left[P_{\alpha_1+1}(\beta_{-1+\sigma_0,1}) - P_{\alpha_1-1}(\beta_{-1+\sigma_0,1})\right]\right\}$$

$$\int_{-1+\sigma_0}^{\sigma_{Bh}} Q_{\alpha_1}(\beta_{\sigma,1})d\sigma$$

$$= -\sqrt{\pi}\frac{1+\sigma_{Bp}}{2}\left[\frac{1}{\alpha_1(1+\alpha_1)}\frac{\cos\frac{\alpha_1\pi}{2}\Gamma\left(\frac{\alpha_1}{2}+1\right)}{\Gamma\left(\frac{\alpha_1+1}{2}\right)} \quad {}_2F_1\left(-\frac{\alpha_1+1}{2}, \frac{\alpha_1}{2}; \frac{1}{2}; {\beta_{\sigma_{Bh},1}}^2\right)\right.$$

$$+ \frac{\sin\frac{\alpha_1\pi}{2}\Gamma\left(\frac{\alpha_1+1}{2}\right)}{2\Gamma\left(\frac{\alpha_1}{2}+1\right)}\beta_{\sigma_{Bh},1} \quad {}_2F_1\left(\frac{\alpha_1+1}{2}, -\frac{\alpha_1}{2}; \frac{3}{2}; {\beta_{\sigma_{Bh},1}}^2\right)$$

$$- \frac{1}{\alpha_1(1+\alpha_1)}\frac{\cos\frac{\alpha_1\pi}{2}\Gamma\left(\frac{\alpha_1}{2}+1\right)}{\Gamma\left(\frac{\alpha_1+1}{2}\right)} \quad {}_2F_1\left(-\frac{\alpha_1+1}{2}, \frac{\alpha_1}{2}; \frac{1}{2}; {\beta_{-1+\sigma_0,1}}^2\right)$$

$$\left. - \frac{\sin\frac{\alpha_1\pi}{2}\Gamma\left(\frac{\alpha_1+1}{2}\right)}{2\Gamma\left(\frac{\alpha_1}{2}+1\right)}\beta_{-1+\sigma_0,1} \quad {}_2F_1\left(\frac{\alpha_1+1}{2}, -\frac{\alpha_1}{2}; \frac{3}{2}; {\beta_{-1+\sigma_0,1}}^2\right)\right]$$

$$\int_{\sigma_{Bh}}^{\sigma_{Fh}} P_{\alpha_2}(\beta_{\sigma,2})d\sigma = -i\frac{\sqrt{\frac{-{b_2}^4 + 16{a_2}^2{c_2}^2}{{a_2}^2}}}{2\sqrt{{b_2}^2 + 4a_2c_2}}\frac{1}{1+2\alpha_2}\{P_{\alpha_2+1}(\beta_{\sigma_{Fh},2}) - P_{\alpha_2-1}(\beta_{\sigma_{Fh},2})$$

$$- [P_{\alpha_2+1}(\beta_{\sigma_{Bh},2}) - P_{\alpha_2-1}(\beta_{\sigma_{Bh},2})]\}$$

$$\int_{\sigma_{Bh}}^{\sigma_{Fh}} Q_{\alpha_2}(\beta_{\sigma,2})d\sigma$$

$$= i\sqrt{\pi}\frac{\sqrt{\frac{-{b_2}^4 + 16{a_2}^2{c_2}^2}{{a_2}^2}}}{2\sqrt{{b_2}^2 + 4a_2c_2}}\left[\frac{1}{\alpha_2(1+\alpha_2)}\frac{\cos\frac{\alpha_2\pi}{2}\Gamma\left(\frac{\alpha_2}{2}+1\right)}{\Gamma\left(\frac{\alpha_2+1}{2}\right)} \quad {}_2F_1\left(-\frac{\alpha_2+1}{2},\frac{\alpha_2}{2};\frac{1}{2};{\beta_{\sigma_{Fh},2}}^2\right)\right.$$

$$+ \frac{\sin\frac{\alpha_2\pi}{2}\Gamma\left(\frac{\alpha_2+1}{2}\right)}{2\Gamma\left(\frac{\alpha_2}{2}+1\right)}\beta_{\sigma_{Fh},2} \quad {}_2F_1\left(\frac{\alpha_2+1}{2},-\frac{\alpha_2}{2};\frac{3}{2};{\beta_{\sigma_{Fh},2}}^2\right)$$

$$- \frac{1}{\alpha_2(1+\alpha_2)}\frac{\cos\frac{\alpha_2\pi}{2}\Gamma\left(\frac{\alpha_2}{2}+1\right)}{\Gamma\left(\frac{\alpha_2+1}{2}\right)} \quad {}_2F_1\left(-\frac{\alpha_2+1}{2},\frac{\alpha_2}{2};\frac{1}{2};{\beta_{\sigma_{Bh},2}}^2\right)$$

$$\left. - \frac{\sin\frac{\alpha_2\pi}{2}\Gamma\left(\frac{\alpha_2+1}{2}\right)}{2\Gamma\left(\frac{\alpha_2}{2}+1\right)}\beta_{\sigma_{Bh},2} \quad {}_2F_1\left(\frac{\alpha_2+1}{2},-\frac{\alpha_2}{2};\frac{3}{2};{\beta_{\sigma_{Bh},2}}^2\right)\right]$$

$$\int_{\sigma_{Fh}}^{\sigma_F} P_{\alpha_3}(\beta_{\sigma,3})d\sigma = -i\frac{\sqrt{\frac{-{b_3}^4 + 16{a_3}^2{c_3}^2}{{a_3}^2}}}{2\sqrt{{b_3}^2 + 4a_3c_3}}\frac{1}{1+2\alpha_3}\{P_{\alpha_3+1}(\beta_{\sigma_F,3}) - P_{\alpha_3-1}(\beta_{\sigma_F,3})$$

$$- [P_{\alpha_3+1}(\beta_{\sigma_{Fh},3}) - P_{\alpha_3-1}(\beta_{\sigma_{Fh},3})]\}$$

$$\int_{\sigma_{Fh}}^{\sigma_F} Q_{\alpha_3}(\beta_{\sigma,3})d\sigma = i\sqrt{\pi}\frac{\sqrt{\frac{-{b_3}^4+16{a_3}^2{c_3}^2}{{a_3}^2}}}{2\sqrt{{b_3}^2+4a_3c_3}}\left[\frac{1}{\alpha_3(1+\alpha_3)}\frac{\cos\frac{\alpha_3\pi}{2}\Gamma\left(\frac{\alpha_3}{2}+1\right)}{\Gamma\left(\frac{\alpha_3+1}{2}\right)} \quad {}_2F_1\left(-\frac{\alpha_3+1}{2},\frac{\alpha_3}{2};\frac{1}{2};{\beta_{\sigma_F,3}}^2\right)\right.$$

$$+\frac{\sin\frac{\alpha_3\pi}{2}\Gamma\left(\frac{\alpha_3+1}{2}\right)}{2\Gamma\left(\frac{\alpha_3}{2}+1\right)}\beta_{\sigma_F,3} \quad {}_2F_1\left(\frac{\alpha_3+1}{2},-\frac{\alpha_3}{2};\frac{3}{2};{\beta_{\sigma_F,3}}^2\right)$$

$$-\frac{1}{\alpha_3(1+\alpha_3)}\frac{\cos\frac{\alpha_3\pi}{2}\Gamma\left(\frac{\alpha_3}{2}+1\right)}{\Gamma\left(\frac{\alpha_3+1}{2}\right)} \quad {}_2F_1\left(-\frac{\alpha_3+1}{2},\frac{\alpha_3}{2};\frac{1}{2};{\beta_{\sigma_{Fh},3}}^2\right)$$

$$\left.-\frac{\sin\frac{\alpha_3\pi}{2}\Gamma\left(\frac{\alpha_3+1}{2}\right)}{2\Gamma\left(\frac{\alpha_3}{2}+1\right)}\beta_{\sigma_{Fh},3} \quad {}_2F_1\left(\frac{\alpha_3+1}{2},-\frac{\alpha_3}{2};\frac{3}{2};{\beta_{\sigma_{Fh},3}}^2\right)\right]$$

$$\int_{\sigma_F}^{\sigma_{Fc}} P_{\alpha_4}(\beta_{\sigma,4})d\sigma = -i\frac{\sqrt{\frac{-{b_4}^4+16{a_4}^2{c_4}^2}{{a_4}^2}}}{2\sqrt{{b_4}^2+4a_4c_4}}\frac{1}{1+2\alpha_4}\{P_{\alpha_4+1}(\beta_{\sigma_{Fc},4})-P_{\alpha_4-1}(\beta_{\sigma_{Fc},4})$$

$$-\left[P_{\alpha_4+1}(\beta_{\sigma_F,4})-P_{\alpha_4-1}(\beta_{\sigma_F,4})\right]\}$$

$$\int_{\sigma_F}^{\sigma_{Fc}} Q_{\alpha_4}(\beta_{\sigma,4})d\sigma$$

$$= i\sqrt{\pi}\frac{\sqrt{\frac{-{b_4}^4+16{a_4}^2{c_4}^2}{{a_4}^2}}}{2\sqrt{{b_4}^2+4a_4c_4}}\left[\frac{1}{\alpha_4(1+\alpha_4)}\frac{\cos\frac{\alpha_4\pi}{2}\Gamma\left(\frac{\alpha_4}{2}+1\right)}{\Gamma\left(\frac{\alpha_4+1}{2}\right)} \quad {}_2F_1\left(-\frac{\alpha_4+1}{2},\frac{\alpha_4}{2};\frac{1}{2};{\beta_{\sigma_{Fc},4}}^2\right)\right.$$

$$+\frac{\sin\frac{\alpha_4\pi}{2}\Gamma\left(\frac{\alpha_4+1}{2}\right)}{2\Gamma\left(\frac{\alpha_4}{2}+1\right)}\beta_{\sigma_{Fc},4} \quad {}_2F_1\left(\frac{\alpha_4+1}{2},-\frac{\alpha_4}{2};\frac{3}{2};{\beta_{\sigma_{Fc},4}}^2\right)$$

$$-\frac{1}{\alpha_4(1+\alpha_4)}\frac{\cos\frac{\alpha_4\pi}{2}\Gamma\left(\frac{\alpha_4}{2}+1\right)}{\Gamma\left(\frac{\alpha_4+1}{2}\right)} \quad {}_2F_1\left(-\frac{\alpha_4+1}{2},\frac{\alpha_4}{2};\frac{1}{2};{\beta_{\sigma_F,4}}^2\right)$$

$$\left.-\frac{\sin\frac{\alpha_4\pi}{2}\Gamma\left(\frac{\alpha_4+1}{2}\right)}{2\Gamma\left(\frac{\alpha_4}{2}+1\right)}\beta_{\sigma_F,4} \quad {}_2F_1\left(\frac{\alpha_4+1}{2},-\frac{\alpha_4}{2};\frac{3}{2};{\beta_{\sigma_F,4}}^2\right)\right]$$

For elongated estuaries, $\frac{dN_0}{dy} \ll \frac{dN_0}{dx}$ terms related to $\frac{dN_0}{dy}$ can be neglected. Equation 3.6 is often simplified to an ordinary differential equation (Winant 2007; Ross et al, 2017), however, the floating aquaculture farm occupies a finite portion of the estuary, where $\frac{dN_0}{dy}$ and $\frac{dN_0}{dx}$ are likely the same order of magnitude near the farm. Therefore, equation 3.6 is not simplified but solved numerically using a finite element method. The boundary conditions for equation 3.6 are prescribed tidal amplitude at the mouth and zero gradient of tidal amplitude along the shoal and at the end of the estuary. Note that equation 3.6 is generic and applicable to non-elongated estuaries or bays, where $\frac{dN_0}{dy}$ and $\frac{dN_0}{dx}$ are the same order of magnitude.

E.4 Subtidal Flow

The temporal average of equations 3.1b, c and equation 3.2 provides the governing equations for subtidal flow

$$\frac{\partial}{\partial x}\left(h\int_{-1}^{0}\overline{u_s}d\sigma + \overline{\eta_0 u_0|_{\sigma=0}}\right) + \frac{\partial}{\partial y}\left(h\int_{-1}^{0}\overline{v_s}d\sigma + \overline{\eta_0 v_0|_{\sigma=0}}\right) = 0 \quad (E10.a)$$

$$\frac{1}{h^2}\frac{\partial}{\partial\sigma}\left(\widetilde{A_z}\frac{\partial\overline{u_s}}{\partial\sigma}\right) + f\overline{v_s} - g\frac{\partial\overline{\eta_s}}{\partial x} = \overline{u_0\frac{\partial u_0}{\partial x}} + \overline{v_0\frac{\partial u_0}{\partial y}} + \overline{w_0\frac{\partial u_0}{\partial z}} + \frac{g}{\rho_0}\frac{\partial\rho}{\partial x}h\sigma + \frac{2\overline{u_0 v_0}}{R+y} \quad (E10.b)$$

$$\frac{1}{h^2}\frac{\partial}{\partial\sigma}\left(\widetilde{A_z}\frac{\partial\overline{v_s}}{\partial\sigma}\right) - f\overline{u_s} - g\frac{\partial\overline{\eta_s}}{\partial y} = \overline{u_0\frac{\partial v_0}{\partial x}} + \overline{v_0\frac{\partial v_0}{\partial y}} + \overline{w_0\frac{\partial v_0}{\partial z}} - \frac{\overline{{u_0}^2 - {v_0}^2}}{R+y} \quad (E10.c)$$

where, $\overline{\eta_s}$, $\overline{u_s}$, $\overline{v_s}$, $\overline{w_s}$ are also known as Eulerian average water level and velocities (Winant, 2008). The subtidal along channel baroclinic pressure gradient is $\frac{g}{\rho_0}\frac{\partial\overline{\rho}}{\partial x}h\sigma$ where it is assumed that the tidally averaged along channel density gradient, $\frac{\partial\overline{\rho}}{\partial x}$, is independent of depth. $\frac{2\overline{u_0 v_0}}{R+y}$ and $\frac{\overline{{u_0}^2 - {v_0}^2}}{R+y}$ are the centrifugal forces.

Let

$$F_x = -\left[\overline{u_0\frac{\partial u_0}{\partial x}} + \overline{v_0\frac{\partial u_0}{\partial y}} + \overline{w_0\frac{\partial u_0}{\partial z}}\right] - \frac{2\overline{u_0 v_0}}{R+y} - \frac{1}{h^2}\overline{\left(\frac{\eta_0}{h}\right)\frac{\partial}{\partial\sigma}\left(A_Z\frac{\partial u_0}{\partial\sigma}\right)}$$

$$F_y = -\left[\overline{u_0\frac{\partial v_0}{\partial x}} + \overline{v_0\frac{\partial v_0}{\partial y}} + \overline{w_0\frac{\partial v_0}{\partial z}}\right] + \frac{\overline{{u_0}^2 - {v_0}^2}}{R+y} - \frac{1}{h^2}\overline{\left(\frac{\eta_0}{h}\right)\frac{\partial}{\partial\sigma}\left(A_Z\frac{\partial v_0}{\partial\sigma}\right)}$$

where

$$\frac{\partial u_0}{\partial x} = \frac{\partial u_0}{\partial\tilde{x}} - \frac{\partial u_0}{\partial\sigma}\left(\frac{\sigma}{H}\frac{\partial H}{\partial\tilde{x}}\right), \quad \frac{\partial u_0}{\partial y} = \frac{\partial u_0}{\partial\tilde{y}} - \frac{\partial u_0}{\partial\sigma}\left(\frac{\sigma}{H}\frac{\partial H}{\partial\tilde{y}}\right), \quad \frac{\partial u_0}{\partial z} = \frac{1}{H}\frac{\partial u_0}{\partial\sigma}$$

$$\frac{\partial y_0}{\partial x} = \frac{\partial y_0}{\partial\tilde{x}} - \frac{\partial y_0}{\partial\sigma}\left(\frac{\sigma}{H}\frac{\partial H}{\partial\tilde{x}}\right), \quad \frac{\partial y_0}{\partial y} = \frac{\partial y_0}{\partial\tilde{y}} - \frac{\partial y_0}{\partial\sigma}\left(\frac{\sigma}{H}\frac{\partial H}{\partial\tilde{y}}\right), \quad \frac{\partial y_0}{\partial z} = \frac{1}{H}\frac{\partial y_0}{\partial\sigma}$$

$$\frac{\overline{u_0 v_0}}{R+y} = \frac{Re(U_0)Re(V_0) + Im(U_0)Im(V_0)}{R+y}$$

$$\frac{\overline{{u_0}^2 - {v_0}^2}}{R+y} = \frac{|U_0|^2 - |V_0|^2}{2(R+y)}$$

$$\frac{2}{h^2}\overline{\left(\frac{\eta_0}{h}\right)\frac{\partial}{\partial\sigma}\left(A_Z\frac{\partial u_0}{\partial\sigma}\right)} = -\frac{Re(N_0)Re\left(-i\omega U_0 - fV_0 + g\frac{\partial N_0}{\partial x}\right) + Im(N_0)Im\left(-i\omega U_0 - fV_0 + g\frac{\partial N_0}{\partial x}\right)}{h}$$

$$-\frac{2}{h^2}\overline{\left(\frac{\eta_0}{h}\right)\frac{\partial}{\partial\sigma}\left(A_Z\frac{\partial v_0}{\partial\sigma}\right)} = -\frac{Re(N_0)Re\left(-i\omega V_0 + fU_0 + g\frac{\partial N_0}{\partial y}\right) + Im(N_0)Im\left(-i\omega V_0 + fU_0 + g\frac{\partial N_0}{\partial y}\right)}{h}$$

To decouple Coriolis force, $\mathcal{w}^{\pm} = \overline{u_s} \pm i\bar{v}$, $sl^{\pm} = \frac{\partial\overline{\eta_s}}{\partial x} \pm i\frac{\partial\overline{\eta_s}}{\partial y}$, $\mathbb{F}^{\pm} = F_x \pm iF_y$

$$\frac{1}{h^2}\frac{\partial}{\partial\sigma}\left(A_z\frac{\partial\mathcal{w}^+}{\partial\sigma}\right) - if\mathcal{w}^+ - sl^+ + \mathbb{F}^+ = 0 \qquad (E11.a)$$

$$\frac{1}{h^2}\frac{\partial}{\partial\sigma}\left(A_z\frac{\partial\mathcal{w}^-}{\partial\sigma}\right) + if\mathcal{w}^- - sl^- + \mathbb{F}^- = 0 \qquad (E12.a)$$

Eddy viscosity structure

$$A_z = \begin{cases} A_0(\sigma+1)\left(\sigma_{Bp}-\sigma\right) & -1 \le \sigma \le \sigma_{Bh} \\ A_0\left[\left(A_{Bh}-{A_s}^*\right)\left(\frac{\sigma}{\sigma_{Bh}}\right)^2+{A_s}^*\right] & \sigma_{Bh} \le \sigma \le 0 \end{cases} \qquad (E13)$$

where

$$A_{Bh} = (\sigma_{Bh}+1)\left(\sigma_{Bp}-\sigma_{Bh}\right)\ A_0 = \kappa\widetilde{u^*}h\ \ {A_s}^* = \frac{A_s}{A_0}$$

Parabolic-Parabolic structure, $n = 2$, eddy viscosity is 1st order differentiable at σ_{Bh}, so that $\sigma_{Bh} = \frac{2\left({A_s}^*-\sigma_{Bp}\right)}{\sigma_{Bp}-1} < \sigma_{Bp}$

$${A_s}^* > \frac{\sigma_{Bp}\left(\sigma_{Bp}+1\right)}{2}$$

$$A_0 = \kappa\widetilde{u^*}h$$

$$A_z = \kappa\widetilde{u^*}h(\sigma+1)\left(\sigma_p-\sigma\right) = A_0(\sigma+1)\left(\sigma_p-\sigma\right) \quad -1 \le \sigma \le \sigma_h$$

$$A_z = A_0\left(A_I - A_s\left|\frac{\sigma}{\sigma_h}\right|^n + A_s\right) = A_0\left(A_I - A_s\frac{\sigma}{\sigma_h} + A_s\right) \qquad \sigma_h \le \sigma \le 0$$

$$A_I = (\sigma_h+1)\left(\sigma_p-\sigma_h\right)$$

No slip boundary conditions were applied at bottom.

$\sigma = -1+\sigma_0$, $w_1 = 0$

E.5 Solution of velocity profiles

E.5.1 Layer 1 $-\mathbf{1} \le \boldsymbol{\sigma} \le \boldsymbol{\sigma_h}$

$$w_1 = C_{1,1}P_{\alpha_1}(\beta_{\sigma,1}) + C_{1,2}Q_{\alpha_1}(\beta_{\sigma,1}) - \frac{isl}{a}$$
$$+ \frac{i(2\alpha_1)}{a(1+\sigma_{Bp})}\left[P_{\alpha_1}(\beta_{\sigma,1})\int_{-1+\sigma_0}^{\sigma}\frac{F(k)Q_{\alpha_1}(\beta_{k,1})}{P_{\alpha_1}(\beta_{k,1})Q_{\alpha_1+1}(\beta_{k,1}) - P_{\alpha_1+1}(\beta_{k,1})Q_{\alpha_1}(\beta_{k,1})}dk\right.$$
$$\left. - Q_{\alpha_1}(\beta_{\sigma,1})\int_{-1+\sigma_0}^{\sigma}\frac{F(k)P_{\alpha_1}(\beta_{k,1})}{P_{\alpha_1}(\beta_{k,1})Q_{\alpha_1+1}(\beta_{k,1}) - P_{\alpha_1+1}(\beta_{k,1})Q_{\alpha_1}(\beta_{k,1})}dk\right]$$

Note that, $P_\upsilon(z)Q_{\upsilon+1}(z) - P_{\upsilon+1}(z)Q_\upsilon(z) = -\frac{1}{\upsilon+1}$, therefore

$$w_1 = C_{1,1}P_\alpha(\beta_\sigma) + C_{1,2}Q_\alpha(\beta_\sigma) - \frac{isl}{a}$$
$$-\frac{i(2\alpha_1)(\alpha_1+1)}{a(1+\sigma_p)}\left[P_{\alpha_1}(\beta_{\sigma,1})\int_{-1+\sigma_0}^{\sigma}\mathbb{F}(k)Q_{\alpha_1}(\beta_k)dk - Q_{\alpha_1}(\beta_\sigma)\int_{-1+\sigma_0}^{\sigma}\mathbb{F}(k)P_{\alpha_1}(\beta_k)dk\right]$$

Decompose $C_{1,1}$ and $C_{1,2}$ into three components, such that

$$w_1 = C_{1,1,1}P_{\alpha_1}(\beta_{\sigma,1}) + C_{1,2,1}Q_{\alpha_1}(\beta_{\sigma,1}) + \left[C_{1,1,2}P_{\alpha_1}(\beta_{\sigma,1}) + C_{1,2,2}Q_{\alpha_1}(\beta_{\sigma,1}) + 1\right]\frac{-isl}{a}$$
$$-\frac{i(2\alpha_1)(\alpha_1+1)}{a(1+\sigma_p)}\left[P_{\alpha_1}(\beta_{\sigma,1})\int_{-1+\sigma_0}^{\sigma}\mathbb{F}(k)Q_{\alpha_1}(\beta_{k,1})dk\right.$$
$$\left. - Q_{\alpha_1}(\beta_{\sigma,1})\int_{-1+\sigma_0}^{\sigma}\mathbb{F}(k)P_{\alpha_1}(\beta_{k,1})dk\right] \qquad (E14)$$

where,

$$a^{\pm} = \mp f$$

$$\alpha_1 = \frac{1}{2}\left(-1 + \frac{\sqrt{A_0 + 4iah^2}}{\sqrt{A_0}}\right)$$

$$\beta_{\sigma,1} = \frac{1 + 2\sigma - \sigma_p}{1 + \sigma_p}$$

$$\beta_{k,1} = \frac{1 + 2k - \sigma_p}{1 + \sigma_p}$$

E.5.2 Layer 2 $\boldsymbol{\sigma \geq \sigma_h}$

$$w_2 = C_{2,1}P_{\alpha_2}(\beta_{\sigma,2}) + C_{2,2}Q_{\alpha_2}(\beta_{\sigma,2}) - \frac{isl}{a}$$
$$- \frac{i(\alpha_2)(\alpha_2 + 1)\sqrt{A_s - A_I}}{a\sqrt{A_S}\sigma_h}\left[P_{\alpha_2}(\beta_{\sigma,2})\int_{\sigma_h}^{\sigma}\mathbb{F}(k)Q_{\alpha_2}(\beta_k)dk\right.$$
$$\left. - Q_{\alpha_2}(\beta_{\sigma,2})\int_{\sigma_h}^{\sigma}\mathbb{F}(k)P_{\alpha}(\beta_{k,2})dk\right]$$

$$w_2 = C_{2,1,1}P_{\alpha_2}(\beta_{\sigma,2}) + C_{2,2,1}Q_{\alpha_2}(\beta_{\sigma,2}) + \left[C_{2,1,2}P_{\alpha_2}(\beta_{\sigma,2}) + C_{2,2,2}Q_{\alpha_1}(\beta_{\sigma,1}) + 1\right]\frac{-isl}{a}$$
$$- \frac{i(\alpha_2)(\alpha_2 + 1)\sqrt{A_s - A_I}}{a\sqrt{A_S}\sigma_h}\left[P_{\alpha_2}(\beta_{\sigma,2})\int_{\sigma_h}^{\sigma}\mathbb{F}(k)Q_{\alpha_2}(\beta_k)dk\right.$$
$$\left. - Q_{\alpha_2}(\beta_{\sigma,2})\int_{\sigma_h}^{\sigma}\mathbb{F}(k)P_{\alpha}(\beta_{k,2})dk\right] \qquad (E15)$$

where,

$$\alpha_2 = \frac{1}{2}\left(-1 + \frac{\sqrt{A_0(A_I - A_S) - 4iah^2{\sigma_h}^2}}{\sqrt{A_0}\sqrt{A_I - A_s}}\right)$$

$$\beta_{\sigma,2} = \frac{\sqrt{-A_I + A_s}\sigma}{\sqrt{A_S}\sigma_h}$$

$$\beta_{k,2} = \frac{\sqrt{-A_I + A_s}k}{\sqrt{A_S}\sigma_h}$$

The surface boundary conditions and interfacial boundary conditions are

$$\sigma = 0,\ \frac{1}{h}\frac{\partial u_1}{\partial \sigma} = -\frac{1}{h^2}\overline{\eta_0 \frac{\partial^2 u_0}{\partial \sigma^2}},\ \frac{1}{h}\frac{\partial v_1}{\partial \sigma} = -\frac{1}{h^2}\overline{\eta_0 \frac{\partial^2 v_0}{\partial \sigma^2}}$$

$$\sigma = \sigma_h,\ w_1 = w_2,\ \frac{\partial w_1}{\partial \sigma} = \frac{\partial w_2}{\partial \sigma}$$

E.5.3 Solution for subtidal surface slope

The subtidal velocities are defined as $u_T = \overline{u_s} + \frac{1}{h}\overline{\eta_0 u_0|_{\sigma=0}}$ and $v_T = \overline{v_s} + \frac{1}{h}\overline{\eta_0 v_0|_{\sigma=0}}$ (Robinson, 1983; Li and O'Donnell, 2005). Therefore, equation 3.7a becomes

$$\frac{\partial}{\partial x}\left(h\int_{-1}^{0} u_T d\sigma\right) + \frac{\partial}{\partial y}\left(h\int_{-1}^{0} v_T d\sigma\right) = 0 \quad (E16).$$

Two conservative conditions are introduced, where the cross-sectionally integrated along channel transport is equivalent to the river discharge, which is neglected in this work. Additionally, the depth integrated across channel transport is zero, resulting in

$$\int_{-B}^{B} h\int_{-1}^{0} u_T d\sigma\, dy = 0 \quad (E17.a)$$

$$h\int_{-1}^{0} v_T d\sigma = 0 \quad (E17.b).$$

Assuming the along channel subtidal surface slope $\frac{\partial \overline{\eta_s}}{\partial x}$ is constant across the channel, $\frac{\partial \overline{\eta_s}}{\partial x}$ and $\frac{\partial \overline{\eta_s}}{\partial y}$ were obtained by substituting the depth integrated subtidal current velocity, which was obtained by solving from equations 16 and 17.

$$\int_{-B}^{B}\left(h\int_{-1}^{0} u d\sigma + \overline{\eta_0 u_0|_{\sigma=0}}\right) = 0$$

$$h\int_{-1}^{0} v_T d\sigma = 0$$

Assume subtidal wave level slope is constant across the estuary

$$g\frac{\partial\overline{\eta_s}}{\partial x}=\frac{i}{4B}\int_{-B}^{B}\left(\frac{\mathscr{g}^{+}}{\mathcal{M}^{+}}+\frac{\mathscr{g}^{-}}{\mathcal{M}^{-}}+\left(\frac{1}{\mathcal{M}^{+}}+\frac{1}{\mathcal{M}^{-}}\right)\overline{\eta_0 u_0|_{\sigma=0}}+\left(\frac{1}{\mathcal{M}^{+}}-\frac{1}{\mathcal{M}^{-}}\right)i\overline{\eta_0 v_0|_{\sigma=0}}\right)dy$$

$$g\frac{\partial\overline{\eta_s}}{\partial y}=\frac{2i\overline{\eta_0 v_0|_{\sigma=0}}+\mathscr{g}^{+}-\mathscr{g}^{-}}{\mathcal{M}^{+}+\mathcal{M}^{-}}+\frac{i(M^{+}-M^{-})}{\mathcal{M}^{+}+\mathcal{M}^{-}}g\frac{\partial\overline{\eta_s}}{\partial x}$$

where

$$\mathcal{M}=-h\left[C_{1,1,2}\int_{-1+\sigma_0}^{\sigma_h}P_{\alpha}(\beta_{\sigma})d\sigma+C_{1,2,2}\int_{-1+\sigma_0}^{\sigma_h}Q_{\alpha}(\beta_{\sigma})d\sigma+C_{2,1,2}\int_{\sigma_h}^{0}P_{\alpha_2}(\beta_{\sigma,2})d\sigma+C_{2,2,2}\int_{\sigma_h}^{0}Q_{\alpha_2}(\beta_{\sigma,2})d\sigma\right.$$
$$\left.+(1-\sigma_0)\right]\frac{1}{a}$$

$$\mathscr{g}=h\left\{C_{1,1,1}\int_{-1+\sigma_0}^{\sigma_h}P_{\alpha}(\beta_{\sigma})d\sigma+C_{1,2,1}\int_{-1+\sigma_0}^{\sigma_h}Q_{\alpha}(\beta_{\sigma})d\sigma\right.$$
$$-\frac{i(2\alpha_1)(\alpha_1+1)}{a(1+\sigma_p)}\int_{-1+\sigma_0}^{\sigma_h}\left[P_{\alpha}(\beta_{\sigma})\int_{-1+\sigma_0}^{\sigma}\mathbb{F}(k)Q_{\alpha}(\beta_k)dk-Q_{\alpha}(\beta_{\sigma})\int_{-1+\sigma_0}^{\sigma}\mathbb{F}(k)P_{\alpha}(\beta_k)dk\right]d\sigma$$
$$+C_{2,1,1}\int_{\sigma_h}^{0}P_{\alpha_2}(\beta_{\sigma,2})d\sigma+C_{2,2,1}\int_{\sigma_h}^{0}Q_{\alpha_2}(\beta_{\sigma,2})d\sigma$$
$$-\frac{i(\alpha_2)(\alpha_2+1)\sqrt{A_s-A_I}}{a\sqrt{A_S}\sigma_h}\int_{\sigma_h}^{0}\left[P_{\alpha_2}(\beta_{\sigma,2})\int_{-1+\sigma_0}^{\sigma}\mathbb{F}(k)Q_{\alpha_2}(\beta_k)dk\right.$$
$$\left.\left.-Q_{\alpha_2}(\beta_{\sigma,2})\int_{-1+\sigma_0}^{\sigma}\mathbb{F}(k)P_{\alpha_2}(\beta_{k,2})dk\right]\right\}$$

$$\int_{-1+\sigma_0}^{\sigma_h}P_{\alpha_1}(\beta_{\sigma,1})d\sigma=\frac{1+\sigma_p}{2(1+2\alpha_1)}\left\{P_{\alpha_1+1}(\beta_{\sigma_h,1})-P_{\alpha_1-1}(\beta_{\sigma_h,1})-\left[P_{\alpha_1+1}(\beta_{-1+\sigma_0,1})-P_{\alpha_1-1}(\beta_{-1+\sigma_0,1})\right]\right\}$$

$$\int_{-1+\sigma_0}^{\sigma_h} Q_{\alpha_1}(\beta_{\sigma,1})d\sigma$$

$$= -\sqrt{\pi}\frac{1+\sigma_p}{2}\left\{\frac{1}{\alpha_1(1+\alpha_1)}\frac{\cos\frac{\alpha_1\pi}{2}\Gamma\left(\frac{\alpha_1}{2}+1\right)}{\Gamma\left(\frac{\alpha_1+1}{2}\right)}\left[\ {}_2F_1\left(-\frac{\alpha_1+1}{2},\frac{\alpha_1}{2};\frac{1}{2};{\beta_{\sigma_h,1}}^2\right)\right.\right.$$

$$\left. - \ {}_2F_1\left(-\frac{\alpha_1+1}{2},\frac{\alpha_1}{2};\frac{1}{2};{\beta_{-1+\sigma_0,1}}^2\right)\right]$$

$$+\frac{\sin\frac{\alpha_1\pi}{2}\Gamma\left(\frac{\alpha_1+1}{2}\right)}{2\Gamma\left(\frac{\alpha_1}{2}+1\right)}\left[\beta_{\sigma_h,1}\ \ {}_2F_1\left(\frac{\alpha_1+1}{2},-\frac{\alpha_1}{2};\frac{3}{2};{\beta_{\sigma_h,1}}^2\right)\right.$$

$$\left.\left. - \beta_{-1+\sigma_0,1}\ \ {}_2F_1\left(\frac{\alpha_1+1}{2},-\frac{\alpha_1}{2};\frac{3}{2};{\beta_{-1+\sigma_0,1}}^2\right)\right]\right\}$$

$$\int_{\sigma_h}^{0} P_{\alpha_2}(\beta_{\sigma,2})d\sigma = \frac{\sqrt{A_S}\sigma_h}{\sqrt{-A_I+A_s}}\frac{1}{1+2\alpha_1}\{P_{\alpha_2+1}(\beta_{0,2}) - P_{\alpha_1-1}(\beta_{0,2}) - [P_{\alpha_2+1}(\beta_{\sigma_h,2}) - P_{\alpha_2-1}(\beta_{\sigma_h,2})]\}$$

$$\int_{\sigma_h}^{0} Q_{\alpha_2}(\beta_{\sigma,2})d\sigma = -\sqrt{\pi}\frac{\sqrt{A_S}\sigma_h}{\sqrt{-A_I+A_s}}\left[\frac{1}{\alpha_2(1+\alpha_2)}\frac{\cos\frac{\alpha_2\pi}{2}\Gamma\left(\frac{\alpha_2}{2}+1\right)}{\Gamma\left(\frac{\alpha_2+1}{2}\right)}\ \ {}_2F_1\left(-\frac{\alpha_2+1}{2},\frac{\alpha_2}{2};\frac{1}{2};{\beta_{0,2}}^2\right)\right.$$

$$+\frac{\sin\frac{\alpha_2\pi}{2}\Gamma\left(\frac{\alpha_2+1}{2}\right)}{2\Gamma\left(\frac{\alpha_2}{2}+1\right)}\beta_{0,2}\ \ {}_2F_1\left(\frac{\alpha_2+1}{2},-\frac{\alpha_2}{2};\frac{3}{2};{\beta_{0,1}}^2\right)$$

$$-\frac{1}{\alpha_2(1+\alpha_2)}\frac{\cos\frac{\alpha_2\pi}{2}\Gamma\left(\frac{\alpha_2}{2}+1\right)}{\Gamma\left(\frac{\alpha_2+1}{2}\right)}\ \ {}_2F_1\left(-\frac{\alpha_2+1}{2},\frac{\alpha_2}{2};\frac{1}{2};{\beta_{\sigma_h,2}}^2\right)$$

$$\left.-\frac{\sin\frac{\alpha_2\pi}{2}\Gamma\left(\frac{\alpha_2+1}{2}\right)}{2\Gamma\left(\frac{\alpha_2}{2}+1\right)}\beta_{\sigma_h,2}\ \ {}_2F_1\left(\frac{\alpha_2+1}{2},-\frac{\alpha_2}{2};\frac{3}{2};{\beta_{\sigma_h,2}}^2\right)\right]$$

E.6 Validation of vertical eddy viscosity parameterization canopy flow

The vertical profiles of nondimensional along channel velocity and Reynolds stress in channel flow with suspended canopy computed from analytical model proposed in this work were compared with

experimental data from Plew (2011). Four experimental cases were picked up from the experiment (run B12 ~ 15). The water depth was 0.2 m, the penetration of canopy was 0.1 m, and canopy density varies from 0.477 ~ 1.908 m^{-1}. The model resolves flow structure of canopy flow including the bottom boundary layer, the mixing layer, and the drag layer (Figure E1.a). In order to quantitatively examine the agreement among the model result and laboratory measurement, the root-mean-square error of velocity, $RMSE = \sqrt{\frac{\sum_{i=1}^{n}(u_i^{model} - u_i^{measure})}{n}}$ was computed, which was around 0.0037 ~ 0.0047 m/s among the four cases. The normalized root-mean-square error $RMSE/\bar{u}$ = 3.3 ~ 5.5% meaning that the overall error is relatively small comparing with depth averaged velocity. Note that maximum deviation among model result and measurement occurred closed to the bottom boundary, where relative error was around 10% (Figure E1.a).

The vertical distribution of the Reynolds stress from the model agreed well with measurement. The Reynolds stress profile presented two peak values where one was closed to the bottom and the other was at the lower edge of the canopy (Figure E1.b). The normalized root-mean-square error of Reynolds stress was around 22 ~ 25%. Since the Reynolds stress is a higher order description of flow conditions where deviations among model results and measurements were amplified. The model overestimated the Reynolds stress closed the bottom while slightly underestimated the Reynolds stress at bottom edge of the canopy (Figure E1.b), which was consistent with the velocity underestimation near bottom and near lower edge of canopy. Overall, the analytical model result agreed favorably with experimental measurements. Consequently, the 5-layer piecewise parabolic parameterization works well on mimicking the structure of vertical eddy viscosity in canopy flow especially in the mixing layer.

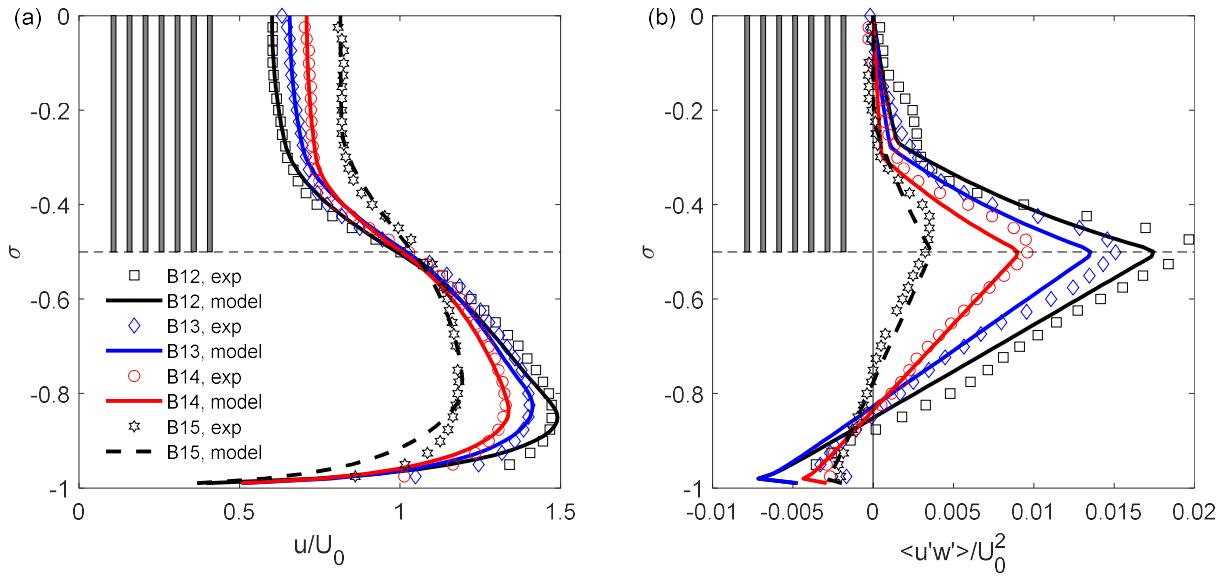

Figure E1. Validation of analytical model with laboratory experiments. (a) nondimensional along channel velocity (u/U_0). (b) nondimensional Reynolds stress ($\langle u'w' \rangle / U_0^2$). U_0 is depth averaged along channel velocity. Markers denote measurements while lines denote model results with various canopy densities. Grey bars denote the canopy layer. The selected experimental cases B12 ~ B15 have the same canopy penetration of half water depth but with various canopy densities 1.908 m^{-1} (B12), 1.272 m^{-1} (B13), 0.954 m^{-1} (B14), and 0.477 m^{-1} (B15).

E.7. Verification of tidal flow

The semidiurnal (M2) tidal current velocity in along (u_0) and across (v_0) channel direction from the model was compared with those reconstructed from the field measurements in the main channel near the farm's seaward boundary. The amplitude of u_0 reconstructed from the field observations was 0.44 m/s at z = -0.9 m in the main channel, while u_0 from model with farm was around 0.42 m/s, which was slightly underestimated by 6.5% (Figure E2). Without considering the farm, the amplitude of u_0 decreased by 0.05

m/s, suggesting that along channel tidal current velocity increased in the main channel due to farm-induced flow bypassing.

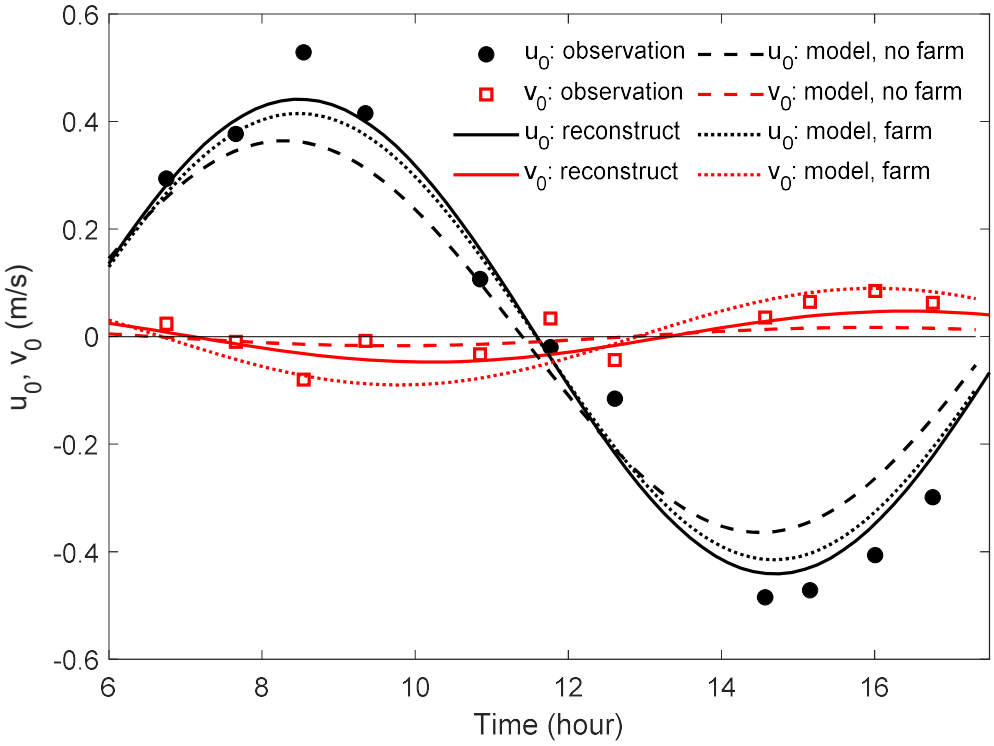

Figure E2 Time series of along (u_0) and across (v_0) semidiurnal (M2) tidal current at water depth of -0.9 m in the main channel near farm's seaward boundary. Markers denote current along (circle) and across (square) velocity collected from field on June 27, 2017 (Liu and Huguenard, 2020). Solid lines denote along (black) and across (red) M2 tidal current velocity reconstructed from harmonic analysis of field data. Dash lines denote model results of along (black) and across (red) tidal current from without considering the farm. Dotted lines denote model results of along (black) and across (red) tidal current from by considering the farm.

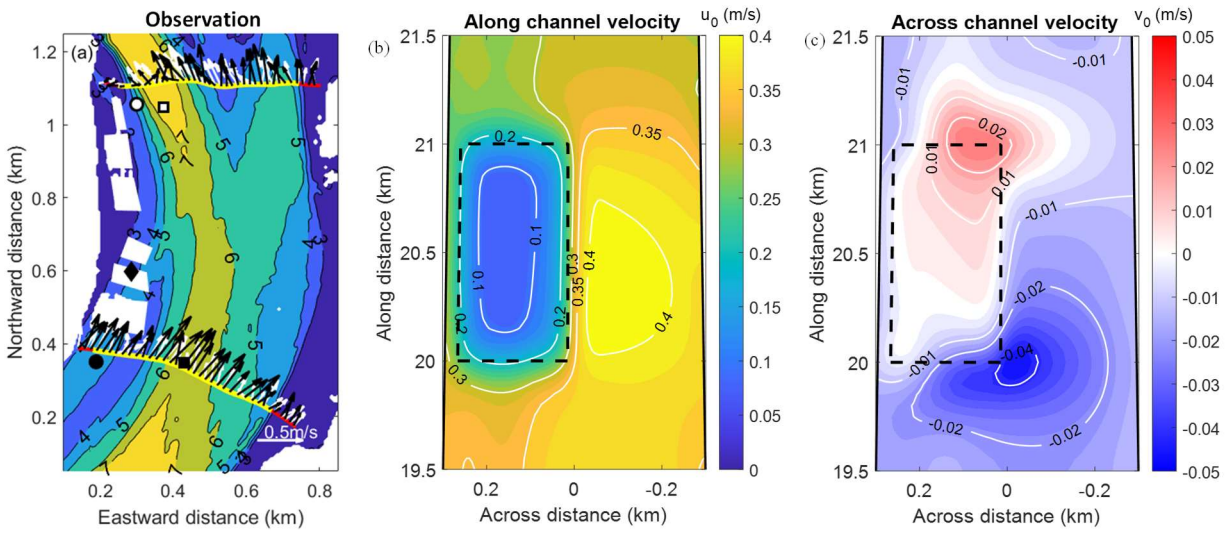

Figure E3 Near surface tidal current velocity at peak flood. (a) Distribution of current velocity across the estuary collected from field on June 27, 2017 (Liu and Huguenard, 2020). Contours are water depth at peak flood, vectors are velocity at 0. 8 m water depth below surface. (b) Distribution of along channel tidal current velocity (u_0) at surface obtained from present model. The dashed box denotes farm area. (c) Distribution of across channel tidal current velocity (v_0) at surface obtained from present model. Red color denotes across channel velocity towards to the left, bule color denote across channel velocity towards to the right.

The amplitude of the observed across channel M2 tidal current (v_0) was 0.047 m/s (Figure E2). Without the farm, v_0 was 0.017 m/s, which was 1/3 of the observed value. With the farm, the amplitude of v_0 reached up to 0.089 m/s which was 1.9 times larger than the observations, though, the farm model case compared favorably with original field collected data at peak flood and peak ebb. This disparity in the M2 v_0 between farm and no farm cases suggests that the farm bypassing identified in Liu and Huguenard (2020) enhanced v_0. Additionally, the phase of v_0 in the farm case was consistent with field observations. Although the magnitude of u_0 and v_0 in the farm case showed a minor deviation from the observations, similar phases among the reconstructed tidal flow and the observations verified the model's performance despite using an idealized bathymetry.

BIOGRAPHY OF THE AUTHOR

Zhilong Liu was born and raised in Shandong, China. He graduated from Pingyuan No. 1 High School and attended Tianjin University in China in 2008. Zhilong obtained his Bachelor's degree and Master's degree in Naval Architecture and Ocean Engineering in 2012 and 2015, respectively. He started his PhD study at the University of Maine in May 2015 with Dr. Qingping Zou working on wind influence on wave breaking. In September 2016, Zhilong transferred to Dr. Kimberly Huguenard's research group to work on hydrodynamic impacts of expanding aquaculture. During his PhD study, he has the following peer-reviewed journal articles and conference proceedings published:

[4] Bricknell, I., Birkle, S, Van Kirk. T., Hamlin, H., Duffy, K., Brawley, S., Capistrant-Fossa, K., Hugenard, K., Byron, C., Van Walsum, G. P., **Liu, Z.**, Zhu, L., Johnston, T., Grebe, G., Taccardi, E., Miller, M., Preziosi, B., Brady, D., Bowden, T., Quigley, C., Moeykens, S., 2020. Cold water aquaculture resilience, a review of the impact of likely scenarios in a climate change vulnerable ecological system. *Review in Aquaculture*. https://doi.org/10.1111/raq.12483

[3] **Liu, Z.**, Huguenard, K., 2020. Hydrodynamic response of a floating aquaculture farm in a low inflow estuary, *Journal of Geophysical Research: Oceans.*

[2] Lieberthal, B., Huguenard, K., Ross, L., **Liu, Z.**, 2019. Intratidal Variability of Water Quality in the Damariscotta River, Maine. *Water*, 11(12), 2603.

[1] Chen, H., Zou, Q., **Liu, Z**. 2017. A coupled RANS-VOF and finite element model for wave interaction with highly flexible vegetation. *Coastal Engineering Proceedings*, 1(35), 25.

Zhilong is a candidate for the Doctor of Philosophy degree in Civil and Environmental Engineering from the University of Maine in May 2021.